

NEOTETHYAN TECTONOSTRATIGRAPHIC EVOLUTION OF SE
ANATOLIAN BASIN, TÜRKİYE

A THESIS SUBMITTED TO
THE GRADUATE SCHOOL OF NATURAL AND APPLIED SCIENCES
OF
MIDDLE EAST TECHNICAL UNIVERSITY

BY

MUSTAFA TUNCER

IN PARTIAL FULFILLMENT OF THE REQUIREMENTS
FOR
THE DEGREE OF DOCTOR OF PHILOSOPHY
IN
GEOLOGICAL ENGINEERING

JANUARY 2023

Approval of the thesis:

**NEOTETHYAN TECTONOSTRATIGRAPHIC EVOLUTION OF SE
ANATOLIAN BASIN, TÜRKİYE**

submitted by **MUSTAFA TUNCER** in partial fulfillment of the requirements for
the degree of **Doctor of Philosophy in Geological Engineering, Middle East
Technical University** by,

Prof. Dr. Halil Kalıpçılar
Dean, Graduate School of **Natural and Applied Sciences** _____

Prof. Dr. Erdin Bozkurt
Head of the Department, **Geological Engineering** _____

Prof. Dr. Nuretdin Kaymakcı
Supervisor, **Geological Engineering Dept., METU** _____

Examining Committee Members:

Prof. Dr. Erdin Bozkurt
Geological Engineering., METU _____

Prof. Dr. Nuretdin Kaymakcı
Geological Engineering., METU _____

Prof. Dr. Bora Rojay
Geological Engineering., METU _____

Assoc. Prof. Dr. Bora Uzel
Geological Engineering., Dokuz Eylül Univ. _____

Assoc. Prof. Dr. Erhan Gülyüz
Geological Engineering., Van Yüzüncü Yıl Univ. _____

Date: 25.01.2023

I hereby declare that all information in this document has been obtained and presented in accordance with academic rules and ethical conduct. I also declare that, as required by these rules and conduct, I have fully cited and referenced all material and results that are not original to this work.

Name Last name : Mustafa Tuncer

Signature :

ABSTRACT

NEOTETHYAN TECTONOSTRATIGRAPHIC EVOLUTION OF SE ANATOLIAN BASIN, TÜRKİYE

Tuncer, Mustafa
Doctor of Philosophy, Geological Engineering
Supervisor : Prof. Dr. Nuretdin Kaymakcı

January 2023, 183 pages

The SE Anatolian basin constitutes the northern margin of the Arabian Plate in SE Türkiye and contains a continuous sedimentary succession from the pre-Cambrian to the recent. It has evolved mainly into four tectonic phases, the first phase includes the Pre-Cambrian to Permian continental platform stage that constitutes the core sequences of the Arabian platform and is represented by continental to shallow marine, and deep marine deposits, the second phase includes Triassic to Jurassic rift-drift stage of the Neotethys ocean and the basin acted as a passive margin during this stage and characterized by shallow marine deposits with occasional continental deposits in places. The third phase is represented by shallow marine and deep marine deposits and it involves the subduction of the Neotethys mainly during the late Cretaceous and ophiolite obduction at the rim of the Arabian Plate. The fourth sequence includes the terminal closure of the Neotethys and the collision of adjacent continental blocks. This sequence is represented by regressive deep marine to shallow marine and continental clastics.

Overall Upper Cretaceous to Recent basin-fill units are characterized by northwards thickening wedge-shaped geometry such as Upper Cretaceous deep marine Kastel Formation, Upper Cretaceous-Paleocene deep marine Germav Formation, Lower

Miocene shallow and deep marine deposits and Upper Miocene continental clastics. This northward thickening of the basin fill deposits suggests flexural basin development, rapid subsidence, and the creation of accommodation space in front of the thrust front mainly at its northern parts.

Apart from the basin infill of the SE Anatolian basin, several allochthonous units such as the upper Cretaceous Karadut Complex and Koçali Ophiolite were emplaced mainly along the northern rim of the basin. These units are related to an accretionary prism growth during the subduction of the Neotethys oceanic lithosphere northwards. The obduction is associated with deep marine units accreted within the Karadut Complex and ophiolitic sequence fragments (Koçali Ophiolites) as well as fore-arc sequences developed piggyback at the top of the growing accretionary prism. They are characterized by regressive shallow marine to continental deposits accumulated at the top of the growing accretionary prism. A basin-wide shallowing and domination continental deposition almost everywhere in the basin is ascribed to dynamic topography resulting from shallow subduction due to the subduction of the mid-ocean ridge that caused regional uplift and subaerially emergence during the Lower Eocene. The Lower Miocene deep marine deposits in the northern parts of the basin become thinner towards the south in SE Türkiye. Abrupt southwards shift of depocenter, wedge-shape geometry, and facies associations and their distribution indicate peripheral foreland basin deposition as the continental collision took place. The northern boundary of the Arabian Plate considerably contributed to the development of an early Miocene flexural foreland basin. The Upper Miocene to recent sequences is characterized by continental deposits and they unconformably overlie all other units in the basin.

The structures that shape the present tectonic scheme of the basin are dominated by compressional and contractional structures characterized dominantly by thrust faults and fault propagation folds, as well as strike-slip faults that largely accommodated translation of the thrust faults and folds. In addition, some of the structures are developed due to reactivation or inversion of pre-existing structures that developed

mainly during the early Mesozoic opening of the Neotethys ocean. The Triassic-Jurassic normal faults are related to rifting of the Neotethys Ocean while the Late Cretaceous structures are mainly related to ophiolite obduction and thrusting. The late Eocene-to-late Miocene structures are related to accretionary wedge growth and the terminal collision-related thrusting and inversion mainly at the northern rim of the basin. Inversion structures further south of the rim involved the basement and resulted in fault-propagation folds related to the inversion of previous normal faults. One of the best examples of these structures is developed at the base of the Mardin high, Hazro area, Tavan, Sadak, Reşan, and Batman anticlines. In total 358 fault slip data collected from 26 different locations along the interpreted seismic lines, indicate that all of the faults that are interpreted in the seismic sections and exposed on the surface are characterized by almost vertical σ_3 and horizontal σ_1 orientations. However, the overall σ_1 trend changes from NW-SE in the western part of the basin, while it is almost N-S in the center and NE-SW in the eastern part of the basin. This indicates northwards radial fanning of σ_1 directions almost perpendicular to the Bitlis Suture Zone and the northern rim of the basin.

The resulting structures are typical examples of south-verging thin-skinned deformation, manifested by imbricate thrust fault belts and fault propagation in a foreland setting. The basal decollement surface seems to be the Ordovician or Silurian mudstones and shales. Restored balanced cross sections indicate that the western part of the study area experienced a minimum of 32.31% shortening while the central part experienced 19,12% shortening and the eastern areas experienced 16,62% minimum total shortening. Additionally, the maximum and minimum ratios of shortening in sedimentary units are 9,09 % and 5,88 % at the east and the center, respectively.

Keywords: SE Anatolian, Continental Collision, Foreland Basin, Cross Section Restoration, Seismic Interpretation

ÖZ

GD ANADOLU HAVZASININ NEOTETİS TEKTONOSTRATİGRAFİK EVRİMİ, TÜRKİYE

Tuncer, Mustafa
Doktora, Jeoloji Mühendisliği
Tez Yöneticisi: Prof. Dr. Nuretdin Kaymakcı

Ocak 2023, 183 sayfa

Türkiye'nin güneydoğusunda Arap Platformunun kuzey kenarını oluşturan havza, Kambriyen öncesinden yakın zamana kadar kesintisiz bir sedimanter istif içermektedir. Havza başlıca dört tektonik evre geçirmiştir; ilk evre Arap platformunun çekirdek istifini oluşturan ve karasal, sığ denizel ve derin denizel çökellerle temsil edilen Pre-Kambriyen ile Permian kıtasal platform evresini içerir, ikinci evre Neotethys okyanusunun Triyas ila Jura açılma-uzaklaşma evresini içerir ve havza bu evre sırasında pasif bir kenar olarak hareket etmiş ve yer yer karasal çökellerle birlikte sığ denizel çökellerle karakterize edilmiştir. Üçüncü evre sığ deniz ve derin deniz çökelleri ile temsil edilir ve esas olarak Geç Kretase döneminde Neotethys'in dalmasını ve Arap Plakası'nın kenarındaki ofiyolit üzerlemesini içerir. Dördüncü dönem, Neotethys'in son kapanışını ve bitişik kıta bloklarının çarpışmasını içerir. Bu dönem, derin denizden sığ denizel ve karasal klastiklere doğru bir istif ile temsil edilir.

Genel olarak Üst Kretase'den Yakın döneme kadar olan havza dolgu birimleri, Üst Kretase derin denizel Kastel Formasyonu, Üst Kretase-Paleosen derin denizel Germav Formasyonu, Alt Miyosen sığ ve derin denizel çökeller ve Üst Miyosen karasal klastikler gibi kuzeye doğru kalınlaşan kama şekilli geometri ile karakterize

edilmektedir. Havza dolgu çökellerinin kuzeye doğru kalınlaşması, bükülmeli havza gelişimine, hızlı çökmeye ve özellikle kuzey kesimlerinde bindirme cephesinin önünde depolanma alanı oluşumuna neden olmuştur.

Güneydoğu Anadolu havzasının havza dolgusunun yanı sıra, Üst Kretase Karadut Kompleksi ve Koçali Ofiyoliti gibi bir dizi allokton birim, özellikle havzanın kuzey kenarı boyunca yerleşmiştir. Bu birimler, Neotetis okyanus litosferinin kuzeye doğru dalması sırasında oluşan yığışım prizması büyümesiyle ilişkilidir. Ofiyolit üzerlemesi, Karadut Kompleksi ve ofiyolitik seri parçaları (Koçali Ofiyolitleri) içinde biriken derin denizel birimlerle ve büyüyen yığışım prizmasının üstünde bindirme üstü havza olarak gelişen yay önü istifleriyle ilişkilidir. Büyüyen yığışım prizmasının üstünde oluşan regresif sığ denizel ve karasal çökeller ile karakterize edilirler. Havza genelinde sığlaşma ve havzanın hemen her yerinde karasal çökelenin hakim olması, Alt Eosen'de bölgesel yükselme ve su üstüne çıkan okyanus ortası sırtın sığ dalmasından kaynaklanan dinamik topografyaya dayandırılmaktadır. Türkiye'nin güneydoğusunda havzanın kuzey kesimlerindeki Alt Miyosen derin denizel çökeller güneye doğru incelmektedir. Depozonun, kama şeklindeki geometrinin ve fasiyes ilişkilerinin ve bunların dağılımının aniden güneye doğru kayması, kıtasal çarpışma gerçekleşirken üzerlenen kıta üstünde önülke havza çökeliğini işaret etmektedir. Arap Plakasının kuzey sınırı, erken Miyosen bükülme ön havzasının gelişimine önemli ölçüde katkıda bulunmuştur. Üst Miyosen'den yakın zamana kadar olan istifler karasal çökellerle karakterize edilir ve havzadaki diğer tüm birimlerin üzerine uyumsuz olarak gelirler.

Havzanın mevcut tektonik şemasını şekillendiren yapılar, baskın olarak bindirme fayları ve fay ilerleme kıvrımlarının yanı sıra doğrultu atımlı faylar olup büyük ölçüde bindirme fayları ve kıvrımların hareketini sağlayan sıkışma ve daralma yapıları tarafından kontrol edilmektedir. Buna ek olarak, bazı yapılar, Neotethys okyanusunun erken Mesozoik açılımı sırasında gelişen önceden var olan yapıların yeniden aktif hale gelmesi veya terslenen yapılar nedeniyle gelişmiştir. Triyas-Jura normal fayları Neotetis Okyanusu'nun açılması ile ilgiliyken, Geç Kretase yapıları

esas olarak ofiyolitüzerlemesi ve bindirmesi ile ilgilidir. Geç Eosen-Geç Miyosen yapıları, yığışım prisma büyümesi ve son olarak havzanın kuzey kenarındaki çarpışmaya bağlı bindirme ve terslenen yapılar ile ilişkilidir. Kenarın daha güneyinde yer alan terslenen yapılar ana temeli içermekte ve önceki normal fayların terslenmesi ile ilişkili fay ilerleme kıvrımları ile sonuçlanmaktadır. Bu yapıların en iyi örneklerinden biri Mardin yükselimi, Hazro bölgesi, Tavan, Sadak, Reşan ve Batman antiklinallerinin tabanında gelişmiştir. Yorumlanan sismik hatlar boyunca 26 farklı konumdan toplanan toplam 358 fay kayma verisi, sismik kesitlerde yorumlanan ve yüzeyde açığa çıkan tüm fayların neredeyse dikey σ_3 ve yatay σ_1 yönleri ile karakterize olduğunu göstermektedir. Bununla birlikte, genel σ_1 yönü havzanın batı kesiminde KB-GD yönünde değişirken, merkezde neredeyse N-S ve havzanın doğu kesiminde NE-SW yönündedir. Bu, σ_1 yönlerinin Bitlis Sütür Zonu'na ve havzanın kuzey kenarına neredeyse dik olarak kuzeye doğru radyal yayılımını göstermektedir.

Ortaya çıkan yapılar, birbirine bindirme faylar ve bir önülke havzası ortamında fay ilerleme kıvrımları ile kendini gösteren, güneye doğru ince kabuk deformasyonun tipik örnekleridir. Taban dekolmanı yüzeyinin Ordovisiyen veya Silüriyen çamurtaşları ve şeylleri olduğu görülmektedir. Restore edilmiş balanslı kesitler, çalışma alanının batı kısmının minimum %32,31 kısalma yaşadığını, orta kısmının %19,12 kısalma yaşadığını ve doğu alanlarının minimum %16,62 toplam kısalma yaşadığını göstermektedir. Ayrıca, sedimanter birimlerdeki maksimum ve minimum kısalma oranları doğuda ve merkezde sırasıyla %9,09 ve %5,88'dir.

Anahtar Kelimeler: GD Anadolu, Kıtasal Çarpışma, Önülke Baseni, Enine Kesit Restorasyonu, Sismik Yorumlama

To my family

ACKNOWLEDGMENTS

Many people contributed and supported the completion of this thesis. I would like to express my sincere gratitude, although words are weak considering their contribution and support.

I would like to express my sincere gratitude to my supervisor, Prof. Dr. Nuretdin Kaymakcı, for all his efforts, enthusiastic encouragement, and his essential guidance. His educational philosophy inspired me to be independent in all steps of my thesis. I greatly appreciate the opportunity Prof. Dr. Nuretdin Kaymakcı has given me to work with him.

Besides my supervisor, I would like to thank Assoc. Prof. Dr. Erhan Gülyüz for his help and support in improving the quality of my thesis and his guidance during the fieldwork and analysis of the data.

My PhD committee members, Prof. Dr. Bora Rojay, Prof. Dr. Erdin Bozkurt, and Assoc. Prof. Dr. Bora Uzel is deeply appreciated for their critical suggestions for improving the quality of this thesis.

It would have been impossible to conduct this research without the seismic and well datasets provided by Turkish Petroleum. I would like to express my deepest thanks to Turkish Petroleum.

I would also like to thank Dr. Remzi Aksu, Mahmut Utmanoğulları, and Muhammed Fatih Ayyıldız, for sharing their experiences during field studies.

I would like to thank my colleagues Görkem Yağcı, Ahmet Zeki Yücesoy, Abdul Qayyum, Ahmed Abdelmaksoud, Furkan Gündoğdu, and Halil Şeker for their help and support.

Last but not least, I would like to express my special thanks to my wife Sümeyye Tuncer for her endless support, understanding, patience, and love. Finally, I would like to thank my little son, Mustafa Mirza Tuncer, who made his appearance in this world in the middle of this study and made his parents very happy.

TABLE OF CONTENTS

ABSTRACT.....	v
ÖZ	viii
ACKNOWLEDGMENTS	xii
TABLE OF CONTENTS.....	xiii
LIST OF TABLES	xvi
LIST OF FIGURES	xvii
CHAPTERS	
1 INTRODUCTION	1
1.1 Introduction	1
1.2 Aim of the Study	4
1.3 Methods of the Study	6
1.4 The layout of the Thesis	6
1.5 Geological Setting and Literature Survey	7
1.5.1 Regional tectonic plate setting	8
1.5.2 Crystalline Basement	9
1.5.3 Sedimentary Units.....	15
2 METHODOLOGY	33
2.1 Data and Methods of study.....	33
2.2 Mapping	35
2.2.1 Mapping Units	35
2.2.2 Mapping Structures	36
2.3 Stratigraphical Analyses.....	37

2.3.1	Facies Determination.....	37
2.3.2	Mapping Facieses	39
2.3.3	Well and Section Correlations.....	39
2.4	Kinematic Analyses	39
2.4.1	Fold Analyses	40
2.4.2	Determinations of Syn-depositional Unconformities.....	40
2.4.3	Paleostress Analyses.....	42
2.5	Cross-section Constructions	43
2.5.1	2-D Seismic Interpretation	43
2.6	Cross-section Balancing and Restoration	48
2.6.1	Velocity Modelling/Depth Conversion	52
2.6.2	Shortening Ratio Calculations.....	54
3	ANALYSIS AND INTERPRETATIONS	55
3.1	Morphotectonics	55
3.2	Stratigraphy.....	62
3.2.1	Facieses Distribution	74
3.2.2	Well Section Correlations.....	83
3.3	Kinematic Analyses	96
3.3.1	Fold Analyses	96
3.3.2	Progressive Unconformities	106
3.3.3	Paleostress Analyses.....	110
3.4	Cross Sections.....	116
3.4.1	2D Seismic Interpretation.....	116
3.5	Cross-Section Construction and Balancing	142

3.5.1	Balancing and Shortening Ratio Calculations	142
4	DISCUSSION	149
4.1	Structural Evolution of the SE Anatolian Basin.....	149
4.2	Stratigraphic (Framework) Characteristics of the SE Anatolian Basin..	151
5	CONCLUSION.....	157
	REFERENCES	161
	APPENDICES	
A.	Collected paleostress data	171
B.	Paleostress location photos.....	181
	CURRICULUM VITAE.....	183

LIST OF TABLES

TABLES

Table 1.1 Contact relationships from pre-Cambrian to upper Miocene units	18
Table 2.1 Workflow of the study.....	34
Table 3.1 Contact relationships and their depositional environments of classes from pre-Cambrian to Upper Miocene units.	73
Table 4.1 Results of fold analyses in Adiyaman, Diyarbakir, and Batman-Siirt sub-areas.	100
Table 5.1 Results of paleostress inversion	114
Table 6.1 Regional shortening results of the Adiyaman, Diyarbakır, and Batman-Siirt sub-areas.	143

LIST OF FIGURES

FIGURES

- Figure 1.1 Simplified tectonic scheme around Türkiye (Kaymakci et al. 2010). 3
- Figure 1.2 Location and b) the tectonic framework of the study area c) Geological map of SE Anatolian based on the surface and compilation of existing map (derived from the Turkish Petroleum Company database). 5
- Figure 1.3 The figure shows a simplified geological map of the study area, compiled from the Turkish Petroleum Company database and the geological map of MTA 2002. 16
- Figure 1.4. Simplified stratigraphic section of the SE Anatolian Basin. 17
- Figure 1.5. Pictures from the field demonstrate a) and b) Paleozoic succession in Derik (Mardin region) and c) Tut (Adiyaman region). 20
- Figure 1.6 The illustration depicts the contact relationship with unconformity level between middle-late Ordovician (Bedinan Formation) and Aptian to Cenomanian (Mardin Group) in Mardin High, Mardin region. 21
- Figure 1.7 The pictures demonstrate a) late Silurian to late Devonian succession (Diyarbakır Group), b) sandstones with cross-bedding within the Hazro Formation in Hazro High, and c) contact relationship between late Silurian to late Devonian (Diyarbakır Group) and the Upper Permian (Tanin Group) in Hazro High, Diyarbakır region. 22
- Figure 1.8 The pictures show contact relationships between the Aptian to Cenomanian (Mardin Group), the late Campanian to early Maastrichtian deposits (Sayindere and Kastel formations), and the allochthonous Karadut Complex (upper Cretaceous) in Adiyaman region. 26
- Figure 1.9 The images show contact relationships between a) the Şırnak Group (Terbüzek, Besni, and Germav formations) (Upper Cretaceous), Hoya Formation (middle Eocene-Oligocene), and Şelmo Formation (Upper Miocene) and b) the Germav Formation (upper Cretaceous-Paleocene), Gercüş Formation (lower Eocene) and Hoya Formation (middle Eocene-Oligocene) in Adiyaman region. ... 29

Figure 1.10 Picture a) shows the Lice Formation (lower Miocene), which includes evaporite deposits (b and c) in the Batman-Siirt region.	30
Figure 2.1 The distribution wells and 2D seismic line locations in the study area. Circles indicate the wells' locations and 2D seismic lines (red and blue lines).....	36
Figure 2.2 Orientations of structures and distributions are shown on the map in the study area.....	38
Figure 2.3 A genetic model of syntectonic unconformities in areas where deformation and deposition are related (after Riba, 1976 and Anadòn 1986 et al., 1986).....	41
Figure 2.4 The position of the regional and local cross-section lines.	44
Figure 2.5 Generated synthetic seismograms that tied the well to seismic data illustrating all the components used to generate the synthetic seismogram.....	46
Figure 2.6 The figure showing the synthetic seismogram was matched with the seismic traces to obtain each horizon for target formation tops.....	47
Figure 2.7 Screen snapshot of Petrel software shows various faults and target horizons.	48
Figure 2.8 Stereonet plot displaying the suggested section plane orientations of regional cross sections.....	51
Figure 2.9 Digitized faults and folds visualized in the map view of the study area.	52
Figure 2.10 This figure shows the interval velocity map of the Upper Cretaceous shallow marine unit.	53
Figure 3.1 a-e) Length-weighted rose diagram of all the structures, folds, thrust or reverse faults, tension fractures, and strike slip faults of the SE Anatolian of the basin. f) right lateral Riedel shear diagram generated using $\sim 04^\circ$ oriented maximum principal stress, revealing potential structural trends in SE Anatolian.....	57
Figure 3.2 Length-weighted rose diagram of all structures, folds, thrust or reverse faults, and strike slip faults of the SE Anatolian of the basin in Adiyaman, Diyarbakir, and Batman-Siirt.	58

Figure 3.3 The age and motion of structures (thrust/reverse faults and normal faults) of the SE Anatolian basin (modified from Perinçek et al., 1992).....	59
Figure 3.4 Length-weighted rose diagram of thrust/reverse and normal faults of the SE Anatolian of the basin.	60
Figure 3.5 Picture shows the imbricate thrust structure in the intensely deformed upper Cretaceous Karadut Complex (flysch) in the Adiyaman sub-area.....	60
Figure 3.6 Field views of Late Miocene thrust emplacement around the north of Siirt region. a) Eocene-Miocene flysch (Çüngüş Formation) thrust over lower Miocene flysch (Lice Formation), b) close-up view of the thrust fault.	61
Figure 3.7 a) Field view of Late Miocene thrust emplacement south of Hazro High in Diyarbakir subarea. b) Field view of Late Miocene thrust emplacement south of Mardin High in Diyarbakir subarea.	62
Figure 3.8 a) Aerial photo of Dodan Anticline with bedding attitudes. This fold is presumably related to a fault propagation fold. Tsge: lower Eocene Gercüş Formation, Tm: middle Eocene-Oligocene Midyat Group, Tl: lower Miocene Lice Formation. b) Simplified sketch of a fault-propagation fold.	63
Figure 3.9 a) Aerial photo of Tavan Anticline is presumably related to fault propagation folds with measurements of bedding attitudes. (Tsge: lower Eocene Gercüş Formation, Tm: middle Eocene-Oligocene Midyat Group, Tl: lower Miocene Lice Formation. b) Fundamental properties of the fault-propagation folds.	64
Figure 3.10 Facies map of the research area.	65
Figure 3.11 The map illustrates Pre-Cambrian-upper Permian units on the surface of the study area. Red circles indicate the location of S01 rocks.....	66
Figure 3.12 The map illustrates Paleozoic-Mesozoic rocks on the surface of the study area.	66
Figure 3.13 The map illustrates Triassic-Jurassic shallow marine sediments on the surface of the study area.....	67

Figure 3.14 The map illustrates Upper Cretaceous continental and deep marine sediments and Cretaceous shallow marine sediments on the surface of the study area.	68
Figure 3.15 The map illustrates Mesozoic ophiolites and the Karadut complex on the surface of the study area.	68
Figure 3.16 The map illustrates the distribution of Upper Cretaceous-Paleocene continental clastics and shallow and deep marine deposits.	69
Figure 3.17 The map illustrates middle Eocene-Oligocene shallow and deep marine sediments, lower Eocene continental clastics, middle Eocene Maden Group, and Eocene-lower Miocene deep marine sediments on the surface of the study area. ..	70
Figure 3.18 The map illustrates lower Miocene shallow and deep marine sediments on the surface of the study area.	71
Figure 3.19 The map illustrates upper Miocene continental clastics on the surface of the study area.	71
Figure 3.20 The map illustrates Pliocene-Quaternary basalts on the surface of the study area.	72
Figure 3.21 The map illustrates Pliocene-Quaternary alluvium on the surface of the study area.	72
Figure 3.22 Isopach map of Triassic-Jurassic sediments (Stratigraphic class S05). Thickness values range between 0-2365 m, and contours indicate the thickness (in m) of Triassic-Jurassic sediments. Normal faults are shown as bolder black lines.	75
Figure 3.23 Isopach map of Lower Cretaceous shallow marine sediments (Base of Stratigraphic class S06 – Lower Cretaceous). Thickness values range between 0-697 m and contours indicate the thickness (in m) of Lower Cretaceous sediments.	76
Figure 3.24 a) Isopach map of Upper Cretaceous units.	77
Figure 3.25 a) Isopach map of Upper Cretaceous shallow marine units. The contours indicate the thickness in meters. b) Late Cretaceous thrust faults and the continental clastics that were deposited in front of the Late Cretaceous Thrust fault.	

Thickness values range between 0-388 m, and contours indicate the thickness (in m) of Upper Cretaceous sediments.	78
Figure 3.26 Isopach maps of a) Upper Cretaceous-Paleocene sediments and b) deep marine Germav Formation.	79
Figure 3.27 The isopach map of Lower Eocene continental clastics (Stratigraphic class S12). This figure emphasizes the possible location of the Early Eocene fault (black dash lines) that developed in Lower Eocene time and continental clastics deposited in front of the Early Eocene thrust fault. Thickness values range between 0-1176 m, and contours indicate the thickness (in m) of Lower Eocene sediments.	80
Figure 3.28 a) Isopach map of middle Eocene-Oligocene sediments (shallow marine and deep marine deposits – Stratigraphic class of S13 and S14). Thickness values range between 0-1684 m, and contours indicate the thickness (in m) of Middle Eocene-Oligocene sediments, b) Isopach map of middle Eocene-Oligocene shallow marine sediments (Stratigraphic class S13). Thickness values range between 0-1600 m, and contours indicate the thickness (in m) of Middle Eocene-Oligocene shallow marine sediments.....	81
Figure 3.29 The isopach map of deep marine lower Miocene sediments and the locations of the well-developed possible wedge-tops axis (black dash line), foredeep axis (dark pink dash line), and fore bulge axis (blue dash line). a) Lice Formation (Stratigraphic class S16) b) Firat Formation (Stratigraphic class S15). Contours are thicknesses in meters.	82
Figure 3.30 Isopach map of Upper Miocene continental clastics (Stratigraphic class S17) s. Thickness values range between 0-1230 m, and contours indicate the thickness (in m) of Lower Miocene sediments.	83
Figure 3.31 Stratigraphic well correlation section across the SE Anatolian from west to east. The location of the inset is shown. Numbers and letters represent significant stratigraphic boundaries and formations.	88

Figure 3.32 Stratigraphic well correlation section across the SE Anatolian from west to east. The location of the inset is shown. Numbers and letters represent significant stratigraphic boundaries and formations.....	89
Figure 3.33 Stratigraphic well correlation section across the SE Anatolian from west to east. The location of the inset is shown. Numbers and letters represent significant stratigraphic boundaries and formations.....	90
Figure 3.34 Stratigraphic well correlation section across the SE Anatolian from west to east. The location of the inset is shown. Numbers and letters represent significant stratigraphic boundaries and formations.....	91
Figure 3.35 Stratigraphic well correlation section across the SE Anatolian from north to south in Adiyaman subarea. The location of the inset is shown. Numbers and letters represent significant stratigraphic boundaries and formations.	92
Figure 3.36 Stratigraphic well correlation section across the SE Anatolian from north to south in Diyarbakir subarea. The location of the inset is shown. Numbers and letters represent significant stratigraphic boundaries and formations.	93
Figure 3.37 Stratigraphic well correlation section across the SE Anatolian from north to south in Batman-Siirt subarea. The location of the inset is shown. Numbers and letters represent significant stratigraphic boundaries and formations.	94
Figure 3.38 The figure illustrating the histogram of dip amounts of bedding planes and the rose diagram of strikes of bedding attitudes in Adiyaman, Diyarbakir, and Batman-Siirt subareas.....	97
Figure 3.39 a-c) Positive flower structure (Alidag Anticline) along the Adiyaman Fault Zone around Adiyaman subarea. b) Positive flower structure (Cendere Anticline) along the Adiyaman Fault Zone around Adiyaman subarea.	98
Figure 3.40 Structural map of the SE Anatolian Basin	99
Figure 3.41 The SE Anatolian basin's major folds are depicted in the following β - and $-\pi$ diagrams. The folds are shown in figure 3.40.	101
Figure 3.42 Fold classification based on symmetry and plunge (Fleuty, 1964; Hatcher and Bailey, 2020).....	105

Figure 3.43 Classification of folds based on the interlimb angle (modified after Fleuty, 1964, and Nabavi and Fossen, 2021). The rectangle represents the folds encountered in the study area.	106
Figure 3.44 a) Pictures with field sketches showing a progressive unconformity a) 90 km northeast of Adiyaman. b) 30 km northeast of Batman.	107
Figure 3.45 Uninterpreted and interpreted seismic profile across the Hazro High. Note thinning of the deposits southwards implying, thrusting-related sedimentation.	107
Figure 3.46 a) Aerial google map of the northwest Siirt region area highlighting outcrop exposures and stratigraphic units. b) Photograph and line drawing showing the angular unconformity between the Lice Formation (Sandy shale and sandy marl-lower Miocene) and Selmo Formation (upper Miocene) conglomerate and sandstone. c) Cross section (A-A') through the growth strata from south to north.	109
Figure 3.47 Field photographs of brittle structures located in the Batman-Siirt subarea. a) Within the lower Eocene Gercüş Formation, intensely sheared reverse faults evolved in the eastern Batman-Siirt subarea. b) Tilted normal faults within the lower Eocene Gercüş Formation in the eastern Batman-Siirt subarea. Note slight thickening on the downthrown blocks of the faults implying their syntectonic origin. c) Reverse fault within the upper Miocene Şelmo Formation (Upper Miocene) in the eastern Batman-Siirt subarea.	111
Figure 3.48 Geological map of SE Anatolian displaying paleostress sampling sites.	113
Figure 3.49 Paleostress inversion results, distribution, and orientation of the principal stresses represented on a tectonic map of SE Anatolian.	115
Figure 3.50 Uninterpreted and interpreted seismic profiles with stratigraphic horizons and faults marked. The seismic line 1 is shown at vertical exaggeration x2.	118

Figure 3.51 Uninterpreted and interpreted seismic profiles with stratigraphic horizons and faults marked. The seismic line 2 is shown at vertical exaggeration x2.	120
Figure 3.52 Uninterpreted and interpreted seismic profiles with stratigraphic horizons and faults marked. The seismic line 3 is shown at vertical exaggeration x2.	122
Figure 3.53 Uninterpreted and interpreted seismic profiles with stratigraphic horizons and faults marked. The location of the seismic line 4 is shown at vertical exaggeration x2.	124
Figure 3.54 Uninterpreted and interpreted seismic profiles with stratigraphic horizons and faults marked. The location of the seismic line 5 is shown at vertical exaggeration x2.	126
Figure 3.55 Uninterpreted and interpreted seismic profiles with stratigraphic horizons and faults marked. The seismic line 6 is shown at vertical exaggeration x2.	129
Figure 3.56 Uninterpreted and interpreted seismic profiles with stratigraphic horizons and faults marked. The seismic line 7 is shown at vertical exaggeration x2.	131
Figure 3.57 Uninterpreted and interpreted seismic profiles with stratigraphic horizons and faults marked. The seismic line 8 is shown at vertical exaggeration x2.	133
Figure 3.58 Uninterpreted and interpreted seismic profiles with stratigraphic horizons and faults marked. The seismic line 9 is shown at vertical exaggeration x2.	135
Figure 3.59 Uninterpreted and interpreted seismic profiles with stratigraphic horizons and faults marked. The seismic line 10 is shown at vertical exaggeration x2.	138
Figure 3.60 Uninterpreted and interpreted seismic profiles with stratigraphic horizons and faults marked. The seismic line 11 is shown at vertical exaggeration x2.	140

Figure 3.61 Cross and balanced cross-section with estimates of the minimum shortening and thrust geometries in the Adiyaman sub-area.	144
Figure 3.62 Cross and balanced cross-section with estimates of the minimum shortening and thrust geometries in the Diyarbakir sub-area.	145
Figure 3.63 Cross and balanced cross-section with estimates of the minimum shortening and thrust geometries in the Batman-Siirt sub-area.	146
Figure 4.1 Conceptual model showing the tectonic position of the SE Anatolian Basin from Triassic to recent.	153

CHAPTER 1

INTRODUCTION

1.1 Introduction

Opening and closure history of the southern Neotethys Ocean is well-recorded in the deposits of the SE Anatolian basin. The SE Anatolian basin has a thick (>14km) Paleozoic to Quaternary sedimentary cover. Tectonically, the basin is located on both Tauride-Anatolide Block (TAB) at the north and the Arabian platform at the south (Figure 1.1). Today, the border between these tectonic blocks is defined as Bitlis-Zagros Suture Zone (BZSZ). However, the southern margin of the TAB contains Arabian Platform-origin almost E-W trending metamorphic slices with 185 to 72 Ma peak and retrograde metamorphism ages, respectively (Oberhansli et al., 2012; Bröcker et al., 2013; Davoudian et al., 2016). The unmetamorphosed equivalents of these units are found on the Arabian platform as late Paleozoic – early Mesozoic sedimentary sequences (Barrier et al., 2014) representing Cambrian to Carboniferous platform sequences of the core sequences of the Arabian Platform and the rift-dirft sequences of the Neotethys Ocean. The Jurassic-Cretaceous arc-related magmatic bodies are also exposed along the north of BZSZ and its eastern continuation, the Sanandaj-Sirjan complex (Urumieh-Dokhtar magmatic arc) (e.g., Babazadeh et al., 2017). On the other hand, Eocene (e.g Doğanşehir) and even younger (lower Miocene) (Taşlıçay) arc-related intrusions are also exposed along the north of the suture zone (Babazadeh et al., 2017; Karaoğlan et al., 2013; Açlan and Duruk, 2018). Ophiolitic bodies with late Cretaceous metamorphic sole ages (Parlak et al., 2009; Karaoğlan et al., 2013, Robertson et al., 2015) are cut by almost the same age or slightly younger intrusions and exposed as tectonic slices at the north of BZSZ or they are found as basement rocks below sedimentary sequences at the south of the suture zone. By considering the regional picture given above, the SE Anatolian basin

should have recorded at least 3 three major tectonic events: (i) rifting-opening of the southern branch of Neotethys, (ii) closure of the ocean, and (iii) continental collision. However, there are debates about the timing and the number of subduction/collision events in the region. One group suggests that only one subduction/collision event ended in the late Cretaceous (Hall, 1974; Beyarslan and Bingöl, 2000; Sar et al., 2019; Ertürk et al., 2018; Ertürk et al., 2022). Unlike the first model, the other group suggests one subduction model gives Eocene timing for the collision event (Jolivet and Facenna, 2000; Argard et al., 2005; Allen and Armstrong, 2008). The other model similarly indicating a single subduction gives Oligo-Miocene time interval for the collision event (Şengör et al., 1984; Yılmaz, 1993; Robertson et al., 2007; Okay et al., 2010; Schildgen et al., 2014). Another similar model also exists in the literature, but the supporter of the model suggests Eocene soft and Early Miocene hard collision events (Robertson et al., 2012; Ballato et al., 2017; Darin et al., 2018). On the other hand, a double subduction model is also proposed. In this model, late Cretaceous and Oligo-Miocene time intervals are suggested as the timing of collision events (Oberhänsli et al., 2012; Karaoğlan et al., 2016; Yılmaz, 2019; Yılmaz et al., 2022).

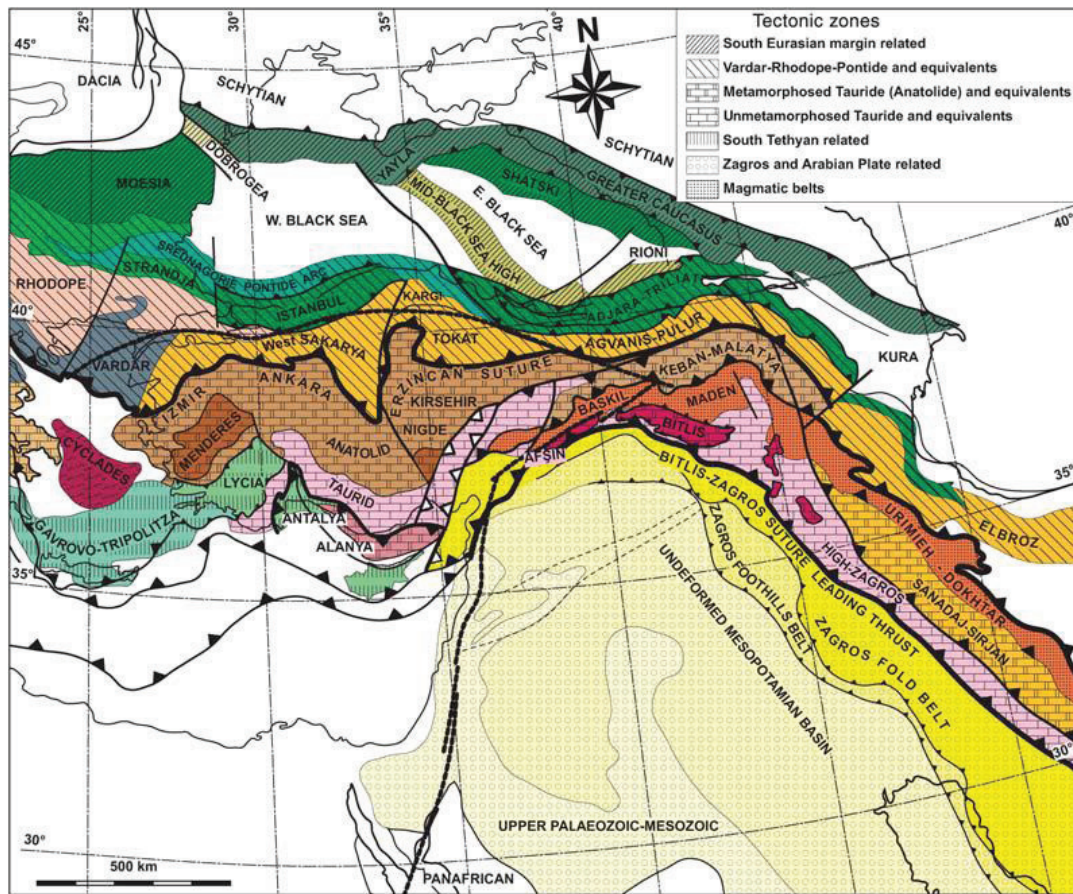


Figure 1.1 Simplified tectonic scheme around Türkiye (Kaymakci et al. 2010).

Although their critics support the models given above, a complete tectono-stratigraphic model of the SE Anatolian basin reflecting whole (Cambrian to recent) Neotethyan evolution is still missing in the literature. On the other hand, some local studies dealing with Oligo-Miocene sedimentary sequences are present, and they give information about the collisional period of the basin (e.g Husing et al., 2009; Gülyüz et al., 2020; Sun et al., 2021). However, a study dealing with whole sedimentary sequences of the SEA Basin in order to understand reflections of (i) timing and trend of Arabian plate rifting, (ii) subduction initiation/s, (iii) collision event/s on sedimentary record is missing in the literature. In this regard, transitions between (a) prolonged passive margin sequences deposited in front of (north) Arabian plate (rifting and partly subduction stage), (b) sequences of which facies

controlled by the location of accretionary prism/s (subduction stage), and (c) foreland sequences (collision stage/s) is still not well-known.

1.2 Aim of the Study

The study area is bounded by BZSZ in the north, the Mediterranean sea in the west, the political border of Iran in the east, and the Syrian and Iraqi borders in the South (Figure 1.2).

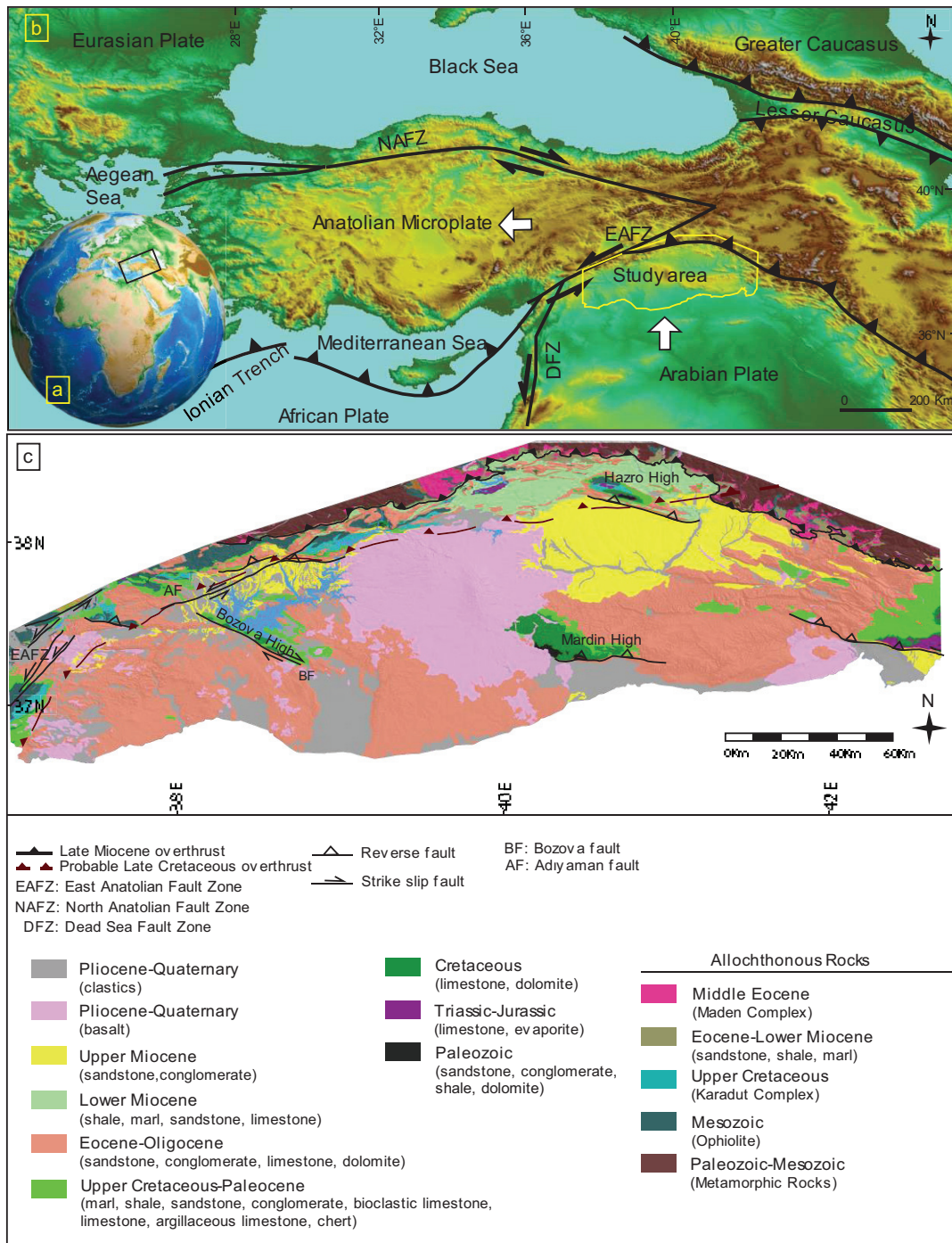


Figure 1.2 Location and b) the tectonic framework of the study area c) Geological map of SE Anatolian based on the surface and compilation of existing map (derived from the Turkish Petroleum Company database).

The main aim of the study is to determine the tectono-stratigraphical evolution of the SE Anatolian Basin regarding the rifting of the Arabian plate and the subduction/collision history of the southern Neotethys. For this reason, tools of structural geology, (such as fault and fold kinematic analyses) and stratigraphy/sedimentology (mainly sequences stratigraphy and facies modeling) are used in the study. In this sense, the primary data sources of the study are composite well logs, 2D seismic lines, fault plane measurements, bedding measurements, and facies maps.

1.3 Methods of the Study

Several methodologies are integrated into the study. These methodologies include field-based measurements/observations and analytical techniques supported by well logs and 2D seismic datasets. In this regard, thesis methodology consists of two primary categories, which are field studies and office work.

Field studies cover data collection for (i) kinematic and cross-section balancing and (ii) stratigraphic and sedimentologic analyses.

1.4 The layout of the Thesis

The thesis is organized into the following chapters:

Chapter 1 introduces the literature review and introduces the thesis by presenting information regarding the purpose, scope, geological background, and tectonic location of the study area.

Chapter 2 provides information about research methods, including mapping, stratigraphy-sequence relationships, kinematic analyses, cross-section construction, and balancing.

Chapter 3 documents the deformation and kinematic history of the basin and associated structures. The outcomes of cross-section construction, distribution of facies, and correlation of wells with 2D seismic interpretation are presented.

Chapter 4 provides all integrated data in the earlier chapters, discusses the spatial-temporal evolution of the SE Anatolian Basin, and constructs a regional geological model.

Chapter 5 documents information about key findings and emphasizes the main conclusions of this study.

1.5 Geological Setting and Literature Survey

The interaction of the African, Arabian, and Eurasian plates creates one of the most complicated tectonic zones in the Alpine Himalayan orogenic belt in southern Türkiye. During the continued post-Paleozoic northward movement of the northern passive margin of the Arabian Plate, the present tectonic elements were formed, resulting in consumed the Neo-Tethyan Ocean along the north-dipping subduction zone (Şengör and Yılmaz, 1981; Cater and Tunbridge, 1992; Dilek et al., 1990; Yılmaz, 1993). After the consumption of the Neo-Tethyan Ocean, the final collision occurred along the Anatolide/Tauride Platform and the Arabian Platform (Stampfli and Borel, 2002; Golonka, 2004). As a result of this collision, Bitlis-Zagros Orogen (Şengör and Yılmaz 1981) was formed, one of the most complex segments of the Alpine-Himalayan orogenic belt.

The SE Anatolian Basin is a remarkable region for researching subduction, collision processes, and evolutionary histories. However, the number of geological studies is simply inadequate because of the region's geological complexity and lack of a sufficient amount of available subsurface data. However, with the permission of the Turkish Petroleum Corporation to use seismic profiles and well-log data in the region, detailed subsurface interpretations have increased in recent years.

1.5.1 Regional tectonic plate setting

Geologically, the evolution of Türkiye corresponds to the evolution of the Paleotethys and Neo-Tethys oceans that developed between supercontinents Laurasia in the north and Gondwana in the south. According to Ketin (1966), three main tectonic blocks, including the Arabian platform in the southeast, the Anatolide-Tauride block, are a part of Gondwana, in the center, and the Pontides are a part of Laurasian in the north in Türkiye. Tectonic units of Türkiye amalgamated between Bitlis-Zagros and İzmir-Ankara-Erzincan suture zones, in the south and north, respectively (Figure 1.1). According to Şengor and Yılmaz (1981), the imbricated layers of metamorphosed remnants from the Paleotethys and Neotethys oceans represent these suture areas. Görür et al. (1984) proposed the existence of another suture zone within the northern branch of the Neotethys, which they referred to as the Intra-Tauride suture zone. This suture zone was thought to separate the Kırşehir Block from the Taurides.

During the middle to late Triassic, the southern Neotethys rifted to generate an east-west trending basin along the northern boundary of Gondwana. Rifting was followed by the eruption of alkaline basalts, subsidence, and the beginning of deep-water deposition (Robertson et al., 2007). During the Late Triassic and Early Jurassic, spreading likely started. Passive margins developed such as the Keban Platform and the Arabian Foreland in the north and south during the Jurassic-Cretaceous time.

Beginning with the onset of northward intra-oceanic subduction, an ophiolitic complex of the latest Cretaceous, Kocali complex, thrust over the Mesozoic succession of the Arabian platform and overlain by the latest Cretaceous to Miocene shelf-type deposits.

According to Livermore and Smith (1984), convergence ceased throughout the Paleocene. During the Paleocene and Early Eocene time, the residual oceanic basin's northern margin partially eroded and exposed and transgression and regression were common. Conditions of a passive margin have been developed again along the

Arabian margin, and the convergence started again. The further convergence is also supported by Robertson et al. (2004). According to this study, northward subduction occurred and, the remaining oceanic material rolled back southwards causing, in crustal extension during the middle Eocene. The exhumed Bitlis-Puturge massifs were rifted and filled with extrusive rock units affected by subduction concerning this extension. It is believed that northward subduction was prevalent during the Oligocene. During the following collision, this region of the active edge underwent subduction erosion.

The southern Neotethys proceeded to subduct until it collided with the Arabian platform in the Early Miocene (Okay et al., 2010; Darin et al., 2018; Ballato et al., 2017; Gülyüz et al., 2020). Internal southerly thrusting over Miocene marine deposits resulted in a further shortening of the already developed thrust stack. By the middle of the Miocene, the Arabian foreland had been flexurally down warped, and finally overridden. Along the South Anatolian major thrust, the whole thrust pile was placed southward over the Miocene foredeep (Husing et al., 2009). Folding and reverse faulting occurred on the foreland due to this event. The thrust belt was disturbed by suture shortening, and southern Neotethys in this area had closed entirely in the Late Miocene, together with thickening (Şengör et al., 1984; Husing et al., 2009). During the Plio-Quaternary, further, shortening occurred, and tectonic escape along the left-lateral East Anatolian Fault developed in the study area (Sengör et al. 1984; Robertson et al., 2007).

1.5.2 Crystalline Basement

The SE Anatolian basin is surrounded by crystalline basement units, consisting of magmatic, metamorphic, and ophiolitic and associated rocks.

1.5.2.1 Ophiolites

Ophiolites have contributed significantly to our understanding of Earth processes such as orogeny and collision tectonics and offer information about ancient ocean basins and upper mantle and the development of ancient continental margins (Dilek, 2003). It is essential to identify their origins and tectonic positions for comprehensive paleogeographical reconstructions and explanation of the development of the associated sedimentary basin. Ophiolites are widespread in Türkiye and provide information about the closing and opening of ocean basins. According to Karaođlan et al. (2012), the Late Cretaceous ophiolites are divided into two belts and part of the Mesozoic Tethyan ophiolites. From east to west, the ophiolites are displayed by Guleman, K m rhan, Berit, and Goksun, which developed about 84-90 Ma in the north of Bitlis-Puturge metamorphics massif. On the other hand, the ophiolites between the Arabian platform in the south and Bitlis-Puturge metamorphic massif are observed tectonically covering the Arabian continental margin and characterized by Kızıldađ and Kocali ophiolites, which were developed between 99 and 102 Ma ago (Karaoglan et al., 2013).

1.5.2.1.1 The Southeast Anatolian Ophiolites

The Guleman, K m rhan, İspendere, Berit, and G ksun ophiolites comprise the Southeast Anatolian ophiolites from east to west. The ophiolites observed along the belt have the following general characteristics.

In the Elazıđ region, the Guleman ophiolite is composed of radiolarites, basaltic pillow lavas, gabbroic rocks, mantle peridotites, and dunites which are placed over the Lice Formation (lower Miocene) of the Arabian platform and is depositionally overlain by the upper Maastrichtian-lower Eocene sandstone and shales defined as Hazar Complex and Maden Group (middle Eocene) (Rigo de Righi and Cortesini 1964; Perin ek 1979). According to Perin ek (1989), the Guleman Ophiolite is Campanian-lower Maastrichtian in age. In the Elazıđ region, K m rhan Ophiolite

consists of mantle tectonites isotropic gabbros, sheeted dykes, ultramafic-mafic cumulates, volcanic and related sedimentary rocks (Beyarslan and Bingol 2000). The Kömürhan Ophiolite thrust over the Maden Group (middle Eocene) and is overlain by the Elazığ magmatic (Late Cretaceous). The Kırkgeçit Formation (middle Eocene) sandstones and shales are deposited on top of the Ophiolite and Elazığ magmatic rocks (Beyarslan and Bingol 2000). The Kömürhan Ophiolite is considered to be 75-85 Ma by Yazgan and Cessex (1991) and Parlak et al. (2006).

The İspendere Ophiolite, constrained by the Maden Group and the Malatya-Keban platform, is located east of the Malatya region. The Malatya-Keban platform was underthrust during Late Cretaceous, and Late Cretaceous volcanic arc granitoids subsequently intruded the İspendere Ophiolite body (Beyarslan & Bingöl, 1996; Karaoğlan et al., 2009). During the middle to late Eocene, they were all thrust over the Maden Group as a unit (Yılmaz, 1993). The İspendere Ophiolite includes ultramafic to mafic cumulates, sheeted dike complex, isolated diabase dikes, mantle tectonites, and volcanics as well as entire ophiolite pseudo-stratigraphy.

As a component of the Tauride Ophiolite belt, the Berit Ophiolite is situated in the SE Tauride thrust belt of Türkiye, Kahramanmaras region. It is believed that the Berit Ophiolite originated in an early oceanic arc at the north of metamorphic massifs during the Late Cretaceous (Robertson et al., 2006) and represents amphibole and plagioclase, Iherzolite, dunites, and harzburgites (Yılmaz, 1993; Karaoğlan, 2005). Approximately 85 Ma ago, it was developed to incorporate onto the Tauride active continental margin to the north, and between 70 and 85 Ma ago, granites began to intrude. The Late Cretaceous Goksun Ophiolite is situated in the Goksun-Afsin, Kahramanmaras region, which is tectonically confined by the Malatya metamorphics in the east-west trending nappe zone of the SE Anatolian orogenic belt in the south and north. It is represented intensely metamorphosed and deformed up to granulite-eclogitic facies (Yılmaz et al., 1993).

1.5.2.1.2 Peri-Arabian Belt Ophiolites

The peri-Arabian belt ophiolites exposed in the SE Anatolian can be represented into two ophiolites which are the Kızıldağ (Hatay) and Koçali Ophiolite in the SE Anatolian.

The Kızıldağ Ophiolite is positioned in the western portion of the Southeastern Taurus ophiolites and represents crustal and peridotite units (Bingöl et al., 2018). The geological characteristics of the Kızıldağ Ophiolite imply that its emplacement is dated to the pre-Maastrichtian because the oldest transgressive layers are represented by Maastrichtian shallow marine deposits (Karaođlan et al., 2013).

Sungurlu (1973) identified the Koçali Complex as the Koçali unit north of Adiyaman. The Koçali Complex, exposed to the north of Adiyaman, comprises the Tarasa volcanics, the Konak Formation, which is represented by basalts, cherts, limestones, and mudstones, and the Kale Formation which consists of diabase, volcanic rocks, gabbros, and mantle peridotites (Perinçek, 1979). The Koçali complex thrust over the Cenomanian-Turonian Karadut Complex, which has pelagic carbonates, sandy shale and marls, radiolarian sediments, and an assemblage of fine-grained to coarse-grained carbonate rocks in the south. According to existing data, the Koçali Complex is Upper Jurassic to Lower Cretaceous in age (Sungurlu, 1973).

1.5.2.2 Metamorphic Rocks around SE Anatolian

The metamorphic massifs in SE Anatolian are identified with the pre-Cambrian to Cretaceous Bitlis-Puturge, Keban-Malatya metamorphics. The metamorphic massifs have the following general characteristics.

Around the Arabian Platform in SE Anatolian, the Bitlis metamorphic massif develops about 500 km long by 30 km broad arc-shaped zone. A narrow zone of Upper Cretaceous to Eocene flysch, Miocene sediments, and ophiolitic melange distinguish it from the main Arabian Platform. The Pre-Cambrian to Cretaceous

Bitlis metamorphic massif represents crystalline basement and upper sedimentary unit forming a nappe complex which emplaces on top of the Cretaceous-Eocene ophiolitic mélangé and flysch sequences (Göncüoğlu and Turhan, 1984; Çağlayan et al., 1984). It rests above Cretaceous and Eocene to Miocene rock units and is covered by Quaternary volcanics and Cenozoic deposits in the north. This unit was ascribed a depositional date of the Devonian-Upper Cretaceous (Oberhänsli et al., 2010). In the north of the study area, the Puturge metamorphic massif appears and represents high-grade metamorphic rocks composed of a variety of schists, amphibolites and gneisses (Erdem and Bingöl, 1995). The Puturge massif is unconformably overlain by the predominantly middle Eocene Maden Group, composed of Eocene age volcanics and sediments. The İspendere and Kömürhan ophiolites thrust over the Puturge metamorphic massif. Campanian to Maastrichtian age is given by Yazgan (1984) based on K/Ar ages of biotite, amphibole, and muscovite.

The Late Paleozoic to Early Mesozoic Keban metamorphic massifs represent metaconglomerate, metasandstone, and metacarbonate rocks and show similar rock units to the Malatya metamorphic massif (Robertson et al., 2007). The Keban unit is emplaced onto the arc magmatics, known as Elazığ magmatics, formed on ophiolites and overlain by Cenozoic unmetamorphosed sedimentary rock units (Robertson et al., 2007). Metacarbonate rocks, meta-cherts, phyllite, mica schist, and meta-clastic rock units are observed in the Malatya metamorphic massifs to the west of the Malatya region (Perincek and Kozlu 1984). The Malatya metamorphic unit is emplaced onto ophiolitic and volcano-sedimentary rock units of an island arc. Based on the interpretation of the available fossil record, Özgül et al. (1982) suggested the Late Permian - the Early Triassic age for the protolith age of the upper section of the Malatya metamorphic unit.

1.5.2.3 Magmatic Rocks around SE Anatolian

The SE Anatolian Orogenic zone, situated between the Arabian and Tauride-Anatolide platforms, is one of the most complex components of the Alpine-

Himalayan system. The zone contains various geochemically distinct magmatic products that are predominant for an extended period of time between the Ediacaran and Quaternary. According to Yılmaz (1993), Yazgan (1983), and Bingöl (1984), the most intense magmatism occurred during the Ediacaran, the Late Triassic to Late Cretaceous, the Middle Eocene, and the Plio-Quaternary.

The arc-related silicic extrusive and intrusive rock units are widespread and composed of Coniacian-Maastrichtian alternations of volcanic and sedimentary rock units (Yazgan and Chessex, 1991). In the Late Cretaceous, calc-alkaline volcanic arc granites developed along the Tauride active continental margin due to north-dipping subduction in the southern Neotethys (Parlak, 2006).

The Ar-Ar and K-Ar isotopic age determinations on the intrusive rocks yielded 85-70 Ma cooling ages (Rızaoglu et al., 2009). Recent U-Pb zircon data from these intrusive rocks yielded 82-84 Ma crystallization (Zircon U-Pb) ages (Karaoglan, 2013). These rocks intrude some of the metamorphic massifs, ophiolites, and volcanic arc units of the Southeast Anatolian. The K-Ar and Ar-Ar isotopic age computations revealed cooling ages ranging from 85 to 70 Ma on the intrusive rocks (Rızaoglu et al., 2009).

In SE Anatolian, the middle Eocene Maden Group is represented by basal clastics, pelagic carbonates interbedded with bioclastic material and silicified chert, red-colored mudstone, green sandstone, and massive limestone blocks, which are located in the Bitlis-Zagros Suture belt, which comprises the imbrication and Nappe zone (Ertürk et al., 2018). In general, the Maden basin developed as a pull-apart basin (Aktas and Robertson, 1984) or a back-arc basin (Yılmaz et al., 1993). Irrespective of the tectonic explanation, it suggests that the Neo-Tethyan Ocean basin stayed open throughout the Cenozoic period, with subduction proceeding in southeastern Türkiye (Kaymakci et al., 2006). While the İspendere Ophiolite is positioned on the Maden Group, which unconformably overlies the Puturge metamorphic massif (Yazgan, 1984; Beyarslan, 1991).

According to Yigitbas and Yılmaz (1996), Eocene volcanics represent arc-type magmatism associated with the later stages of subduction of the southern Neotethys. The Eocene arc-type volcanic and andesitic rock units (Helete volcanics) structurally beneath the Malatya metamorphic massif in the WNW of the study area. The Helete unit is overlain by early Eocene carbonates rich in nummulites (Yigitbaş and Yılmaz 1996).

Basaltic shield and fissure eruptions with transitional tholeiitic-alkaline character constitute most of the post-collisional volcanism. Since the Pliocene, the Karacadag volcano has erupted along an N-S trending set of craters and fissures that may have emerged from a tensional zone on the Arabian Foreland (Şengor and Yılmaz, 1981).

1.5.3 Sedimentary Units

This section explains the sedimentary units of SE Anatolian from the Pre-Cambrian to the Late Miocene. Figures 1.3, 1.4, and Table 1.1 shows the simplified geological map, generalized stratigraphic section, and contact relationships of the study area.

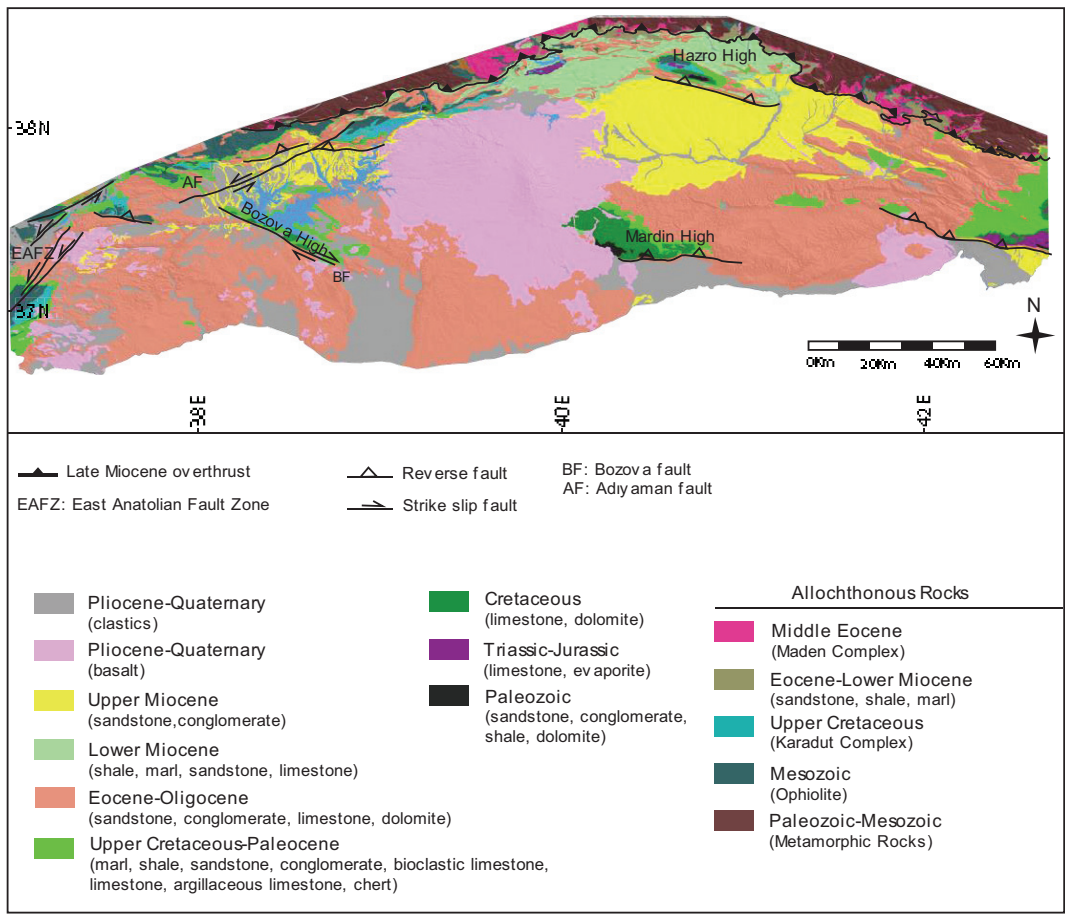


Figure 1.3 The figure shows a simplified geological map of the study area, compiled from the Turkish Petroleum Company database and the geological map of MTA 2002.

AUTOCHTHONOUS LITHOSTRATIGRAPHIC UNITS OF SOUTHEAST TURKEY								
AGE		ROCK UNITS			CLASSES	ENVIRONMENT		
		Group	Formation	Group				
PLIO-QUATERNARY			ALLUVIUM	ALLUVIUM-BASALT	S18, S19			
TERTIARY	MIOCENE	UPPER	ŞELMO	Campanian-Tertiary sequences (closure of Neotethys ocean which involves ophiolite obduction) and terminal collision	S17	CONTINENTAL		
		LOWER	SİLVAN		LİCE	S15, S16	OPEN MARINE SLOPE SHALLOW PLATFORM	
	OLIGOCENE		MİDYAT		FIRAT	S13, S14	SUPRA-TIDAL CONTINENTAL	
	EOCENE	UPPER	GERMİK		HOYA			
		MIDDLE	GERCÜŞ		GERCÜŞ			
CRETACEOUS	PALEOCENE	ŞİRNAK	BELVEREN		BEÇERMAN	S12	SHALLOW PLATFORM CONTINENTAL	
			Ü. GERMAY		Ü. SİNAK			
			A. GERMAY		A. SİNAK			
	UPPER	MAASTRICHTIAN	ŞİRNAK		BESNİ	GARZAN	S10 S09 S11	DEEP MARINE SLOPE SHALLOW PLATFORM CONTINENTAL
					TERBÜZEK	KIRADAĞ		
				Kocaeli Hazan Karadut	KASTEL	BOZOVA		
				SAYINDERE KARABOĞAZ ORTABAĞ	BELOVA			
	LOWER	CAMPANIAN	ADİYAMAN	KARABABA	Cretaceous sequences (initial subduction stage of the southern Neotethys ocean)	S08	DEEP MARINE SHALLOW PLATFORM	
		SANTONIAN	MARDİN	DERDERE				
		TURONIAN		SABUNSUYU				
CENOMANIAN		AREBAN						
ALBIAN		LATDAĞI						
APTIAN								
JURASSIC	UPPER		YOLAÇAN	Triassic-Jurassic rift-drift sequences of Arabian Platform	S05	SHALLOW MARINE		
	LOWER		KOZLUCA			TIDAL FLAT		
TRIASSIC	UPPER	CUDİ	DİNGER			TIDAL FLAT-SABKHA		
			TELHASAN					
			ÇAMURLU					
			GİRMELİ					
	LOWER-MIDDLE	CUDİ	BAKÜK			SUB-TIDAL		
			UZUNGEÇİT					
			ULUDERE					
			YONCALI					
PERMIAN		TANİN	GOMANILIRIK	Pre-Cambrian-Permian core sequences of Arabian Platform	S04	SHALLOW MARINE		
		ZAP	KAS					
CARBONIFEROUS	LOWER	ZAP	KÖPRÜLÜ		Pre-Cambrian-Permian core sequences of Arabian Platform	S03	SHALLOW MARINE	
DEVONIAN	UPPER	DİYARBAKIR	YİĞİNLİ					
	LOWER-MIDDLE		KAYAYOLU					
SILURIAN	UPPER	HABUR	HAZRO					SUPRA-TIDAL INTRA-TIDAL
	MIDDLE-UPPER		DADAŞ					
ORDOVİCIAN	UPPER	HABUR	BEDİNAN					DEEP-SHALLOW MARINE
	LOWER		SEYDİŞEHİR					
CAMBRIAN	UPPER	DERİK	SOSİNK					SHALLOW MARINE
	MIDDLE		KORUK					
	LOWER		ZABUK					
	LOWER		SADAN					
PRE-CAMBRIAN			TELBESEMİ	VOLCANIC-VOLCANOCLASTIC	S01	TIDAL FLAT CONTINENTAL-SHALLOW MARINE		

Figure 1.4. Simplified stratigraphic section of the SE Anatolian Basin.

The units from pre-Cambrian to Pliocene in the SE Anatolian can be grouped into four based on regional tectonic settings in which they deposited, (i) pre-Cambrian - Permian sequences representing the core sequences of the Arabian Platform, (ii) Triassic-Jurassic sequences represent the rift-drift sequences of the Arabian platform, (iii) Cretaceous sequences are regarded as the initial subduction stage of the southern Neotethys ocean, and (iv) Campanian to Tertiary sequences are attributed to the closure of the Neotethys, which involves ophiolite obduction (Campanian-Mastrichtian) and terminal collision of the adjacent continental blocks by Oligocene to Late Miocene.

1.5.3.1 Pre-Cambrian – Permian Units.

These units comprise 15 different formations. By considering the significant unconformities or the name of the locations where the units are widely exposed, these formations are grouped into five different sequences. This segmentation is also used in the TPAO database.

The oldest group is named as Derik group. This group contains five different formations. The oldest formation is the Pre-Cambrian Telbesmi Formation, known as the oldest sedimentary rock unit in the study area. It is defined as the basement of the SE Anatolian basin. This formation is presented by sandstones, shales, volcanoclastics, and diverse volcanic rocks around the Mardin region (Figure 1.5a and b) and shale and volcanic layer-bearing alternations in the NW (Adiyaman) (Figure 1.5c) in the study area (Rigo De Righi and Cortesini, 1964; Sungurlu, 1973; Ala and Moss, 1979; Tardu et al., 1991).

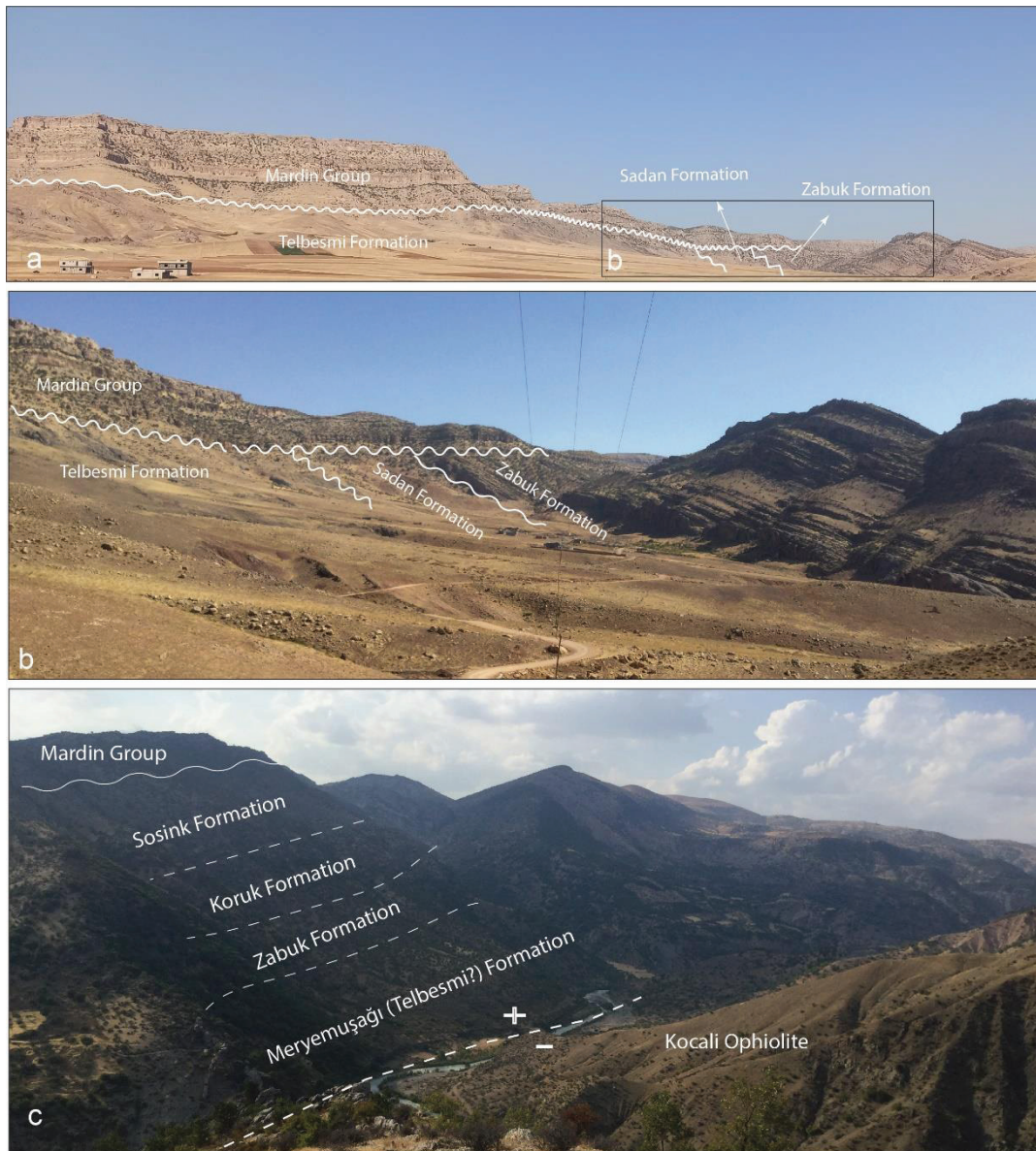


Figure 1.5. Pictures from the field demonstrate a) and b) Paleozoic succession in Derik (Mardin region) and c) Tut (Adıyaman region).

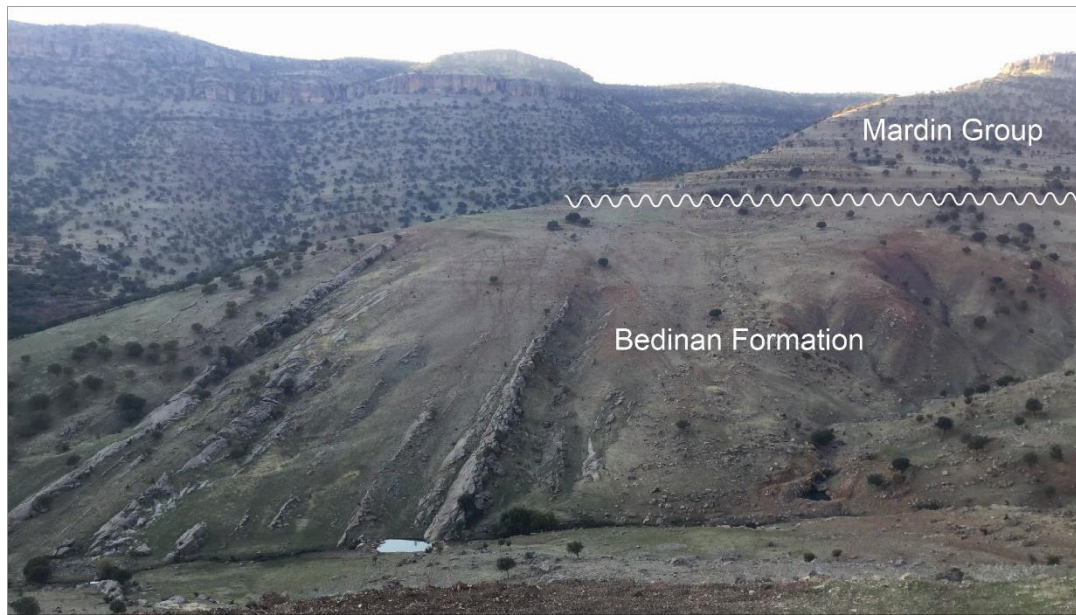


Figure 1.6 The illustration depicts the contact relationship with unconformity level between middle-late Ordovician (Bedinan Formation) and Aptian to Cenomanian (Mardin Group) in Mardin High, Mardin region.

Generally, this unit represents a shallow marine environment with rarely observed volcanic contributions (in the SE). The Cambrian Sadan Formation unconformably covers the massif volcanic packages of the Telbesmi Formation at the south (Figure 1.5). The Sadan Formation is represented by alternations of conglomerate, sandstone, and rarely found shale layers. A shallow marine environment is proposed for the deposition of the unit (Perinçek et al., 1992). The Zabuk Formation conformably overlies the lower Cambrian Sadan Formation. This unit comprises cross-bedded sandstone and conglomerate layers, indicating a continental to the shallow marine environment (Perinçek et al., 1992). The lateral equivalent of this unit is called as lower to middle Cambrian Koruk Formation, comprising dolomitic limestones showing characteristics of a tidal flat environment (Perinçek et al., 1992). The Upper Cambrian Sosink Formation conformably covers the Koruk Formation. From bottom to top, limestone, shale, and alternations of shale and siltstone layers are the components of the formation. This formation is also defined as shallow marine deposits based on fossil assemblages by Perinçek et al. (1992). The

Ordovician Habur group conformably covered the Derik group and was represented by two formations. The Lower Ordovician Seydişehir Formation is the first unit of the group and is represented by dominantly siltstone layers alternating with fossil-bearing sandstone and shale layers deposited in shallow to deep marine environments (Dean et al., 1986). The Middle-Upper Ordovician Bedinan Formation (see figure 1.6) unconformably covers the Seydişehir Formation. Sandstone and gray shale alternations represent the formation that is deposited in shallow to deep marine environments (Tardu, T. 1991, Perinçek et al., 1992).



Figure 1.7 The pictures demonstrate a) late Silurian to late Devonian succession (Diyarbakır Group), b) sandstones with cross-bedding within the Hazro Formation in Hazro High, and c) contact relationship between late Silurian to late Devonian (Diyarbakır Group) and the Upper Permian (Tanin Group) in Hazro High, Diyarbakır region.

The Silurian to Upper Devonian Diyarbakır group unconformably overlies the Habur Group and comprises three formations (Figure 1.7). The Upper Silurian-Lower Devonian Dadaş Formation, composed of sandstone, dark gray shales, and limestone layers, is only exposed around the Diyarbakır region (around Hazro High). Confined marine and deltaic conditions are proposed for the depositional environment of the unit (Perinçek et al., 1992). The Lower-Middle Devonian Hazro Formation conformably overlies the Dadaş Formation and is represented by various sizes of clastics with cross-bedded sandstone and dolomite layers. A shallow marine tide-dominated environment is suggested for the depositional condition of the unit (Perinçek et al., 1992). The Middle-Upper Devonian Kayayolu Formation conformably covers the Hazro Formation. From the bottom top, shale, sandstone thin-bedded dolomite, and evaporitic layers are observed along the unit. Lagunal to supra-tidal isolated areas (around Hazro High) is proposed for the sedimentation of the unit (Perinçek et al., 1992). The Upper Devonian-Lower Carboniferous Zap group unconformably overlies the Diyarbakır Group units and it consists of three formations. The Upper Devonian Yığınlı Formation (Janvier et al., 1984 and Köylüoğlu, 1984) is composed of alternations of limestone and shale layers with rarely observed gravel-bearing sandstone layers. Perinçek (1990) suggests fluvial and deltaic conditions for the deposition of the unit. The Upper-Devonian - Lower Carboniferous Köprülü Formation is represented by black shale layers with alternations of sandstone–siltstone–limestone occurrences. Shallow marine conditions with some reefal occurrences are proposed for the unit (Perinçek et al., 1992). The lower Carboniferous Belek Formation conformably covering the Köprülü Formation (Cebecioğlu and Köylüoğlu, 1986) is composed of bioherms and gray to black biostromal carbonates representing a shallow marine environment (Perinçek et al., 1992). The Upper Permian Tanin group unconformably covers the Zap Group and comprises two formations. The Upper Permian Kaş Formation (Bozdoğan, 1987) is only observed around the Diyarbakır region, and it comprises sandstone with intercalated marl-limestone layers and coal-bearing shales. Developed delta plain and fluvial tide-dominated shoreline environments are suggested for the

deposition of the unit (Perinçek et al., 1992). The shallow marine Upper Permian Gomaniibrik Formation is the lateral continuation of the Kaş formation in the region. It comprises shale, sandstone with coal, and bioclastic limestone layers (Bozdoğan et al., 1987 and Tardu et al., 1991) (Figure 1.7 c).

1.5.3.2 Triassic-Jurassic Sequences

These units comprise 12 different formations. By considering the significant unconformities or the name of the locations where the units are widely exposed, these formations are grouped as two different sequences. This segmentation is also used in the TPAO database. The first group is named as Lower-Middle Triassic Çığlı Group, which consists of four formations. Although all formations have similar characteristics as being continental to shallow marine sequences and comprising mainly red beds and marl layers, they have different formation names in the literature due to a lack of regional stratigraphic correlations. Therefore, detailed descriptions of the formations (Yoncalı, Bulakbaşı, Uludere, and Uzungeçit Formations) are not given here. A similar analogy is also valid for the Cudi Group units which conformably covers the Çığlı group. The main composition of the group can be represented by dolomite, limestone, evaporite, and rarely observed siltstone and shale layers. A shallow marine environment is proposed for the depositional condition of the formations (Bakük, Girmeli, Çamurlu, Telhasan, Dinçer, Kozluca, Yolaçan, and Latdağı formations) of the group (Perinçek et al., 1992). Although all of the formations are transitional in some parts, there are two observable unconformities between the formations; (i) between the Kozluca and Yolaçan Formations, and (ii) between the Yolaçan and Latdağı formations. Even though the title of this section only covers Triassic and Jurassic sequences; the uppermost parts of the Latdağı Formation are defined as Aptian in age by Perinçek et al. (1992). However, here the unit is considered as a member of the mainly Jurassic Cudi group since most of the units were deposited in the late Jurassic time interval.

1.5.3.3 Cretaceous Sequences

These units are composed of 17 different formations. By considering the major unconformities or the name of the locations where the units are widely exposed, these formations are grouped as three different sequences. This segmentation is also used in the TPAO database. The Aptian – Lower Campanian Mardin Group unconformably covers the Cudi group units. This group comprises four formations. The Aptian Areban Formation comprises basal conglomerates, sandstone, sandy limestone, shale, and fine-grained dolomite layers. Beach, coastal plains, and deltaic depositional conditions are proposed for the unit (Perinçek et al., 1992). The Albian-Cenomanian Sabunsuyu Formation conformably overlying the Areban Formation is composed dominantly of dolomite and is rarely observed limestone layer. This unit is defined as restricted lagoonal, tidal flat to shallow sub-tidal carbonates (Perinçek et al., 1992). The Cenomanian – Turonian Derdere Formation (Wagner and Pehlivan, 1987) unconformably covers the Sabunsuyu Formation. It is represented by dolomitized limestone, organically rich limestone, and benthic foraminifera-bearing limestone layers. Sub-aerial and developed anoxic conditions are proposed for the depositional environment of the unit (Perinçek et al., 1992). The Coniacian – Lower Campanian (Yılmaz and Duran, 1997) Karababa Formation unconformably covering the Derdere Formation is composed of highly organic-rich limestone, dolomite, and bioclastic limestone layers. Intrashelf semi-restricted anoxic environments proceeded shallowing upwards lagoonal to tidal flat conditions is suggested for the deposition of the unit (Perinçek et al., 1992). The middle Campanian Adıyaman group (Tuna, 1973; Sungurlu, 1973; Güven et al., 1992; Perinçek et al., 1992) unconformably cover the units of the Mardin group (Figure 1.8).

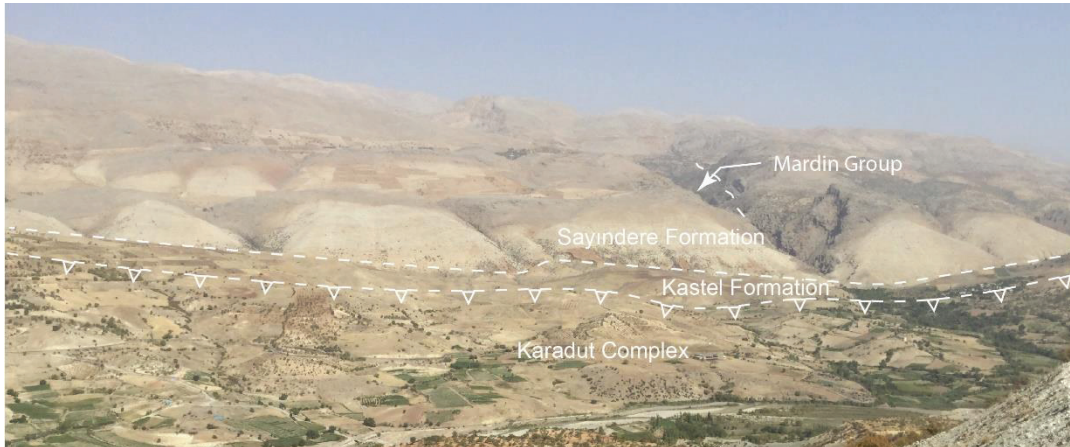


Figure 1.8 The pictures show contact relationships between the Aptian to Cenomanian (Mardin Group), the late Campanian to early Maastrichtian deposits (Sayındere and Kastel formations), and the allochthonous Karadut Complex (upper Cretaceous) in Adıyaman region.

This group comprises four formations (Ortabağ, Karaboğaz, Sayındere, and Beloka Formations) represented by similar sedimentary characteristics (deep marine facies with organically rich layers). All formations are laterally and vertically transitional, and there is no reasonable explanation for using different formation names. The Upper Campanian – Maastrichtian Lower Şırnak group conformably covers the units of the Adıyaman Group. Nine formations create the group. The Upper Campanian – Lower Maastrichtian Kastel (at the north) Formation is represented by deep marine sequences comprising planktonic foraminiferal shale, marls alternated with sandstone, and conglomerate layers. The southerly equivalent of the formation is named as Bozova Formation. This formation is also represented by a deep marine environment but it contains gray marl, and calcareous shales that grade into limestones (Perinçek et al., 1992). These deep marine formations are unconformably covered by continental red beds. These continental clastics are named as Terbüzek Formation (Upper Maastrichtian) in the north and Kıradağ Formation (Upper Maastrichtian) in the south (Perinçek et al., 1992). The Upper Maastrichtian Garzan (at the east) and Besni (at the west) Formations are represented by shallow marine deposits mainly consisting of rudist-bearing reefal limestone layers (Rigo de Righi

and Cortesine, 1964; Sungurlu, 1973). Although these formations unconformably cover the continental deposits (Terbüzek and Kıradağ Formations), they conformably cover the deep marine sequences of the Kastel and Bozova formations. The Upper Maastrichtien Alt Germav Formation has vertically and laterally transitional contacts with the shallow marine (Garzan and Besni formations) and deep marine (Kastel and Bozova formations) formations. This unit is also defined as a deep marine unit, composed of alternating gray-grayish to green marl, shale, fine-grained sandstone, and locally observed conglomerate layers (Özer, 1993). The lateral equivalents of the Alt Germav Formation are named Alt Sinan (fossiliferous carbonates – shallow marine) and Antak (red clastics and shales – continental) formations (Perinçek, 1990; Güven et al., 1992; Perinçek et al., 1992).

1.5.3.4 Tertiary Sequences

These units comprise 15 different formations. By considering the major unconformities or the name of the locations where the units are widely exposed, these formations are grouped as three different sequences. This segmentation is also used in the TPAO database.

The deep marine sequences (Üst Germav Formation) of the Paleocene Upper Şırnak group conformably cover the units of the Lower Şırnak group. However, the shallow marine equivalents of the deep marine sequences (Üst Sinan Formation) unconformably overlie the Lower Şırnak Group units. The Middle to Upper Paleocene continental deposits in the region is named Kayaköy (evaporites) and Antak (red beds) Formations. These formations are laterally transitional to each other and vertically transitional with the Üst Sinan Formation. Also, they have no observable contact with the Üst Germav Formation. The Upper Paleocene shallow marine carbonates of the group are named Belveren (at north) and Becirman (at south) Formations. These formations unconformably cover the deep marine (Üst Germav Formation), shallow marine (Üst Sinan Formation), and continental (Antak and Kayaköy Formations) units in the region. The Lower Eocene Gerçüş Formation

is the uppermost unit of the Şırnak Group. This unit is represented by continental clastics (red color clastics and evaporites). The contact relationship between the Gerçüş Formation and the shallow marine (Belveren and Becirman Formations) and deep marine (Üst Germav) is defined as unconformable (Rigo de Righi and Cortesini, 1964; Sungurlu, 1973; Perinçek, 1979) (Figures 1.8 and 1.9).



Figure 1.9 The images show contact relationships between a) the Şırnak Group (Terbüzek, Besni, and Germav formations) (Upper Cretaceous), Hoya Formation (middle Eocene-Oligocene), and Şelmo Formation (Upper Miocene) and b) the Germav Formation (upper Cretaceous-Paleocene), Gercüş Formation (lower Eocene) and Hoya Formation (middle Eocene-Oligocene) in Adıyaman region.

The Middle Eocene - Oligocene Midyat group unconformably covers the units of the lower groups. This group consists of three formations. The Middle Eocene-Oligocene Hoya Formation is represented by shallow marine carbonate (thickly bedded limestones) and dolomite layers (Sungurlu, 1973; Sungurlu et al., 1985). This formation grades laterally and vertically into the marly chalky carbonates of the sloop to deep marine sequences of the Gaziantep Formation. The Hoya and Gaziantep Formations also vertically grade into shallow marine to continental deposits (clastics, carbonates, and evaporate alternations) of the Germik Formation (Perinçek et al., 1992). The Lower Miocene Silvan Group unconformably covers the Midyat group sequences. This group contains two formations. The Lower Miocene Fırat Formation comprises dominantly bioclastic limestone and shallow marine carbonates (Akıncı et al., 2016). This formation vertically grades into deep marine sequences of the Lower Miocene Lice Formation represented by turbiditic sandstone, siltstone bedded shale alternations, and marls (Akıncı et al., 2016) (Figure 1.10).



Figure 1.10 Picture a) shows the Lice Formation (lower Miocene), which includes evaporite deposits (b and c) in the Batman-Siirt region.

The Upper Miocene continental clastics of the Şelmo Formation unconformably cover the units of all groups, and it represents the commencement of the regional scale continental deposition in the region after long-lasting marine-related deposition.

CHAPTER 2

METHODOLOGY

A Multidisciplinary approach was required to integrate and interpret the surface and subsurface dataset in the concept of regional tectonic context. Paleo-stress inversion analyses, fold analyses, well log and seismic data analyses, cross-section construction, and balancing is conducted throughout the study to better understand the spatiotemporal characteristics of deformation stages and associated structures identified in the field. Table 2.1 summarizes the workflow of the study.

2.1 Data and Methods of study

The methods of the study rely on two datasets that include available surface and subsurface data.

This study used a published 1/500000 scale geological map (prepared by a Turkish Petroleum Company (TPAO) Geologist in 1980') as a base map. The digital elevation model (DEM) of the research area (taken from USGS), together with the collected 4604 bedding attitudes and available seismic lines/well-logs, were used to construct cross sections. Also, such data was used for fold analyses for the folds found in the Adiyaman, Diyarbakir, and Batman-Siirt sub-areas of SE Anatolian.

In the context of paleostress inversion analyses, 358 fault slip data were collected from fault planes displacing lower Eocene to upper Miocene units at 26 different sites in the study area (Appendix A and B). Fault plane attitudes, slickensides, and movement sense orientations, locations, and relative dating markers (if possible) were measured in the field for each measurement site.

Table 2.1 Workflow of the study

Basic Workpackages	Sub-Workpackages	Surface data	Subsurface data		Main Outputs	Aim
			Well logs	Seismic sections		
Mapping	Mapping Units/facies	x			The first facies map of SEAOB	
	Mapping Structures	x				
	Facies determination	x	x			
Stratigraphy	Determining spatial continuities of facieses	x	x	x	Sequence stratigraphical evolution of the region	
	Well/section correlations	x	x	x		
	Fold analyses	x				
Kinematic Analyses	Unconformity (Syn/Post-depositional) determinations	x		x	Determination of deformation phases	
	Paleostress Analyses	x				
	2-D seismic interpretation (based on sequences)	x		x		
Cross-section constructions	Velocity modelling/depth conversion			x	3-D facies and structural model of the region	
	Shortening ratio calculations			x		
Cross-section balancing	Shortening ratio calculations	x			Validating cross-sections and spatio-temporal shortening ratio calculations	
				x		

The Turkish Petroleum Company contributed the 2D seismic and well data set utilized for this study. It includes One hundred forty-four well data sets including, twenty-three well logs (with formation top information) (resistivity, density, gamma ray, and spontaneous potential), eight well checkshot surveys. Well, reports, sedimentological information, and field observations were also used to better conduct stratigraphy of the region by borehole section correlation based on newly described facies determinations and their distributions in 3D space. One hundred forty-four wells penetrated the Paleozoic strata, allowing us to model the almost whole stratigraphy of the study area. The well data set spans a region of approximately 55200 km² with a 15-30 km (average) distance between wells (Figure 2.1).

Eighty-six 2D seismic profiles were utilized for this study. Thirty-four section lines of the total are oriented parallel to the strike major structures of the basin, while the rest are aligned perpendicular to the strike of major structural features of the basin. All seismic data were in SEG-Y format. 33 of 2D seismic data could not be interpreted due to low data quality. 42 of them with moderate quality were poorly interpreted. However, eleven lines (blue lines in Figure 2.1) with good quality were interpreted, and those sections were used for cross-section construction and balancing. The distribution of the well and 2D seismic data set is displayed in Figure 2.1.

The Petrel Schlumberger Modeling Software, version 2017.4, and Midland Valley (MOVE), version 2018.1, were conducted in this study for 2D seismic and well data interpretation.

2.2 Mapping

2.2.1 Mapping Units

There are 63 different formations described (by researchers and TPAO geologists) in SE Anatolian. However, the number of formations were reduced to 19 class based

on facies characteristics and age information. The Petrel Schlumberger Modeling Software, version 2017.4, and Global Mapper Software, version 21.0, were conducted to produce age versus facies maps in this study.

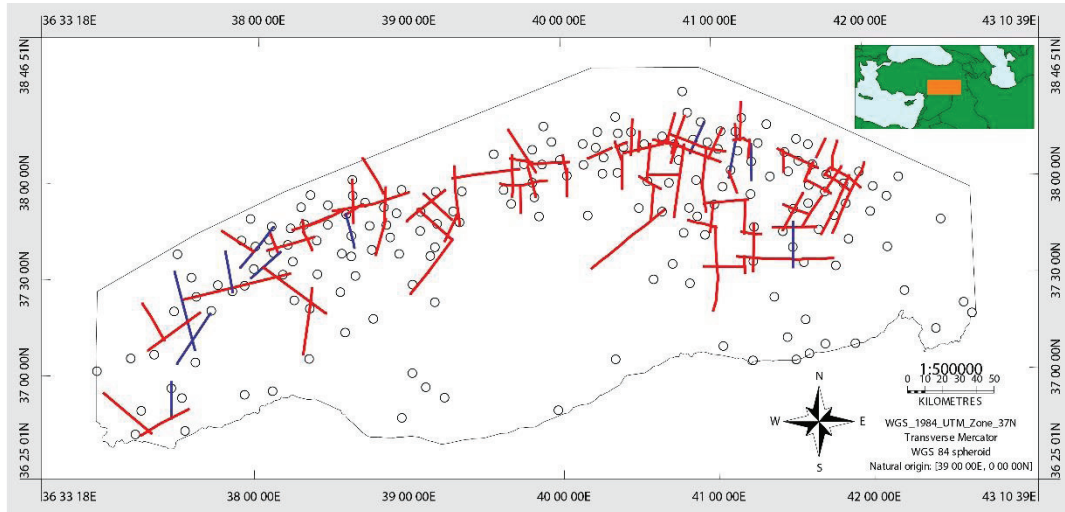


Figure 2.1 The distribution wells and 2D seismic line locations in the study area. Circles indicate the wells' locations and 2D seismic lines (red and blue lines).

2.2.2 Mapping Structures

Four thousand six hundred four bedding orientations were collected systematically, and DEM of the research area (taken from USGS) are used for the construction of cross sections and the features of the folds along the fold and thrust belt in Adiyaman, Diyarbakir and Batman-Siirt subareas of SE Anatolian. Three thousand sixty-eight measurements of the bedding attitude were used to better understand the features and spatial distribution of the folds. The Stereonet 11 Software by Allmendinger was used in this study for the fold analyses.

The structural base map and field observations (trace of 34 thrust and three strike-slip faults mapped by satellite images and over five km-long faults traced and illustrated) are used for length-weighted fault orientation analysis. For this purpose,

the SE Anatolian basin is divided into nine domain areas (Figure 2.2), based on variations in structural trends and the curvature of the basin rim.

We identified and separated the available data sets as fractures, fold axes, and faults in the study area. We divided each structure into distances of 100 m to create length-weighted rose diagrams of the structures.

Relative ages of the faults were done by taking into account cross-cutting relationships, available growth structures, literature data, and seismic interpretations (terminations of reflections or fold limbs or kink bands on the seismic section) on 2D seismic sections.

2.3 Stratigraphical Analyses

One hundred forty-four wells that penetrate Paleozoic rock units, eighty-six 2-D seismic data sets, and prepared surface/subsurface facies maps are used to establish the stratigraphical frame of the research area and to understand spatiotemporal facies associations.

2.3.1 Facies Determination

The research area has 63 different formations that researchers have identified and mapped. However, they were classed here based on their ages and facies characteristics. In this sense, 19 facies-age classes were determined in this study. The resultant facies distribution maps were used to understand possible erosional surfaces, deposition trends, and the base of sedimentological cycles and their correlative conformities (e.g Mitchum et al., 1977). In this context, the stratigraphic classes were created by considering (almost) same-age continental, shallow marine, and deep marine deposits.

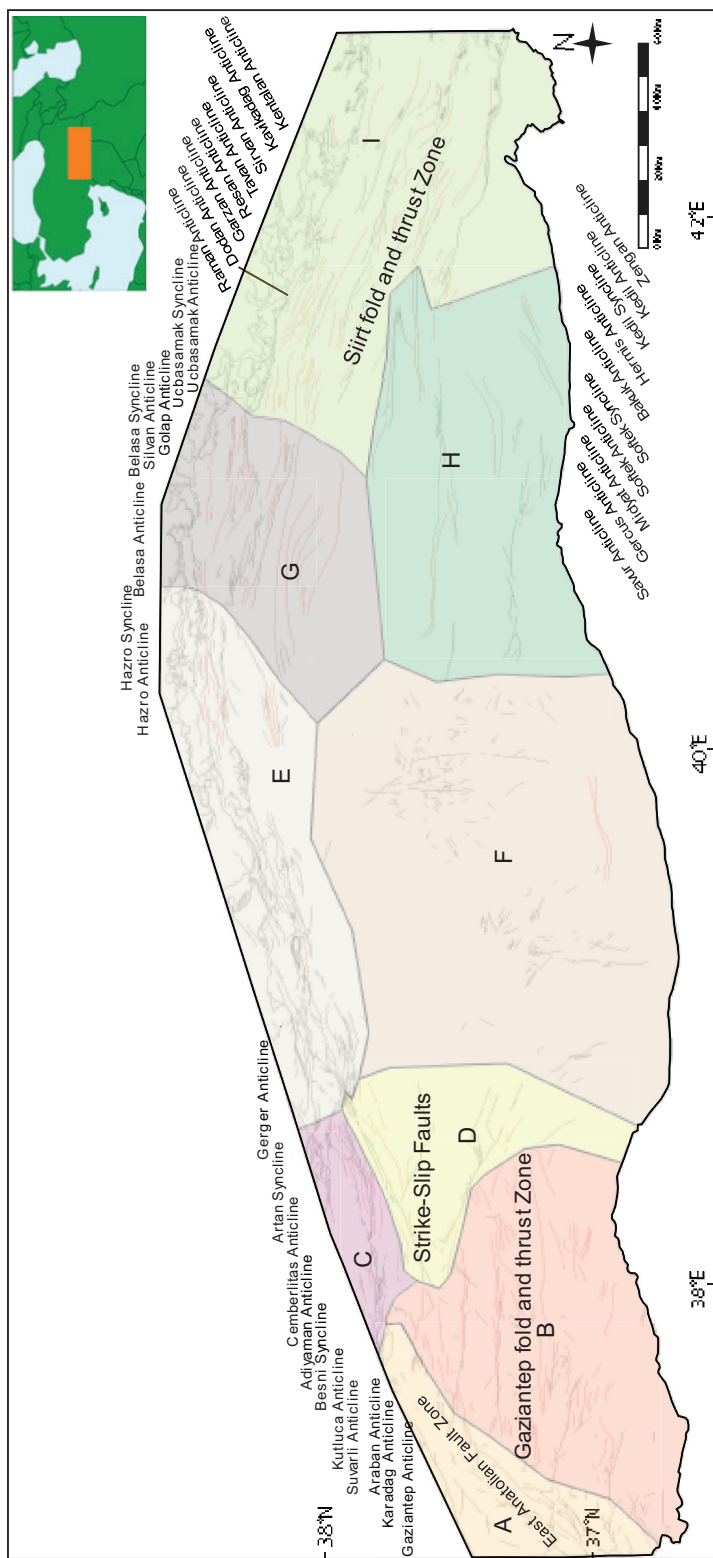


Figure 2.2 Orientations of structures and distributions are shown on the map in the study area.

2.3.2 Mapping Facies

The isopach maps illustrate the distribution of facies in thickness of the selected geological time, which can be utilized for various geological interpretations, particularly when examining the depositional environment of formations and stratigraphic thickness. In this study, firstly, formations were classed together according to their ages and depositional environment. Then, the isopach maps were produced primarily by one hundred forty-four well data and depth-converted horizon tops obtained from seismic interpretation in Petrel software. Each isopach map illustrates the thickness distribution of each stratigraphic class.

2.3.3 Well and Section Correlations

Twenty-three well logs were interpreted to determine formation tops using gamma-ray (GR) and sonic (DT) logs. Sixty-six wells are used for formation tops for stratigraphical correlation purposes. Here, the tops of the newly created stratigraphic classes were considered. Thus, deposition patterns could be presented for each defined period. In this context, seven different well-correlated sections were prepared. Four of them are oriented in the E-W direction while the rest are scattered in various directions. The sections produced here were also used for isopach map constructions.

2.4 Kinematic Analyses

In order to understand the kinematic history of the basin, fold analyses, unconformity (syn/post depositional) determinations, and paleostress analyses were conducted.

2.4.1 Fold Analyses

Fold analysis was carried out in order to understand the geometries of the folds exposed in the study area and to derive kinematic interpretations by determining the spatial and temporal changes in the geometrical features of the folds in space.

Three thousand sixty-eight measurements of the bedding attitude were used to better understand the features and spatial distribution of the folds.

In addition to the rose diagram of the strike of bedding attitudes and histogram of dip amounts of bedding planes in three sub-areas, 31 β - and $-\pi$ diagrams were generated (seven in western, eight in central, and sixteen in eastern subareas) by using stereonet v11 software by Rick Allmendinger. Using the methods developed by Allmendinger (2021), Stereonet 11 software was used to create the β - and $-\pi$ diagrams of the folds. Contour diagrams are constructed using % 1 area contouring, and the axial planes and attitudes of hinge lines are computed using the mean pole directions of each limb of the folds.

2.4.2 Determinations of Syn-depositional Unconformities

Growth strata are proximal syntectonic successions that evolved due to uplift, surface tilting, and erosional denudation of various geological structures (Riba, 1976; Anadòn et al. 1986). This part aims to establish a close relationship and correlation between simultaneous sedimentation and tectonic development for understanding the kinematics of folding and faulting, the sedimentological properties of growth layers around the fold, and the timing of deformation, which are all critical for hydrocarbon exploration programs.

Identifying syntectonic discordances or unconformities is the first step in analyzing growth layers (Riba, 1976). These discordances were classified by Riba (1976) as progressive syntectonic unconformities, which are a succession of strata that flatten up sections but have no apparent dip discordance between beds, and angular

unconformities, which are surfaces that separate successions of strata with noticeable different bedding dips. Figure 2.3 shows the genetic model of progressive and syntectonic angular unconformities proposed by Riba (1976).

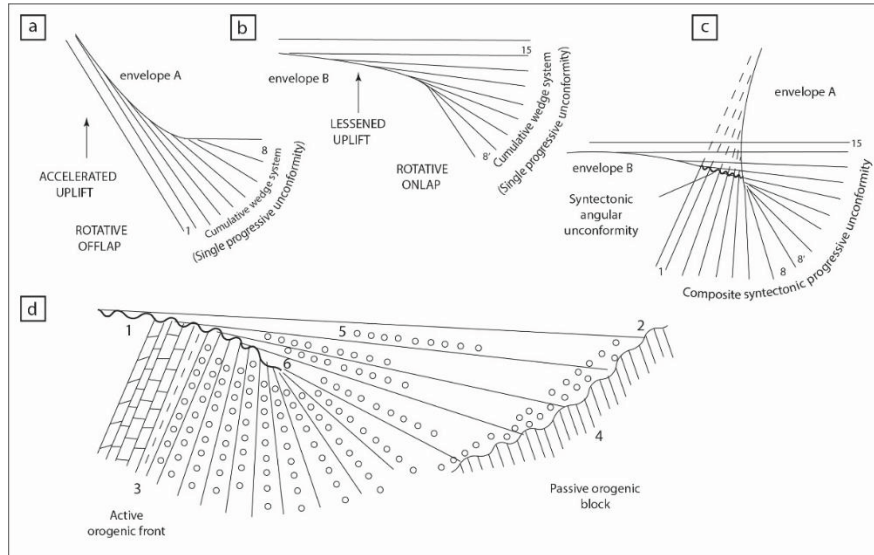


Figure 2.3 A genetic model of syntectonic unconformities in areas where deformation and deposition are related (after Riba, 1976 and Anadòn 1986 et al., 1986).

The dataset for this study consists of 78 bedding attitudes, tapering wedges of strata, and seismic sections where they are available. The technique we used to classify syntectonic unconformity types included the following:

- 1) Package for identified growth strata (the presence of a tapering wedge of strata)
- 2) presence of a high-angle dip discordance and a less obvious, low-angle but measurable dip discordance within flattening up stratigraphic succession (generally 2-5°),
- 3) a sharp increase in grain size or massive sandstones directly adjacent to fault or unconformity surfaces.

2.4.3 Paleostress Analyses

Paleostress analysis is the technique of identifying the principal stress orientations utilizing fault slip data obtained from field measurements of the orientations of the fault planes and slip data (Kaymakci et al., 2006). Slip directions are typically inferred using slickenlines, frictional grooves, or fibrous lines. The purpose of this study is to collect kinematic indicators on fault surfaces where faults are uninterpreted on seismic sections due to poor seismic data quality and to use the paleostress inversion method to unravel the kinematic evolution of faults and associated structures in the SE Anatolian basin as well as to determine the principal stress orientations of each deformation episode.

In the context of kinematic research, 358 fault slip data were collected in age from upper Cretaceous-Paleocene to upper Miocene at 26 different sites in the study area (Appendix A and B). When we collected fault slip data, we considered several criteria, including collecting as much fault slip data as possible (at least four) for each stress solution in a homogeneous rock body and avoiding measurements on corrugated fault surfaces. Fault plane attitude, slickenside, movement sense orientation, and relative dating markers, if it is possible, were measured in the field for each fault. Additionally, sampling in a site was performed following Kaymakci et al. (2000), which specify that all data points within the site must be within a radius of around 50 m to maintain structural homogeneity (Hancock, 1985).

Numerous approaches have also been proposed for paleostress inversion solutions (e.g., Angelier, 1984; 1994; Shan et al., 2003). They suggest that the fault plane evolves in a direction parallel to maximum shear stress. Moreover, the movement of a fault does not affect other faults in about the same tectonic regime. The primary outcomes of these analyses are the determination of the orientation of maximum (σ_1), intermediate (σ_2), and minimum (σ_3) principal stress axes as well as the calculation of the shape ratio of the principal stress differences ($\phi = (\sigma_2 - \sigma_3) / (\sigma_1 - \sigma_3)$). The outputs are utilized to determine the stress regime, which is essentially described as extensional, strike-slip, or compressional, where σ_1 , σ_2 , and σ_3 close to vertical,

respectively. Radial compressional, radial extensional, transpressive, and transtensional regimes can also be possible in addition to these basic (pure) regimes. All relevant analyses were conducted by using Wintensor software (version 5.9.2).

2.5 Cross-section Constructions

To construct a cross-section, field data including bedding orientations (4604 measurements), outcrop traces e.g, boundaries formations, locations, and types of structures, a 1:500000 geological map, and DEM of the research area are used and interpreted along the fold and thrust belt in the Adiyaman, Diyarbakir, and Batman-Siirt subareas of SE Anatolian.

Three regional (one in the western, one in the central, and one in the eastern sub-areas) cross-sections were constructed using 2D seismic profiles (Figure 2.4), surface data, and 36 wells.

2.5.1 2-D Seismic Interpretation

The principal dataset utilized for this study is 86 2D seismic surveys of the SE Anatolian basin (see for locations of well and 2D seismic lines Figure 2.1 and 2.5), consisting of 34 section lines oriented parallel to the strike major structures of the basin and 52 section lines aligned perpendicular to the strike of major structural features of the basin, and come in the form of digital files with SEG-Y format of the seismic data. These data were obtained from the TPAO database store.

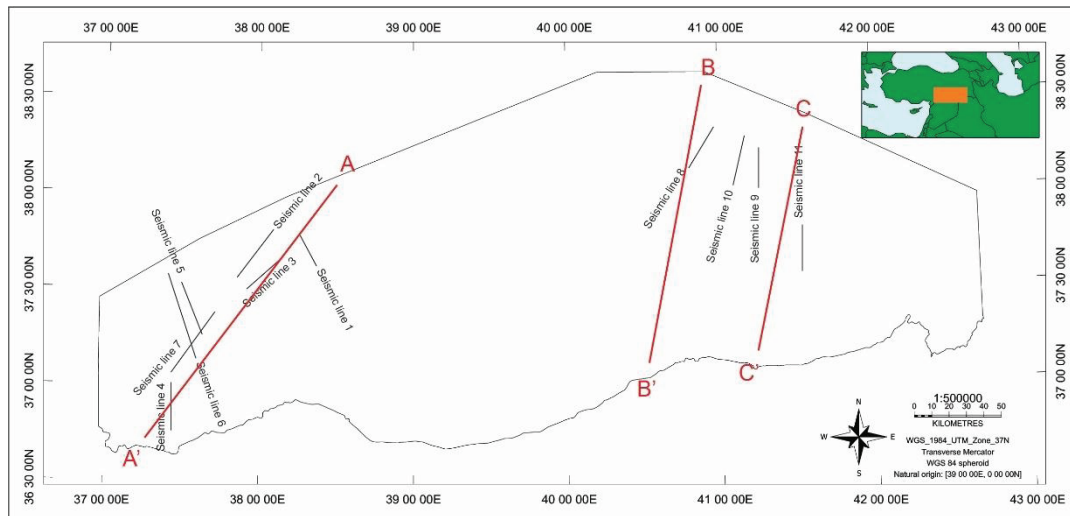


Figure 2.4 The position of the regional and local cross-section lines.

2.5.1.1 Seismic Analyses (Interpretation)

The main approaches for interpreting the seismic sections are picking and tracking consistent seismic reflectors laterally, identifying structural features which search for structural traps containing hydrocarbons, displaying the geometry of structures, and identifying stratigraphic boundaries. The workflow of seismic analyses includes the following steps;

- a) seismic well-tie,
- b) picking horizons and faults,
- c) domain conversion using velocity map and picked a time to construct horizon's depth maps,
- d) creating the geologically-seismic cross-sections and,
- e) the interpretation of the various maps and cross-sections.

Schlumberger's Petrel (2017) software was utilized for this study.

2.5.1.2 Synthetic Seismogram Generation and Seismic-to-Well Tie

Synthetic seismograms are artificial seismic traces extracted from seismic data, used to establish correlations and pick between geological information from well logs such as target formation tops and seismic reflections. The eight well logs, including density (R_{hob}), gamma-ray (GR), and sonic (DT) logs, were mainly used for correlation purposes and the generation of synthetic seismograms.

Establishing the link between seismic reflections and stratigraphy is one of the primary techniques for analyzing seismic data. The first step in this study has been carried out by tying the seismic data to the well data. Typically, well information and seismic data are converted from depth to time and back to depth. Seismic data mainly provides time values, while synthetics provide time and depth values used to verify reflection events.

In the well-tie technique, in conjunction with the density log, the calibrated sonic log was utilized to determine the acoustic impedance (AI), which is used to establish the reflectivity coefficient (RC). For the construction of the synthetic seismogram, a wavelet is required. Using the wavelet toolkit in Petrel, deterministic, analytical, and statistical methods were tried to determine the wavelet, with the deterministic method achieving the best fit among them. The resulting RC and wavelet were used to construct a synthetic seismogram (Figure 2.5). After producing the synthetic generation, the retrieved trace around the well was matched with a seismicogram. This derived trace represents the actual seismic data utilized for the synthetic matching. The synthetic trace could then be moved, stretched, or squeezed to establish the best possible match between the synthetic seismogram and the seismic trace.

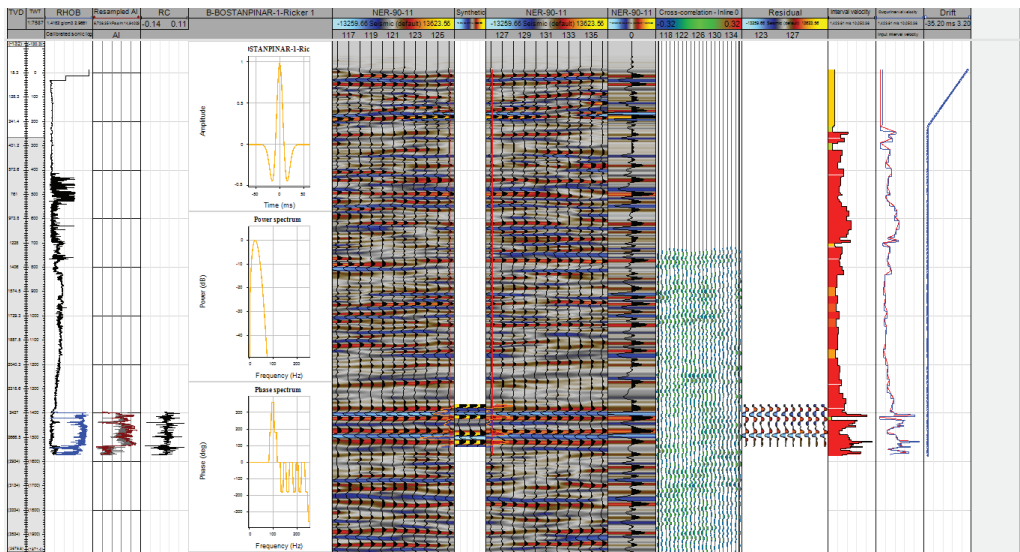


Figure 2.5 Generated synthetic seismograms that tied the well to seismic data illustrating all the components used to generate the synthetic seismogram.

The seismogram was then presented on the vertical sections and utilized to connect the formation tops on the seismogram to those on the nearby vertical seismic section (Figure 2.6).

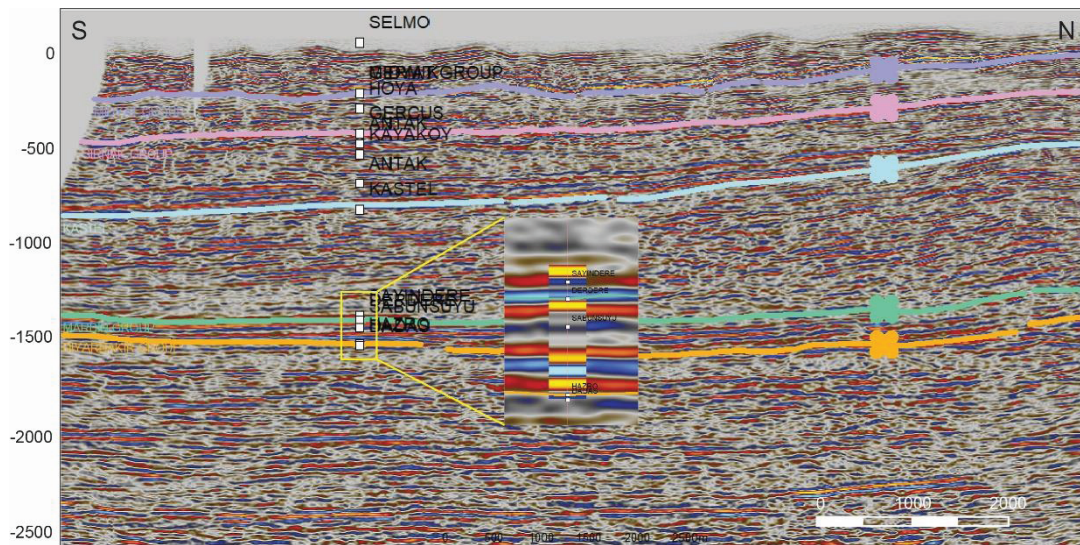


Figure 2.6 The figure showing the synthetic seismogram was matched with the seismic traces to obtain each horizon for target formation tops.

2.5.1.3 Horizon and Fault Interpretation

Horizon and fault interpretations are performed to understand the structural architecture of the study area. The horizon and fault interpretation generally was difficult due to poor reflection resolution and structural complexity in the fold and thrust belts in the northern areas of the study area. Generally, it is preferred to pick horizons before fault pickings for better visualization of fault traces. Horizons were selected depending on the tops of defined stratigraphic classes (seismic-facies classes) provided by the wells. Amplitude similarity and attribute of phase were managed to find each horizon's layer continuity when the horizons were identified.

Thirteen different horizons (based on stratigraphic classes) are determined by tying and matching seismic lines with 11 seismic sections and 8 check-shot data. The manual interpretation routine was applied for the horizon and reflector terminations, and abrupt changes in reflection attributes were taken into account during tracing the horizons and the structures. The faults were manually located and interpreted in

Petrel software. The faults and horizons were picked on the 2D vertical display (e.g. Figure 2.7).

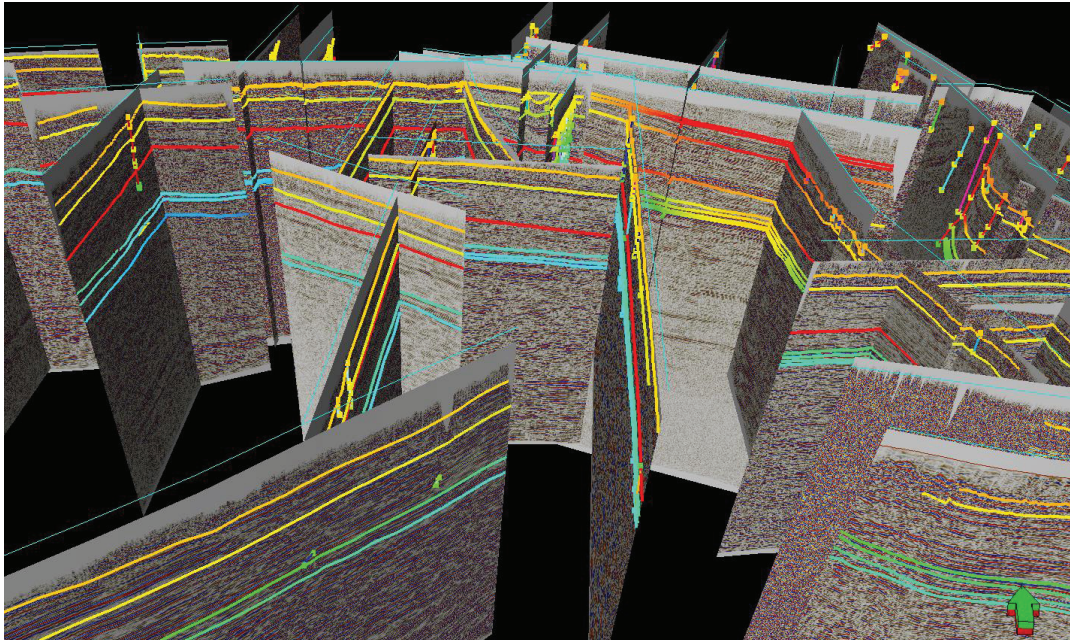


Figure 2.7 Screen snapshot of Petrel software shows various faults and target horizons.

2.6 Cross-section Balancing and Restoration

Geometric consistency of the balanced sections must be admissible and viable (Elliott, 1983). An essential test for the viability of a cross-section is demonstrating that line lengths throughout the stratigraphic sequence are equal when the section is restored to an undeformed state. Balancing a cross-section involves restoring beds to their original horizontality while maintaining bed thickness and length. The cross-section is viable if beds can be restored to an unstrained state and have equal length (Elliott, 1983). When horizontal, beds are in the state in which they were deposited and unstrained. Beds are restored to horizontal by setting one of the ends of the cross-section as a pin line, which maintains position while beds extend past the opposite

end of the cross-section (Dahlstrom, 1969). If the cross-section does not balance, then it is not an acceptable structural model.

The overall objectives of balancing are to restore deformed rock to its original state or its accurate palinspastic restoration and to establish the geological sequence of events such as the timing of structural events and hydrocarbon migration, understanding of the tectonic history, and check whether the interpreted cross-section was geometrically valid (Tearpock and Bischke 2002). Structural balancing is based on the idea that during the interpretation process, the interpreter must neither add nor delete volume (Goguel, 1962). A concept of mass conservation is the key to admissible geologic interpretations and constructions.

In this study, to examine the geometry of the basin and to accurately determine the shortening rates in three sub-areas of the basin, three regional cross-sections created by surface/subsurface data were balanced. The locations of these regional cross-sections and seismic section lines are given in Figure 2.4.

To construct and calculate shortening rates in 3 sub-areas in the study region, we followed the approach given below for the segments of the sections without seismic data.

Firstly, the availability of dip data and well data is considered to decide on the optimum orientations of each section (Figure 2.8). During section line, position selection, 445, 1238, and 1804 bedding measurements were available in the Adiyaman, Diyarbakir, and Batman-Siirt sub-areas, respectively. We found out that from west to east, N27E, N12E, and N18E directions are the best directions for the three subareas in the study area, respectively (Figures 2.8 and 2.9). During section constructions, a specified distance (~1.5-2 km) from the section line was determined to collect dip data and reflect their apparent dip values on section lines.

Secondly, a template horizon was constructed based primarily on Ramsey's (1967) parallel folding (1B fold classes-constant layer thickness) by utilizing isogons of separated dips where available. After that, the previously generated (template)

horizon was used as a reference layer for the original (real) layers, which were created by the software automatically considering the thickness of the units and geometric relations of the 1B fold type.

Thirdly, the sections were fit to geological/structural map and topography. Some general rules are followed during the structural restoration processes, such as the conservation of rock volume and deformation mode (brittle faulting). The approaches utilized in kinematic structural restorations are divided into two categories: unfolding restoration and moving on fault restorations. We used flexural-slip unfolding processes in this study using Midland valley (MOVE) software.

In this method, after digitizing all structure locations (faults, formation boundaries, etc.), the flexural-slip unfolding technique is utilized. For this, the thickness of stratigraphic cycles and created uppermost bed lines were maintained. This approach assumes a defined pin line (the axial plane of the section) to specify the region of no-slip and reconstruct a slip system parallel to the defined template bed. Pin lines are used for measurements and consistency of bed length during the cross-section balancing. In order to verify a cross-section, unfolding, movement on the fault plane and calculation of the amount of shortening stages are required.

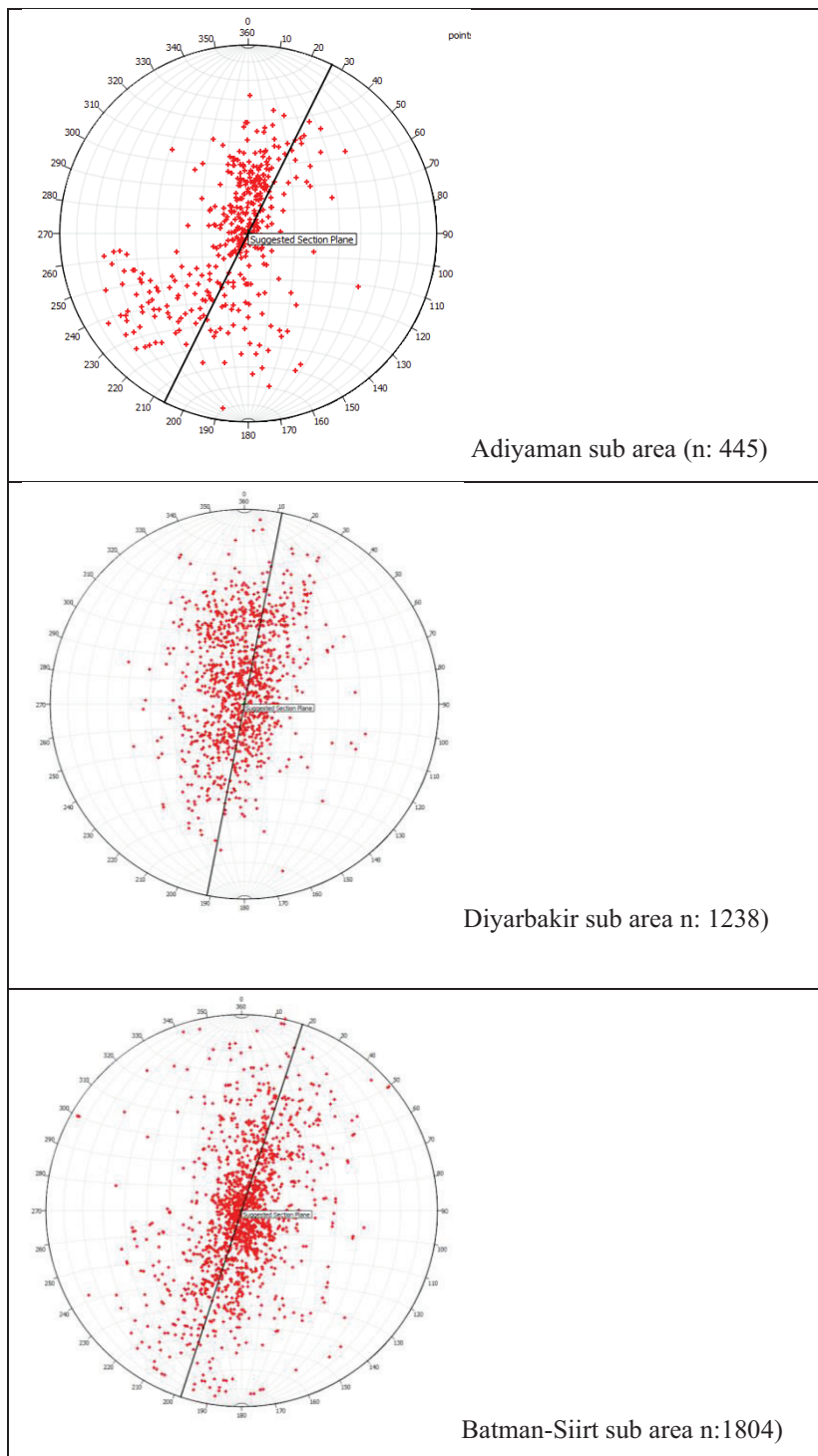


Figure 2.8 Stereonet plot displaying the suggested section plane orientations of regional cross sections.

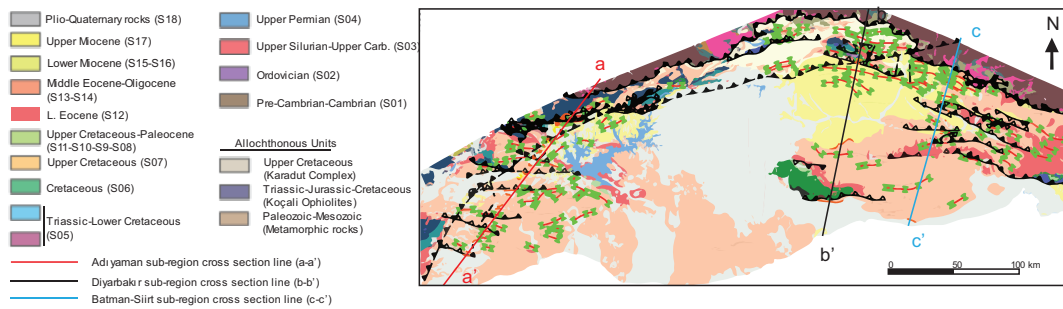


Figure 2.9 Digitized faults and folds visualized in the map view of the study area.

2.6.1 Velocity Modelling/Depth Conversion

Depth conversion removes inherent time-related ambiguities in the correlation of internal events through the 2D seismic and verifying structure. Tie the existing wells and accurately predicting depths at new well locations are the main of reliable depth conversion (Etris et al., 2002). Time-depth conversion processing is required to visualize the structural features of horizons and faults effectively. The inputs for the velocity model were checkshot data, the well top depths, and the picked seismic time horizons to create a velocity model and convert the seismic data from the time domain to the depth domain. Within the study area, a velocity map of the top of the Mardin Group was constructed (Figure 2.10).

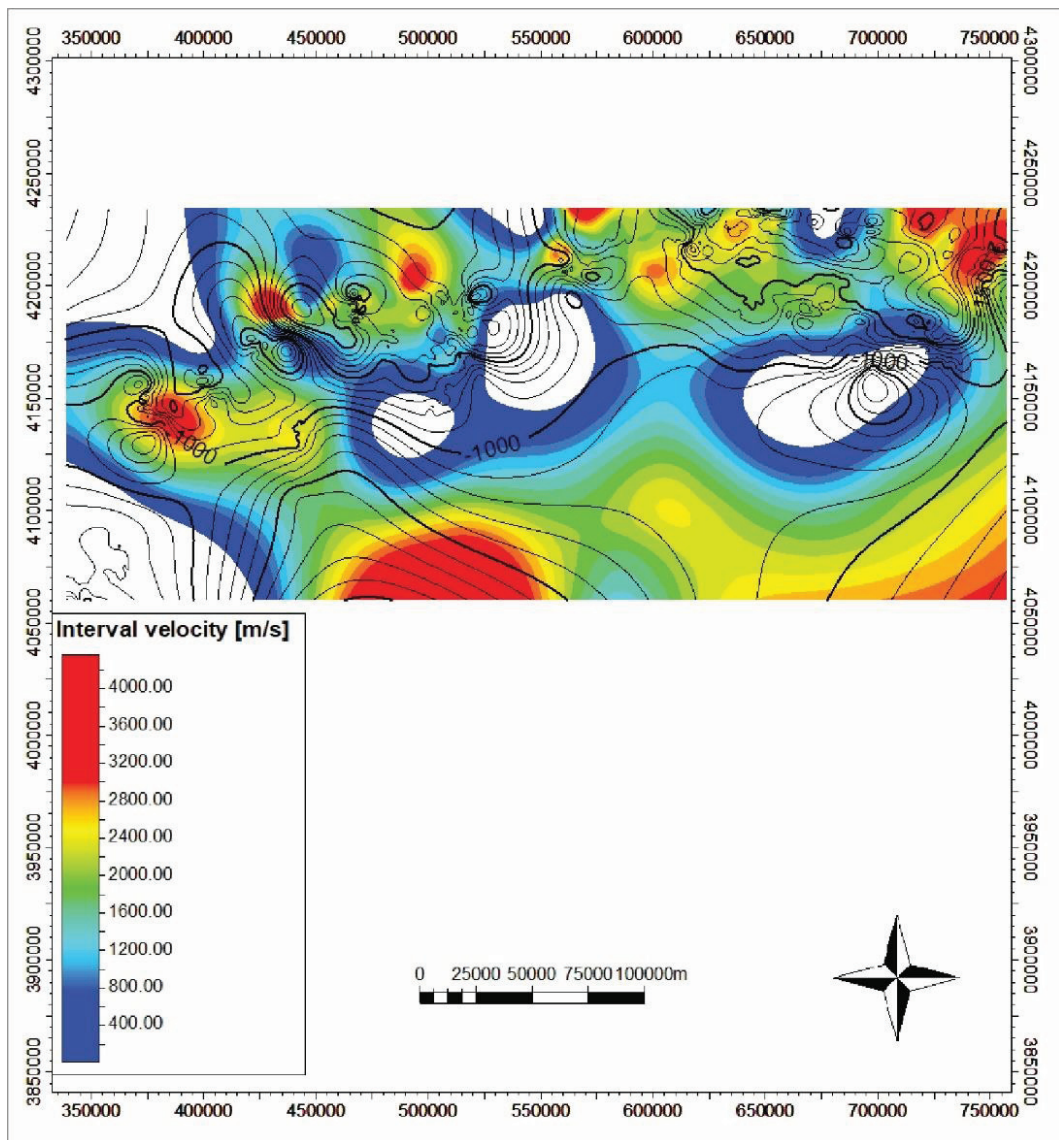


Figure 2.10 This figure shows the interval velocity map of the Upper Cretaceous shallow marine unit.

2.6.2 Shortening Ratio Calculations

Three regional cross-sections were restored for each of the three sub-areas to compare shortening evolution from W to E in the research area. The shortening rates along the sections were calculated by using the lengths of deformed and undeformed sections in percentage and formulated by;

Shortening = Observed Bed Length - Width of Structure at Regional

and,

% Shortening = $100[(\text{Width of Structure at Regional} - \text{Observed Bed Length}) / \text{Width of Structure at Regional}]$

CHAPTER 3

ANALYSIS AND INTERPRETATIONS

3.1 Morphotectonics

Morphotectonics is defined as a tectonically induced morphological feature or structurally associated morphological feature that can be separated from adjacent regions by its characteristics, elevation, relief, geology, and structures (Hills et al., 1961). The delineation of the domain boundaries is based on interpretation and expert judgment.

The study area is dominated by compressional and contractional structures manifested by thrust and reverse faults. They control mainly the northern margin of the study area along the southern foothills of the Bitlis Zagros Sutures Zone. The southern extensions of these contractional structures were developed mainly within the northern edge of the Arabian Platform and are manifested as a reverse fault that is developed mainly at the cores of south verging fold-propagation and fault-bend folds, such as Areban, Yavuzeli anticlines in the west and Botan, Sadak, Tavan, Dodan, Reşan anticlines in the east.

The dominant structures in the study area are interpreted using available literature and field data (Figure 3.1). Considering the tectonic styles, density, and the type of dominant structures, the study area is divided into nine morphotectonic domains (Figure 3.2). The dominant attitudes of the structures in Domain A are oriented N47E, N88W in Domain B, N80E in Domain C, N85W in Domain D, N77E in Domain E, N15W in Domain F, N80W in Domain G, N80E in Domain H, and N65W in Domain I (Figure 3.2). The attitudes of all structures in the whole study area concentrated in the N82W direction (Figure 3.1 a), almost E-W direction parallel to the main trend of the Bitlis Suture in Türkiye.

Likewise, orientations and the densities of the structures in the study area also differ. They are primarily concentrated along the rim, eastern and western margins of the study area. The frequency of the structures in the central part of the study area is lower. This possibly is due to the deformation's intensity decreasing towards the central parts but also because this area is covered with young basaltic rocks and Plio-Quaternary alluvial that hinders the structures. According to Rose diagrams, In addition to analyzing all structure data, the orientations of fold axes, reverse or thrust faults, strike-slip faults, and tension fractures are N83W, N86E, N36E, and N04E, respectively (Figure 3.1 b-e).

The domain (A) represents the East Anatolian Fault zone, and the main trends of the structures (N47E) are suitable with the trend of the fault zone. The domain (B) represents the reverse faults located at the west-southwest of the study area, and the mean trends of the structures show the N88W direction. The domain (C) represents the thrust/reverse faults northwest of the study area. The mean trend of the structures in this domain is similar to the domain (B) but slightly differs from it by N80E direction. The domain (D) represents the strike-slip faults (one right-lateral and one left-lateral fault) at the central west of the basin. The mean directions in this domain were calculated as N60W and N65E. The domain (E) represents the reverse and thrust fault zone at the central north of the study area. The N77E direction represents the main trends of the structure in that domain. The domain (F) represents the tension fractures and normal faults observed on the Plio-Quaternary volcanic rocks. The mean trend of these structures (N15W) is almost perpendicular to the ones of thrust/reverse faults in the region. The domain (G) represents the reverse/thrust fault zone at the central NE of the study area. The mean trend of the domain is N80W. The domain (H) represents the reverse fault zone at the central south of the study area. The N80E direction represents the mean trend of the structures found in the domain. The domain (I) represents the thrust/reverse faults observed at the NE corner of the study area, and the mean trends of this domain indicate the N65W direction.

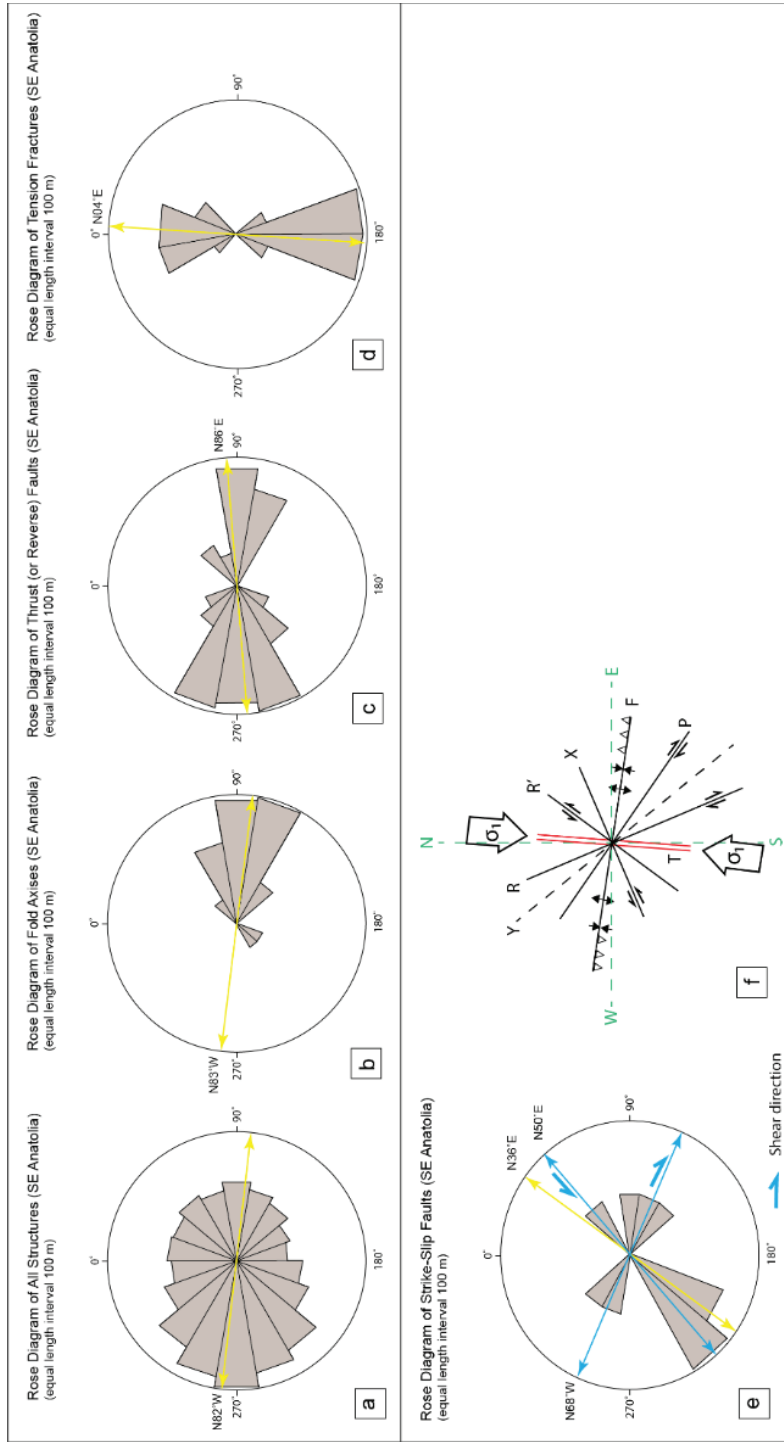


Figure 3.1 a-e) Length-weighted rose diagram of all the structures, folds, thrust or reverse faults, tension fractures, and strike slip faults of the SE Anatolian of the basin. f) right lateral Riedel shear diagram generated using $\sim 04^\circ$ oriented maximum principal stress, revealing potential structural trends in SE Anatolian.

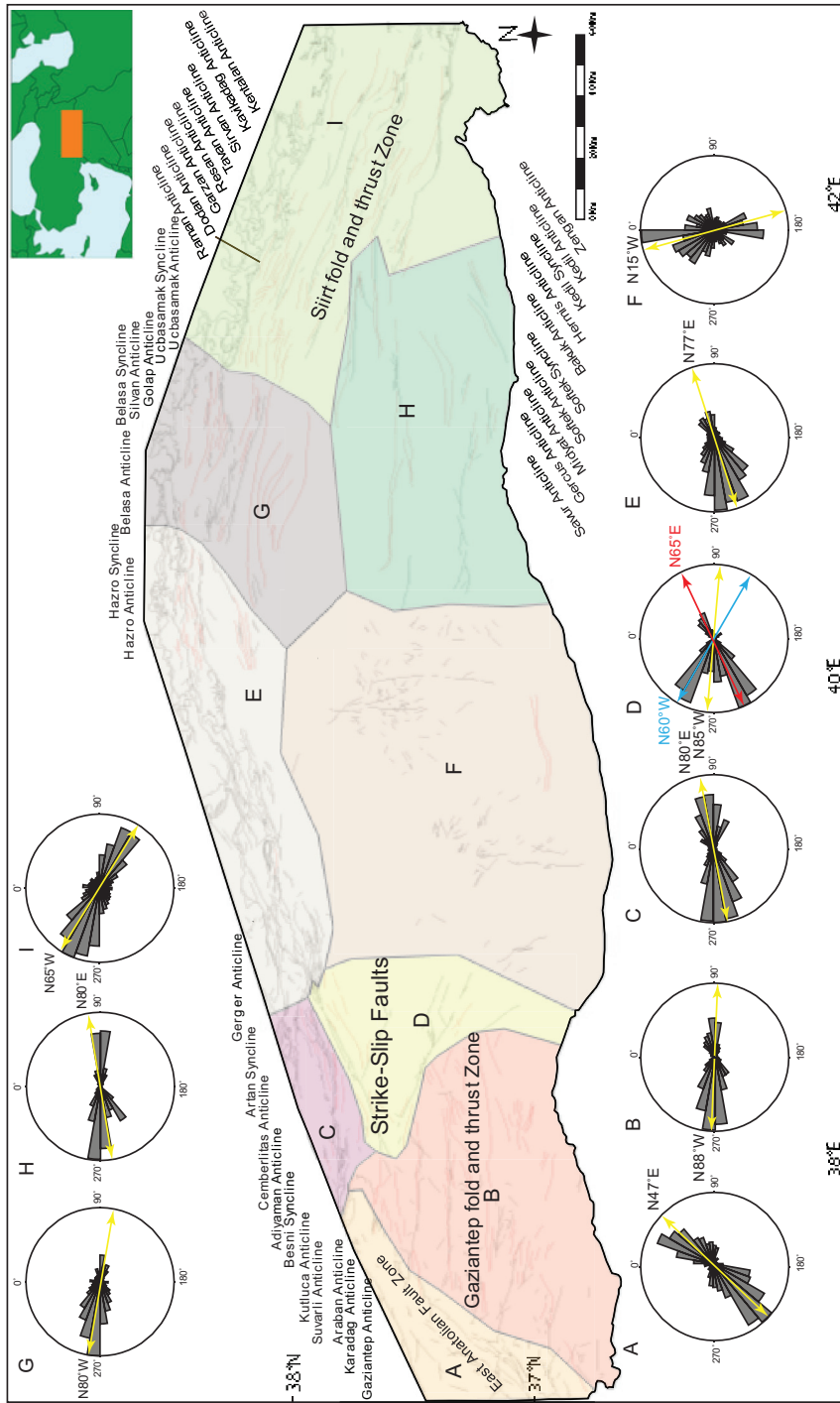


Figure 3.2 Length-weighted rose diagram of all structures, folds, thrust or reverse faults, and strike slip faults of the SE Anatolian of the basin in Adiyaman, Diyarbakir, and Batman-Siirt.

In addition to the rose diagrams considering only the trends of the structures, here we construct a new class of analyses regarding the age and motion of the faults (Figure 3.3). In this sense, the length-weighted rose diagrams of the structures given in Figure 3.4 indicated that the orientations of thrust (or reverse) faults in Late Miocene, Late Eocene-Miocene, Late Cretaceous age, and Triassic-Jurassic normal faults are calculated as N86E, N84W, N75E, and N88W, respectively (Figure 3.4). The age and kinematics of the faults are based on well-logs, seismic interpretations, as well as information obtained from Perinçek et al. (1992).

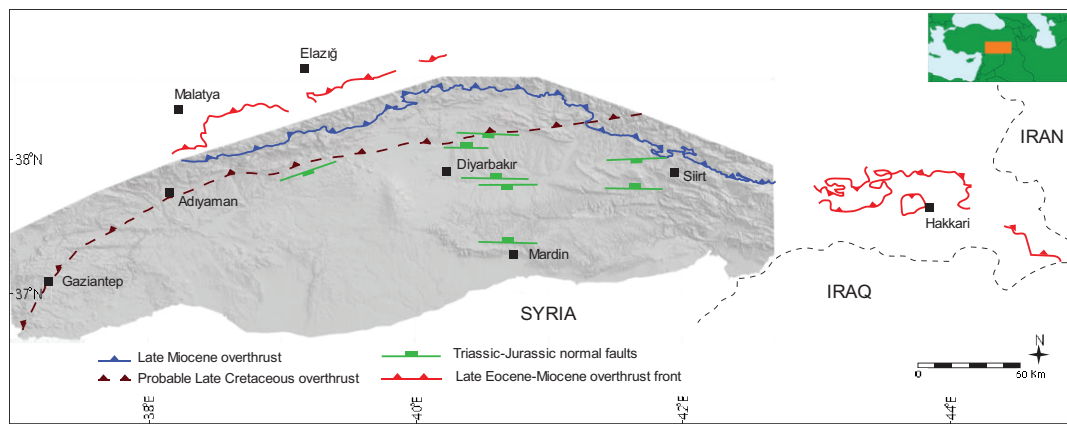


Figure 3.3 The age and motion of structures (thrust/reverse faults and normal faults) of the SE Anatolian basin (modified from Perinçek et al., 1992).

The thrusting of oceanic material onto the carbonate shelf at the northern margin of the Arabian plate during the latest Cretaceous period is observed by the contact relationships of two major allochthonous rock units of southeastern Anatolian (Koçali and Karadut complexes). These allochthonous units are found on top of the Upper Cretaceous Kastel Formation in the region. The reflection of the thrusting is also observed as thrust imbricate and duplex structures within the Koçali and Karadut Complex in the study area (Figure 3.5).

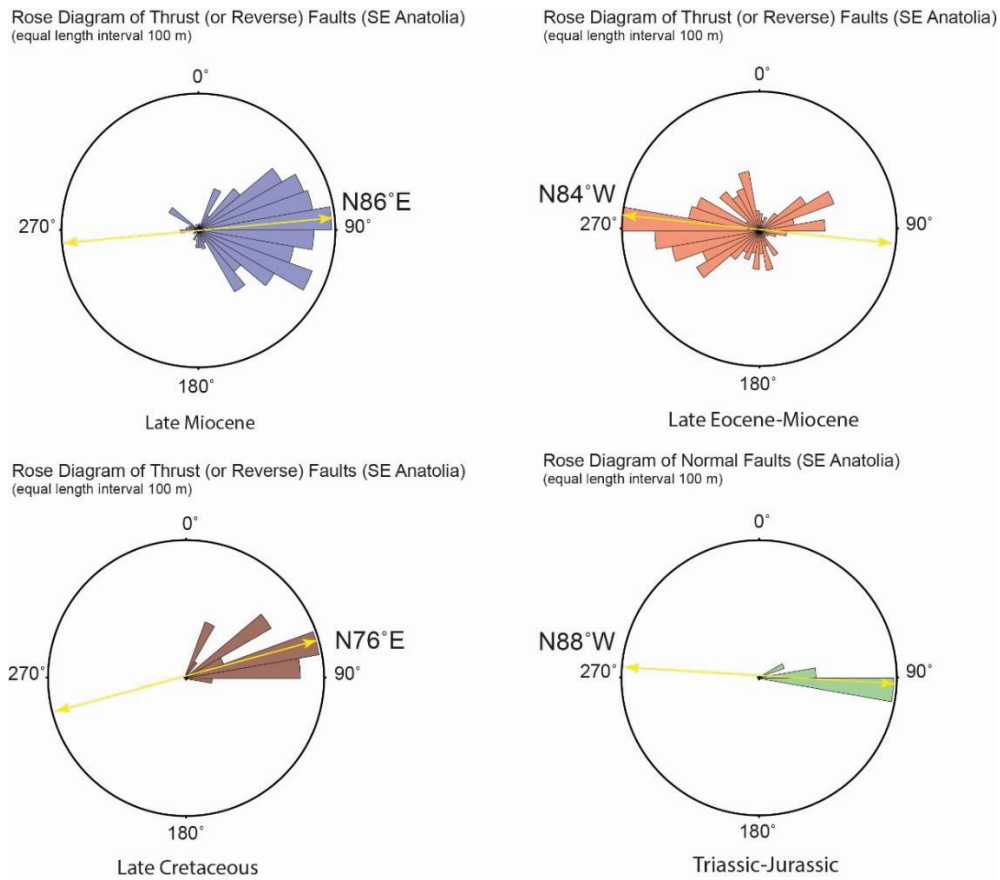


Figure 3.4 Length-weighted rose diagram of thrust/reverse and normal faults of the SE Anatolian of the basin.



Figure 3.5 Picture shows the imbricate thrust structure in the intensely deformed upper Cretaceous Karadut Complex (flysch) in the Adiyaman sub-area.

The arc-shaped Late Miocene thrust fault (see Figure 1.3) forms the contact between Late Miocene continental clastics and basin-fill and defines the northern boundary of the basin. The Late Miocene thrust trends approximately NE-SW, W-E, and NW-SE in Adiyaman, Diyarbakir, and Batman-Siirt subareas, respectively. The Paleozoic to Middle Eocene allochthonous units thrust over the upper Miocene Şelmo Formation and lower Lice Formation, where the Şelmo Formation was not exposed on the North Arabian plate margin (Figure 3.6 a and b). In addition to the basin-bounding Late Miocene thrust fault, the southeastern Anatolian contains reverse faults observed in basin interiors (Figure 3.7).

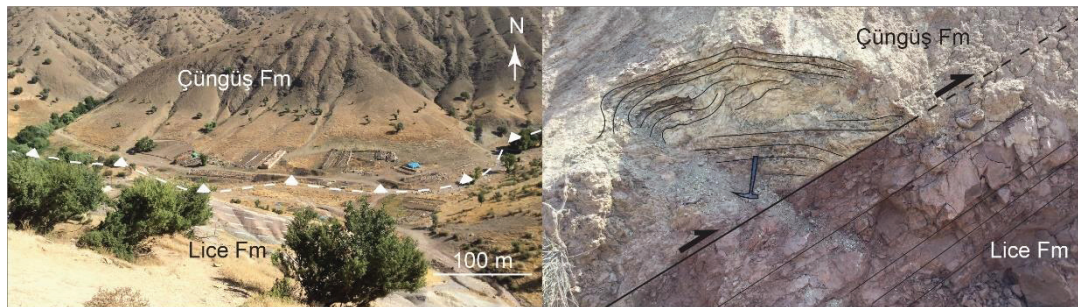


Figure 3.6 Field views of Late Miocene thrust emplacement around the north of Siirt region. a) Eocene-Miocene flysch (Çüngüş Formation) thrust over lower Miocene flysch (Lice Formation), b) close-up view of the thrust fault.

Southeast Anatolian contains reverse faults with nearly identical trends, NE-SW, W-E, and NW-SE, from the western, central, and eastern portions of the study area, respectively. Generally, reverse faults extend nearly parallel to the fold axes' hinge line and extend in the same direction as their axes. Reverse faults have emerged in front of the Late Miocene thrust zone in the whole area. In contrast, some reverse faults in western and eastern areas are classified as blind reverse faults (i.e., they do not reach the surface) since the folds observed in the region show typical characteristics of fault propagation folds indicating blind thrusts (Figures 3.8 and 3.9).

3.2 Stratigraphy

In the literature, the units in the study area are divided into 63 different lithostratigraphic units. Based on their age and facies characteristics, they are simplified into 19 stratigraphic classes (Figure 3.10). The simplified classes are depicted in 11 different facies maps (Figure 3.11-3.21) and Table 3.1, highlighting their distribution, depositional environments, and contact relationships.

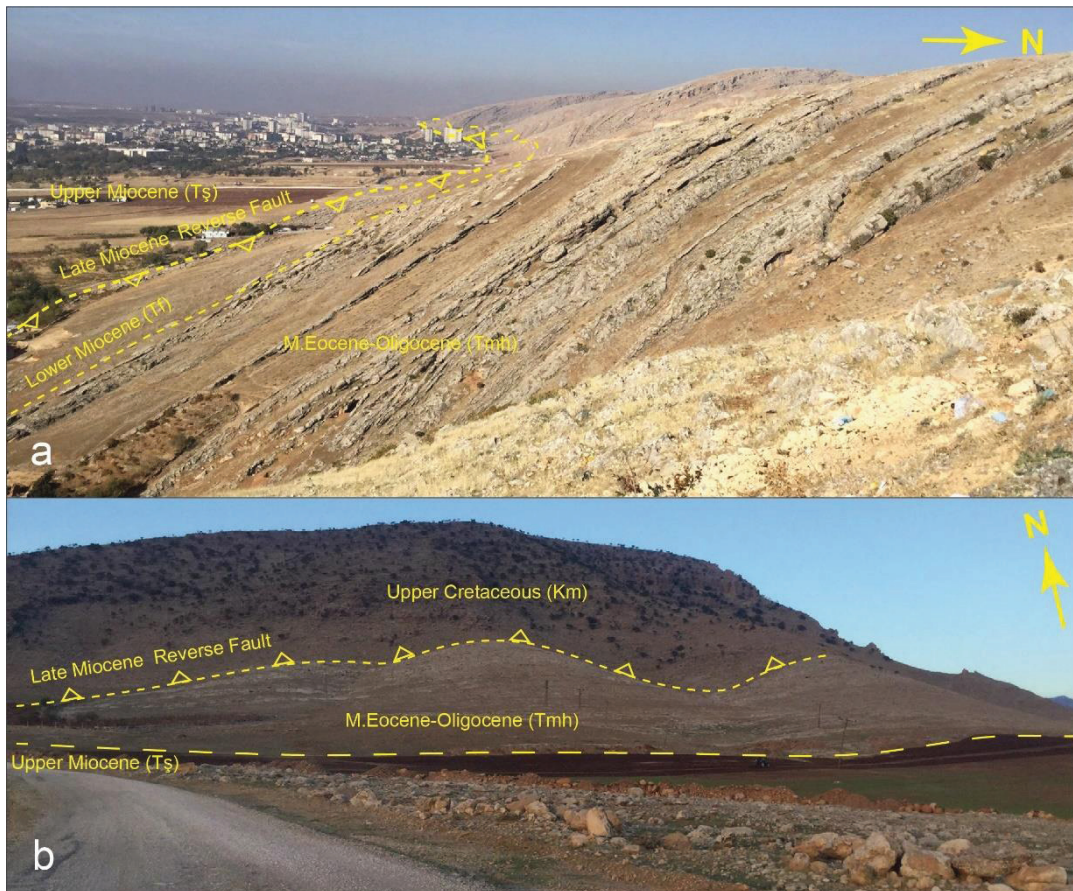


Figure 3.7 a) Field view of Late Miocene thrust emplacement south of Hazro High in Diyarbakir subarea. b) Field view of Late Miocene thrust emplacement south of Mardin High in Diyarbakir subarea.

The oldest stratigraphic rocks are coded as S01, containing pre-Cambrian basement (Telbesmi Formation) and Cambrian continental to shallow marine deposits of Sadan, Zabuk, Koruk, and Sosink formations. These units crop out at the NW corner

of the study area (around Adıyaman) and south of the study area around Mardin High (Figure 3.11).

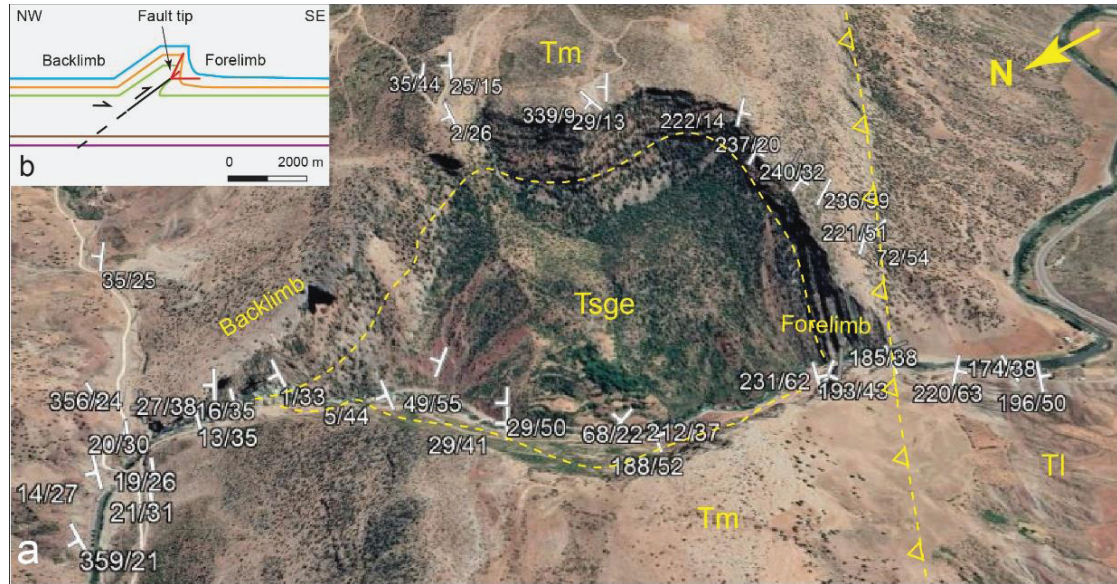


Figure 3.8 a) Aerial photo of Dodan Anticline with bedding attitudes. This fold is presumably related to a fault propagation fold. Tsge: lower Eocene Gercüş Formation, Tm: middle Eocene-Oligocene Midyat Group, Tl: lower Miocene Lice Formation. b) Simplified sketch of a fault-propagation fold.

The second S02 class comprises shallow marine deposits of Ordovician Bedinan and Seydişehir formations. This class crops out only around Mardin High (Figure 3.11).

S03 class contains shallow marine to relatively deeper marine deposits of Upper Silurian – Devonian and Lower Carboniferous Dadaş, Hazro, Kayayolu, Yiğınlı, Köprülü, and Belek formations. This class unit exposes only in Hazro High (Figure 3.11).

S04 class comprises shallow marine deposits of Upper Permian Kaş and Gomanibrik Formations. This unit crops out around Hazro High and Şırnak-Hakkari region (Figure 3.11).

The Paleozoic-Mesozoic metamorphic rocks distribution of the study area is widespread along the northern side of the Late Miocene thrust front. However, the

unmetamorphosed equivalents of these units are exposed in locally small areas in the south of the Miocene frontal thrust around the Mardin High and the Hazro High (Figures 3.11 and 3.12).

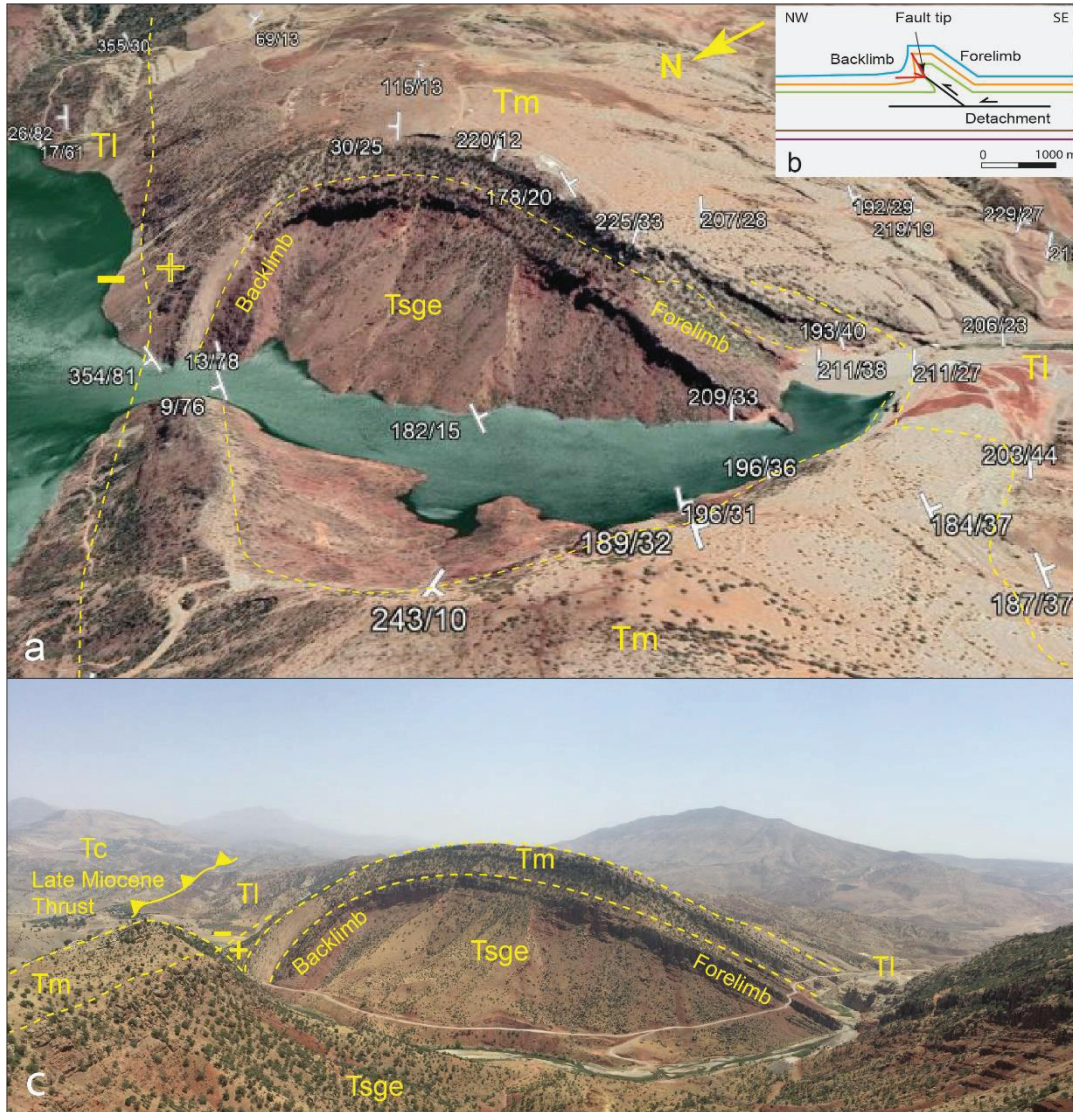


Figure 3.9 a) Aerial photo of Tavan Anticline is presumably related to fault propagation folds with measurements of bedding attitudes. (Tsge: lower Eocene Gercüş Formation, Tm: middle Eocene-Oligocene Midyat Group, Tl: lower Miocene Lice Formation. b) Fundamental properties of the fault-propagation folds.

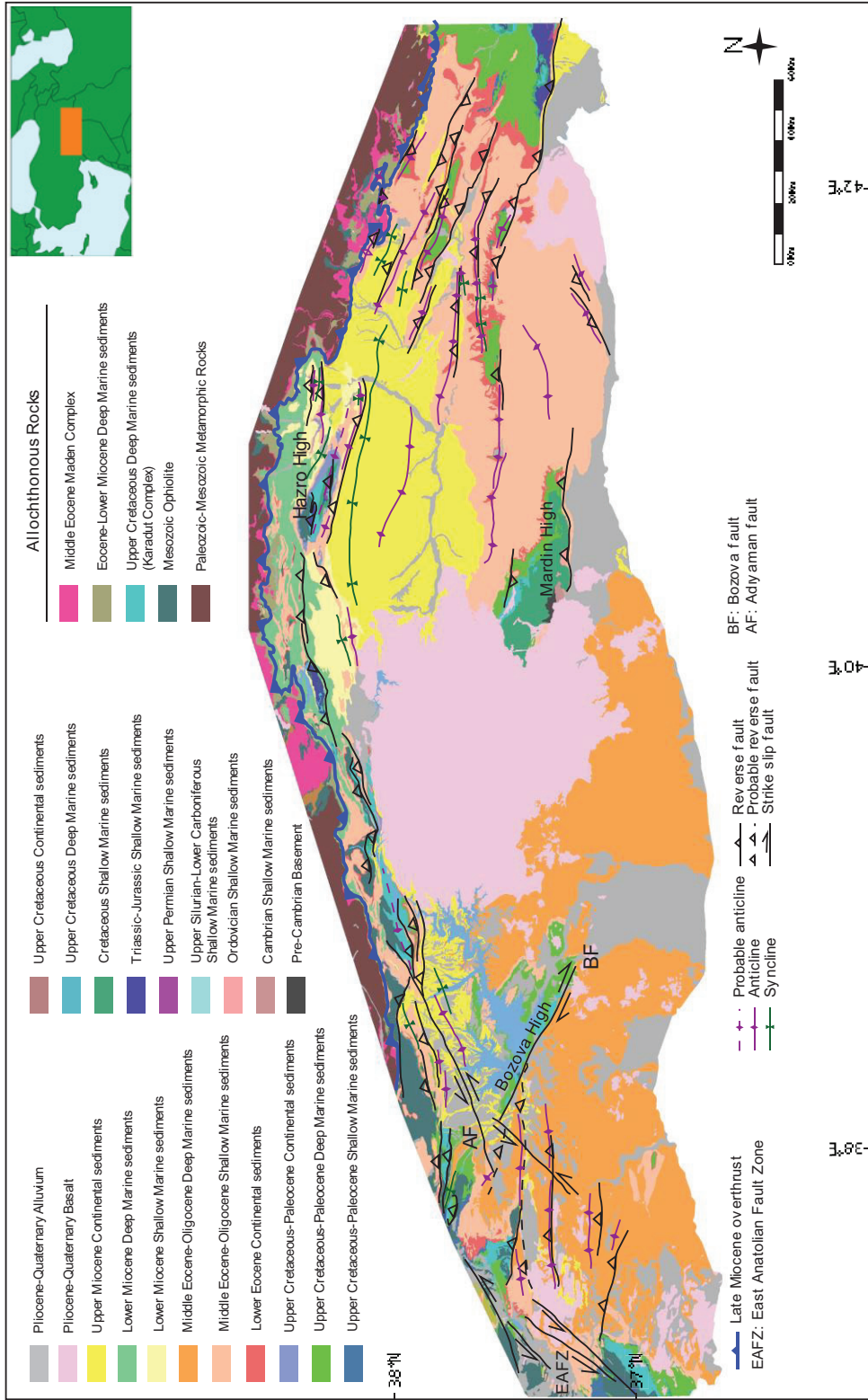


Figure 3.10 Facies map of the research area.

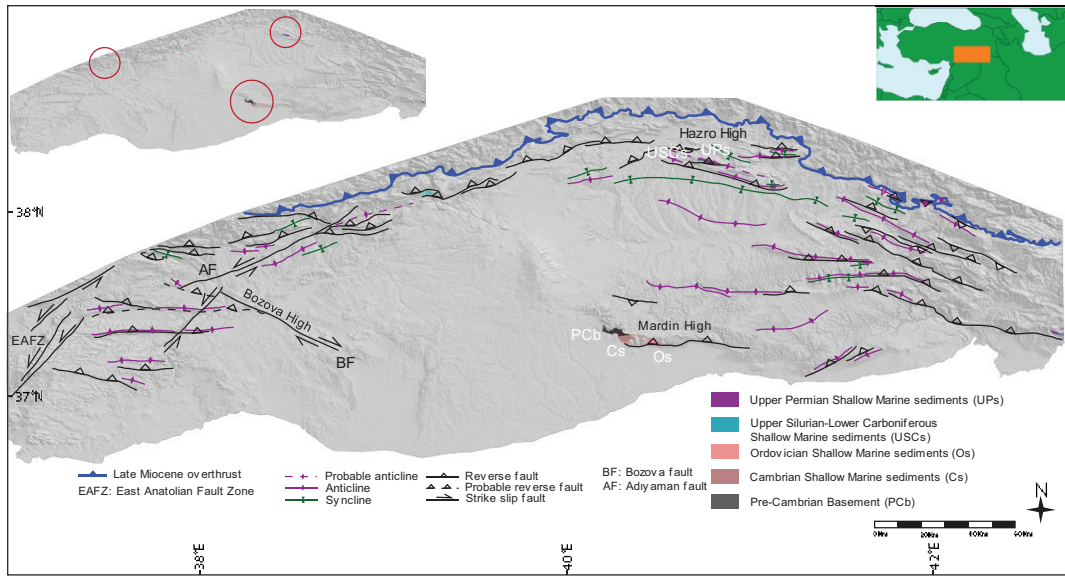


Figure 3.11 The map illustrates Pre-Cambrian-upper Permian units on the surface of the study area. Red circles indicate the location of S01 rocks.

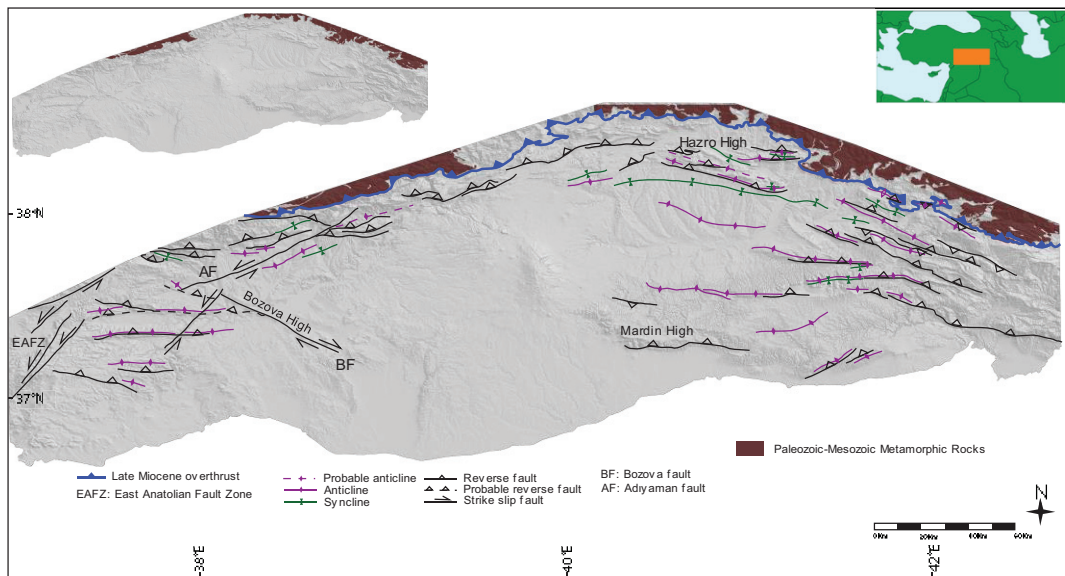


Figure 3.12 The map illustrates Paleozoic-Mesozoic rocks on the surface of the study area.

The classes above cover the core units of the Arabian Plate and they show continental and shallow marine environment characteristics, while some isolated outcrops indicate a relatively deeper marine environment.

S05 class is composed of shallow marine and rarely observed continental deposits of Triassic-Jurassic age formations belonging to Çığlı and Cudi groups. These units are found around the northern margin (NW of Hazro High) and SE corner (Şırnak-Hakkari) of the study area (Figure 3.13).

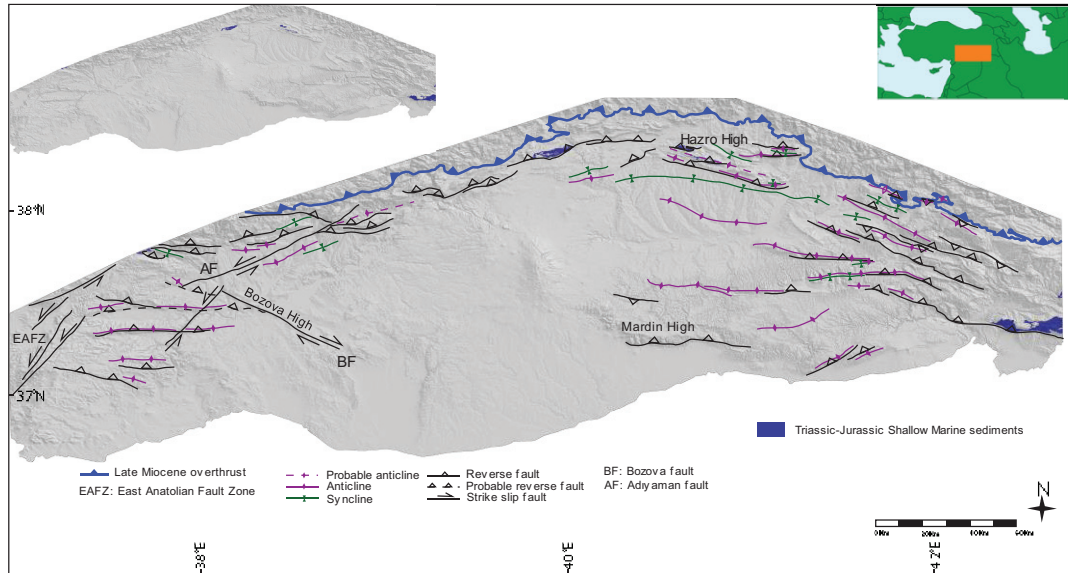


Figure 3.13 The map illustrates Triassic-Jurassic shallow marine sediments on the surface of the study area.

S06 class consists of shallow marine deposits of Cretaceous Areban, Sabunsuyu, Derdere, and Karababa formations. Exposures of the class are observed around the older class units, where their uplift is controlled by thrust faults (Figure 3.14).

S07 class comprises deep marine units of Upper Cretaceous deep marine deposits of Kastel, Bozova, Sayindere, Karaboğaz, and Ortabağ formations. These units crop out north, northwest, and west of the study area (Figure 3.14).

S08 class contains continental deposits of Upper Cretaceous Terbüzek and Kıradağ Formations. This class crops out only around the Adiyaman region (NW of the study area) (Figure 3.14).

The Mesozoic ophiolites (e.g., Kocali Ophiolites, which exposed the NW and W sides of the basin) and Upper Cretaceous deep marine Karadut Complex generally

exposed the northern side of the possible Late Cretaceous thrust front in the study area. The approximately NE-SW trend becomes the dominant trend of the basin (Figure 3.15).

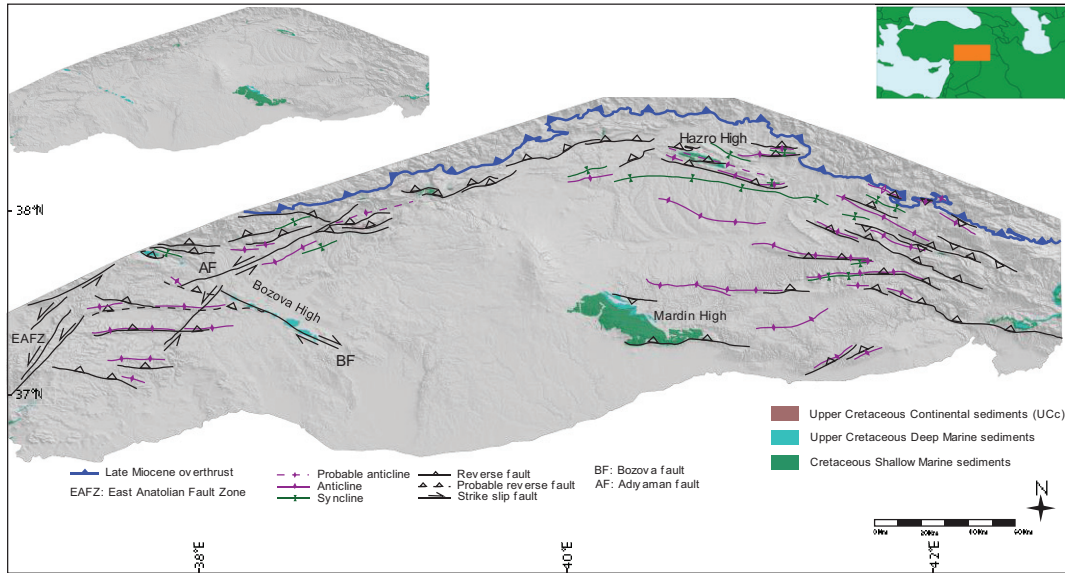


Figure 3.14 The map illustrates Upper Cretaceous continental and deep marine sediments and Cretaceous shallow marine sediments on the surface of the study area.

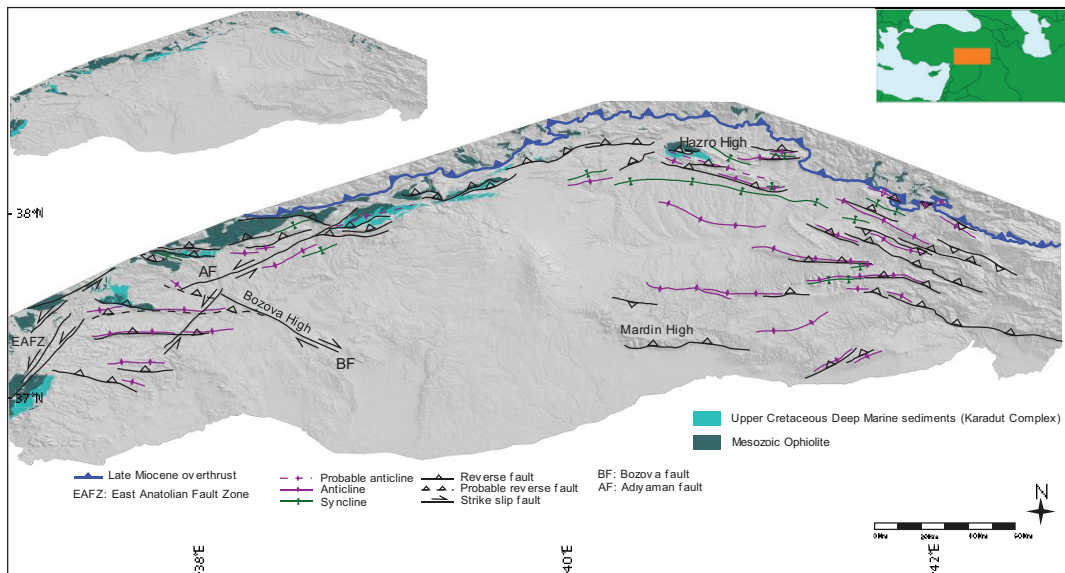


Figure 3.15 The map illustrates Mesozoic ophiolites and the Karadut complex on the surface of the study area.

S09 class comprises shallow marine deposits of Upper Cretaceous-Paleocene Besni, Garzan, A. Sinan, U. Sinan, Becirman, and Belveren formations. These units crop out at the NW and East of the study area (Figure 3.16).

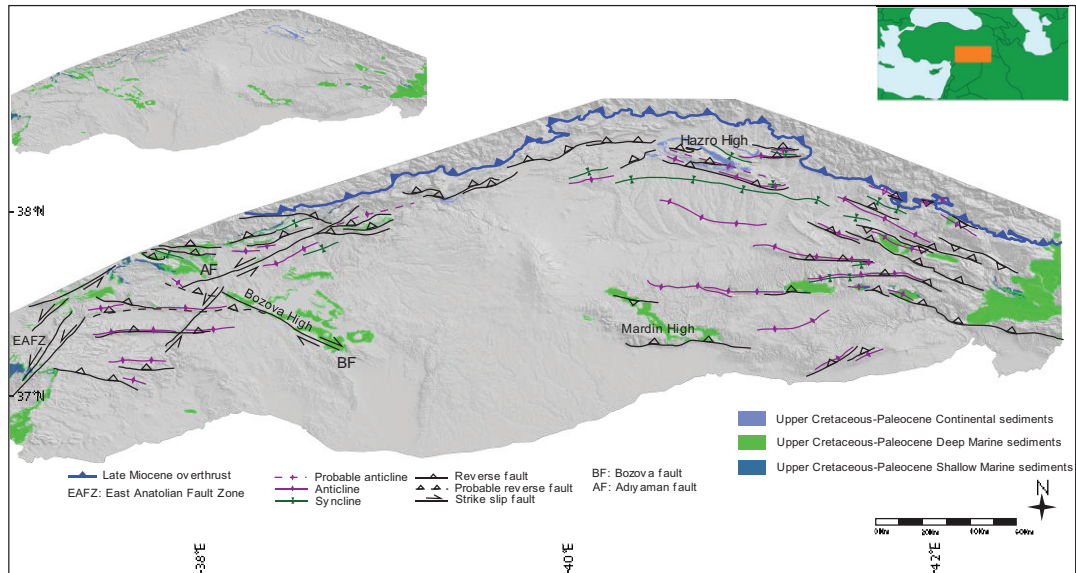


Figure 3.16 The map illustrates the distribution of Upper Cretaceous-Paleocene continental clastics and shallow and deep marine deposits.

S10 class comprises deep marine units of Upper Cretaceous-Paleocene A. Germav and Ü. Germav formations. These formations cover relatively large areas in the study area, and they are observed in various parts of the study area (Figure 3.16).

S11 class units consist of Upper-Cretaceous but dominantly Paleocene continental deposits of Antak formation. This unit crops out around Hazro High (Figure 3.16).

S12 class is composed of Lower Eocene continental deposits of the Gercüş Formation. This unit mainly crops out at the margin of the fault-controlled highs, such as Hazro-Mardin highs and the northern rim of the basin (Figure 3.17).

S13 class comprises Middle Eocene-Oligocene shallow marine deposits of Hoya and Germik Formations. Relatively narrow outcrop patches of the unit follow the basin's northern rim but they cover large areas at the East of the basin (Figure 3.17).

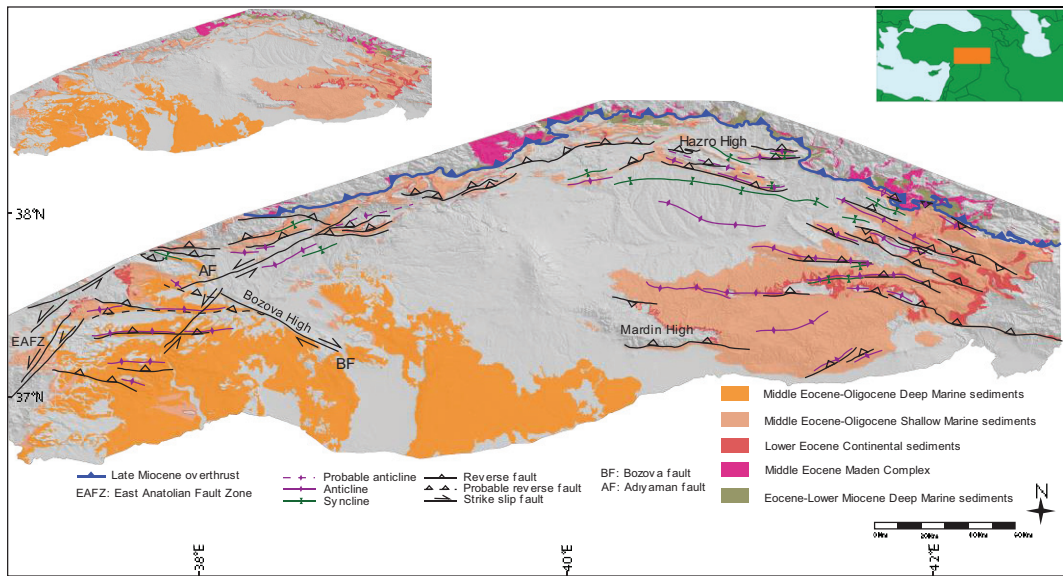


Figure 3.17 The map illustrates middle Eocene-Oligocene shallow and deep marine sediments, lower Eocene continental clastics, middle Eocene Maden Group, and Eocene-lower Miocene deep marine sediments on the surface of the study area.

S14 class consists of Middle Eocene-Oligocene deep marine sediments of Gaziantep formation. The outcrops of the unit are observed as the lateral continuation of S13 class units, but this class unit mainly covers large areas at the center and the southwest of the basin. Otherwise, in the north of the Late Miocene thrust front, the middle Eocene Maden Group and Eocene-lower Miocene deep marine rocks are exposed (Figure 3.17).

S15 class is composed of Lower Miocene shallow marine deposits of the Fırat Formation. This unit crops out north of the basin (Figure 3.18).

S16 class contains Lower Miocene deep marine deposits of the Lice formation. This unit mainly crops out at the northern flank of S15 class units (Figure 3.18).

S17 class comprises Upper Miocene continental deposits of the Şelmo Formation. This unit covers large areas at the east of the basin, but it is also observed as a cover unit at some parts of the study area (Figure 3.19).

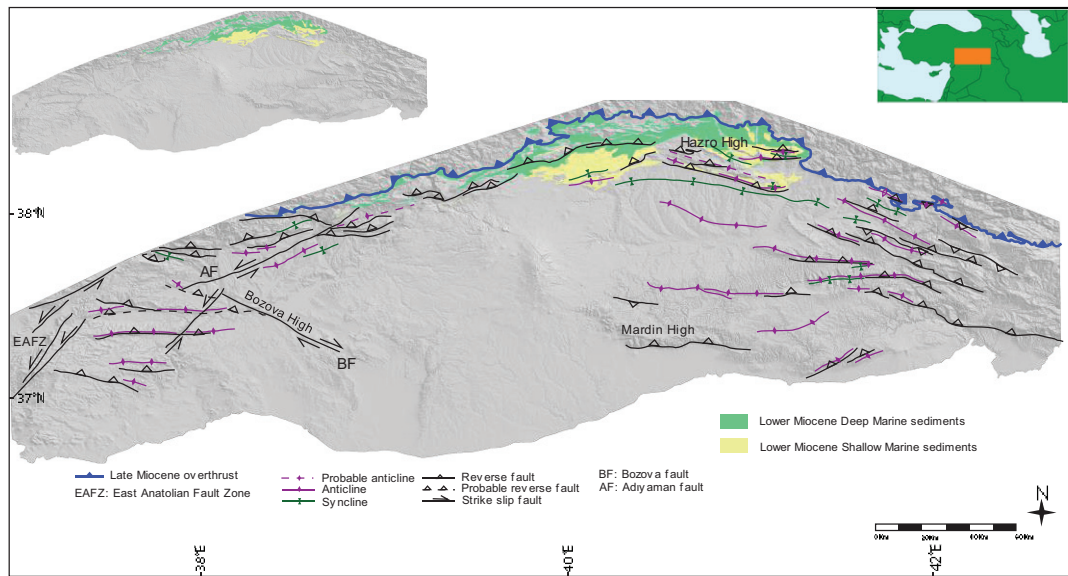


Figure 3.18 The map illustrates lower Miocene shallow and deep marine sediments on the surface of the study area.

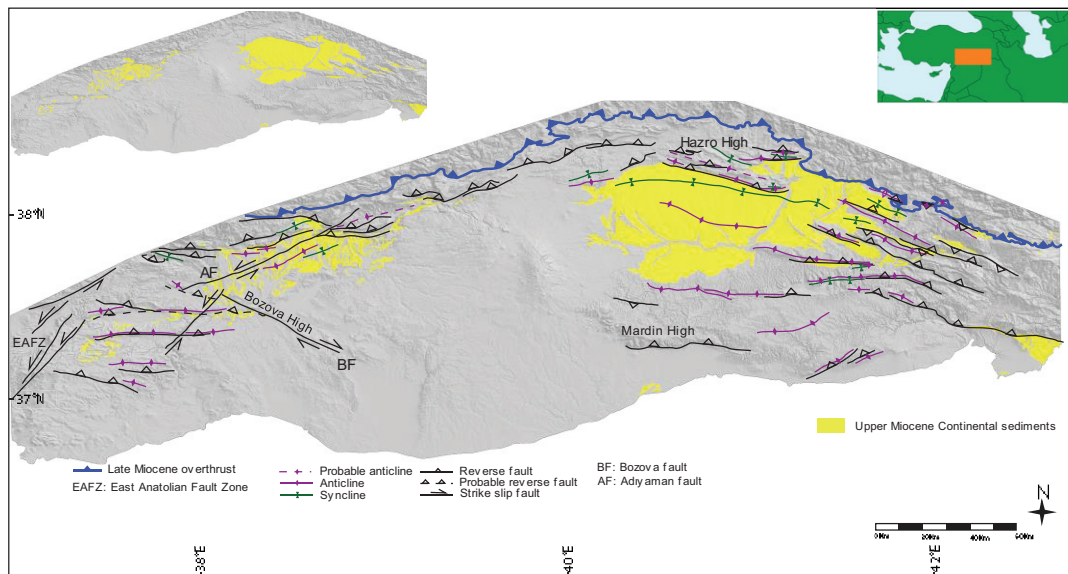


Figure 3.19 The map illustrates upper Miocene continental clastics on the surface of the study area.

S19 class represents the Plio-Quaternary deposits of the region. They are followed around active rivers and cover relatively large areas south of the study area (Figure 3.21).

S18 class is composed of Plio-Quaternary volcanic. It covers large areas at the center of the basin. Also, it is found as isolated outcrop patches at some places in the region (Figure 3.20).

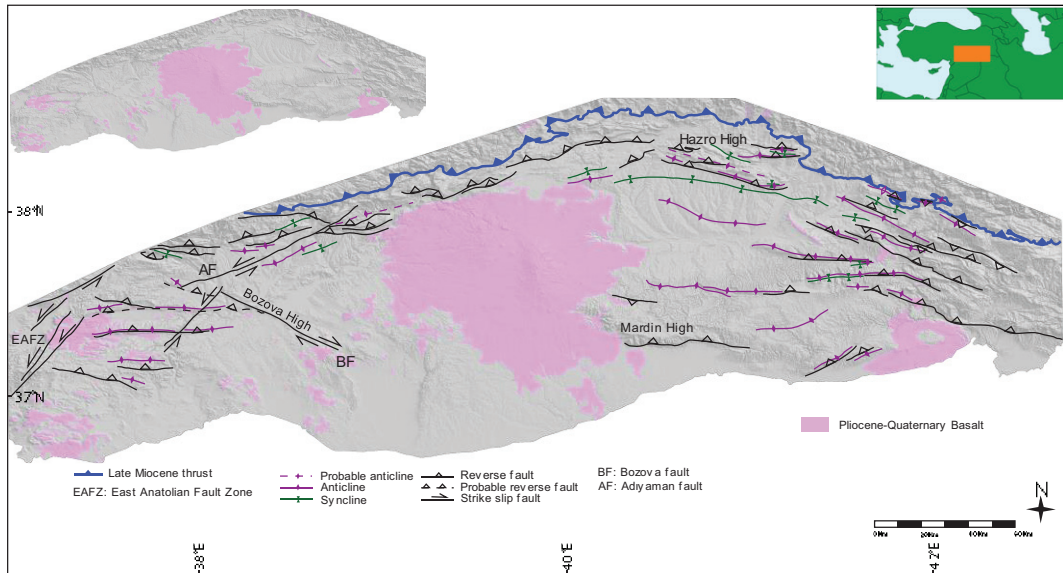


Figure 3.20 The map illustrates Pliocene-Quaternary basalts on the surface of the study area.

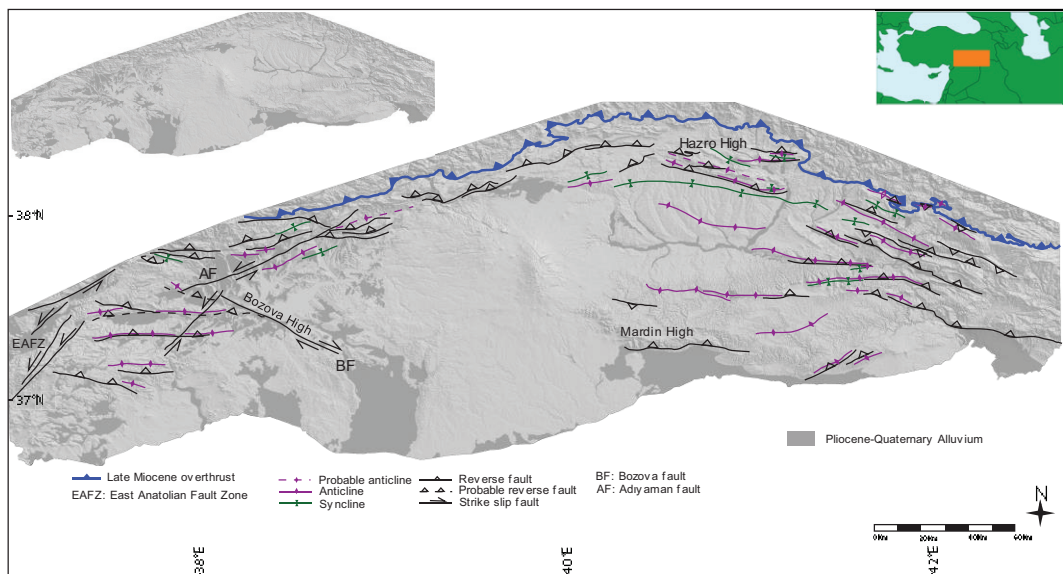


Figure 3.21 The map illustrates Pliocene-Quaternary alluvium on the surface of the study area.

Table 3.1 Contact relationships and their depositional environments of classes from pre-Cambrian to Upper Miocene units.

		Upper Miocene		Lower Miocene		Middle Eocene-Oligocene		Lower Eocene	Upper Cretaceous-Paleocene			Upper Cretaceous		Cretaceous	Triassic-Jurassic	Upper Permian	Upper Silurian-Lower Carboniferous	Habur Group	Derik Group	Crystalline Basement
		Şelmo (Continental clastics) (S17)	Deep Marine (S16)	Shallow Marine (S15)	Deep Marine (S14)	Shallow Marine (S13)	Continental clastics (S12)	Deep Marine (S10)	Continental clastics (S11)	Shallow Marine (09)	Continental clastics (S08)	Deep Marine (S07)	Shallow Marine (S06)	Shallow Marine (S05)	Shallow Marine (S04)	Shallow Marine (S03)	Shallow Marine (S02)	Basement-Shallow Marine (S01)		
Upper Miocene	Şelmo (Continental clastics) (S17)	NA	U	U	U	U	U	NO	NO	NO	NO	NO	NO	NO	NO	NO	NO	NO	NO	U/TC
Lower Miocene	Deep Marine (S16)	NA	C	U	U	U	U	NO	NO	NO	NO	NO	NO	NO	NO	NO	NO	NO	NO	TC
Middle Eocene-Oligocene	Shallow Marine (S15)	U	C	NA	U	U	U	NO	NO	NO	NO	NO	NO	NO	NO	NO	NO	NO	NO	TC
	Deep Marine (S14)	U	U	MA	C	NA	U	U	U	U	U	U	U	U	U	U	U	U	U	U
Lower Eocene	Shallow Marine (S13)	U	U	U	C	NA	U	U	U	U	U	U	U	U	U	U	U	U	U	U
	Continental clastics (S12)	NO	NO	U	NO	U	U	U	U	U	U	U	U	U	U	U	U	U	U	U
Upper Cretaceous-Paleocene	Deep Marine (S10)	NO	NO	NO	NO	U	U	U	U	U	U	U	U	U	U	U	U	U	U	U
	Continental clastics (S11)	NO	NO	NO	NO	U	U	U	U	U	U	U	U	U	U	U	U	U	U	U
Upper Cretaceous	Shallow Marine (09)	NO	NO	NO	NO	U	U	U	U	U	U	U	U	U	U	U	U	U	U	U
	Continental clastics (S08)	NO	NO	NO	NO	U	U	U	U	U	U	U	U	U	U	U	U	U	U	U
Cretaceous	Deep Marine (S07)	NO	NO	NO	NO	U	U	U	U	U	U	U	U	U	U	U	U	U	U	U
	Shallow Marine (S06)	NO	NO	NO	NO	U	U	U	U	U	U	U	U	U	U	U	U	U	U	U
Upper Permian	Shallow Marine (S05)	NO	NO	NO	NO	U	U	U	U	U	U	U	U	U	U	U	U	U	U	U
	Shallow Marine (S04)	NO	NO	NO	NO	U	U	U	U	U	U	U	U	U	U	U	U	U	U	U
Upper Silurian-Lower Carboniferous	Shallow Marine (S03)	NO	NO	NO	NO	U	U	U	U	U	U	U	U	U	U	U	U	U	U	U
	Shallow Marine (S02)	NO	NO	NO	NO	U	U	U	U	U	U	U	U	U	U	U	U	U	U	U
Derik Group	Basement-Shallow Marine (S01)	NO	NO	NO	NO	U	U	U	U	U	U	U	U	U	U	U	U	U	U	U
Crystalline Basement		U/TC	TC	TC	U	U	U	U	U	U	U	U	U	U	U	U	U	U	U	U
NA/: No contact relatif; C: Conformal; U: Unconformal; TC: Tectonic contact																				

3.2.1 Facies Distribution

Among the 19 different stratigraphic classes defined in this study, the classes S01, S02, and S16-S19 are encountered in only a few of the wells which limited the possibility of determining their spatial distribution precisely. On the other hand, the remaining 13 stratigraphical classes are penetrated in a sufficient number of wells, and their isopach maps could be prepared in order to determine their spatial distribution and change in their thickness.

The thickness of the mapped stratigraphical units is variable in each well, possibly due to repetition related to thrusting and sometimes imbrication (multiple repetitions). More importantly, the main problem of thickness variation is related to obscured faults that have offset less than the thickness of the rock package so that no apparent repetition or omission could be observed in the well logs. To overcome this problem, wherever such repetition is observed in the well logs, the lowermost package of the stratigraphical unit is used instead. The thicknesses on the hanging wall blocks are therefore omitted. Such imbrications are observed in 20 wells, and these wells are mainly located in the northern parts of the study area as well as around structural highs such as Hazro High.

An isopach map created for the continental and (dominantly) shallow marine units of the S05 stratigraphic class (Triassic-Jurassic) is given in figure 3.22. In addition to the thickness information of the S05, the map includes some approximately W-E trending normal faults determined in some seismic lines. The map also indicates that the thickness of the class significantly increases up to 2365 meters on the eastern and western sides, respectively, whereas it decreases to the central part of the basin (Figure 3.22).

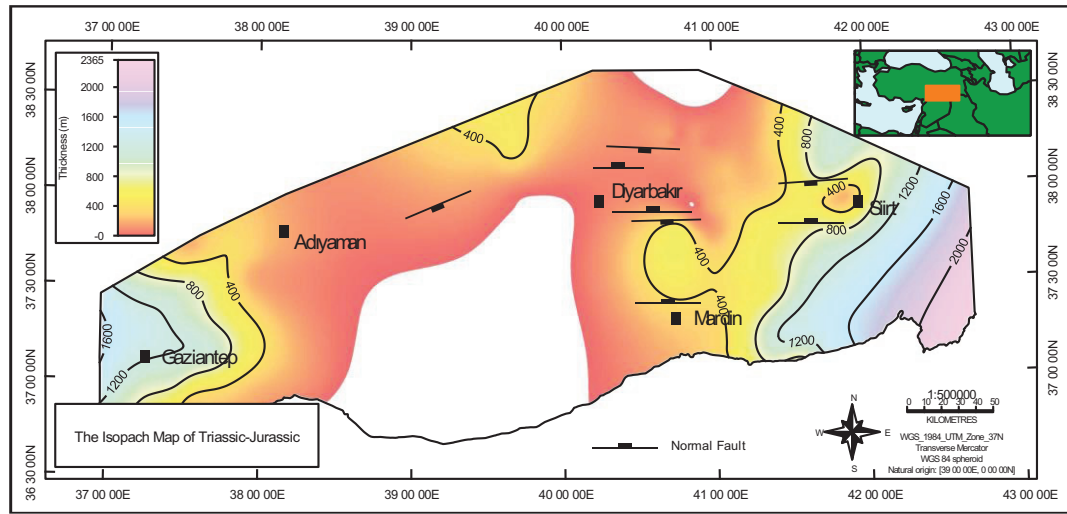


Figure 3.22 Isopach map of Triassic-Jurassic sediments (Stratigraphic class S05). Thickness values range between 0-2365 m, and contours indicate the thickness (in m) of Triassic-Jurassic sediments. Normal faults are shown as bolder black lines.

The isopach map of Lower Cretaceous shallow marine sediment (stratigraphic class S06) (Figure 3.23) shows that the thickness of the class increases substantially in the eastern, western, and southern areas. At the same time, it decreases in the northern areas, especially in the Adiyaman sub-area. On the other hand, there are some local variations in the thickness of the class, such as an abrupt increase in the Diyarbakir and Batman-Siirt sub-areas.

The isopach map of Upper Cretaceous shallow marine successions (Stratigraphic class S06) points out that the successions of the class are common throughout SE Anatolian and Upper Cretaceous (continental, shallow, and deep marine sediments) successions' thickness increases substantially in northern areas (Figure 3.24 a).

The thickness distribution of the Upper Cretaceous deep marine units (Stratigraphic class S07) is given in Figure 3.24 b. The thickness and distribution of these units are widespread in northern areas. However, the comparison between the isopach map of class S07 and S06 indicated that the maximum thickness in the previous isopach (especially around the deepest parts) map is higher than this isopach map. This points out the southward migration of continental and shallow marine units on top of deep

marine sequences. In addition to the isopach maps, the subsurface data indicates that the S07 class units (mainly the Kastel Formation) become thinner as it moves southward and creates a wedge shape geometry.

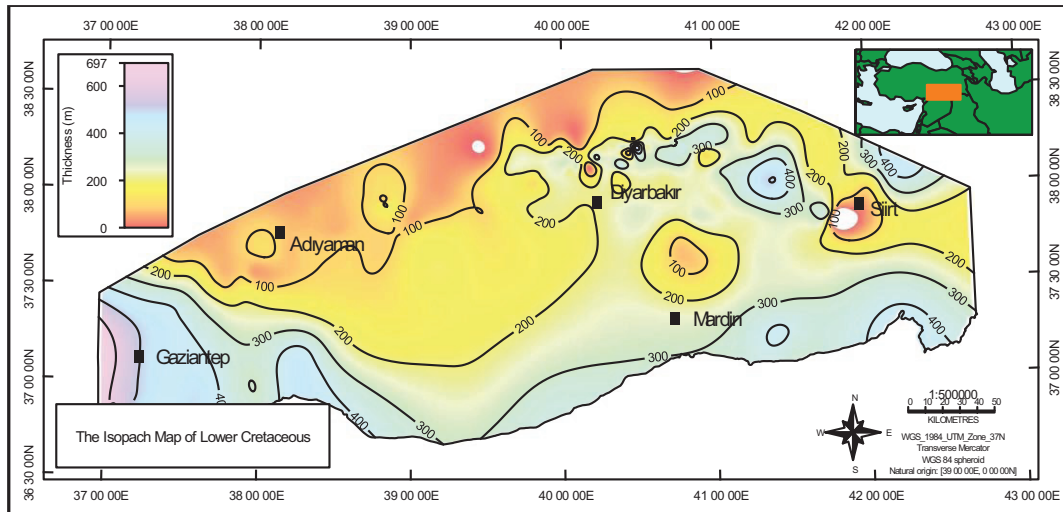


Figure 3.23 Isopach map of Lower Cretaceous shallow marine sediments (Base of Stratigraphic class S06 – Lower Cretaceous). Thickness values range between 0-697 m and contours indicate the thickness (in m) of Lower Cretaceous sediments.

The hangingwall block of the main boundary of the frontal thrust underlies mainly the Koçali and Karadut complex. The thickness of these units increases towards the north (distal to the main frontal thrust) (Figure 3.24c). The thickness distribution of the Upper Cretaceous units, hence the possible location of the continental, shallow marine, and deep marine sediments (Stratigraphic classes of S06, S07, and S08) are depicted: In Figure 3.24a. In the figure foredeep depocenter axis is shown with a dark pink dash line and the fore bulge axis is shown with a blue dash line. The Figure also shows the Upper Cretaceous deep marine units (S07) to emphasize the location of the foredeep depocenter. Note that the maximum thickness in the previous isopach map (Figure 3.24a) is higher than the isopach map in Figure 3.24b. This indicates the southward migration of continental and shallow marine units on top of deep marine sequences. The isopach map of upper Cretaceous allochthonous units (Koçali ophiolites and Karadut Complex) is shown in Figure 3.24c.

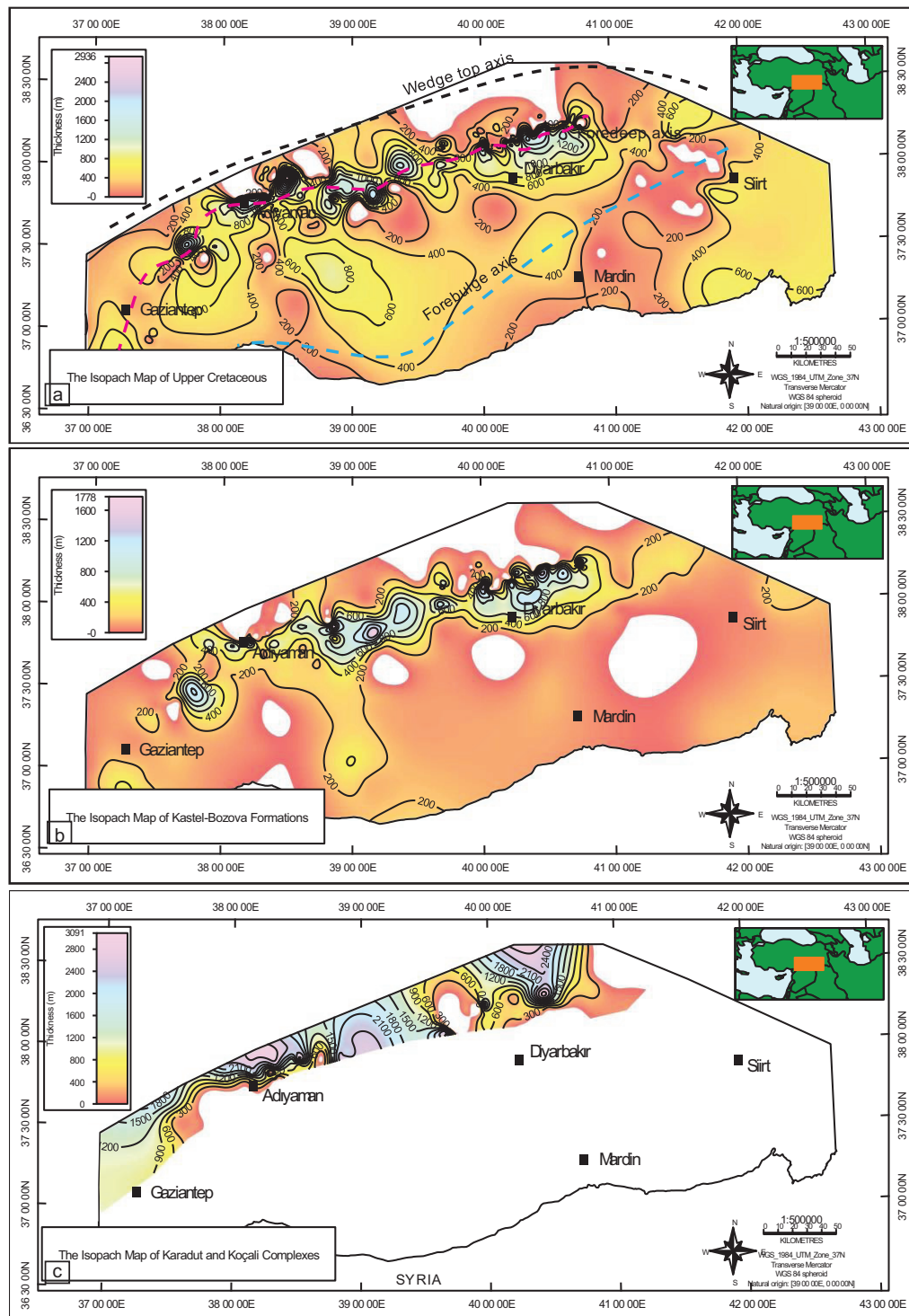


Figure 3.24 a) Isopach map of Upper Cretaceous units.

The thickness distribution of Upper Cretaceous S08 (continental clastics) and S06 (shallow marine) classes are given in Figure 3.25. The figure shows that the thickness

of both classes increases in the west and southwest directions. However, there are some isolated, relatively small areas with thick deposits at some places, probably controlled by the growth of thrust/reverse faults adjacent to these areas.

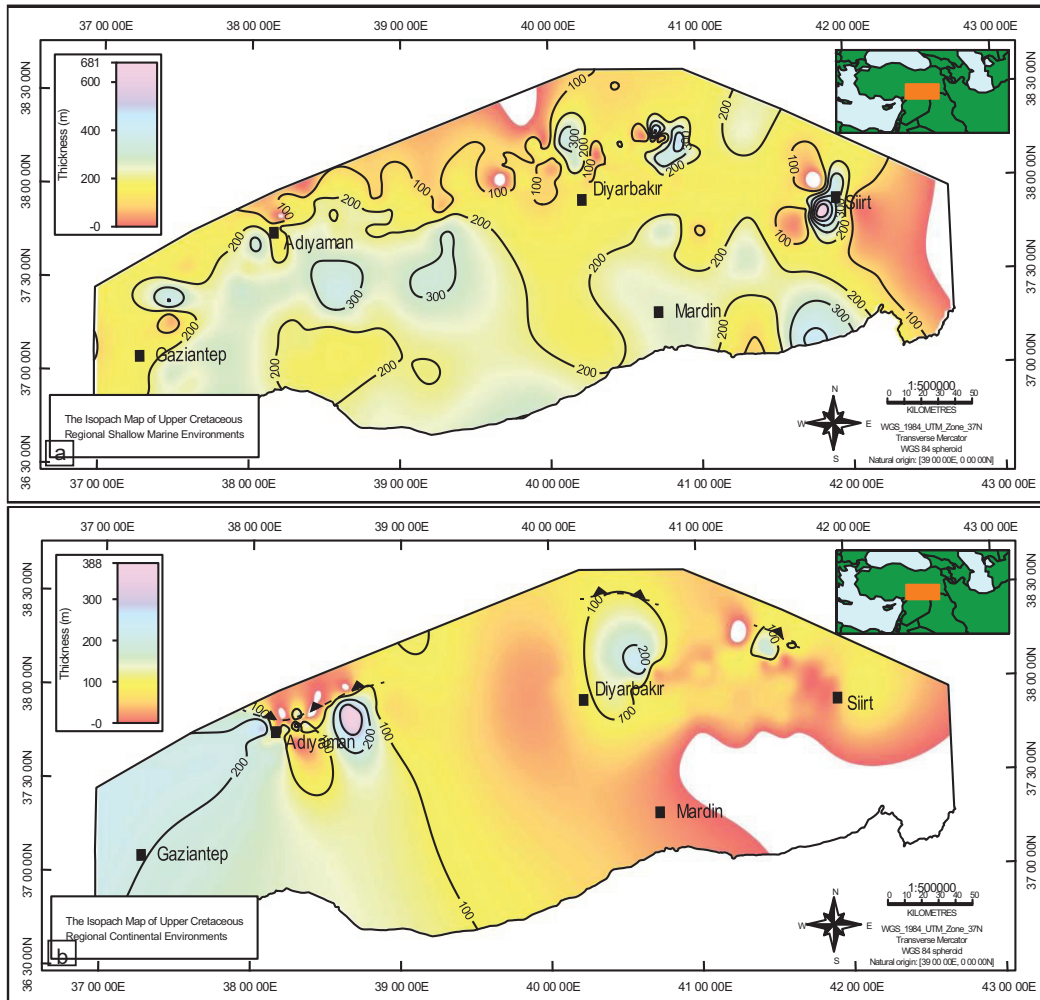


Figure 3.25 a) Isopach map of Upper Cretaceous shallow marine units. The contours indicate the thickness in meters. b) Late Cretaceous thrust faults and the continental clastics that were deposited in front of the Late Cretaceous Thrust fault. Thickness values range between 0-388 m, and contours indicate the thickness (in m) of Upper Cretaceous sediments.

The thickness distribution of the units Upper Cretaceous-Paleocene S09 (shallow marine), S10 (deep marine), and S11 (continental deposits) stratigraphic classes are given in Figure “3.26 a”. The maximum thickness is observed on the northwestern

and eastern sides of the basin where thickening was probably controlled by the thrust faults and the formation thins towards the central areas of the basin. The thickness distribution of the only S10 (deep marine) class units is in accordance with the distribution of the total thicknesses (S09 + S10 + S11). However, the S10 class has the most thickness in the isopach map of the three classes (Figure 3.26 a), reaching up to 1600 m at some places. The comparison of isopach maps given in Figures 3.26a and 3.26b, and well data indicates that the deep marine units grade into their' shallow marine or continental equivalents along the northern rim of the basin.

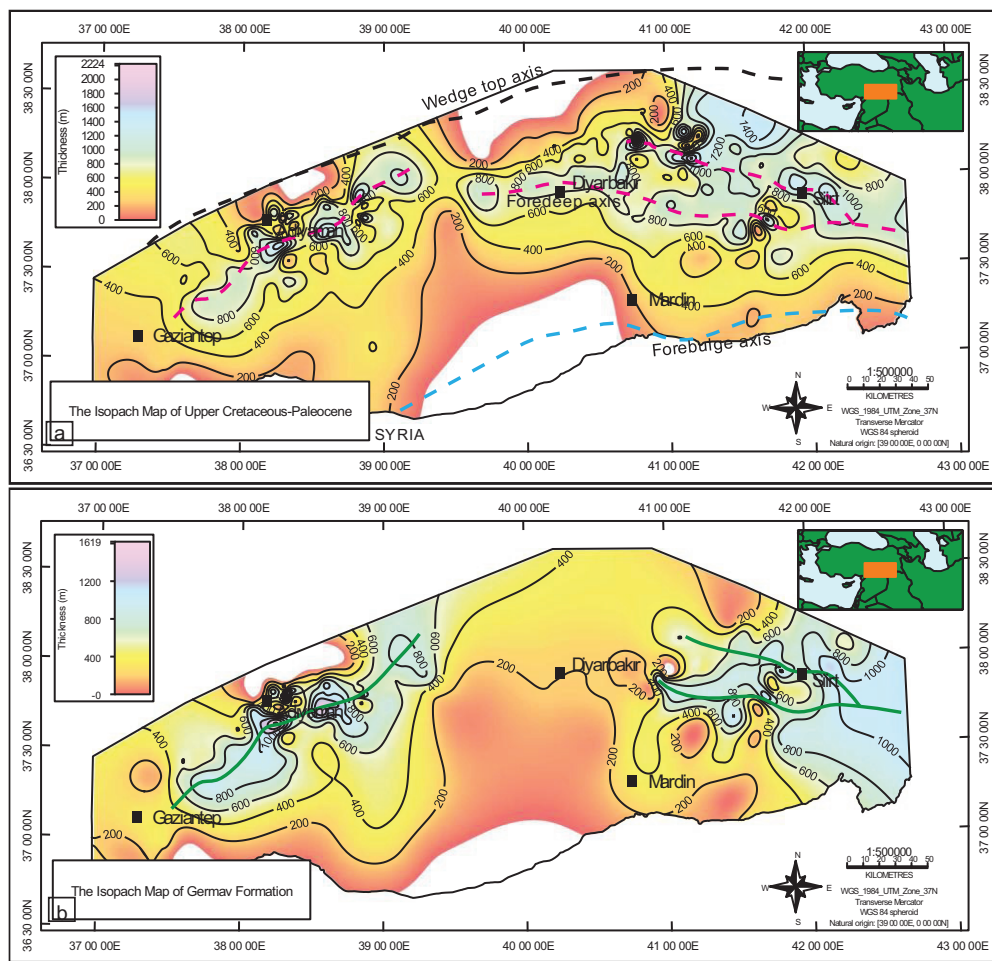


Figure 3.26 Isopach maps of a) Upper Cretaceous-Paleocene sediments and b) deep marine Germav Formation.

The thickness distribution of Lower Eocene (continental deposits) and S12 stratigraphic classes is given in Figure 3.27. Although the outcrops of the class do not cover large areas in the basin, the well data and isopach maps show that it covers almost the whole SE Anatolian Basin. In addition, there is no shallow marine and the deep marine equivalent of this class in the region, while younger classes unconformably cover it.

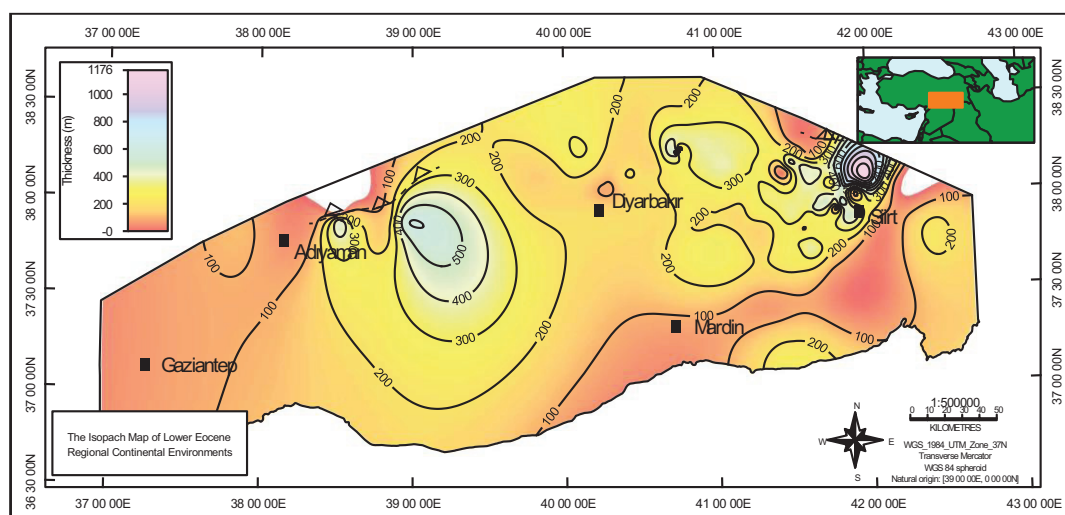


Figure 3.27 The isopach map of Lower Eocene continental clastics (Stratigraphic class S12). This figure emphasizes the possible location of the Early Eocene fault (black dash lines) that developed in Lower Eocene time and continental clastics deposited in front of the Early Eocene thrust fault. Thickness values range between 0-1176 m, and contours indicate the thickness (in m) of Lower Eocene sediments.

The total thickness distribution of Middle Eocene – Oligocene S13 (shallow marine) and S14 (deep marine) stratigraphic classes is given in Figure “3.28 a”. Basically, the isopach maps shows that increasing trend in thickness is towards south and west in the basin during the relevant time interval. Comparing these isopach maps with the ones of older stratigraphic classes indicates southward and westward migration of thicker deposition zones in the basin. Figure “3.28 b” shows only the thickness distribution of Middle Eocene - Oligocene units of the S13 (shallow marine) class. The map shows that shallow marine deposits cover large areas for their deep marine

equivalents and the deeper marine units are only found in the western and southwestern parts of the basin.

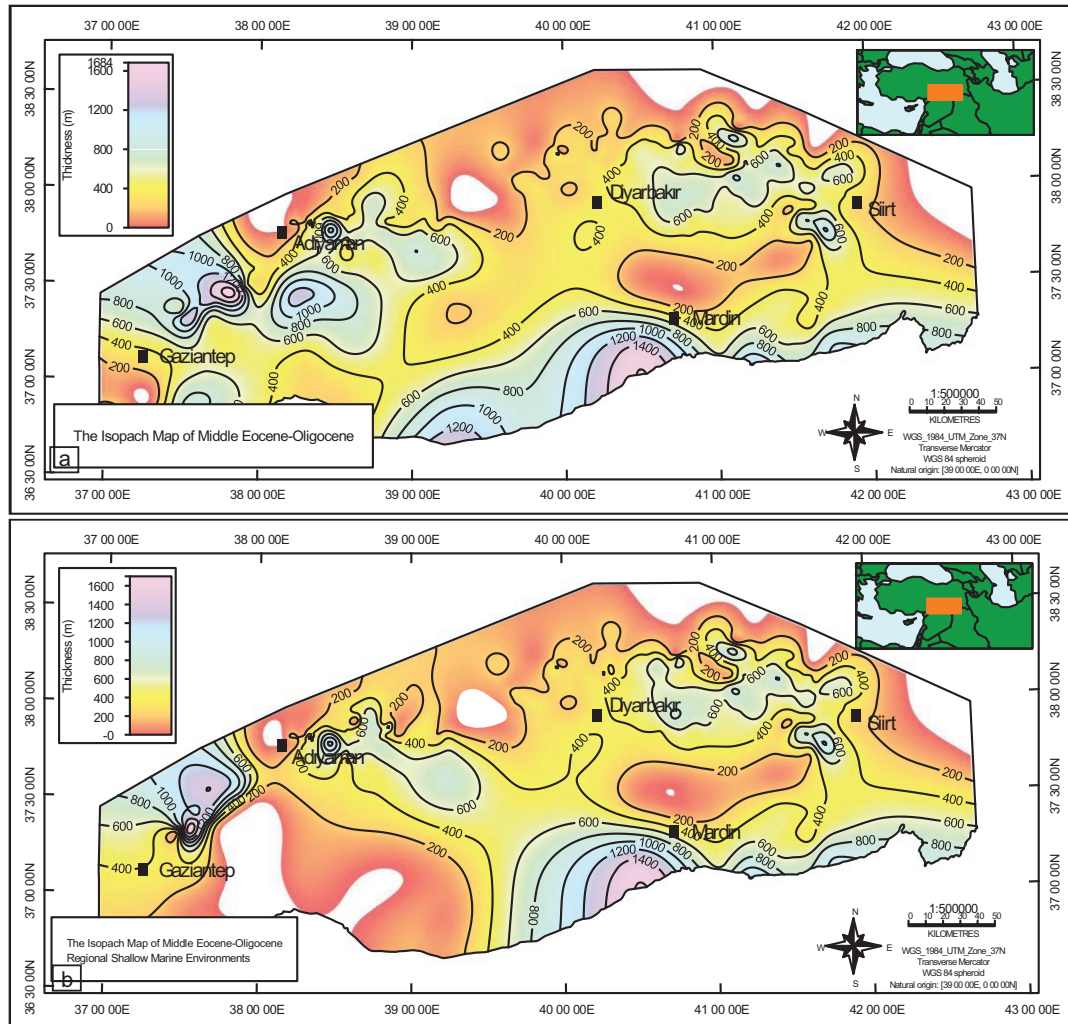


Figure 3.28 a) Isopach map of middle Eocene-Oligocene sediments (shallow marine and deep marine deposits – Stratigraphic class of S13 and S14). Thickness values range between 0-1684 m, and contours indicate the thickness (in m) of Middle Eocene-Oligocene sediments, b) Isopach map of middle Eocene-Oligocene shallow marine sediments (Stratigraphic class S13). Thickness values range between 0-1600 m, and contours indicate the thickness (in m) of Middle Eocene-Oligocene shallow marine sediments.

The total thickness distribution of the Lower Miocene deep marine S16 class is given in Figure “3.29 a” and the shallow marine S15 class in Figure “3.29 b”. The isopach map points out the Lower Miocene units are only found at the north of the basin, and the thickness of the marine units is not high as the marine units of older classes. The location of the deepest point of the Lower Miocene units indicates that the northerly located depozone of the Lower Miocene units is not in accordance with the one of Middle-Eocene – Oligocene units.

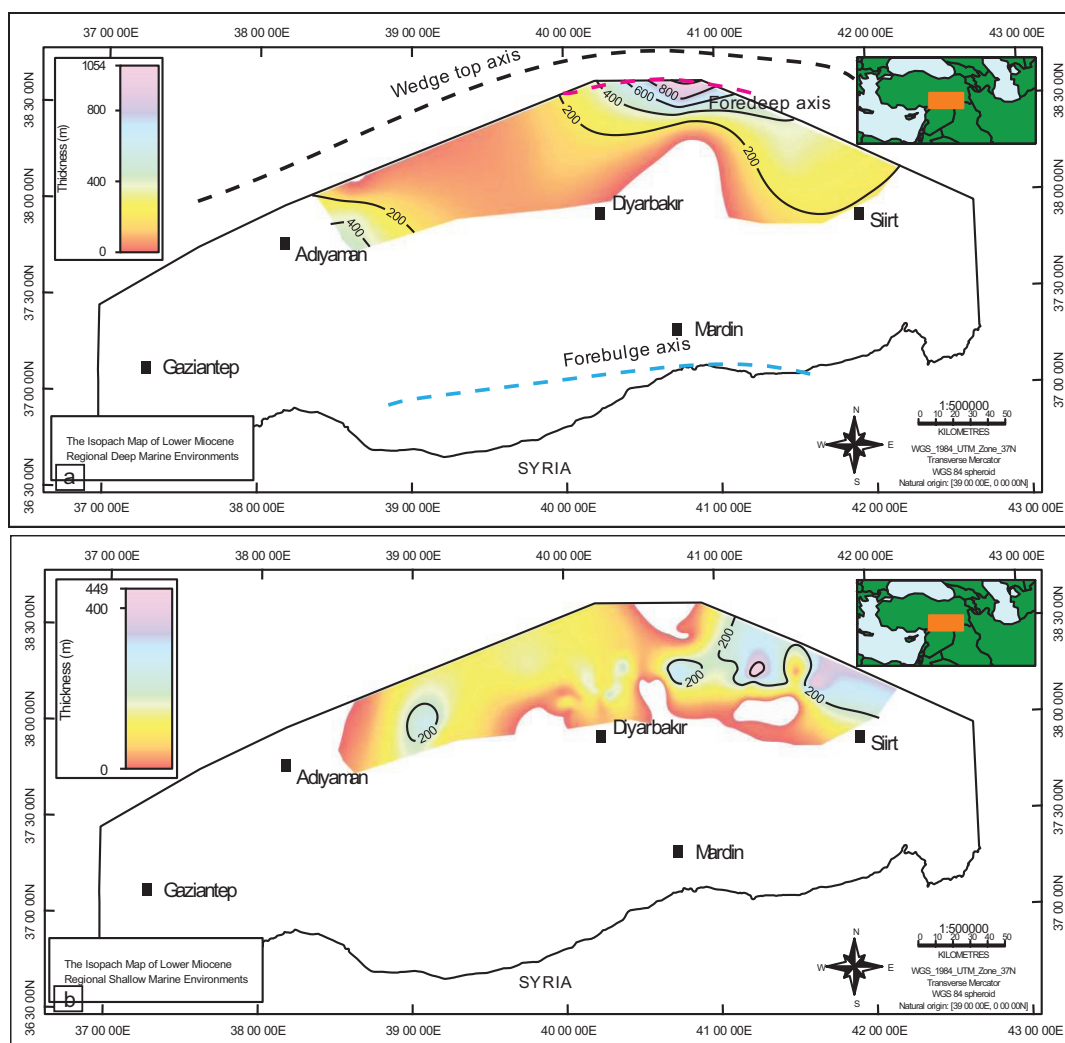


Figure 3.29 The isopach map of deep marine lower Miocene sediments and the locations of the well-developed possible wedge-tops axis (black dash line), foredeep axis (dark pink dash line), and fore bulge axis (blue dash line). a) Lice Formation

(Stratigraphic class S16) b) Firat Formation (Stratigraphic class S15). Contours are thicknesses in meters.

The deep marine Lice Formation displays a foredeep axis in the west and the northeast (red bold lines). The thickness values range between 0-1054 m, and contours indicate the thickness (in m) of Lower Miocene sediments (Figure 3.29a), whereas the thickness values of shallow marine deposits range between 0-449 m (Figure 3.29b) of Lower Miocene shallow marine sediments. The continental deposits are thicker along the northern margin of the basin where they have in contact with the main frontal thrust. In addition, the thickness of the deposits becomes thinner towards the south and in a wedge shape.

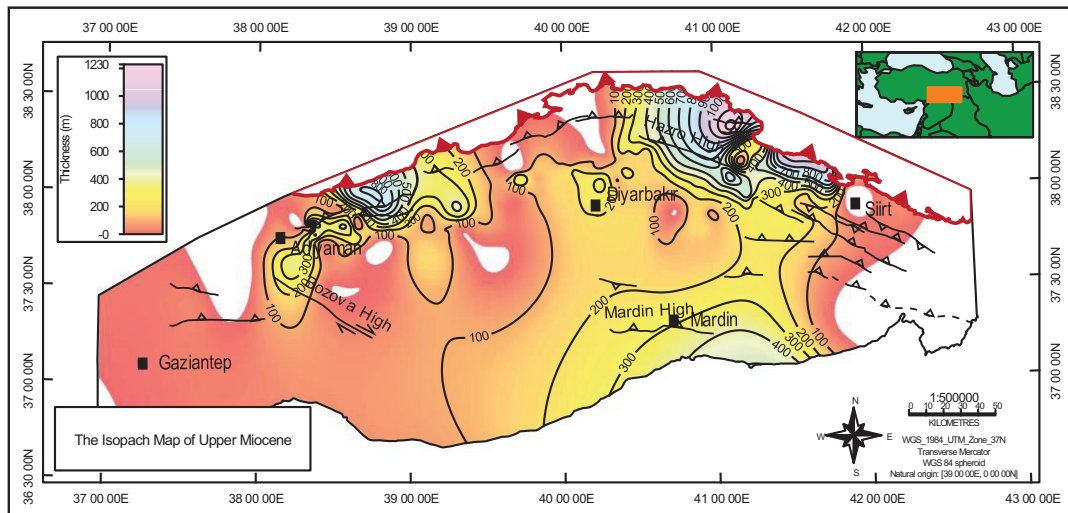


Figure 3.30 Isopach map of Upper Miocene continental clastics (Stratigraphic class S17) s. Thickness values range between 0-1230 m, and contours indicate the thickness (in m) of Lower Miocene sediments.

3.2.2 Well Section Correlations

The purposes of stratigraphic correlation are to determine regional sequences for constructing regional cross-sections and balancing them.

Within the study context, the units exposed in the SE basin were grouped into four. These are; (i) pre-Cambrian -Permian sequences - the core sequences of the Arabian Platform, (ii) Triassic-Jurassic sequences - rift-drift sequences of the Arabian platform, (iii) Cretaceous sequences representing the initial subduction stage of the southern Neotethys ocean and (iv) Campanian to Tertiary sequences representing the complete closure of the Neotethys. Also, the units of the groups were simplified based on their ages and depositional environments as stratigraphic classes (S01 to S19). In this section, we used the terminology constructed here and explained above for the stratigraphical units cut along wells. The following subtitles explain the correlations of wells located along W-E and N-S directions to emphasize the changes in depositional settings in E-W and N-S directions in the basin.

Four main stratigraphical classes of Pre-Cambrian to Permian units are cut by the wells sitting in the E-W direction. These classes are (i) Pre-Cambrian-Cambrian continental to shallow marine units of S01, (ii) Ordovician shallow marine units of S02, (iii) Upper Silurian-Lower Carboniferous shallow marine to relatively deep marine sequences of S03, and (iv) Upper Permian shallow marine deposits of S04.

The Pre-Cambrian-Cambrian (S01) sequences (Figures 3.31, 3.32, 3.33, and 3.34) are penetrated in the W2, W3, W13, W14, W26, W27, W36, and W37 wells from W to E in the northern, central, and southern parts of the Adiyaman sub-area. To the east, these sequences are penetrated by W31, W40, and W41 wells from W to E in the central and southern parts of the Batman-Siirt sub-area. According to the well data set, these sequences are not observed in Diyarbakir and northern Batman-Siirt sub-areas.

The Ordovician sequences (S02) (Figures 3.31, 3.32, 3.33, and 3.34) are cut by W1, W4, W5, W6, W9, W10, and W11 wells in northern areas. In the central part of the study area, W12, W16, W17, W20, W21, W22, W23, W24, W25, W28, W29, W30, W31, and W32 wells penetrate these sequences. The Ordovician sequences are penetrated in all wells in the southern part (close to the Syrian border).

The Upper Silurian-Lower Carboniferous sequences (S03) (Figures 3.31, 3.32, 3.33, and 3.34) are penetrated by W6, W7, W8, W9, and W11 north of Diyarbakir and the Batman-Siir sub-area. These sequences are also penetrated by W16, W18, W19, W20, W22, W23, W29, and W30 wells in the middle-central and eastern areas of the study area. Based on the well data set, the Upper Silurian-Lower Carboniferous sequences are not found in the Adiyaman sub-area.

The Upper Permian sequences (S04) (Figures 3.31, 3.32, 3.33, and 3.34) are penetrated by W7, W9, W10, and W11 in the north and northeast of the study area. W19, W20, W21, W22, W23, W30, W31, and W32 wells penetrate these sequences in the central Diyarbakir region and the eastern sub-area. In the southern areas, these sequences are only penetrated in the W41, which is situated south of the Batman-Siirt sub-area. The Upper Permian sequences are not penetrated in the Adiyaman and southern Diyarbakir sub-areas.

One sequence is defined for the Triassic-Jurassic and sequences of the basin, which is composed of shallow marine S05 stratigraphic class.

The S05 units (Figures 3.31, 3.32, 3.33, and 3.34) are penetrated by W1, W2, W9, W10, and W11 in the westernmost and the easternmost margins of the basin. Three wells (W12, W24, and W25) also penetrate these sequences in the central part of the Adiyaman sub-area. W19, W20, W21, W22, W23, W30, W31, and W32 penetrate S05 around Diyarbakır and Batman areas. In the SW and SE of the study area, these sequences are cut by W33, W34, W35, W36, W40, and W41 wells. The well correlation of these units points out that Triassic-Jurassic shallow marine units of the basin are found in the west and the east of the basin as thick carbonate sequences, while the central part of the basin does not have such sequences.

The Cretaceous shallow marine deposits of S06 are penetrated by all wells in the study area (Figures 3.31, 3.32, 3.33, and 3.34). The well correlation shows that these units are thicker in the south of the basin.

Campanian to Tertiary units of the basin is subdivided into three sub-groups here Upper Cretaceous-Lower Eocene (S07, S08, S09, S10, S11, and S12), Middle Eocene-Oligocene (S13 and S14), and Miocene (S15, S16, and S17) sub-groups.

The Upper Cretaceous-Lower Eocene deep marine (S07 and S10), continental (S08, S11, and S12), shallow marine (S09), sequences are penetrated by all wells except for W1 (in the northwesternmost), W38, and W39 (in central southern areas) (Figures 3.31, 3.32, 3.33, and 3.34). The correlation of the wells indicates that these units are relatively thicker at the center and east of the basin.

The Middle Eocene-Oligocene shallow (S13) and deep marine (S14) sequences are penetrated at W7, W8, W9, W10, and W11 in the northern, central, and northeast of the study area. They also are cut by the W15, W17, W18, W19, W20, W21, W25, W26, W28, W29, W30 wells in the central Adiyaman and Diyarbakir subareas. In the southern areas (close to the Syrian border), all wells penetrate these sequences except for W35 well (Figures 3.31, 3.32, 3.33, and 3.34). The well correlation shows that these units are relatively thicker at the south and northwest of the basin.

The Lower Miocene shallow (S15) and deep marine (S16) sequences are penetrated by W5, W7, W8, and W9 wells in the northern areas. These sequences are not penetrated in the central and southern areas of Adiyaman, Diyarbakir, and Batman-Siirt sub-areas (Figures 3.31, 3.32, 3.33, and 3.34). The well correlation suggests that these units are only found in the north of the basin.

The Upper Miocene continental sequences (S17) are penetrated by W1, W5, W8, W9, W10, and W11 in the northern areas. W13, W14, W15, W16, W17, W18, W19, W20, W21, and W29 wells penetrate these sequences from west to east in the central part of the study area. They are also cut by W37 and W38 wells in southern areas of the Diyarbakir sub-area (Figures 3.31, 3.32, 3.33, and 3.34). The correlation of wells indicates that these continental deposits cover the whole SE Anatolian basin with thicker deposition at the north and thinner deposition at the south.

In addition to these sequences, Plio-Quaternary units are penetrated by W5, W16, W17, and W33 wells in the central and southwest areas of the study region. This unit is represented by basalt.

Moreover, Paleozoic-Mesozoic metamorphic rocks, Mesozoic units including ophiolites, olistostromes, and turbiditic sequences, Eocene-Miocene (chaotic blocky sandstone, shale, known as Çüngüş Fm) and Middle Eocene (volcanic and volcano-sedimentary rocks known as Maden Group) are cut by various wells located at the hangingwall block of the northerly located main basin bounding thrust.

In addition to the correlation of the wells in the E-W direction, here we also correlate some wells which are close to each other and almost adjacent to the N-S elongated cross-sections created by seismic and well-data were given here. These correlations from W to E covers three different N-S line in the basin. The common points of all sections are given as follows;

- (a) The thickness of pre-Cambrian-Cambrian shallow marine units of S01 differs along wells, and they are not cut by all wells. The reason for such discrepancy is that the wells do not penetrate down to the base of S01 units, which are the known oldest rocks in the region.
- (b) The thickness of Ordovician shallow marine units (S02) differs along wells. Along the well correlations at the west (Figure 3.35) and the center (Figure 3.36), these units are getting thicker towards the south and they are not observed along the wells located at the north of the western correlation. The well correlation at the east shows that the thickness of the units abruptly gets thicker at the center of the basin but again abruptly gets thinner towards the south after the well W63 (Figure 3.37).
- (c) The thickness and distribution of shallow to relatively deep marine sediments of S03 vary along wells. Figure 3.35 and 3.37 shows that these units are not observed along the east and the west of the basin. However, figure 3.36 proves that they are only found at the center of the basin with almost similar thickness distribution, but they are not observed at the south of the basin.

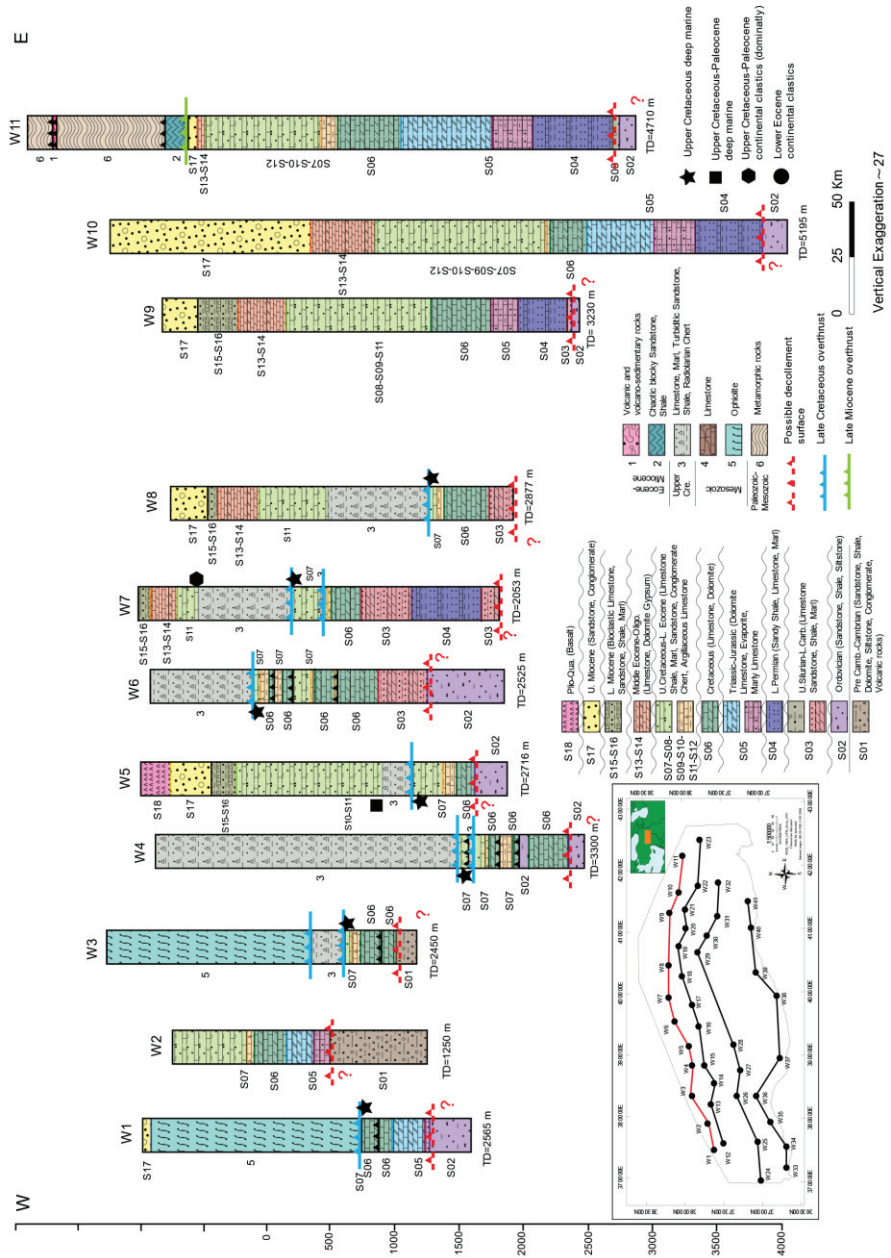


Figure 3.31 Stratigraphic well correlation section across the SE Anatolian from west to east. The location of the inset is shown. Numbers and letters represent significant stratigraphic boundaries and formations.

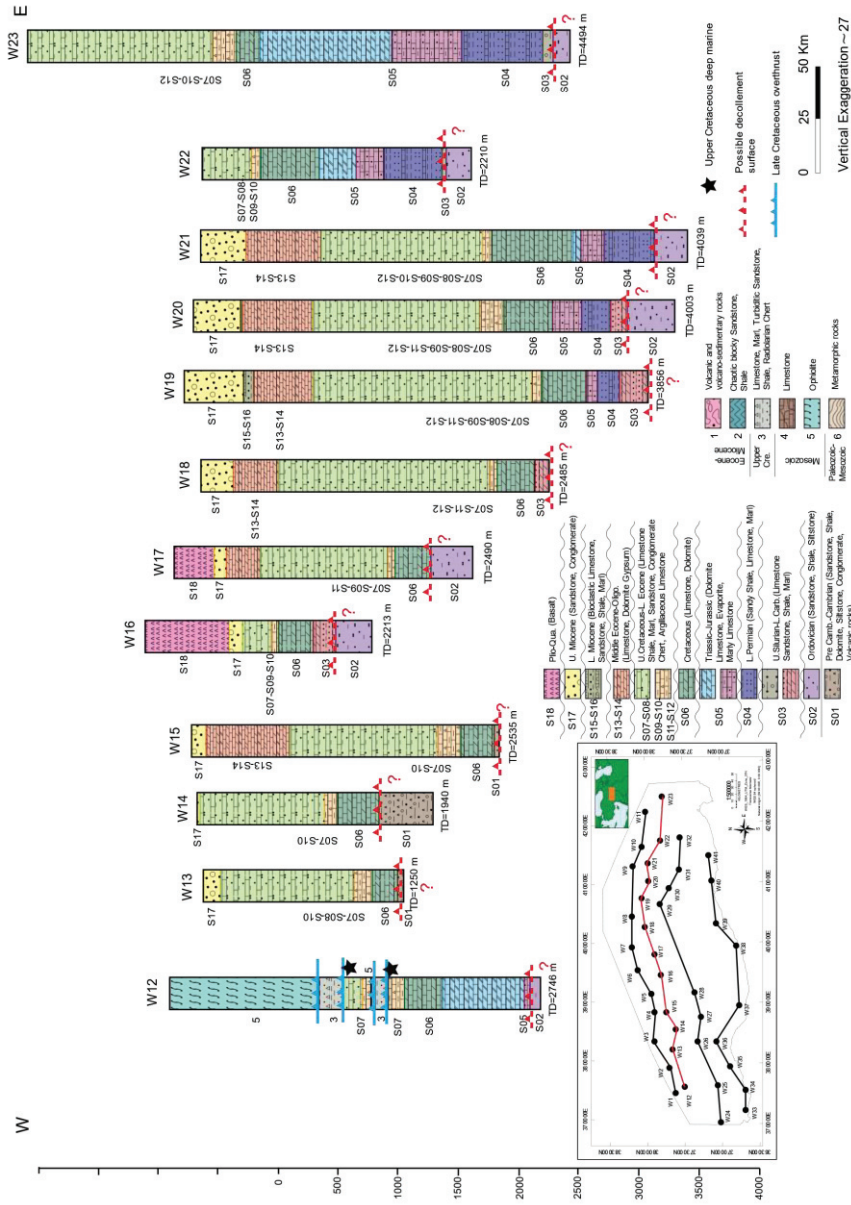


Figure 3.32 Stratigraphic well correlation section across the SE Anatolian from west to east. The location of the inset is shown. Numbers and letters represent significant stratigraphic boundaries and formations.

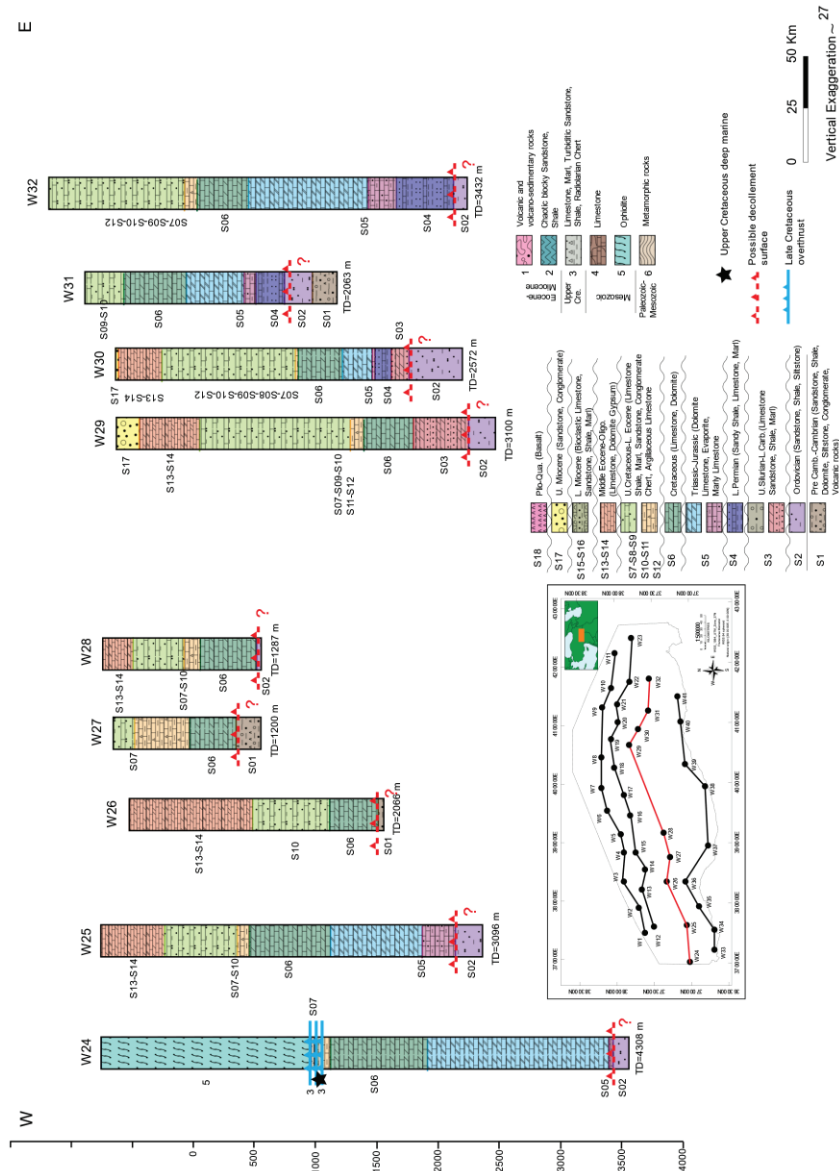


Figure 3.33 Stratigraphic well correlation section across the SE Anatolian from west to east. The location of the inset is shown. Numbers and letters represent significant stratigraphic boundaries and formations.

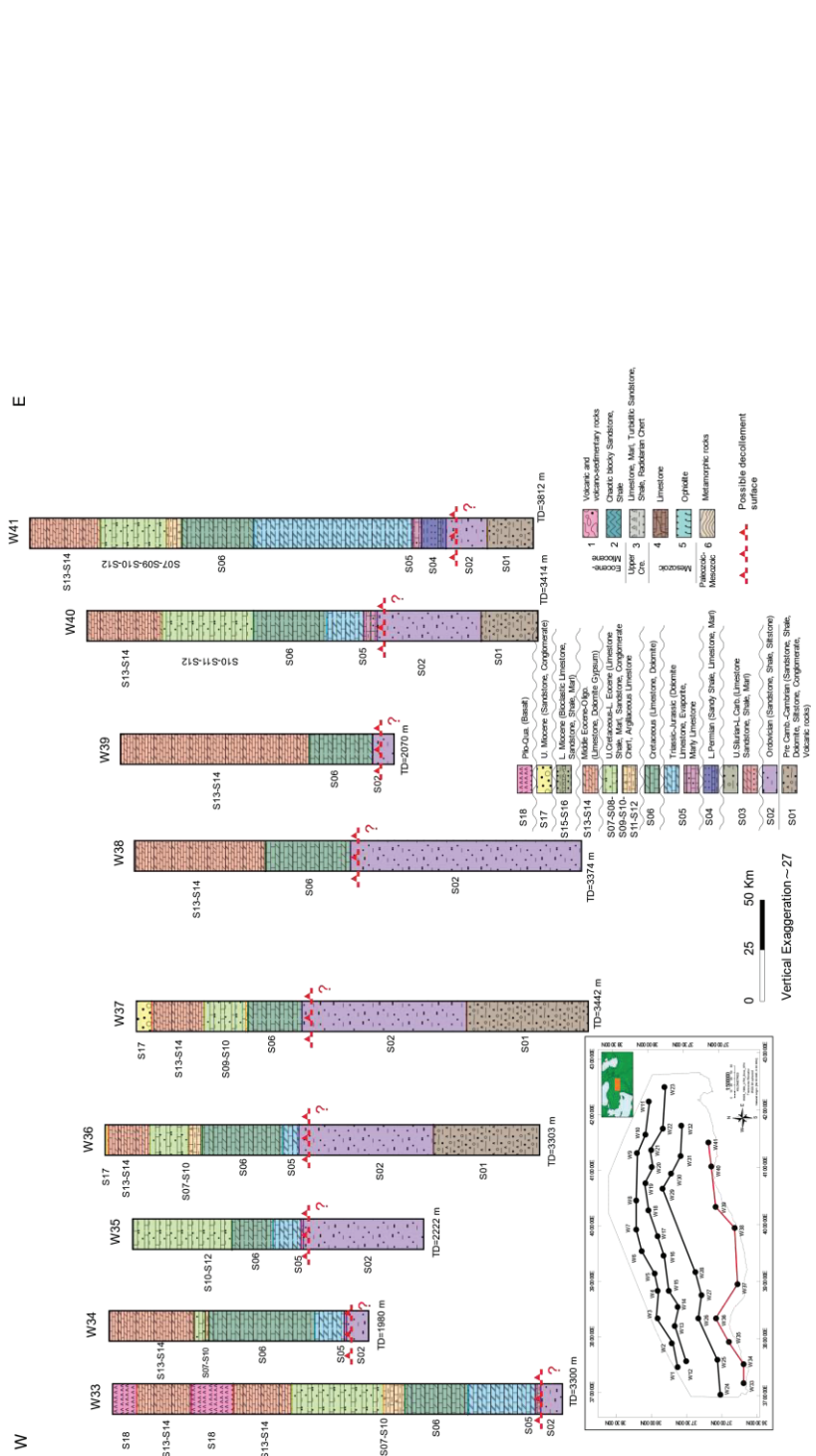


Figure 3.34 Stratigraphic well correlation section across the SE Anatolian from west to east. The location of the inset is shown. Numbers and letters represent significant stratigraphic boundaries and formations.

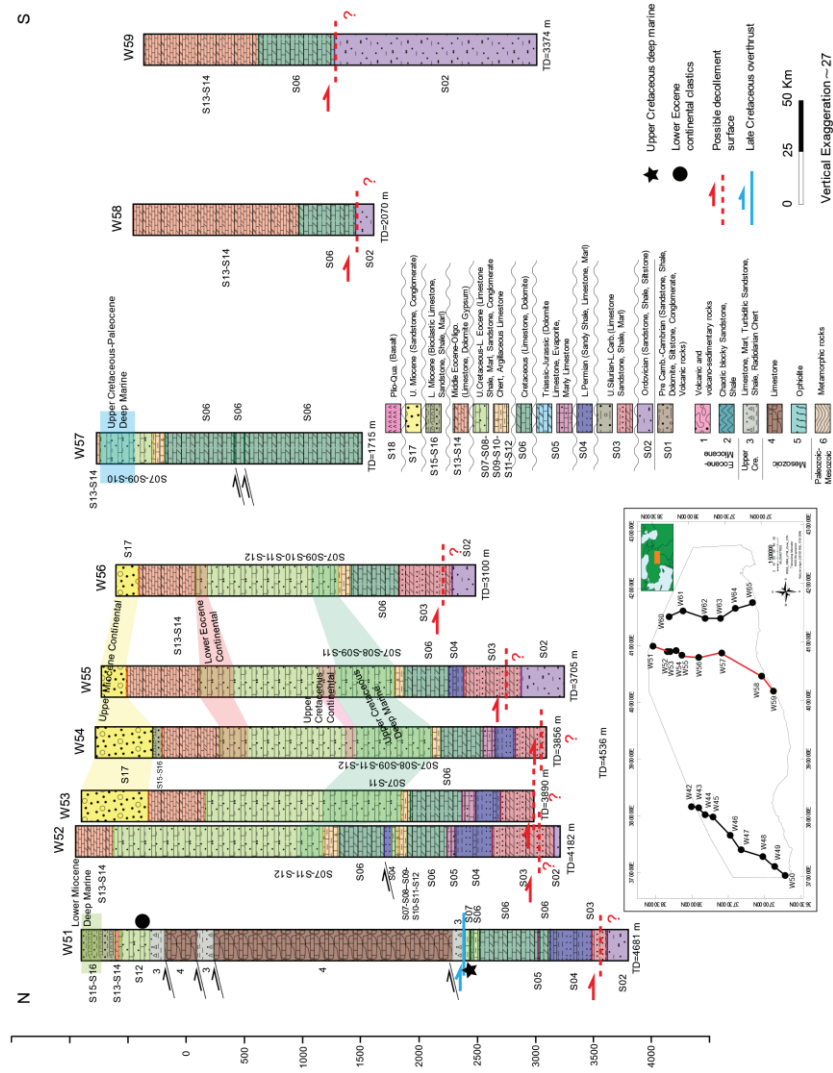


Figure 3.36 Stratigraphic well correlation section across the SE Anatolian from north to south in Diyarbakir subarea. The location of the inset is shown. Numbers and letters represent significant stratigraphic boundaries and formations.

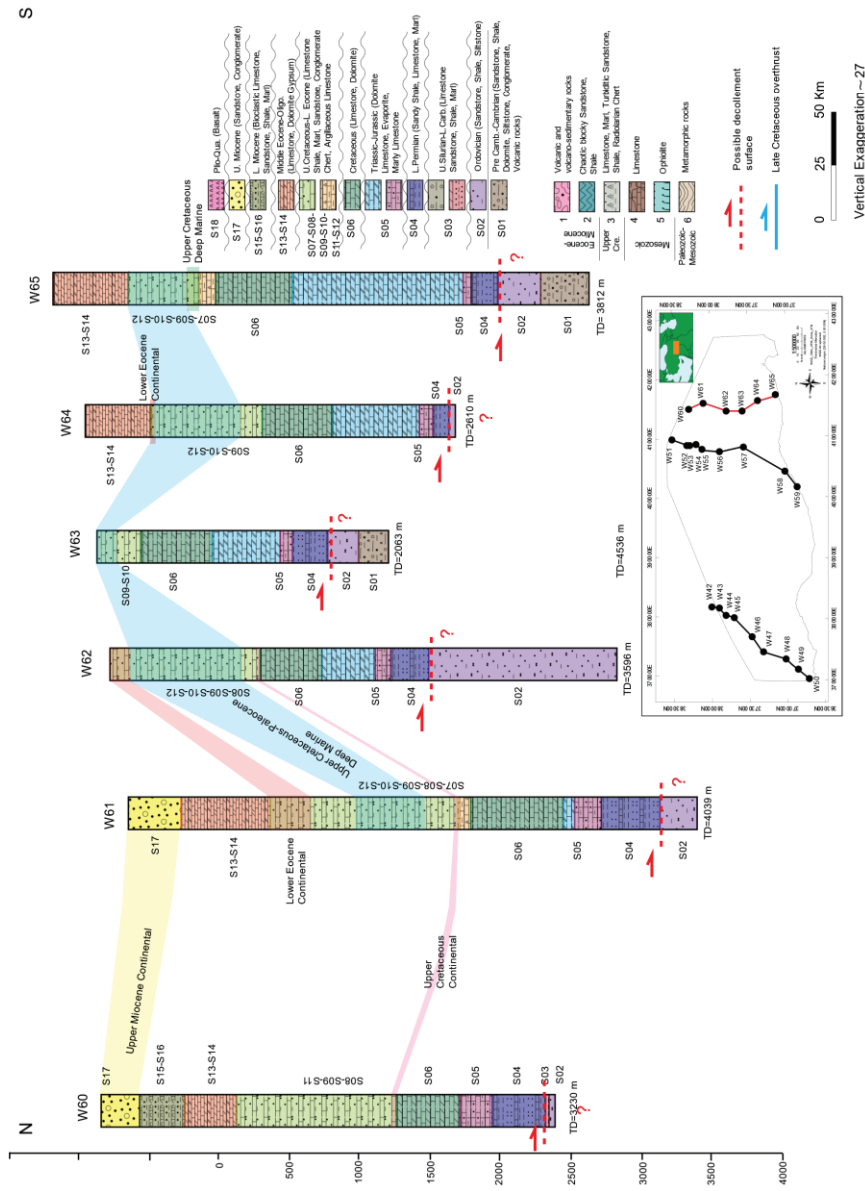


Figure 3.37 Stratigraphic well correlation section across the SE Anatolian from north to south in Batman-Siirt subarea. The location of the inset is shown. Numbers and letters represent significant stratigraphic boundaries and formations.

- (d) The thickness of Upper Permian shallow marine units (S04) is almost the same in the wells penetrating them. However, they are not found at the west of the basin (Figure 3.35) and the south of the central correlation line (Figure 3.36) differs along wells. On the other hand, these units are observed in all wells of the eastern correlation line (Figure 3.37).
- (e) The thickness of Triassic-Jurassic shallow marine units (S05) varies in the basin. They show different thickness distributions in three different correlation lines. At the west, they are not observed at the north, but from the center, they get thicker. At the center, they only observed at the north as very thin (<80m) layers. At the east, they are cut as thin layers in the north of the correlation line, then they get thicker and again thinner up to the center, but they reach the maximum thickness at the south of the correlation line.
- (f) Cretaceous shallow marine units (S06) have almost the same thickness distribution in the basin by being thicker at the center and thinner at the N and S margins of the basin. Also, these units are penetrated by almost all wells in the basin.
- (g) The thickness distribution of Upper Cretaceous to Lower Eocene deep marine (S07 and S10), continental (S08, S11, and S12), and shallow marine (S09) sequences, based on N-S elongated well correlations, shows almost the same trend as being thicker at the North and thinner at the South which creates a wedge shape. Also, the hangingwall units (Koçali and Karadut complex) of the main frontal thrust overlie the thinner extensions of the unit at the north.
- (h) The thickness distribution of Middle Eocene-Oligocene shallow marine (S13) and deep marine (S14) units covers the whole basin. The shallow marine units are thicker at the NW and S-SE, whereas the deep marine units are thicker at only the SW of the basin.
- (i) The thickness distribution of Lower Miocene shallow marine (S15) and deep marine (S16) units only are found at the north of the basin as restricted occurrences.

- (j) The thickness distribution of the Upper Miocene continental deposit (S17) shows that these units are thicker at the N-NE (in front of the main frontal thrust), and they become thinner at the south. Although the units are getting thinner in the south of the basin, they are found almost in the whole basin.

3.3 Kinematic Analyses

Kinematic analyses conducted in the study are fold analyses, syn-depositional unconformity determinations, and, paleostress analyses.

3.3.1 Fold Analyses

The rose diagram of the bedding strikes displays N85W, N75W, and N70W directions in Adiyaman, Diyarbakir, and Batman-Siirt regions, respectively (Figure 3.38). Additionally, the histogram of dip amounts demonstrates primary concentration between 15° to 30°, 20° to 35°, and 10° to 30° in the Adiyaman, Diyarbakir, and Batman-Siirt regions, respectively. In accordance with the bedding planes, folds trend approximately E-W and NW-SE from west to east in the research area. There are seven main folds in Adiyaman, eight in Diyarbakir, and, sixteen in Batman-Siirt regions affecting the basin-fill from west to east. In the Adiyaman region, four of them trend approximately in the E-W direction, two of them trend approximately in the NE-SW direction, and the last one trend in the NW-SE direction. Four folds of the Diyarbakır region trend approximately in the E-W direction, whereas the rest trend in the NW-SE direction. In the Batman-Siirt region, seven of the folds trend approximately in the E-W direction, while the remainder is in the NW-SE direction. In addition to the folds observed close to the main deformation front at the north, in the western portion of the region (around Adiyaman), there are two folds in the basin. These folds are assumed to be the result of a strike-slip system. Hence, they are the exceptions (Figure 3.39). The location of the folds is given in Figure 3.40, and Table 3.2 and Figure 3.41 display the outcomes of the β - and $-\pi$ diagrams of the folds, respectively.

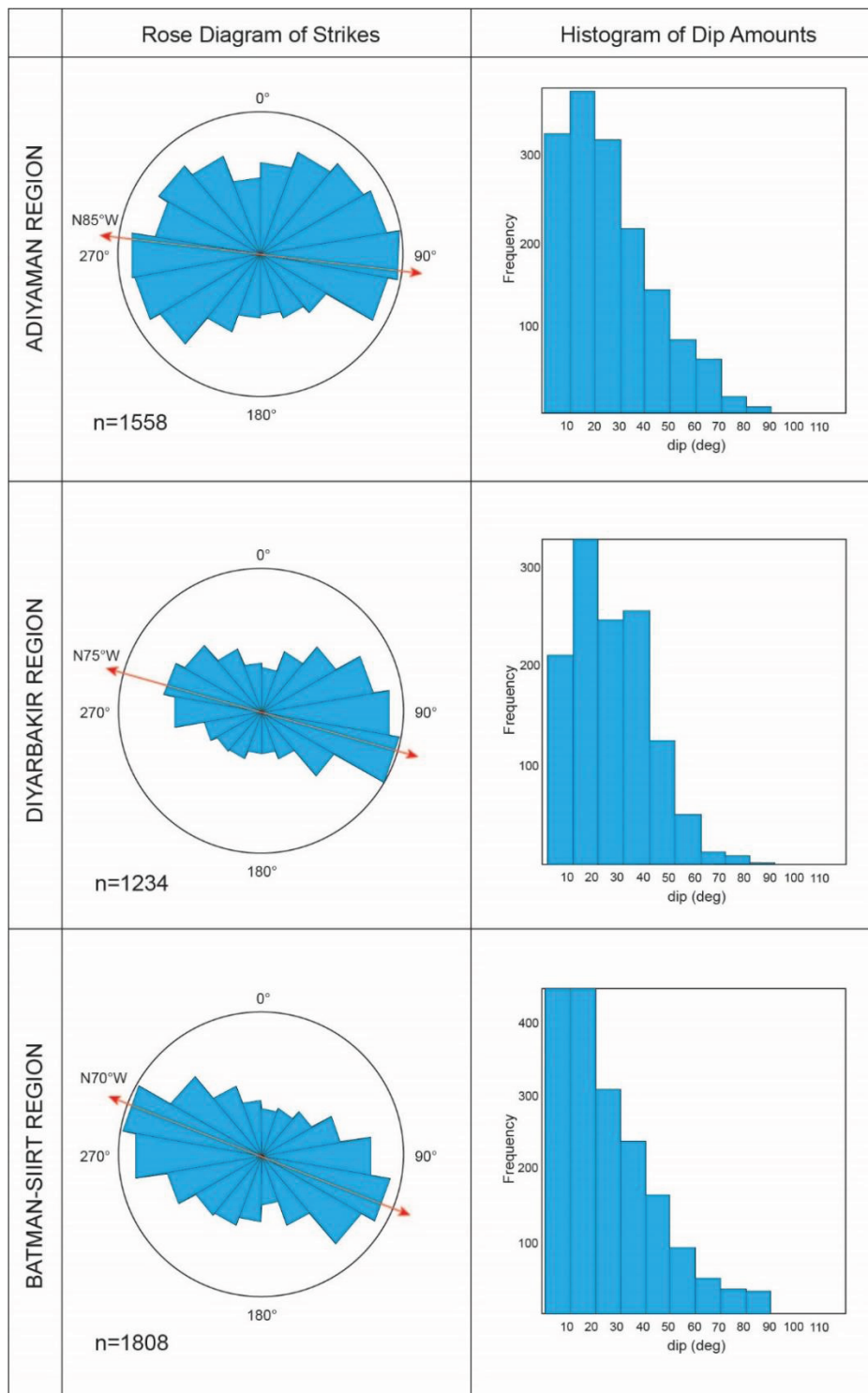


Figure 3.38 The figure illustrating the histogram of dip amounts of bedding planes and the rose diagram of strikes of bedding attitudes in Adiyaman, Diyarbakir, and Batman-Siirt subareas.

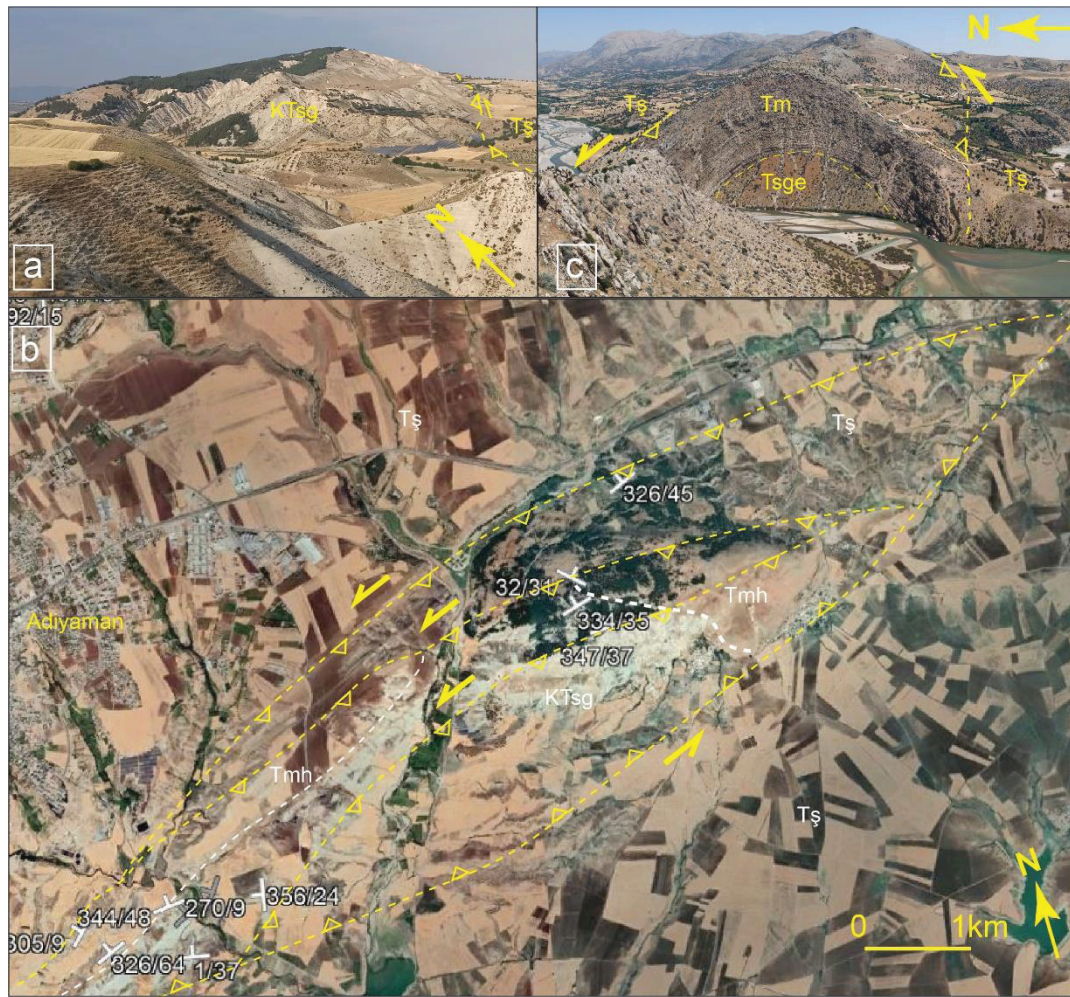


Figure 3.39 a-c) Positive flower structure (Alidag Anticline) along the Adiyaman Fault Zone around Adiyaman subarea. b) Positive flower structure (Cendere Anticline) along the Adiyaman Fault Zone around Adiyaman subarea.

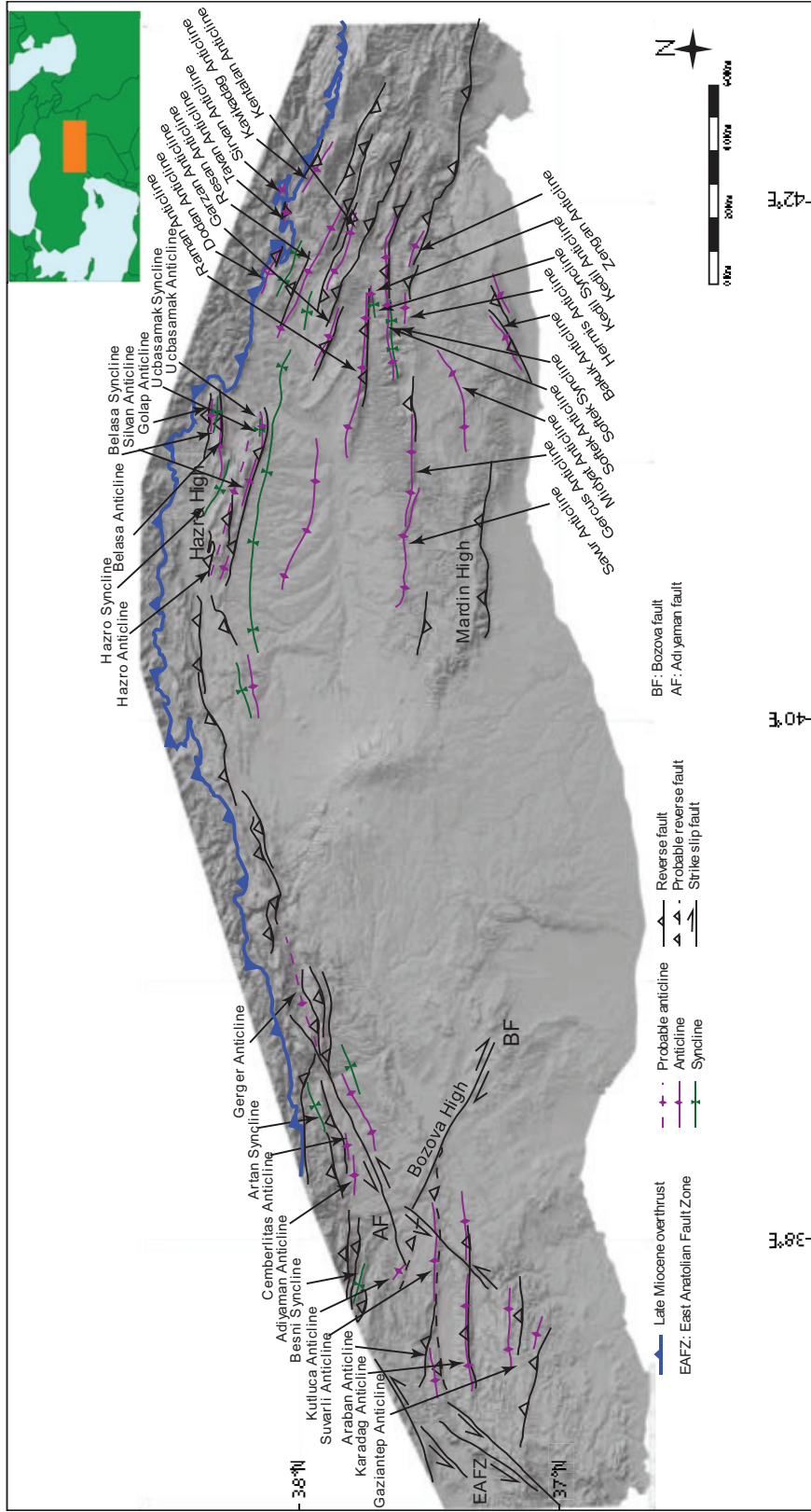


Figure 3.40 Structural map of the SE Anatolian Basin

Table 4.1 Results of fold analyses in Adiyaman, Diyarbakir, and Batman-Siirt sub-areas.

Name of the Fold	n	Fold axis	Axial plane	Interlimb angle	Pole of Limb1	Pole of Limb2
Araban Anticline	60	079°N/02°	N79°E,83°NW	149°	187°N/81°	164°N/68°
Buyukpirin Anticline	19	058°N/13°	N60°E,85°NW	165°	232°N/77°	284°N/72°
Cemberlitas Anticline	26	080°N/05°	N80°E,85°SE	129°	178°N/59°	339°N/62°
Geger Anticline	384	279°N/01°	N81°W,89°NE	159°	182°N/08°	014°N/78°
Kutluca Anticline	14	291°N/01°	N70°W,79°NE	148°	188°N/84°	023°N/63°
Artan Syncline	48	052°N/07°	N53°E,87°NW	165°	284°N/77°	198°N/81°
Besni Syncline	123	124°N/13°	N58°W,79°SW	116°	005°N/67°	227°N/45°
Hazro Anticline	544	110°N/03°	N70°W,81°NE	134°	212°N/76°	015°N/58°
Belasa Anticline	19	300°N/06°	N60°W,89°NE	152°	184°N/75°	054°N/74°
Golap Anticline	57	084°N/05°	N84°E,87°SE	155°	190°N/74°	330°N/79°
Silvan Anticline	36	294°N/02°	N66°E,86°SW	162°	194°N/77°	045°N/84°
Ucbasamak Anticline	67	277°N/04°	N84°W,79°NE	139°	162°N/80°	014°N/58°
Savur Anticline	16	080°N/02°	N80°E,88°NW	164°	187°N/84°	340°N/80°
Belasa Syncline	61	116°N/06°	N64°W,89°NE	169°	338°N/82°	254°N/82°
Ucbasamak Syncline	48	266°N/03°	N86°E,88°NW	160°	010°N/78°	158°N/81°
Bakuk Anticline	21	260°N/01°	N80°E,85°NW	163°	160°N/87°	352°N/76°
Dodan Anticline	177	296°N/03°	N64°W,89°NE	111°	201°N/57°	030°N/54°
Garzan Anticline	11	307°N/05°	N54°W,87°NE	156°	186°N/80°	055°N/74°
Gercus Anticline	31	080°N/01°	N80°E,89°NW	159°	172°N/81°	349°N/78°
Hermis Anticline	38	254°N/03°	N74°E,89°NW	163°	143°N/81°	005°N/81°
Kavikadag Anticline	112	295°N/07°	N63°W,77°SW	143°	194°N/58°	077°N/81°
Kedil Anticline	12	286°N/06°	N75°W,83°NE	145°	169°N/78°	028°N/65°
Kentalan Anticline	149	121°N/01°	N59°W,86°SW	126°	211°N/59°	030°N/67°
Midyat Anticline	75	053°N/01°	N53°E,89°SE	179°	225°N/89°	240°N/89°
Raman Anticline	100	263°N/02°	N83°E,84°NW	154°	159°N/83°	358°N/71°
Resan Anticline	92	108°N/01°	N72°W,89°SW	153°	198°N/76°	017°N/77°
Sirvan Anticline	185	311°N/05°	N49°W,89°SW	139°	209°N/68°	054°N/70°
Softek Anticline	81	256°N/01°	N76°E,86°NW	125°	165°N/67°	346°N/58°
Tavan Anticline	245	285°N/03°	N75°W,83°SW	101°	192°N/43°	019°N/58°
Zengan Anticline	19	309°N/05°	N52°W,84°NE	143°	197°N/77°	049°N/65°
Kedil Syncline	29	275°N/11°	N85°W,89°SW	133°	028°N/65°	162°N/64°
Softek Syncline	69	075°N/02°	N75°E,78°NW	131°	343°N/53°	172°N/78°

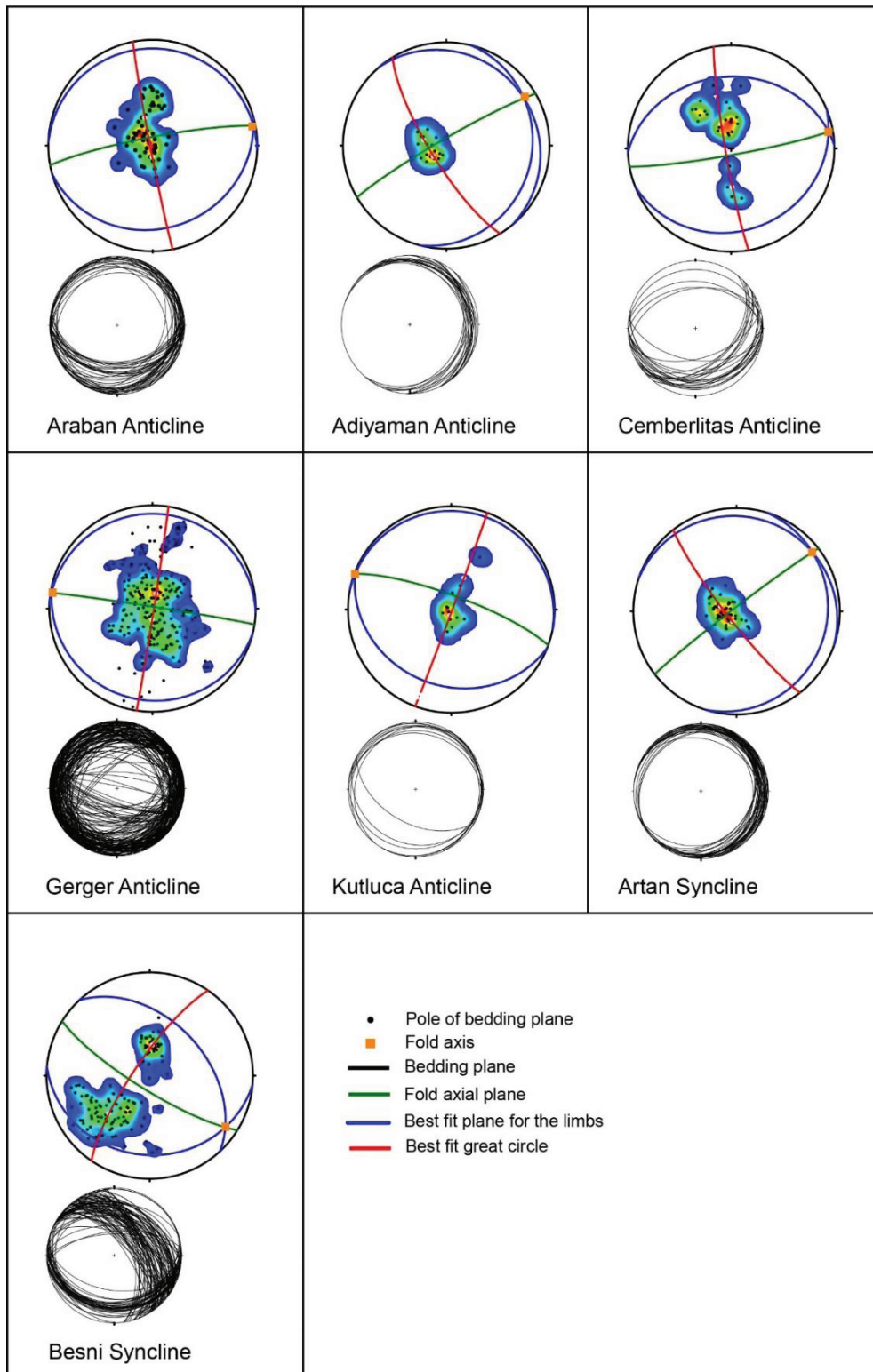


Figure 3.41 The SE Anatolian basin's major folds are depicted in the following β - and $-\pi$ diagrams. The folds are shown in figure 3.40.

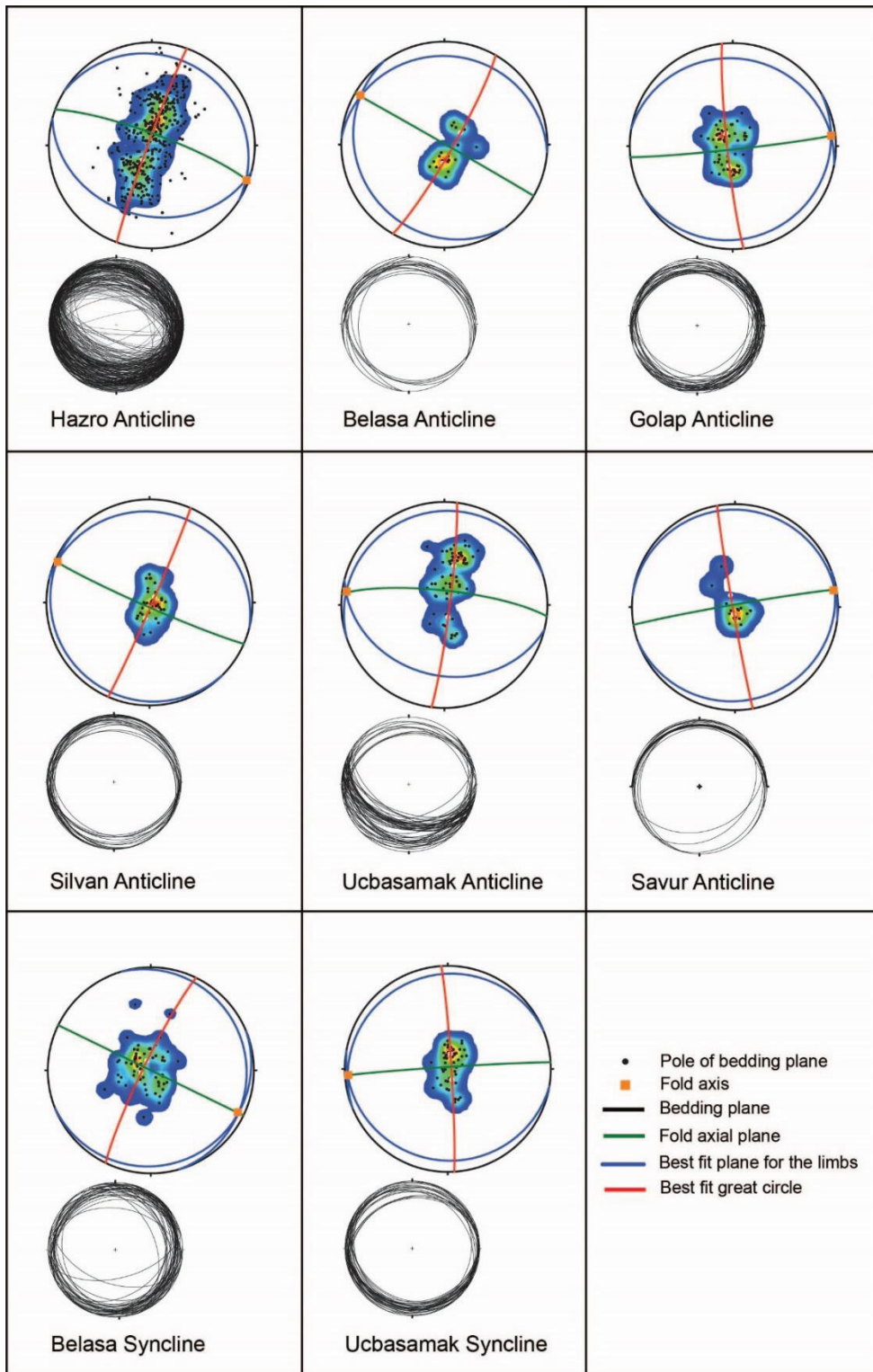


Figure 3.41 (continued)

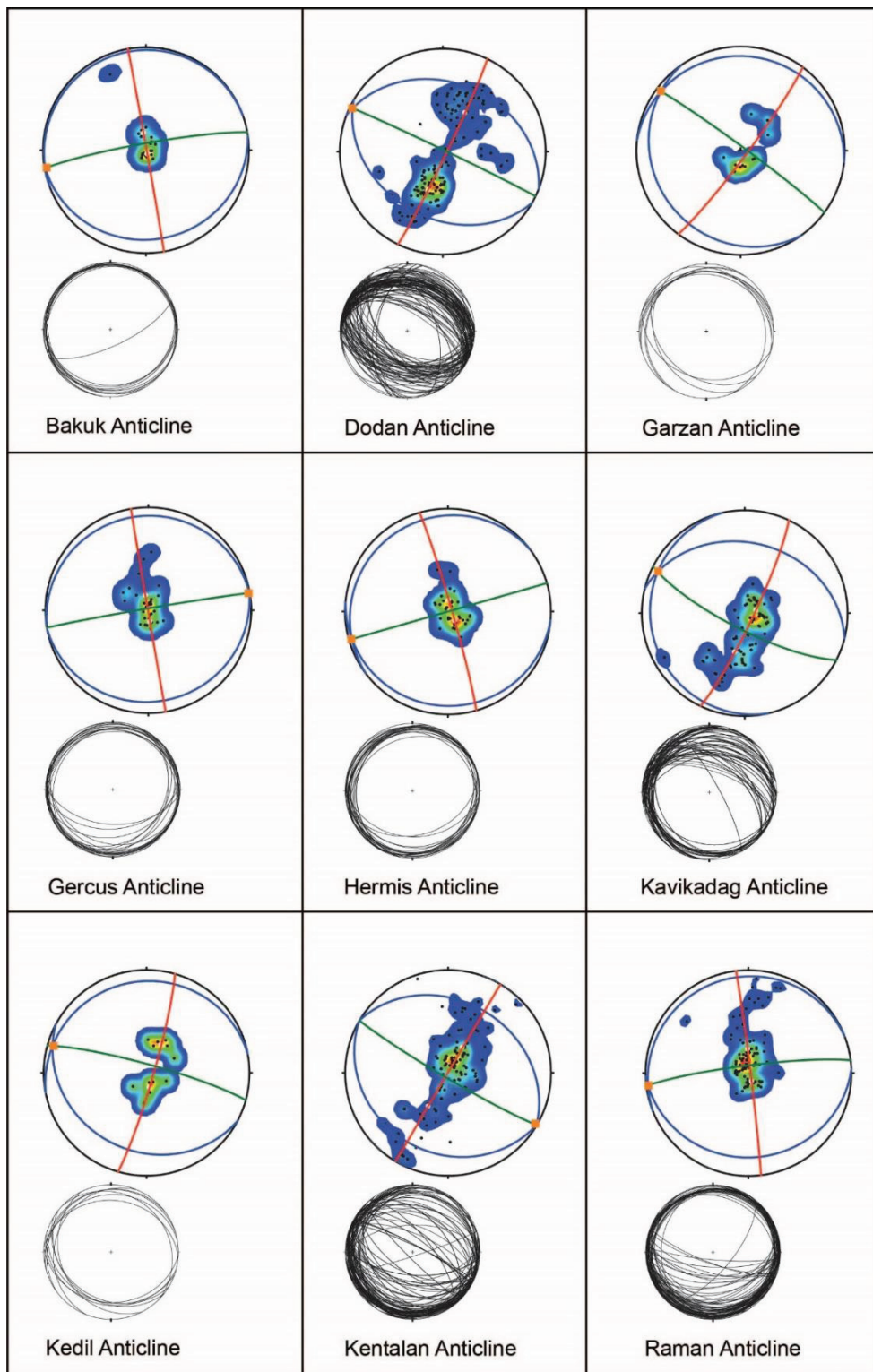


Figure 3.41 (continued)

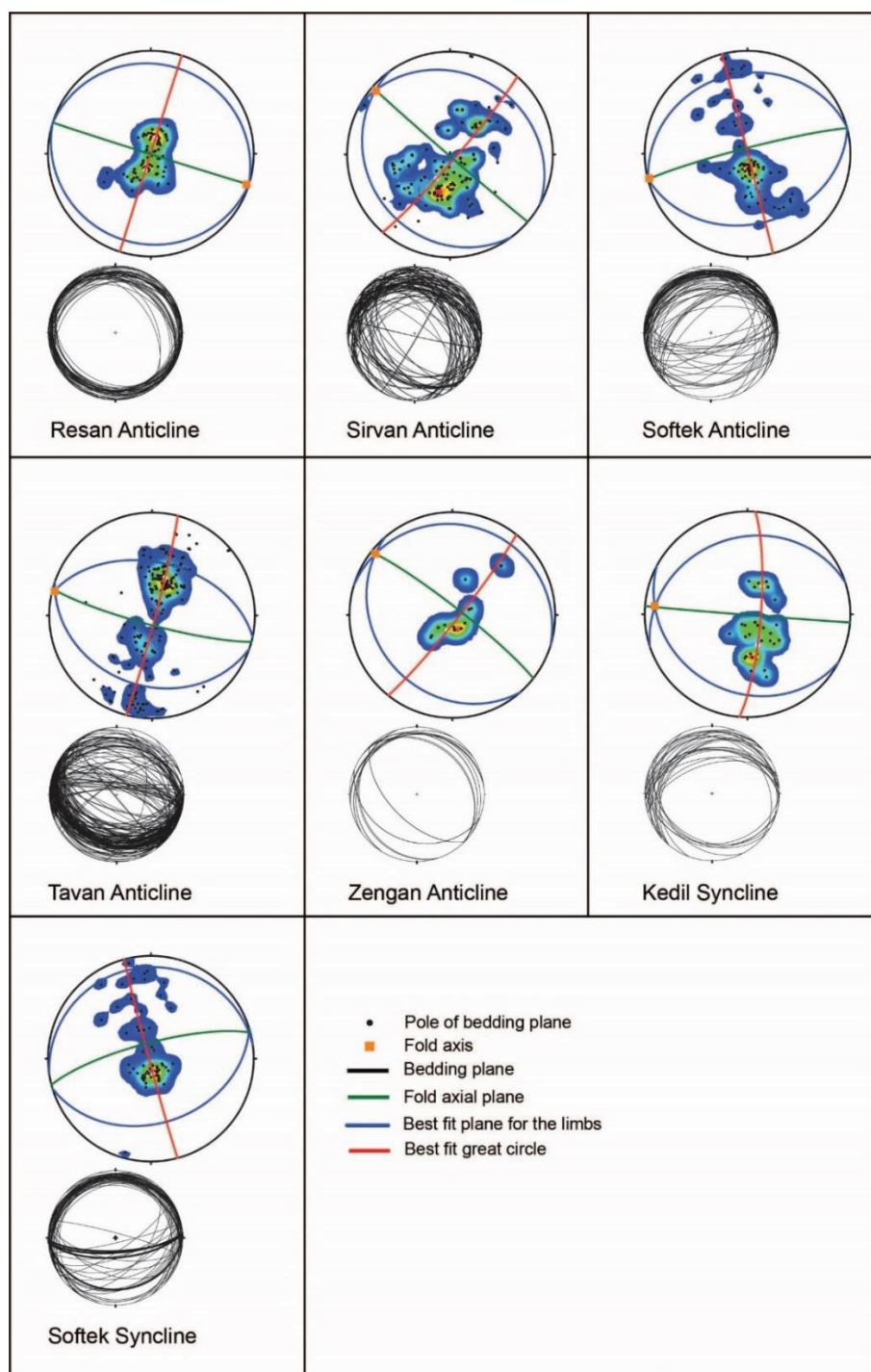


Figure 3.41 (continued)

Additionally, the β - and $-\pi$ diagrams suggest arc-shaped basin margin parallel folding with hinge lines attitudes (NE-SW at the west, E-W at the center, and NW-SE at the east) (Figures 3.42 and 3.43. Moreover, the data indicate that;

- i) Generally, the folds plunge gently subhorizontal, towards NW-SE and E-W from the east to western parts of the study area,
- ii) The inter-limb angles indicate open or gently plunging folds if the Cretaceous or younger rock units are visible at their limbs or cores. This suggests that the tightness of the folds is governed by faults reaching up to the surface or uppermost levels,
- iii) The attitudes of fold axial planes indicate that generally upright folds are located proximal to the basin margin, and steeply inclined folds are located distal to the basin margin in the basin. This indicates that the vergence is due south,
- iv) A left-lateral strike-slip fault system appears to be responsible for developing intra-basinal folds that include Alıdağ and Cendere anticlines located in the western part of the basin.

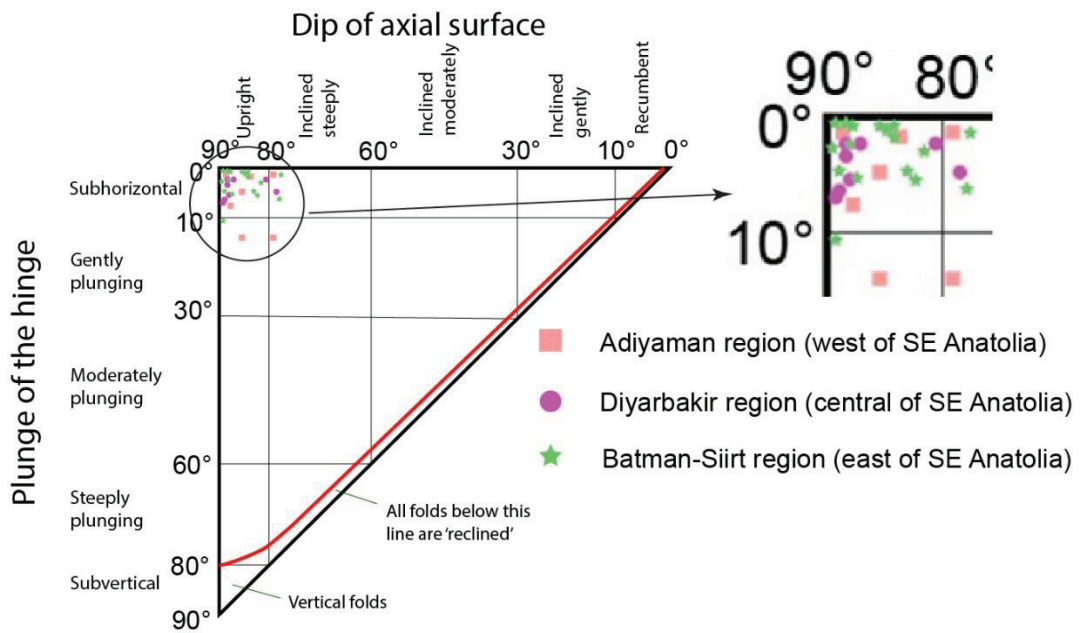


Figure 3.42 Fold classification based on symmetry and plunge (Fleuty, 1964; Hatcher and Bailey, 2020).

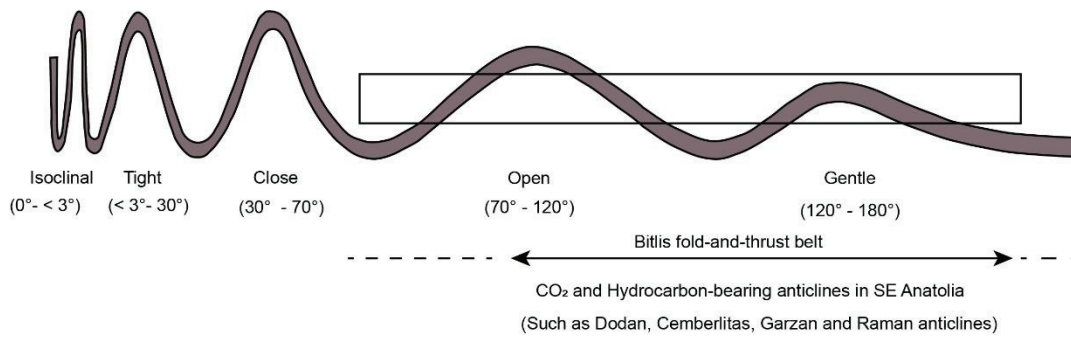


Figure 3.43 Classification of folds based on the interlimb angle (modified after Fleuty, 1964, and Nabavi and Fossen, 2021). The rectangle represents the folds encountered in the study area.

3.3.2 Progressive Unconformities

Two types of syntectonic unconformities, based on criteria given in the methodology, are defined in the Miocene strata exposed in Adiyaman, Diyarbakir, and Batman-Siirt regions, where the exposures are close to the main frontal thrust. The types of unconformities encountered in the field and seismic section depicted in figure 3.44, figure 3.45, and figure 3.46, are considered to emphasize the syn-deformational tectonics in the region.

Additionally, a seismic profile shows a south-vergent thrust system and related sedimentation. The thickness of the units in the line increases from the reverse fault in the north to basinward in the south.

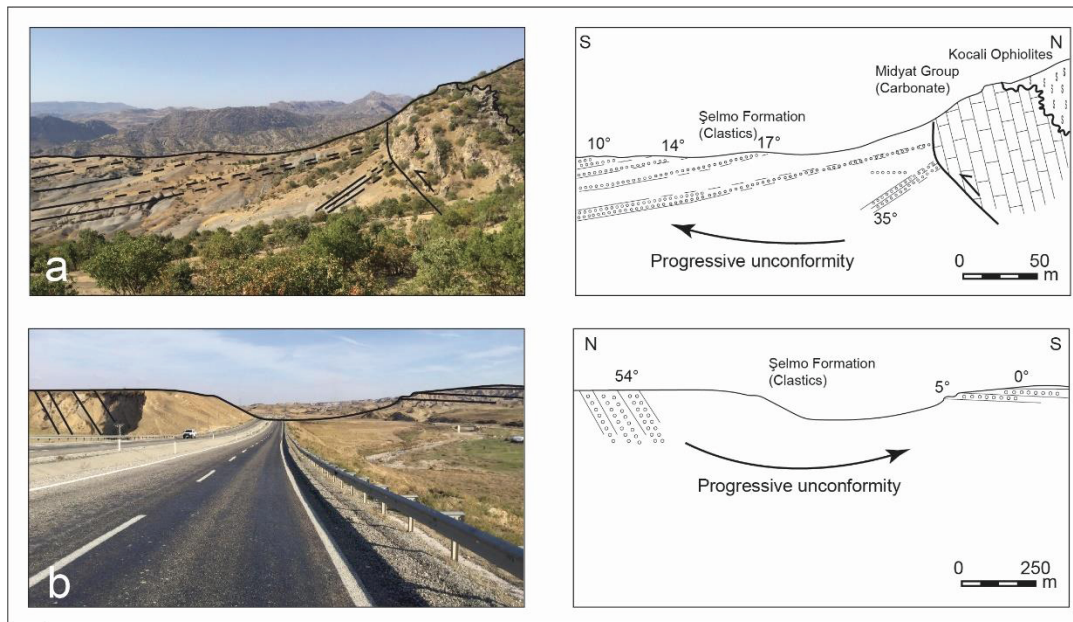


Figure 3.44 a) Pictures with field sketches showing a progressive unconformity a) 90 km northeast of Adiyaman. b) 30 km northeast of Batman.

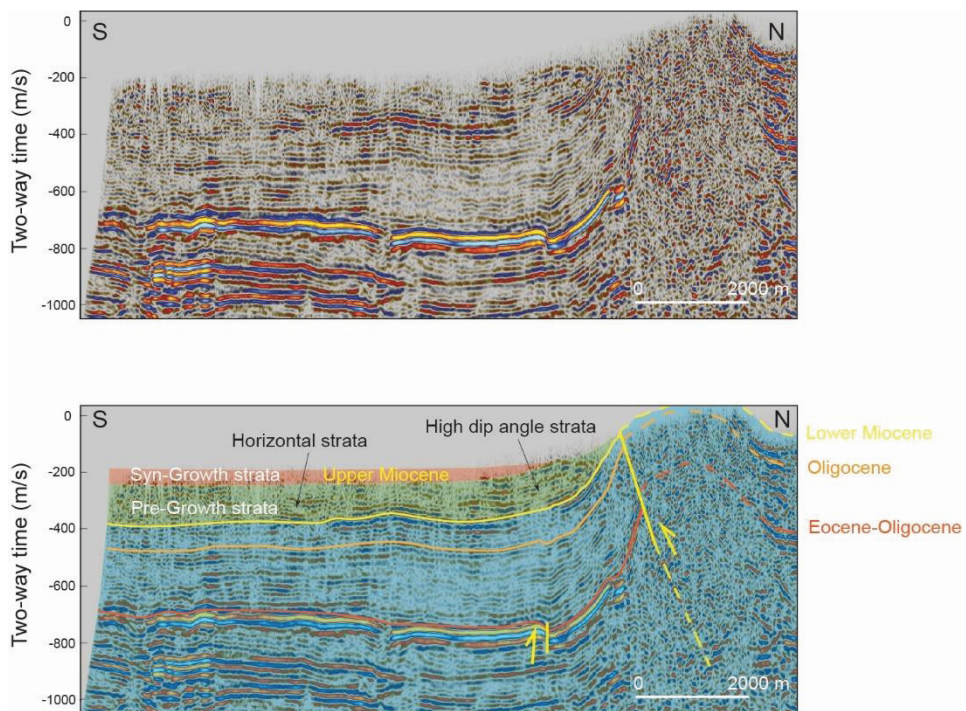


Figure 3.45 Uninterpreted and interpreted seismic profile across the Hazro High. Note thinning of the deposits southwards implying, thrusting-related sedimentation.

Lastly, another progressive unconformity is detected in the Dodan area, which is located about 30 km northeast of Batman city in SE Anatolian in front of the frontal thrust. In this study area, stratigraphic layers are composed of lower Eocene continental deposits of the S12 stratigraphic class (the Gercus Formation). The thickness of this unit is approximately 600 m (data gathered from a few wells) and is represented by red coarse-grained conglomerate and sandstone. It overlies the Middle Eocene-Oligocene shallow marine layers of S13 (the Hoya Formation), which have a thickness of approximately 200-300 m in that region. The upper part consists of the lower Miocene deep marine and shallow marine deposits of S15 and S16 (the Lice and Fırat Formations). The youngest strata observed here are the upper Miocene continental clastics of S17 (The Şelmo Formation), having a thickness of approximately 150 m around the Dodan area.

The conglomerate and sandstone layers of the Şelmo Formation are separated from the lower Miocene deposits by an angular unconformity. This discordance is marked by an angular discordance of up to 19° in proximal areas (Figure 3.46). The dip discordance diminishes with increasing distance (to the south) away from the uplift. This is because the amount of uplift decreases progressively with distance; in other words, the angular unconformity weakens from the direction of tectonic movement. Additionally, the angular unconformity indicates the event of maximum diastrophism. The structural disposition of Miocene rocks at this margin (cross section in Figure 3.46 c) suggests a rotative off-lap followed by a rotative onlap caused by the uplift of the south of the Dodan anticline during the Late Miocene. This pattern can be referred to as “composite progressive unconformity” and can be explained by thrust faulting-related uplift and sedimentary patterns from Early Miocene to Late Miocene.

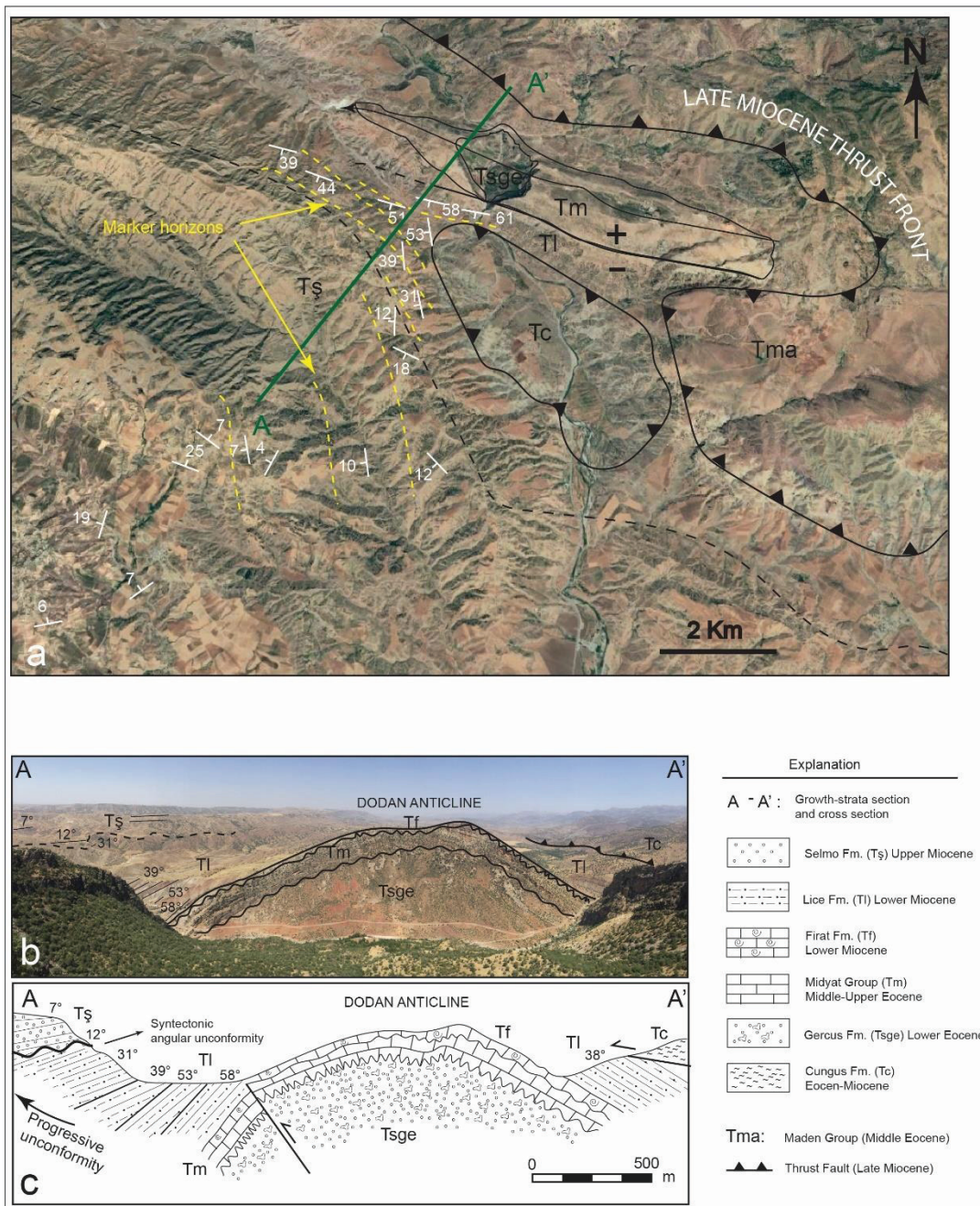


Figure 3.46 a) Aerial google map of the northwest Siirt region area highlighting outcrop exposures and stratigraphic units. b) Photograph and line drawing showing the angular unconformity between the Lice Formation (Sandy shale and sandy marl-lower Miocene) and Selmo Formation (upper Miocene) conglomerate and sandstone. c) Cross section (A-A') through the growth strata from south to north.

3.3.3 Paleostress Analyses

Paleostress analysis is performed only on the surface traces of the fault detected in seismic lines to verify their existence and kinematic characteristics in the field. In other words, fault kinematic interpretations are solely restricted to the seismic lines. Therefore, the results here should be considered supportive data on seismic interpretations. We know that they need to be adequate to reveal the spatial and temporal paleostress evolution of the region. The results of the conducted analyses are summarized in table 3.2 and figure 3.49.



Figure 3.47 Field photographs of brittle structures located in the Batman-Siirt subarea. a) Within the lower Eocene Gercüş Formation, intensely sheared reverse faults evolved in the eastern Batman-Siirt subarea. b) Tilted normal faults within the lower Eocene Gercüş Formation in the eastern Batman-Siirt subarea. Note slight thickening on the downthrown blocks of the faults implying their syntectonic origin. c) Reverse fault within the upper Miocene Şelmo Formation (Upper Miocene) in the eastern Batman-Siirt subarea.

The primary outcomes of the results in table 3.2 and figures 3.47 and 3.48 indicate that all of the measurement sites are represented by almost vertical σ_3 and almost horizontal σ_1 directions. Also, Φ' values (c.f Delvaux et al., 1997) of all measurements (except three sites, L12, L14, and L23, which are transpressive) are between 2.25 and 2.75. This suggests pure compressional kinematics for all sites. This means that the faults determined in seismic lines should be pure thrust or reverse faults. Additionally, the σ_1 direction in almost all measurement sites is in accordance with the elongation of the frontal thrust of the basin. This implies that the sites at the western, central, and eastern portions of the basin are represented by NW-SE, N-S, and NE-SW directed compressional settings. Here, we could not give relative age information for all measurement sites due to a lack of age-proving data in the field. On the other hand, some sites with comparable age data are given in Table 3.2. However, since the age data is not enough to differentiate deformation phases and also all measurements are represented by almost the same σ orientations, the time-dependent paleostress information of the basin could not be given here.

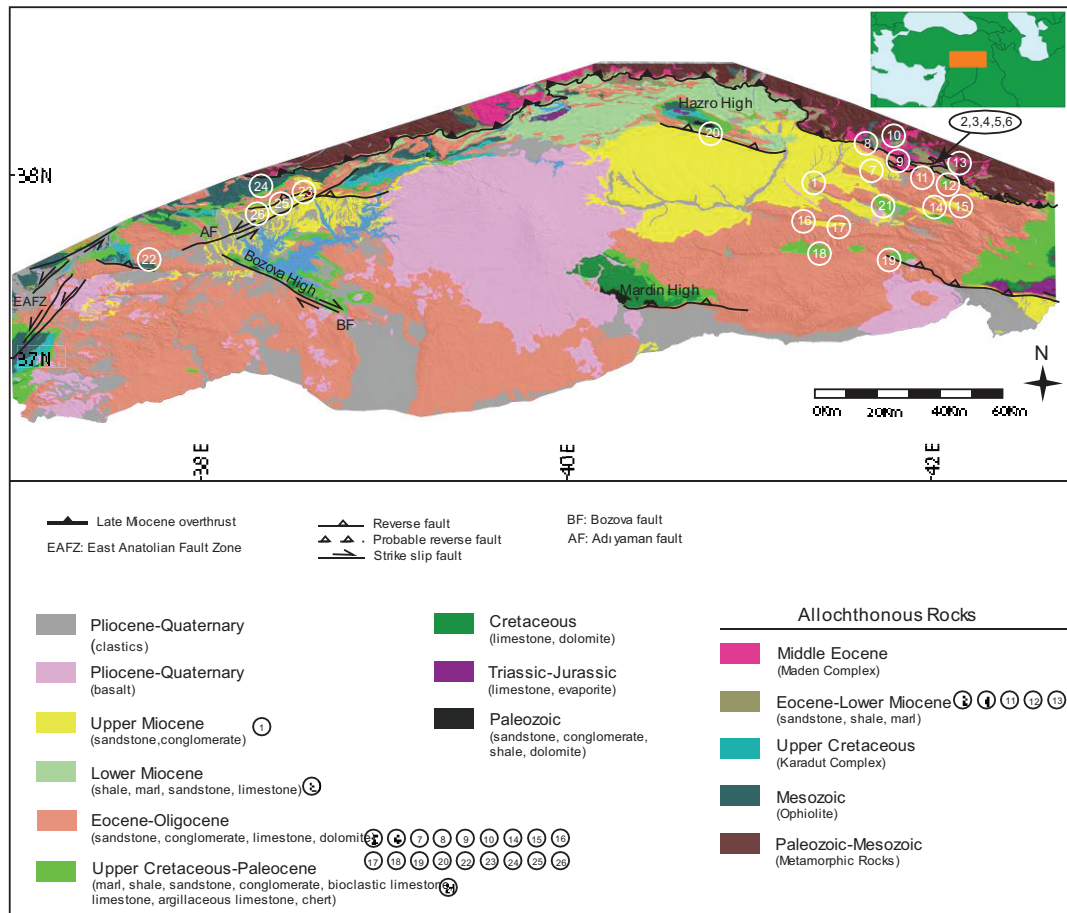


Figure 3.48 Geological map of SE Anatolian displaying paleostress sampling sites.

Table 5.1 Results of paleostress inversion

Site Code	Latitude	Longitude	σ_1 (D°/P°)	σ_2 (D°/P°)	σ_3 (D°/P°)	Φ'	Hosting units
L1	37,959	41,346	083/02	353/02	209/87	2,73	Upper Miocene
L2	38,019	41,939	028/20	290/22	156/60	2,38	Eocene-Lower Miocene
L3	38,053	41,997	176/20	285/41	067/42	2,7	Lower Miocene
L4	38,032	42,031	046/00	136/02	313/88	2,65	Eocene-Lower Miocene
L5	38,055	42,06	032/08	123/05	247/81	2,53	Lower Eocene
L6	38,055	42,061	193/14	298/45	091/41	2,56	M.Eocene-Oligocene
L7	38,084	41,765	165/12	073/11	300/74	2,43	M.Eocene-Oligocene
L8	38,095	41,77	327/21	074/38	215/44	2,5	M.Eocene-Oligocene
L9	38,092	41,767	181/28	275/07	017/61	2,5	Lower Eocene
L10	38,097	41,771	344/09	249/31	088/57	2,42	M.Eocene-Oligocene
L11	38,03	42,02	169/03	259/00	349/87	2,67	Eocene-Lower Miocene
L12	38,002	42,055	020/12	286/15	145/70	2,12	Eocene-Lower Miocene
L13	38,01	42,064	113/27	015/15	260/59	2,5	Eocene-Lower Miocene
L14	37,976	42,062	137/07	046/08	268/79	2,08	Lower Eocene
L15	37,977	42,064	259/15	169/19	024/66	2,42	Lower Eocene
L16	37,743	41,287	187/11	097/01	000/79	2,52	M.Eocene-Oligocene
L17	37,701	41,461	116/03	207/07	360/82	2,5	M.Eocene-Oligocene
L18	37,562	41,365	035/18	302/08	188/70	2,42	Lower Eocene
L19	37,552	41,754	039/01	130/18	307/72	2,5	M.Eocene-Oligocene
L20	38,23	40,775	069/15	337/07	223/73	2,54	M.Eocene-Oligocene
L21	37,843	41,726	161/04	070/14	266/76	2,5	U.Cretaceous-Paleo.
L22	37,482	37,706	034/27	125/02	220/63	2,57	M.Eocene-Oligocene
L23	37,844	38,415	267/23	162/30	028/51	2,15	M.Eocene-Oligocene
L24	37,84	38,404	360/08	268/11	128/76	2,58	M.Eocene-Oligocene
L25	37,838	38,31	016/12	107/08	230/76	2,5	M.Eocene-Oligocene
L26	37,825	38,307	345/30	079/07	180/59	2,5	M.Eocene-Oligocene

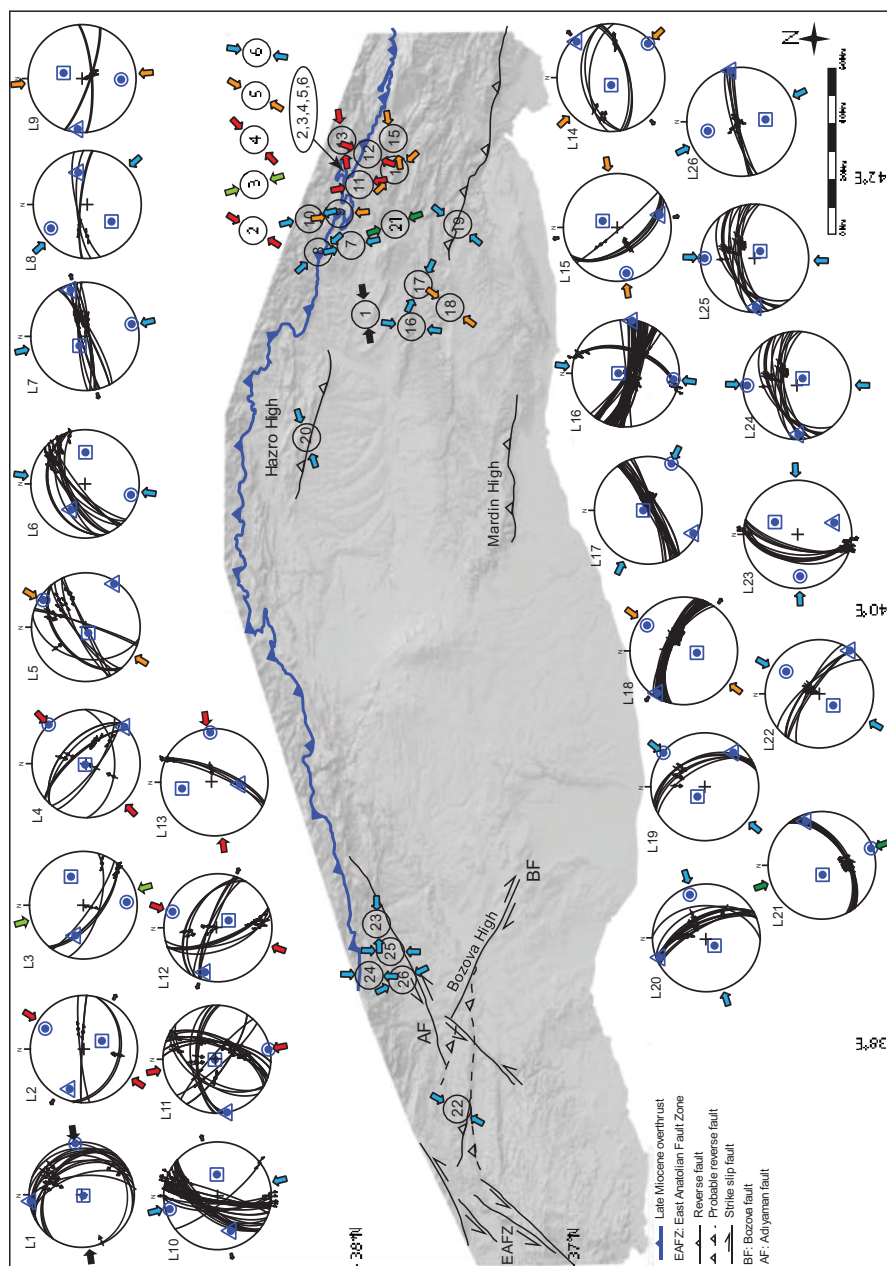


Figure 3.49 Paleostress inversion results, distribution, and orientation of the principal stresses represented on a tectonic map of SE Anatolian.

3.4 Cross Sections

The main structures in the basin are thrust/reverse faults and associated folds. The surface expressions of these structures are observed as open and gentle synclines and anticlines which are transected by (i) thrust faults that emerged and imbricated at some places and (ii) blind thrust faults.

2D seismic reflection data and surface maps (see figure 2.4 for the location of seismic lines and 3.10 for the surface map) were used to figure out the structural style and geometry of the basin succession in the study area. Seismic profiles are generally poor in quality in the northern and deeper parts of the basin and are good in the south.

3.4.1 2D Seismic Interpretation

Eleven seismic lines with good quality were used in the study (Figure 2.4).

Seismic line 1 is located in the north of the Adiyaman sub-area (Figure 3.50). SS1 fault determined along the section, based on field observations, is defined as a NE-SW trending left-lateral strike-slip fault. The approximately NE-SW trending SS3 and SS6 faults are also strike-slip faults and are subparallel to the main trend of the SS1 fault. SS2, SS4, and SS5 are interpreted as antithetic strike-slip faults. The strike-slip faults create offsets on all series. So, they must be associated with the most recent deformation phase of the region. In the seismic section two, NE-SW folds are observed.

Moving from SE to NW, two positive flower structures are defined in the section. They are thought to be the product of the youngest deformation phase, which is manifested by strike-slip faults in the region.

The southern anticline covered by Neogene sediments is a tight anticline (~850 m wide) with lower dip angles at the flanks with respect to the northern anticline.

The northern anticline is a little broad anticline and, almost 1200 m wide. The Upper Cretaceous-Paleogene Germav Formation and Middle Eocene-Oligocene Hoya Formations are exposed in the core of the anticline.

The seismic line 2 is located at the NW of in Adiyaman sub-area (Figure 3.51). The central-north portion of the line could not be interpreted due to poor quality.

Seismic line 2 consist of (i) a possible detachment fault within the Cambrian units (brown line in the section), (ii) four thrust faults, including one south dipping back thrust fault. Seismic data show that all faults affect all the units shown in the section. The folds and thrust faults recognized in the section indicates an association between the development of the folds and faults since the folds are bounded by the faults and their flanks are cut by the faults pointing out fault propagation folds.

The seismic line 3 is located at the central-north area of the Adiyaman sub-area (Figure 3.52). Seismic line 3 consists of a possible detachment, one thrust fault within the Cambrian units (brown line in the section). This section hosts only one thrust fault, which is dipping to the north and displacing all units shown in the section. This fault also creates a fault propagation anticline with a snake head structure.

The seismic line 4 is located at the SW of the Adiyaman sub-area (Figure 3.53). Seismic line 4 consists of four thrust faults. Two of them are south-dipping back thrusts. Seismic data show that all faults (except a back thrust – BT3) affect all units shown in the section. These faults control the shapes of the anticline, and so all folds in the section are fault propagation folds.

The seismic line 5 is located at the NW of the Adiyaman sub-area (Figure 3.54). Seismic line 5 consists of a possible detachment fault within the Middle Triassic-Lower Cretaceous or older units. The section also hosts five thrust faults, two of which are south-dipping back thrusts. All faults except BT5 create displacement of all units shown in the section. The folds detected along the section are fault propagation folds since their geometries are in accordance with the location and the type of the faults.

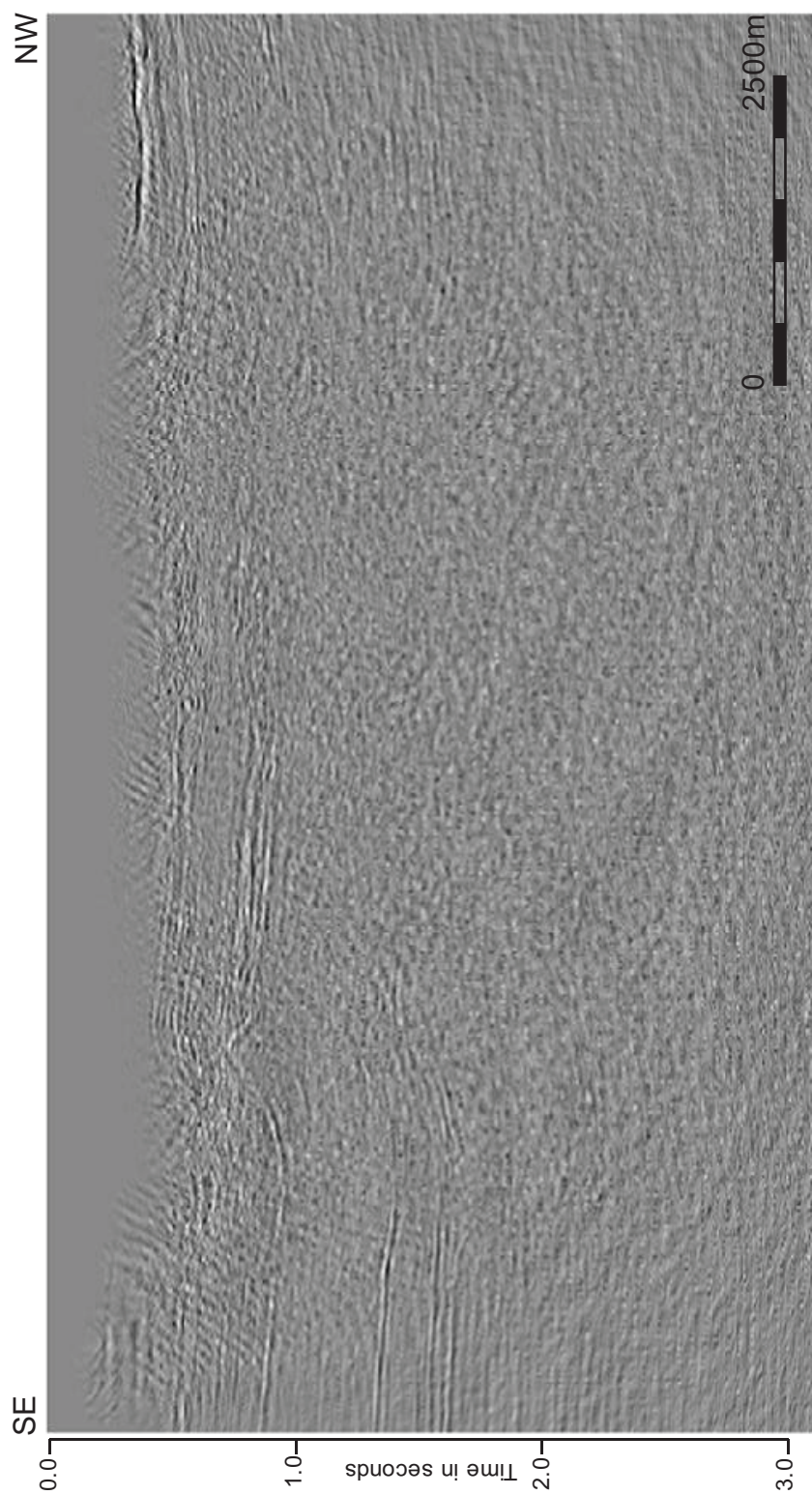


Figure 3.50 Uninterpreted and interpreted seismic profiles with stratigraphic horizons and faults marked. The seismic line 1 is shown at vertical exaggeration x2.

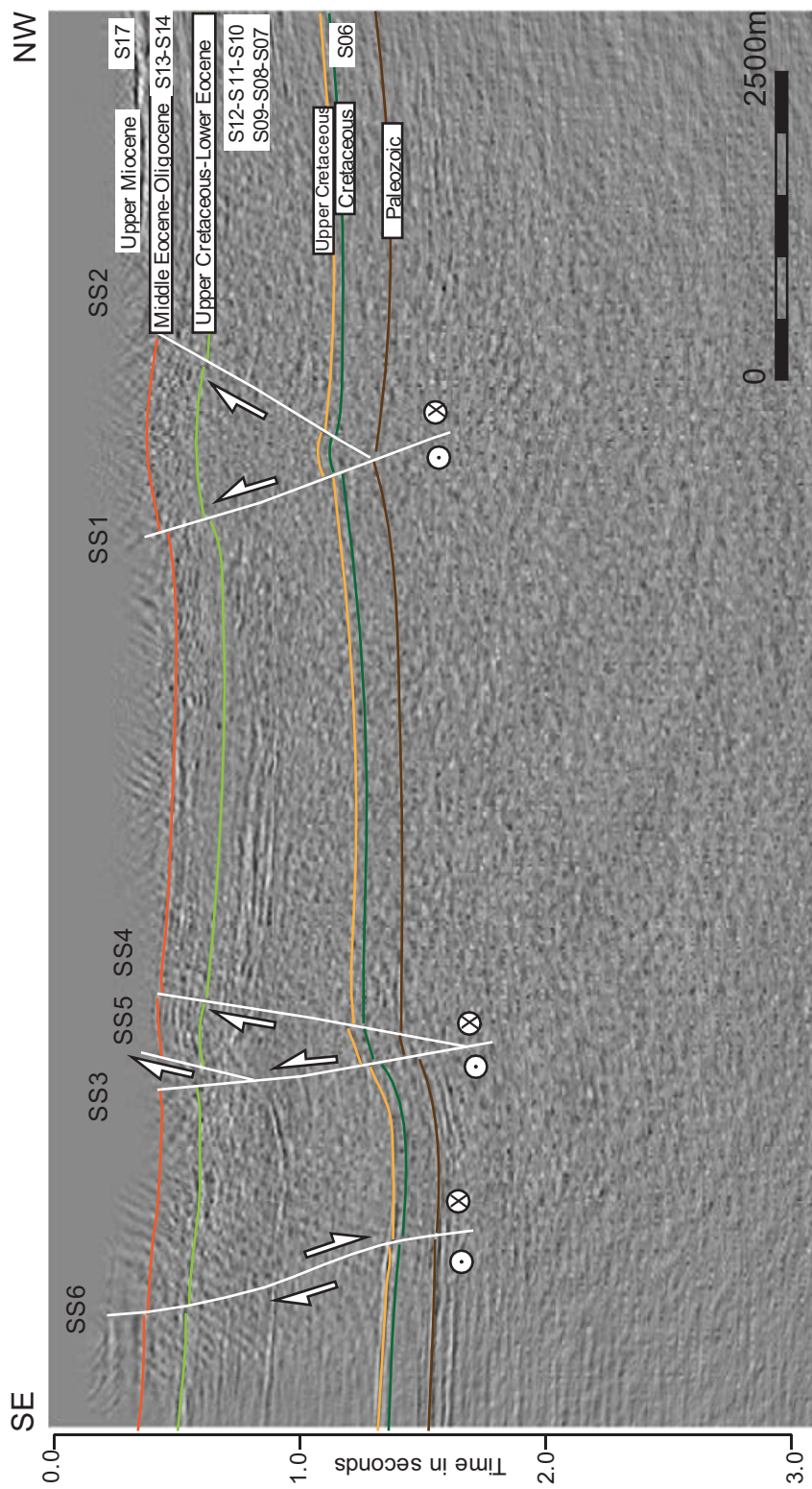


Figure 3.50 (continued)



Figure 3.51 Uninterpreted and interpreted seismic profiles with stratigraphic horizons and faults marked. The seismic line 2 is shown at vertical exaggeration x2.

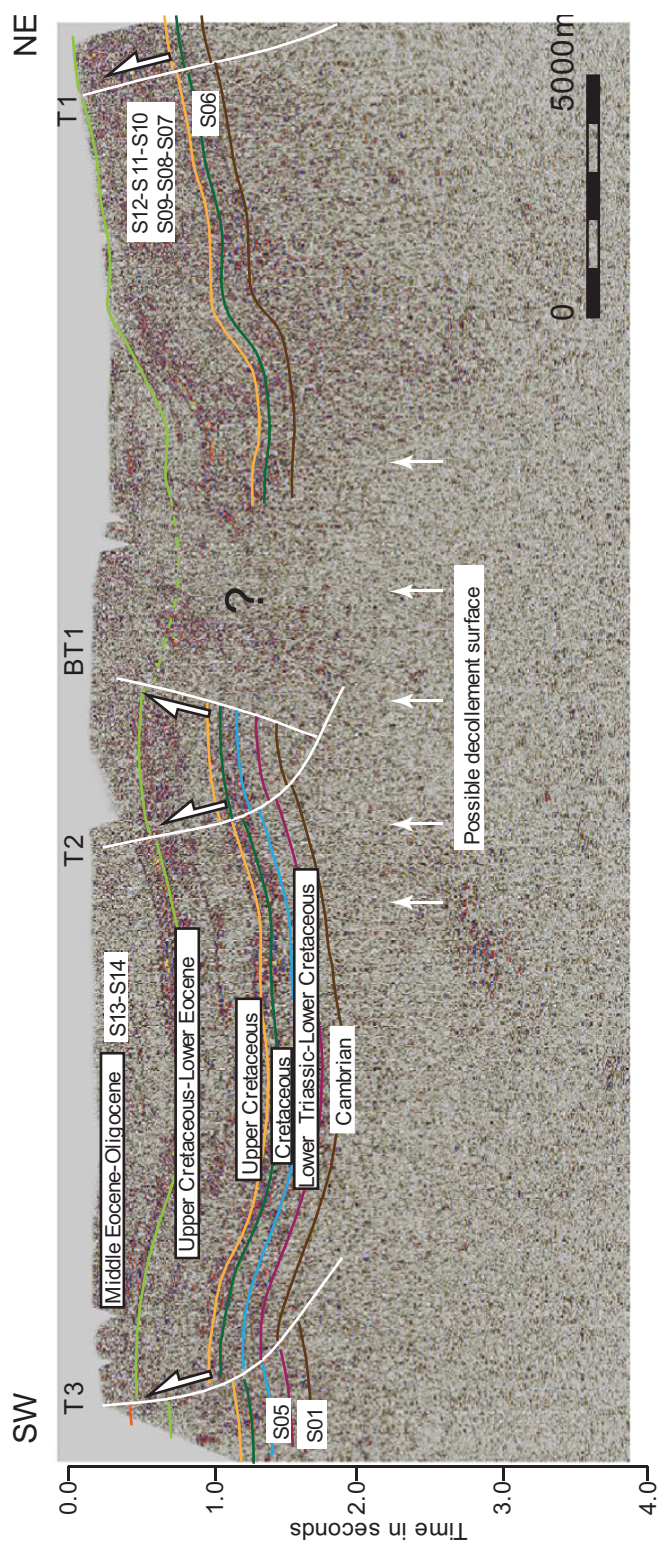


Figure 3.51 (continued)



Figure 3.52 Uninterpreted and interpreted seismic profiles with stratigraphic horizons and faults marked. The seismic line 3 is shown at vertical exaggeration x2.

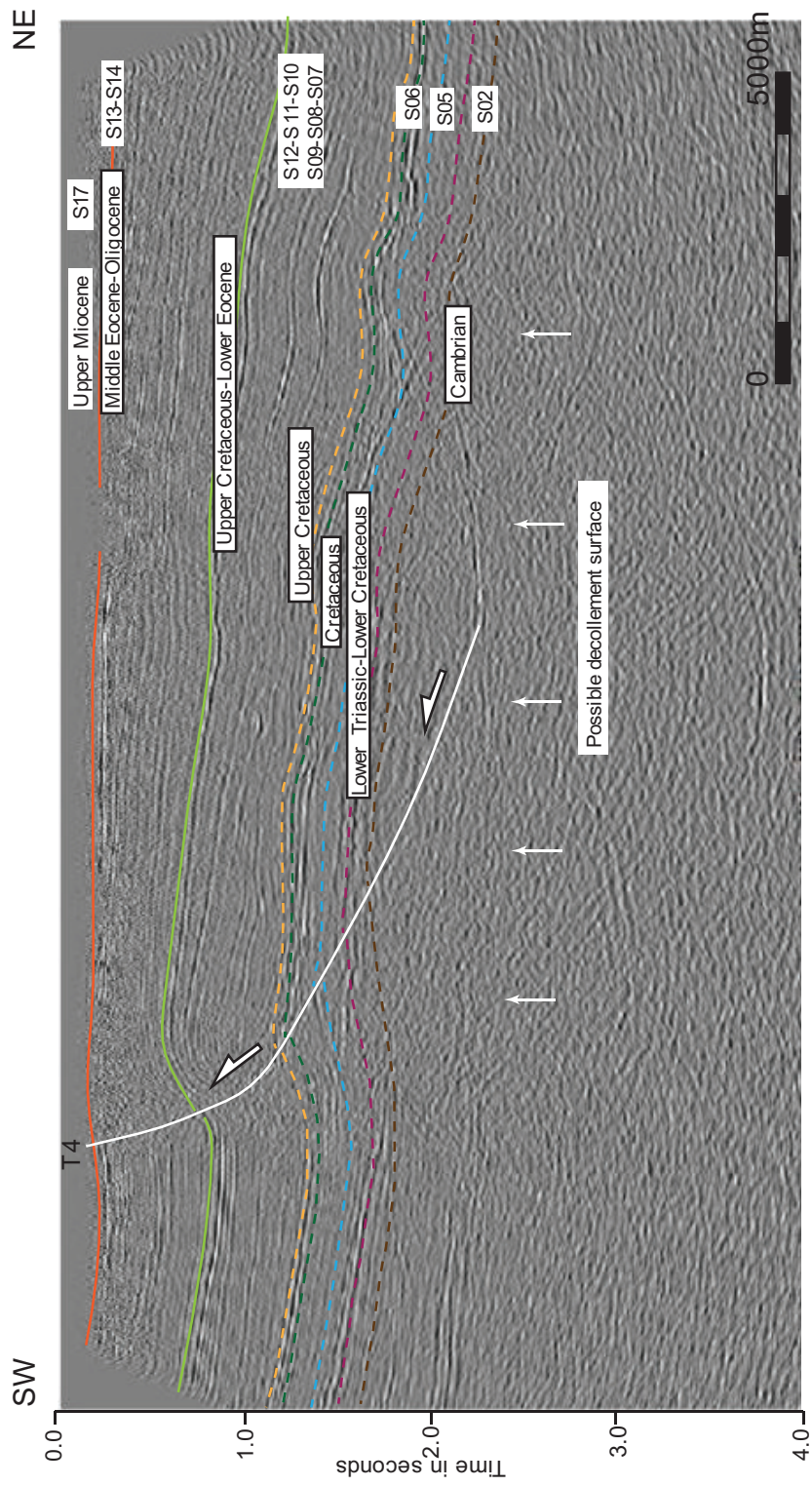


Figure 3.52 (continued)



Figure 3.53 Uninterpreted and interpreted seismic profiles with stratigraphic horizons and faults marked. The location of the seismic line 4 is shown at vertical exaggeration x2.

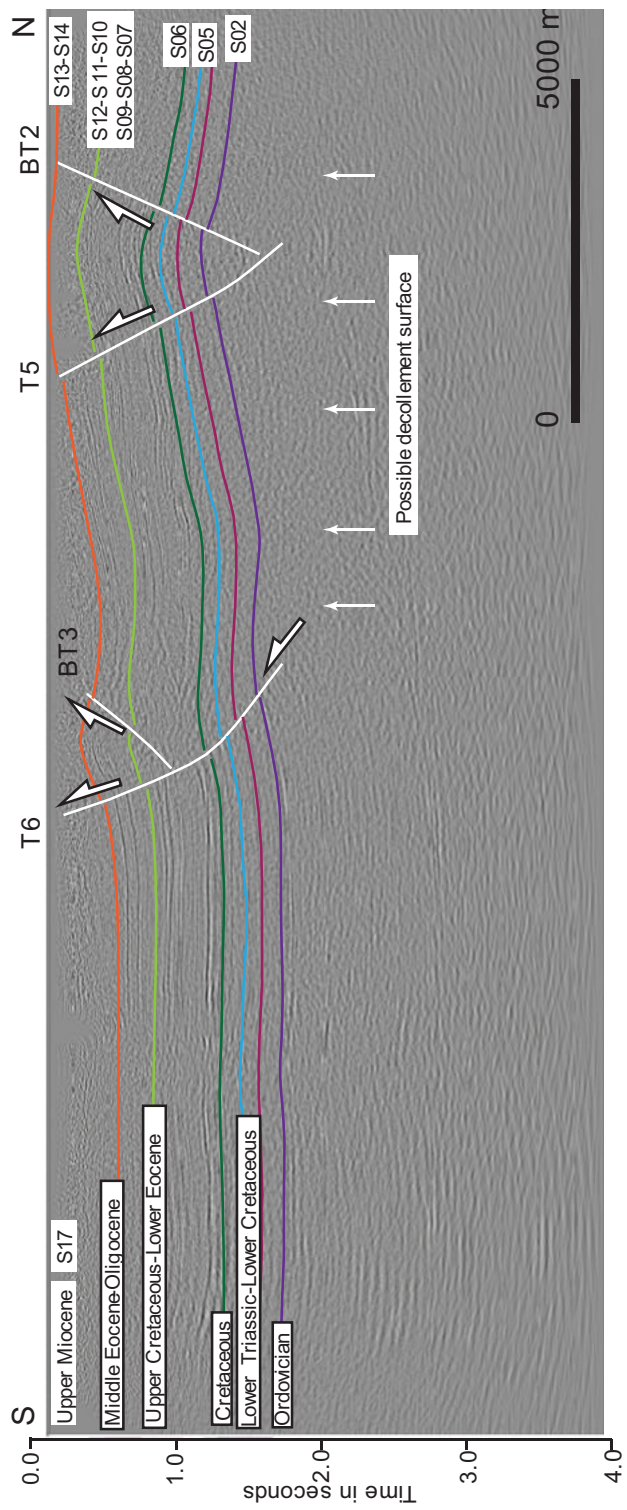
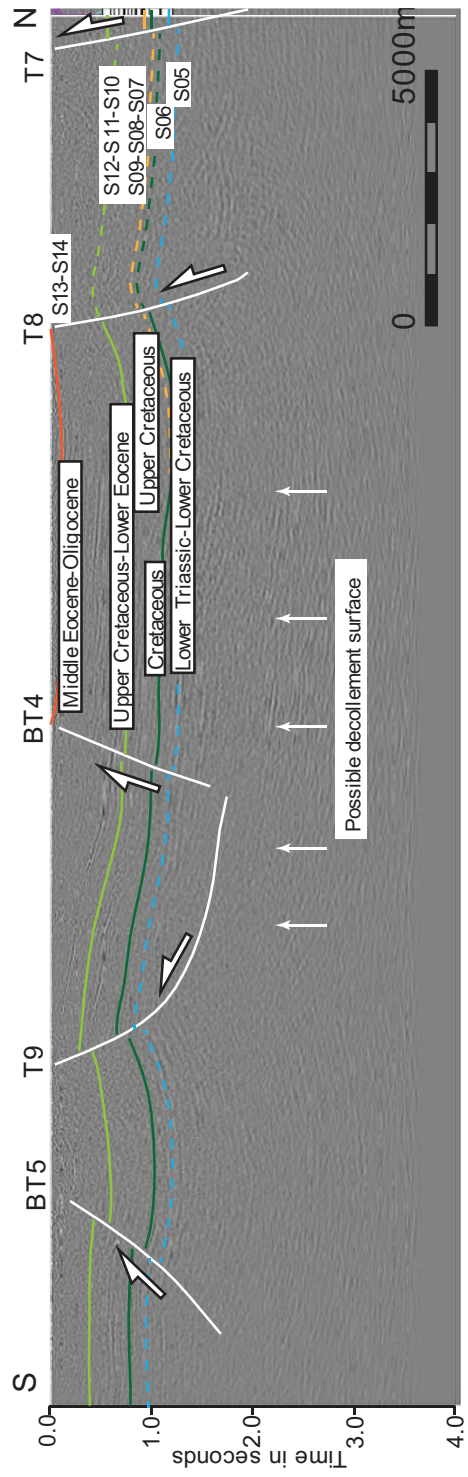


Figure 3.53 (continued)



Figure 3.54 Uninterpreted and interpreted seismic profiles with stratigraphic horizons and faults marked. The location of the seismic line 5 is shown at vertical exaggeration x2.

Figure 3.54 (continued)



The seismic line 6 is located in the central west of the Adiyaman sub-area (Figure 3.55). Seismic line 6 comprises a tight anticline of which development is controlled by two north dipping thrusts and two south dipping back thrusts. All of the faults displace some portions of the units shown in the section. None of them cut all units in the section, so they are blind thrusts.

The seismic line 7 is located at the center of the Adiyaman sub-area (Figure 3.56). Seismic line 7 consists of a possible detachment within the Middle Triassic – Lower Cretaceous units or older units (blue dash line in the section). It also has six thrust faults. Three of them are south-dipping back thrusts. The section has only one open anticline, which is bounded by thrust faults.

The seismic line 8 is located at the N of the Diyarbakır sub-area (Figure 3.57). Seismic line 8 consists of a possible detachment fault within the Ordovician units. Two north-dipping thrust faults, two south-dipping back thrust faults, and an anticline at the center of the section are the major structures observed in the section. One thrust fault (T15) and back thrust fault (BT11) create the maximum offsets, and they cut all the units shown in the section where the other faults are blind thrusts. All of the faults are found within the anticline structure, so they are responsible for the development of the anticline (Hazro High). The relative age of the T15 thrust fault can be determined here as younger than Upper Miocene since it displaces the Upper Miocene Units (Şelmo Formation), and the thickness of the formation gets higher towards the south direction from the surface trace of the fault.

The seismic line 9 is located at the NE of the Diyarbakır sub-area (Figure 3.58). A decollement surface is traced within the Ordovician units in the section. Line 9 consists of two north-dipping thrust faults, one south-dipping back thrust fault, and a series of folds (open anticline-syncline-anticline). All folds are associated with the development of faults.



Figure 3.55 Uninterpreted and interpreted seismic profiles with stratigraphic horizons and faults marked. The seismic line 6 is shown at vertical exaggeration x2.

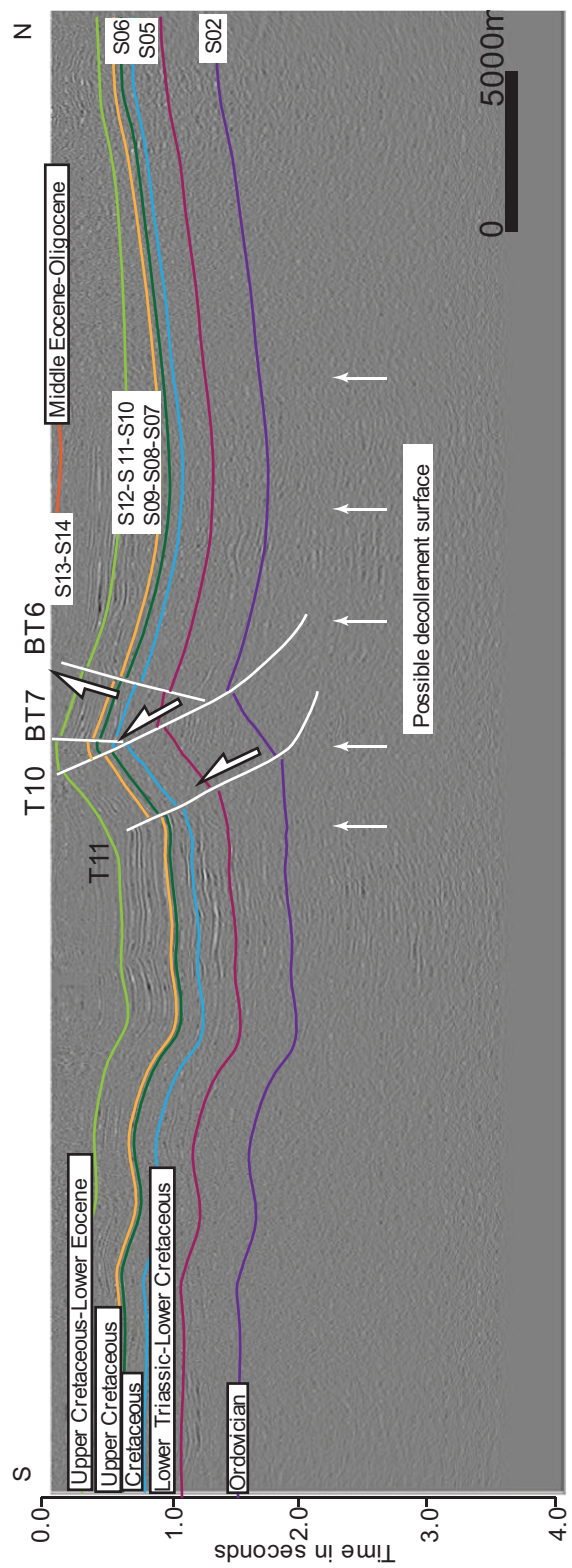


Figure 3.55 (continued)



Figure 3.56 Uninterpreted and interpreted seismic profiles with stratigraphic horizons and faults marked. The seismic line 7 is shown at vertical exaggeration x2.

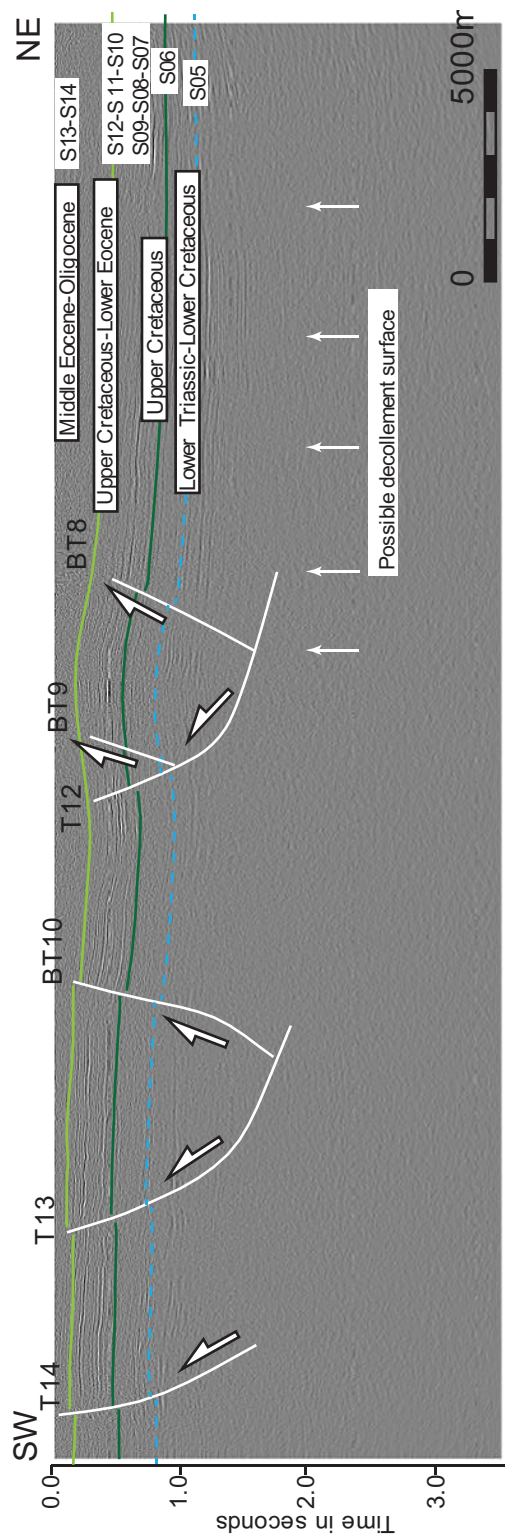


Figure 3.56 (continued)

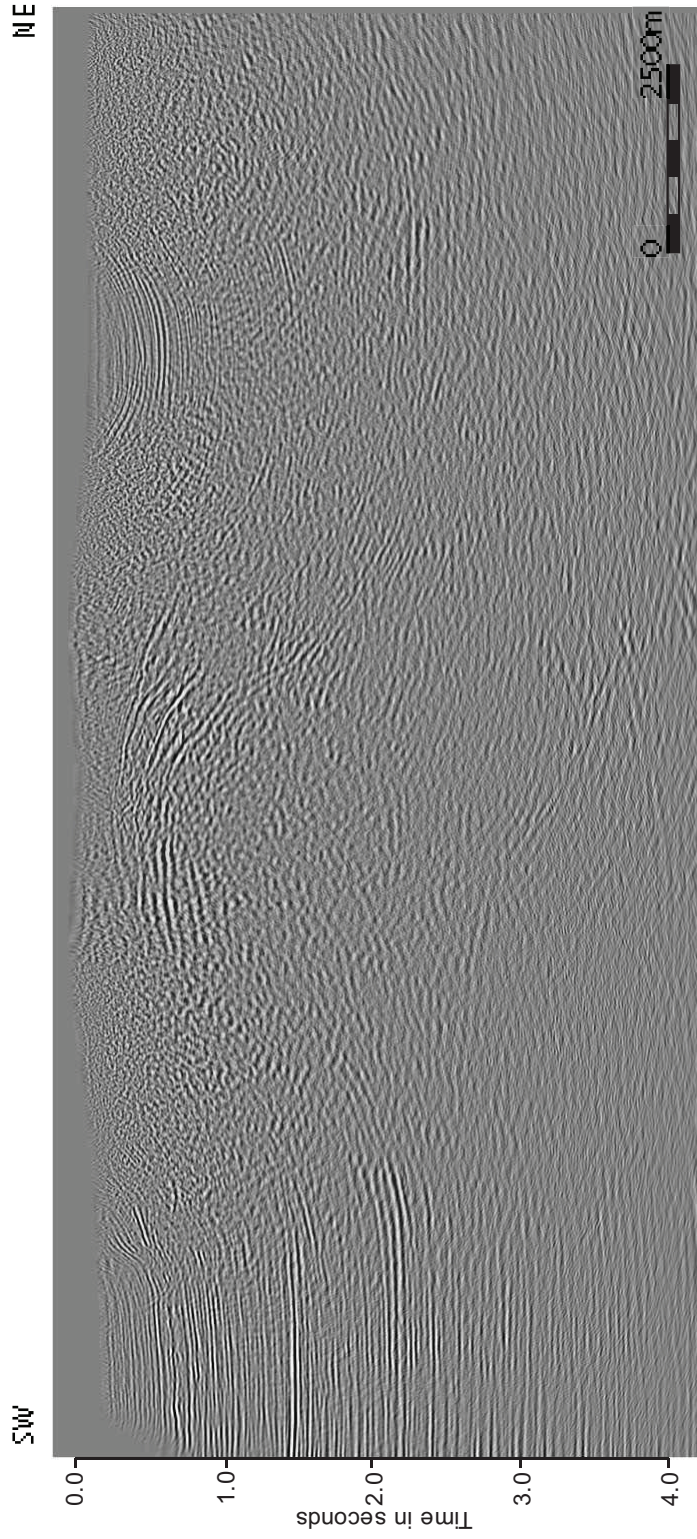


Figure 3.57 Uninterpreted and interpreted seismic profiles with stratigraphic horizons and faults marked. The seismic line 8 is shown at vertical exaggeration x2.

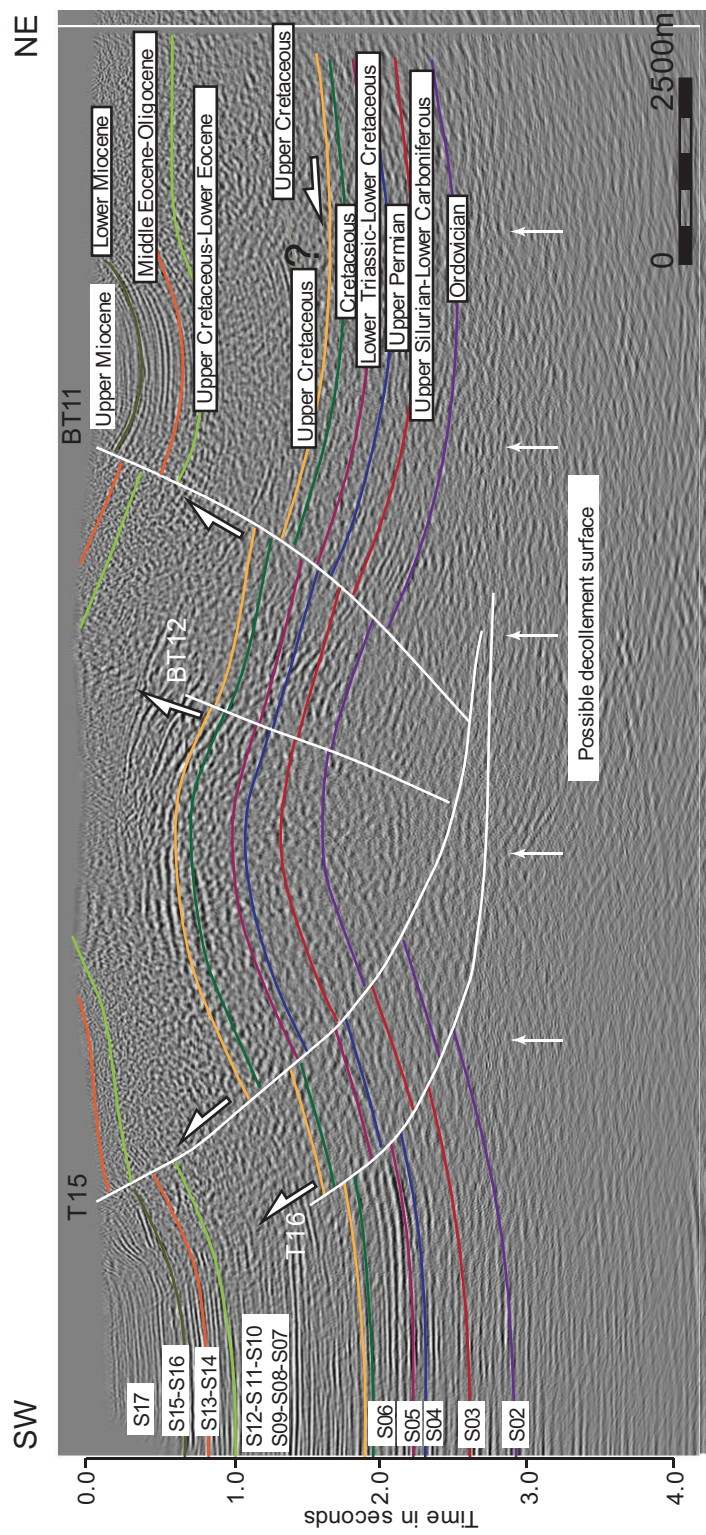


Figure 3.57 (continued)



Figure 3.58 Uninterpreted and interpreted seismic profiles with stratigraphic horizons and faults marked. The seismic line 9 is shown at vertical exaggeration x2.

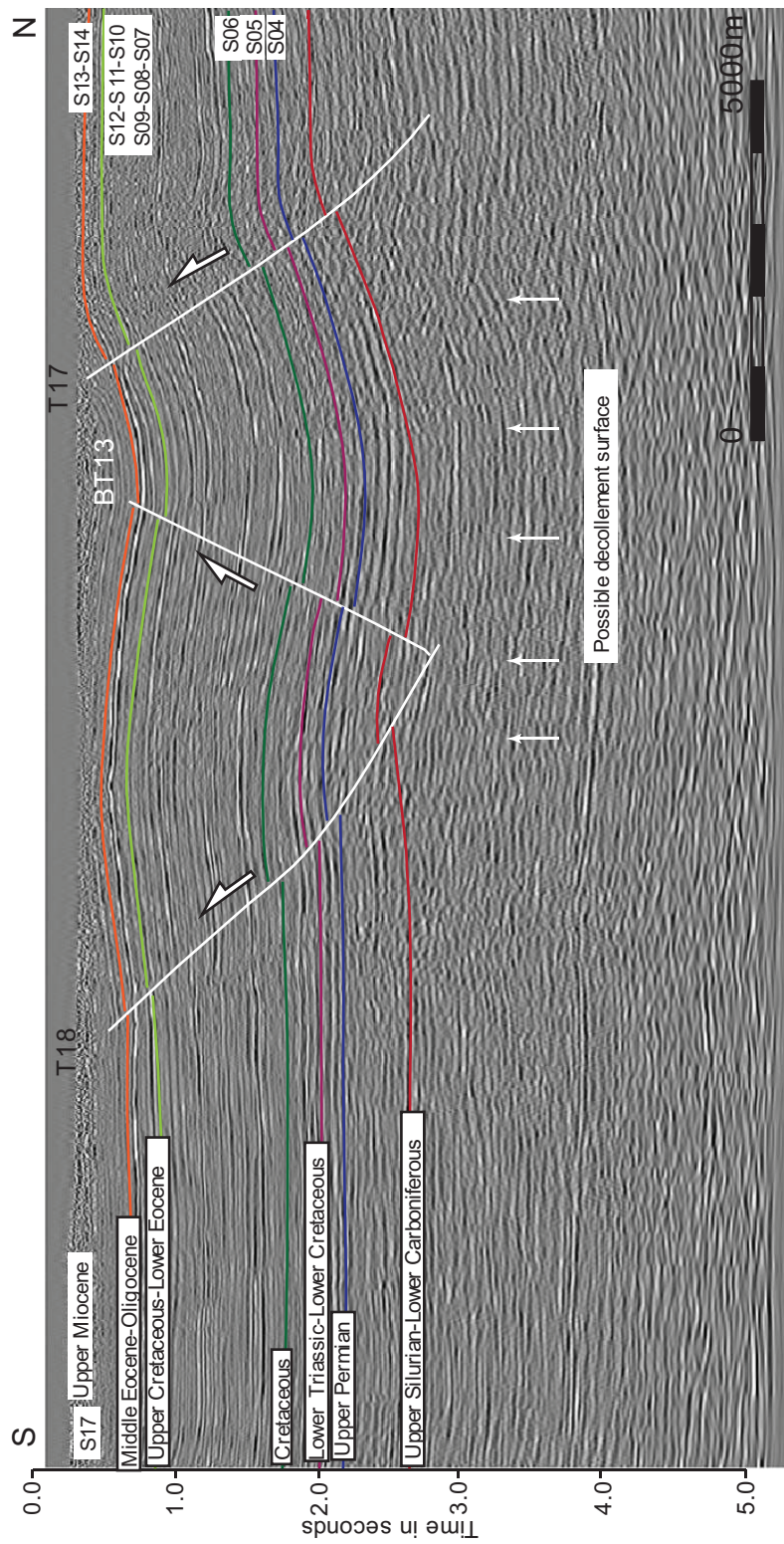


Figure 3.58 (continued)

The seismic line 10 is located at the NE of the Diyarbakir sub-area (Figure 3.59). Seismic line 10 consists of a possible detachment fault surface within the Ordovician strata. It also hosts two north-dipping thrust faults, two south-dipping, and two anticlines which can be defined as pop-up structures bounded by thrust and back thrust faults. The faults shown in the section cut the Upper Miocene units, and the thickness of the Upper Miocene sequences looks thicker on the footwall blocks. This may be related to erosion on the hanging wall deposition on the footwall block.

The seismic line 11 is located at the central W of the Batman-Siirt sub-area (Figure 3.60). Seismic line 11 consists of a possible detachment fault surface within the Ordovician units. Also, two north dipping thrust faults and two south dipping back thrust faults are observed in the section. The youngest unit displaced by the faults is Lower Miocene in age. The folds in the section are bounded by faults.

The common findings of the 2D seismic interpretation studies are summarized below;

- (i) The thickness of the units older than Miocene is almost the same at the footwall and hangingwall blocks of the faults.
- (ii) The major structures in the basin are thrust faults, back thrust faults, and folds (dominantly fault propagation folds).
- (iii) Interlimb angles of the folds get higher towards the south of the basin.
- (iv) The number of thrust faults gets higher towards the north direction in the basin
- (v) The displacement amounts on the faults get higher towards the north.
- (vi) Although the main decollement surface is not observed along the sections due to the location of the possible surface at a relative depth zone which might be defined as a zone with incomprehensible seismic data, the existence of the surface was accepted in our interpretations due to the existence of some seismic lines and some well-logs with distinguishable decollement surface.
- (vii) The vergence of the majority of the structures is due south.



Figure 3.59 Uninterpreted and interpreted seismic profiles with stratigraphic horizons and faults marked. The seismic line 10 is shown at vertical exaggeration x2.



Figure 3.59 (continued)



Figure 3.60 Uninterpreted and interpreted seismic profiles with stratigraphic horizons and faults marked. The seismic line 11 is shown at vertical exaggeration x2.

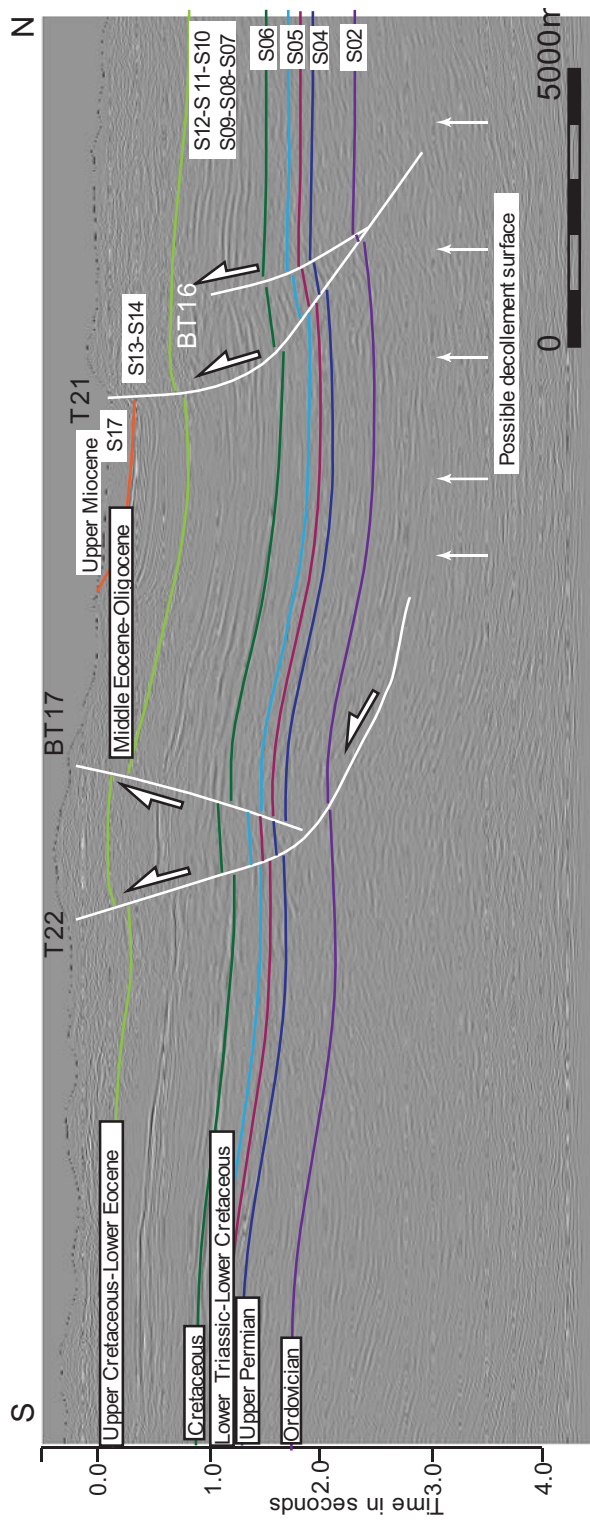


Figure 3.60 (continued)

3.5 Cross-Section Construction and Balancing

Stratigraphic classes defined in this study were used as mainstays for preparing sections since they are traceable in time and space as seismic horizons. The cross-sections and their balanced versions are given in Figures 3.61, 3.62, and 3.63. Three regional cross-sections were constructed by considering tectonic transport direction and the main trends of the major structures observed in the study area. The almost N-S sections cover Adiyaman, Diyarbakır, and Batman-Siirt sub-areas. Hence, they show changes in stratigraphical and structural trends in E-W and N-S directions (Figures 3.61, 3.62, and 3.63).

The line length balancing techniques were applied to cross-sections that are entirely constrained by well, surface, and seismic data sets in some places.

3.5.1 Balancing and Shortening Ratio Calculations

To calculate shortening ratios, two pin lines were chosen for each section, one in the southernmost of the basin when the units are relatively undisturbed (P1) and the other on the hinterland in the north (P2). Pin lines (P1 and P2) were used to calculate shortening ratios while the cross sections were restored. The amount of shortening can be expressed as a strain (e) by dividing the difference in line length by the original line length:

$$e=(L_1-L_0)/L_0$$

The ratios given here must be considered minimum shortening estimates because the sections represent some segments of the basin with relatively high amounts of surface and subsurface data and some other places with higher shortening amounts. The unfolding axes were determined by considering the hinge lines of the major folds. For each fold, the line-length unfolding procedure was followed along the section. After that, unfolded strata were connected by following an unfauling procedure. In the end, the southern pin was fixed, and the unfolded-unfaulted section

was elongated toward the north direction, which allowed us to compare the length differences between the original sections and the balanced sections, hence the calculation of shortening ratios.

The results of the balanced cross sections and calculated shortening (in m and percentages) are listed in Table 3.3, 3.4, and 3.5 and figure 3.61, 3.62, and 3.63 in Adiyaman, Diyarbakır, and Batman-Siirt sub-areas, respectively.

Table 6.1 Regional shortening results of the Adiyaman, Diyarbakır, and Batman-Siirt sub-areas.

Sub-areas	l' (deformed length, m)	l°(the initial length, m)	Shortening (m)	Shortening (%)
Total shortening (Crystalline basement+Sedimentary units-Adiyaman)	185600	274200	88600	32,31
Shortening in sedimentary units (Adiyaman)	184250	197111	12861	6,53
Total shortening (Crystalline basement+Sedimentary units-Diyarbakır)	181421	224316	42895	19,12
Shortening in sedimentary units (Diyarbakır)	172843	183643	10800	5,88
Total shortening (Crystalline basement+Sedimentary units-Batman-Siirt)	145144	174068	28924	16,62
Shortening in sedimentary units (Batman-Siirt)	136900	150580	13680	9,09

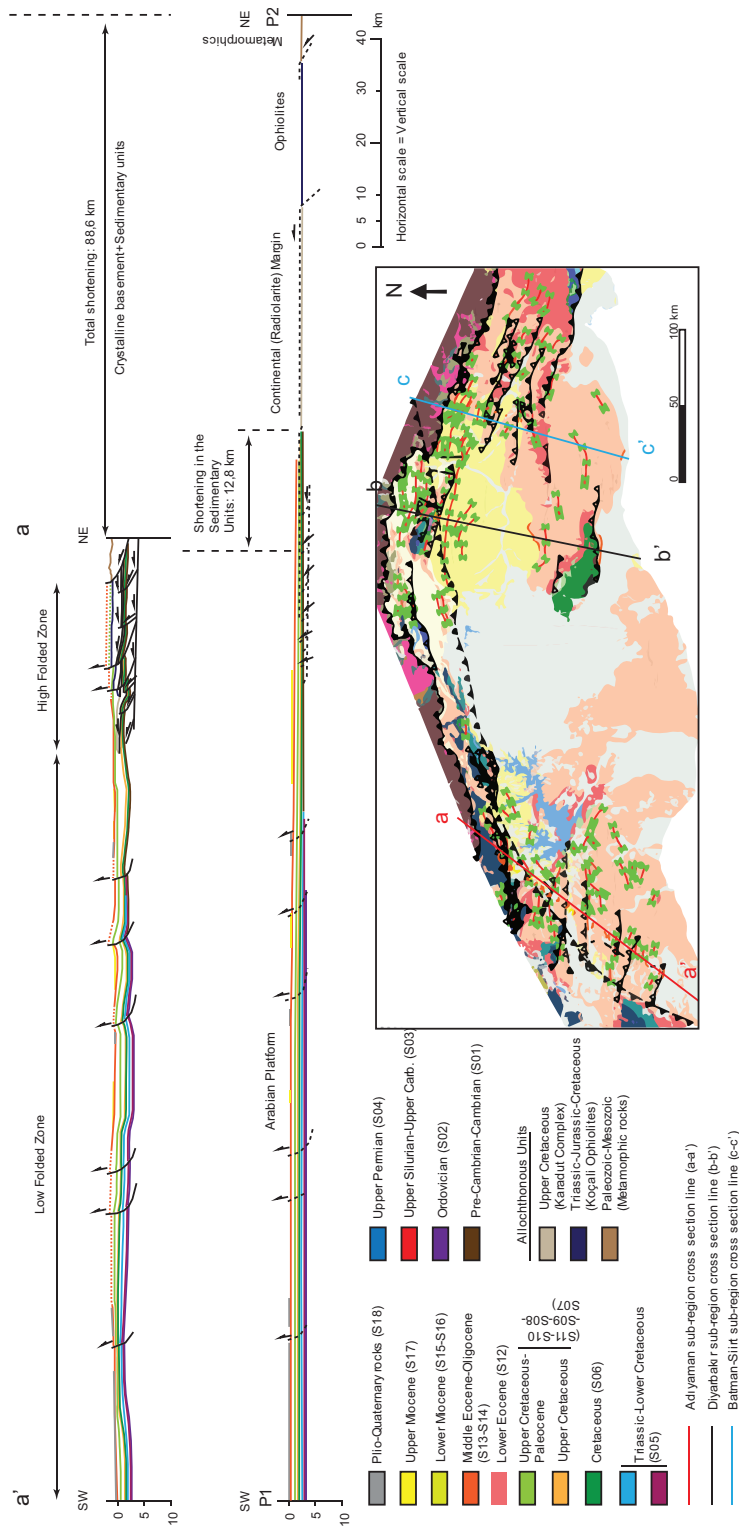


Figure 3.61 Cross and balanced cross-section with estimates of the minimum shortening and thrust geometries in the Adiyaman sub-area.

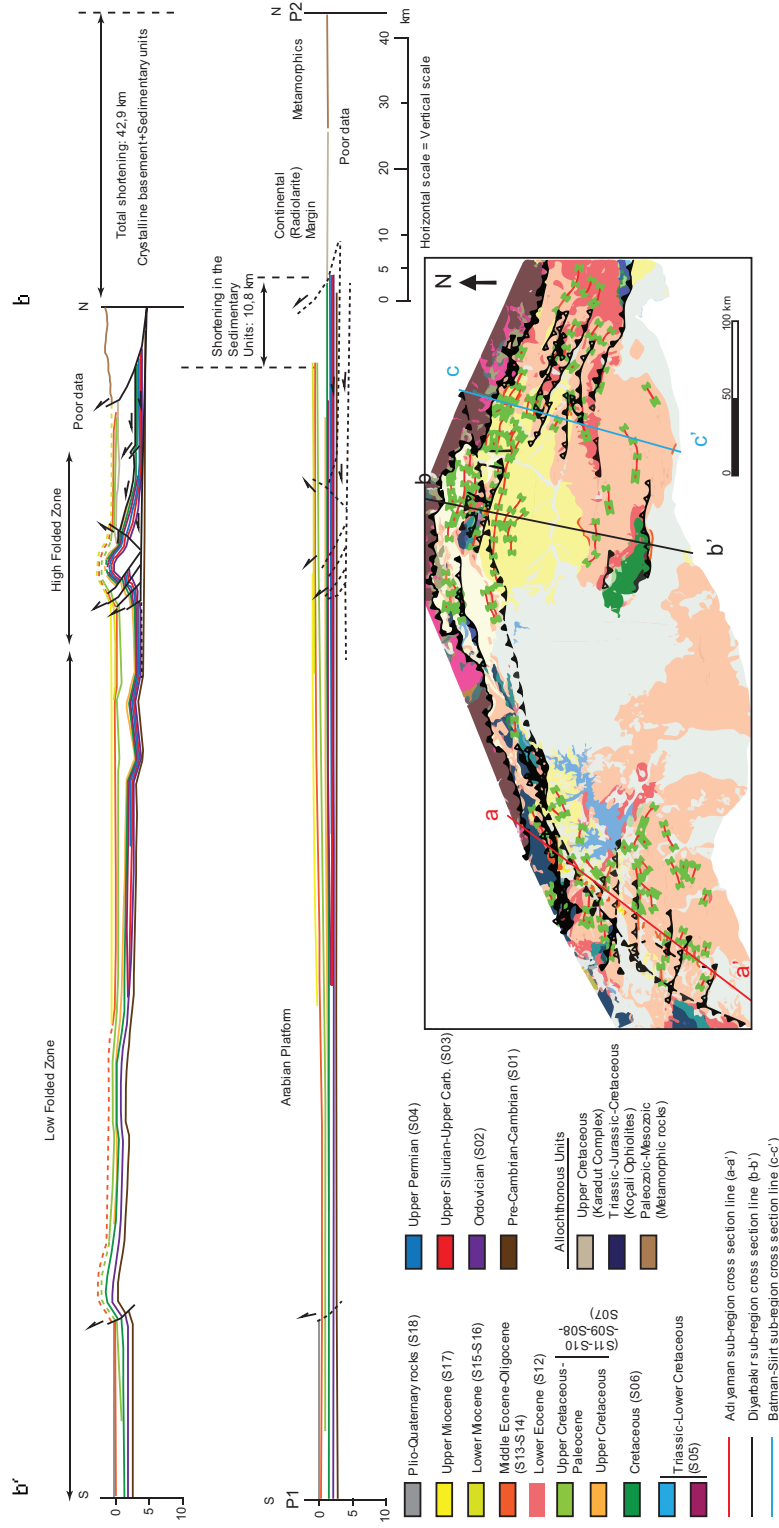


Figure 3.62 Cross and balanced cross-section with estimates of the minimum shortening and thrust geometries in the Diyarbakir sub-area.

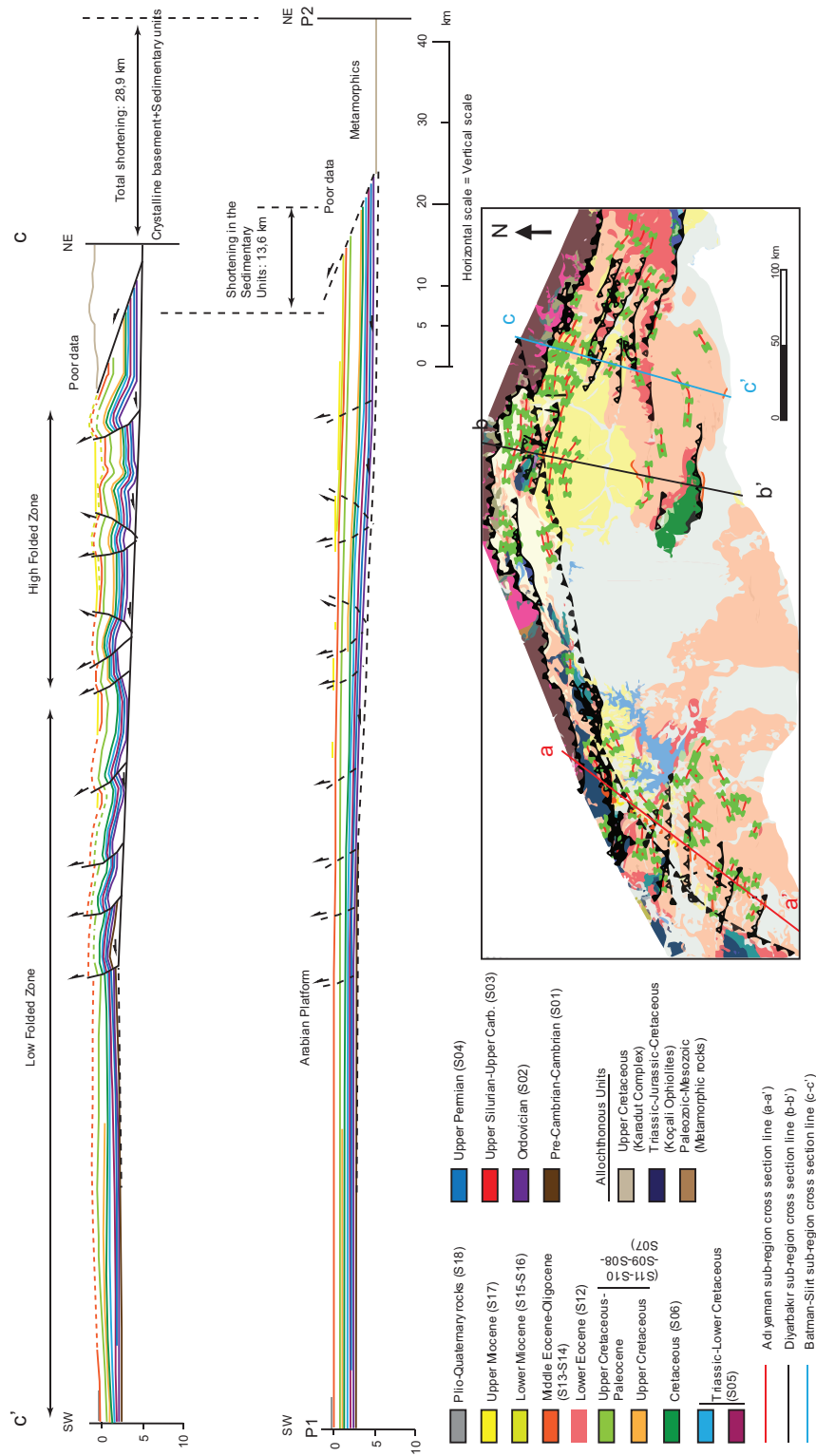


Figure 3.63 Cross and balanced cross-section with estimates of the minimum shortening and thrust geometries in the Batman-Siirt sub-area.

The shortening ratio calculations indicate that;

- a) The maximum total shortening ratio (32,31%) is calculated west of the basin (Adiyaman region).
- b) The minimum total shortening ratio (16,62%) is calculated eastern side of the basin (Batman-Siirt region)
- c) The results of the sedimentary basin of shortening ratio are calculated at 6,53%, 5,88%, and 9,09% in Adiyaman, Diyarbakir, and Batman-Siirt sub-areas, respectively.
- d) Total shortening amounts decrease towards E of the basin.
- e) Shortening in sedimentary units is minimum in the center part of the basin.
- f) The balanced cross sections illustrate that the structure of the fold and thrust belts is rather complex towards the north along the sections.

CHAPTER 4

DISCUSSION

4.1 Structural Evolution of the SE Anatolian Basin

Pre-Cambrian to Permian units of the basin represent the core sequences of the basin and their structural records are not well-protected in their limited outcrops due to overprints of post-depositional deformation phases. The units of the Triassic-Jurassic time interval are interpreted as rift sequences in various studies (e.g., Robertson et al., 2007; Barrier et al., 2014). Here, we also noted some E-W trending normal faults terminating within these units (Figure 3.22 and Figure 3.3), which indicates pre-Cretaceous extension in the region. The Early Cretaceous units are represented by only shallow marine carbonates in the region and are attributed to deposits of the southerly located Arabian passive margin. Although these units are cut by some normal, strike-slip and, reverse faults (Figure 3.50 to 3.60), the age of the faults is younger than the deposition time. The normal faults cutting these units are located in the central south of the basin, and they do not cut younger units, whereas reverse faults are concentrated in the north and cut younger units. This may imply that the normal faults are associated with the flexure on the downgoing plate during the subduction/collision term.

The oldest unit is unconformably covering pre-Cretaceous sequences (mainly Passive margin units of the Arabian plate). Upper Campanian-Lower Maastrichtien Kastel formation is used as a decollement surface by Karadut Complex units (Figure 3.31, 3.32, 3.33, 3.35, and 3.36), which are described as pelagic sediments directly deposited on ophiolitic sequences. It is also tectonically overlain by ophiolites in the region. This association suggests the commencement of an accretionary prism growth in the region.

The Upper Cretaceous to Oligocene units are displaced by post-Oligocene faults (Figure 3.50 to 3.60), and the folds affecting these units show syn-sedimentary character for only post-Oligocene time interval (Figures 3.44, 3.45, and 3.46). This implies that the Upper Cretaceous to Oligocene units do not have structural syn-sedimentary structural records. The faults displacing post-Oligocene units are mainly in reverse (towards south) or thrust (towards north) character. Also, their trends are almost E-W at the center, NE-SW at the west, and NW-SE at the east. This trend is parallel to the northern rim of the basin, and a similar trend is valid for the folds close to the northern margin of the basin. However, the folds towards the south are almost E-W directed. The concentration of thrust/reverse faults is higher in the north and gets lower towards the south. Similarly, folds are tighter at the north and become open towards the south with northerly dipping axial planes. These observations imply intense deformation at the north and southward tectonic transport (vergence). In addition to these reverse/thrust faults, NW-SE and NE-SW trending strike-slip faults displacing Pliocene and younger units (Figure 3.29) and N-S elongated tension fractures/normal faults on Plio-Quaternary volcanic (Figure 3.1 and 3.2) also exist in the region. Although the traces of thrust/reverse faults are not directly observed on post-Miocene units in the study area, the angular relationships between reverse/thrust faults, folds, strike-slip faults, and extensional structures indicate almost N-S directed compressional setting for the region since at least Lower Miocene (Figure 3.1f, 3.49 and Table 3.2).

The post-Oligocene faults responsible for the shortening of the basin determined in seismic lines do not penetrate deeper levels and are only observed on a decollement surface. This indicates thin-skinned deformation and shortening of the basin. The shortening ratios calculated by N-S elongated balanced sections indicate a maximum of 32% and a minimum of 16% ratios for the basin from W to E, but these values are only somewhat reliable since they consider the southward movement of the crystalline basement on sedimentary units. The modeling of such movement is solely controlled by the existence of well data from the north of the main boundary thrust (BZSS), but they are not available for all sections with the same numbers. Therefore,

using shortening ratios from only sedimentary sequences in interpretations is more reliable. In this sense, all ratios are less than 10% (Figure 3.61, 3.62, 3.63, and Table 3.3), and the northerly located fault propagation folds (Figure 3.51 to 3.60) together with thrust/reverse fault are responsible for the main shortenings in the basin. These low rates can be explained by a relatively short-term compressional deformation phase in post-Oligocene to a recent compressional setting. In this regard, these rates together, with northerly concentrated post-Oligocene deformation, may indicate a tectonically quiet period for the pre-Miocene and an active period for post-Oligocene time intervals. Such a division might be attributed to the initiation of continental collision in the region.

4.2 Stratigraphic (Framework) Characteristics of the SE Anatolian Basin

The Paleozoic sedimentation is characterized by continental-shallow- and relatively deep marine units (S01, S02, S03, S04) deposited on the Arabian platform. These units are thought of as the core sequences of the Arabian Platform and they have some unconformities between each other which might be associated with regional sea-level changes and/or Hercynian orogeny (c.f Sharland et al., 2001). These units are penetrated by almost all wells located in the south of the basin. Additionally, they are found as isolated outcrops at Highs such as Hazro High and also, and they are penetrated by some wells (Figure 3.31, 3.32, 3.33, 3.35, 3.36) after allochthonous (ophiolites - Koçali and pelagic sediments-Karadut Complex) units at the north of the main boundary thrust (BZSS). This indicates the amalgamation of Arabian Plate origin units with the Anatolides within the suture zone.

Triassic-Early Cretaceous (>2000m) shallow marine carbonate sequences (S05 and base of S06) of the basin are thought of as the products of the rifting and drifting stage of the Arabian Platform. The age and facies equivalents of these units are found within the Bitlis massif as metamorphic slices, and they are defined as the units with the youngest protolith age in the massif (Oberhanslı et al., 2010). The Arabian plate origin of the Bitlis Massif is discussed in various studies (e.g., Oberhanslı et al.,

2010;2012;2014 and Çetinkaplan et al., 2016). According to these studies, the Bitlis massif is separated from the main Arabian land and is defined as a microcontinent (Figure 4.1). In this regard, these units should be deposited between the southerly-located Arabian Platform and the northerly-located Bitlis Micro-Continent. Our data indicate (i) thicker deposition at the southwest, and southeast and thinner deposition in the north and the central areas of the basin (Figure 3.22), and (ii) continental continuation of these units at north and south (Figure 3.31 to 3,36) prove shallow marine deposition between two passive margins during rifting and drifting stages (Figure 4.1a).

Upper Cretaceous units of the basin (Top of S06, S07, S08, and partly bottoms of S09, S10, and S11) represent the closure stage of the Southern Neotethys Ocean. The total thickness of these units is around 4000m (Figures 3.23, 3.24, and 3.25). Pelagic sequences of radiolarite bearing Karadut Complex units and Koçali Ophiolites thrust over Upper Cretaceous deep marine units of S07 stratigraphic class (the Kastel Formation) at the north of the study area (Figure 3.31, 3.32, 3.33, 3.35 and 3.36). However, shallow marine (top of S06) and continental (S08) classes are not thrust over. This may imply the initiation of an accretionary prism growth in the region where deep marine units are overlain by Karadut Complex/Koçali Ophiolites and shallow marine-continental (S08 and S09) at the top of the flanks of the growing prism (Figure 4.1b). The continental and shallow marine deposits of these classes are unconformably covered by the units of the younger classes represented by continental (S11) and shallow marine (top of S09) deposits. However, an unconformity is not observed between the deep marine units of the older and the younger classes. This may indicate a “unconformities and their correlative conformities” situation in the basin associated with the sea-level changes and/or the growth of accretionary prism above sea level. The southward movement of the depozone during the deposition of younger classes (Figures 3.24 and 3.26) also indicates southward growth for the prism. On the other hand, the inexistence of tectonic contact between the deep marine units of the younger class (S10) and the ophiolites points out the southernmost limit of the prism.

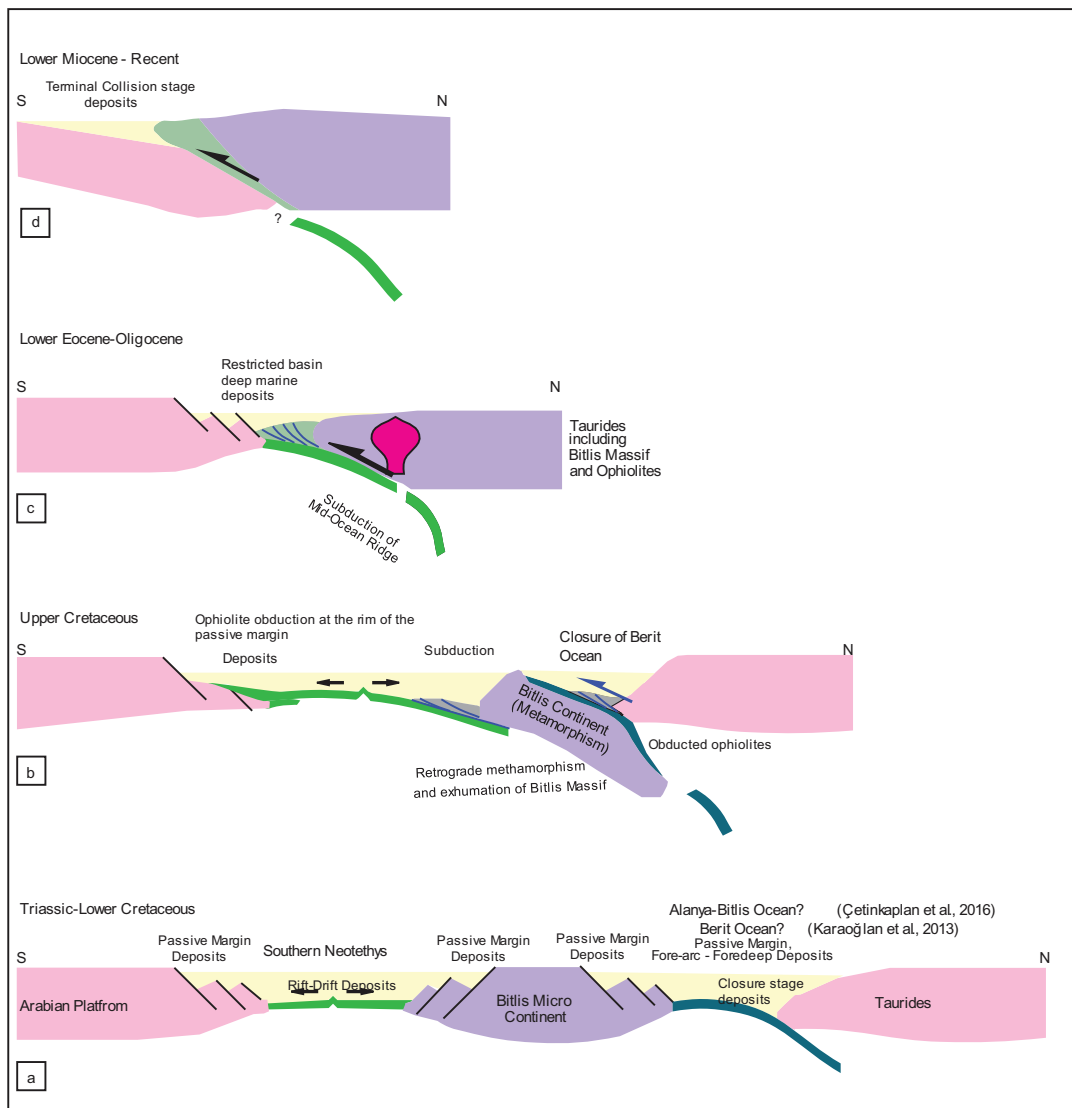


Figure 4.1 Conceptual model showing the tectonic position of the SE Anatolian Basin from Triassic to recent.

The Paleocene continental (top of S11), shallow marine (top of S9), and deep marine (top of S10) are exposed at the north, center, and south of the basin, respectively. This association is also valid for the Upper Cretaceous units of the basin. This implies similar deposition history for these units related to the position and growth of the accretionary prism.

The Lower Eocene continental deposits of the basin cover almost all of southeastern Anatolian, with thicker deposits in the north and thinner deposits in the south (Figure

3.27). Such a large continental deposition might be explained by climate change and/or tectonic effects. However, the literature has no defined thermal event for the Lower Eocene time interval. This suggests tectonic effects on the regional uplift of the region. For the study area, such a regional and rapid uplift might be supported by continental collision; however, the younger marine deposition (S13 to S16) in the basin and collision-related lower Miocene uplift ages of the region (Okay et al., 2010) does not fit this scenario. On the other hand, the subduction of the mid-ocean ridge may explain the abrupt uplift in the region (Figure 4.1c). In this scenario, younger and less-dense oceanic crust is forced to subduct, and almost newly formed subduction is initiated similar to the case of induced subduction initiation (c.f. Zhou and Wada, 2021). In such cases, regional uplift occurs and continental deposition may dominate large areas. The possibility of the subduction of the mid-ocean ridge is also mentioned in the literature. For example, Kaymakçı et al. (2010) indicate that mid-ocean ridge subduction might be responsible for the Eocene-Oligocene compressional tectonics in SE Anatolian. Also, Karaoğlan et al. (2013) suggest mid-ocean ridge subduction for the region and associate it with the high-temperature requirement of the ultra HT/HP metamorphism of Berit Ophiolites during the Lower Eocene.

The Middle Eocene-Oligocene shallow marine (S13) and deep marine (S14) units unconformably cover Lower Eocene continental deposits and older units in the region. The depozone of these units is located at the southern margin of the basin (Figure 3.28), and this location is further south of the depozones of older units. Although these units cover almost all SE Anatolian basin, the shallow marine deposits dominate the sedimentation in the region since they cover larger areas (Figure 3.17) and have higher thicknesses with respect to their deep marine equivalents. This may indicate a long-lived subsidence stage of the region before the subduction of older and denser oceanic crust after mid-ocean ridge subduction.

The Lower Miocene shallow marine (S15) and deep marine (S16) units are only found along the northern margin of the basin, and they unconformably cover older units. The shallow marine deposits are largely exposed in the south with respect to

deep marine deposits; however, they are also found as isolated outcrops along the northerly located main boundary thrust fault (Figure 3.18). Also, the thickness of the deep and shallow marine deposits gets thinner towards the south which indicates a wedge-shaped geometry for the depozone. The depozone of these units is located north of older stratigraphic classes (Figure 3.29). This abrupt shift of depozone, wedge-shaped geometry, and facies distribution pattern (deep marine deposits at the center) indicate foreland basin deposition, hence the commencement of continental collision in the region (Figure 4.1d). These findings are also compatible with the findings of the structural evolution of the basin indicating that shortening started during Early Miocene in the basin.

The Upper Miocene (S17) to recent continental clastics covers all basin units and shows wedge-shaped geometry (Figure 3.30). This indicates the still-active development of the foreland basin.

Evolution of SE Anatolian Basin Regarding Evolution of Southern Neotethys Ocean

Understanding the opening and closure history of the southern Neotethys Ocean requires integrating the data from the Paleozoic to Quaternary sedimentary units of the SE basin and crystalline rocks associated with the evolution of the basin.

Geographically, the ocean is located between Tauride-Anatolide Block (TAB) north and the Arabian platform south (Figure 1.1). However, some studies indicate that the northernmost tip of the Arabian Platform was amalgamated to the TAB, and they are observed as almost E-W trending metamorphic rocks (Bitlis Massif) (Oberhansli et al., 2010;2012; Bröcker et al., 2013; Davoudian et al., 2016). In this regard, the ocean might be considered as an ocean developed by rifting of the Arabian Plate and terminated between the Arabian mainland and TAB, including Arabian Platform origin metamorphic slices. The metamorphism of these slices is attributed to a collision event that occurred during the Upper Cretaceous between the northernmost tip of the Arabian Platform (Bitlis Micro-Continent) and Anatolides (or South Armenian Block) (Oberhansli et al.; 2010; 2012; Karaoğlan et al., 2013; 2016).

During and before this collision event, the southern margin of the Bitlis Micro-Continent was the northern margin of the Southern Neotethys Ocean (Figures 4.1a and b). The relevant time interval is represented by continental, shallow marine, and partly deep marine sedimentation in the ocean. All of these units are interpreted as passive margin deposits in this study since they do not have signs of active margin tectonics. On the other hand, the existence of Late Cretaceous to Lower Miocene arc-related magmatic bodies within and north of Bitlis Massif (Elmas and Yılmaz, 2010; Karaoğlan et al., 2013; Babazadeh et al., 2017; Açlan and Duruk, 2018) indicates a subduction event at the south of the massif. The response of this subduction event is observed in the basin as Upper Cretaceous to Oligocene age sediments associated with the growth of an accretionary prism. Lastly, Lower Miocene continental collision along Bitlis-Zagros Suture Zone is proposed by various studies (e.g Şengör et al., 1984; Yılmaz, 1993; Robertson et al., 2007; Okay et al., 2010; Schildgen et al., 2014; Yılmaz; 2019; Yılmaz et al., 2022). Our findings support this time interval for the collision event. They do not support the other subduction/collision models proposed in the literature, such as (i) subduction/collision event ended in the late Cretaceous (Hall, 1974; Beyarslan and Bingöl, 2000; Sar et al., 2019; Ertürk et al., 2018; Ertürk et al., 2022), (ii) subduction/collision model indicating Eocene for the collision (Jolivet and Facenna, 2000; Argard et al., 2005; Allen and Armstrong, 2008), (iii) collision model suggesting Eocene soft and Early Miocene hard collision events (Robertson et al., 2012; Ballato et al., 2017; Darin et al., 2018).

CHAPTER 5

CONCLUSION

The study has reached the following conclusions.

- A. Stratigraphical and Sedimentological findings have revealed that;
- a) Pre-Cambrian to Pliocene deposits of the SE Anatolian Basin grouped into four based on regional tectonic settings. From these four groups, nineteen classes are defined by considering contemporaneous sedimentation in continental to deep marine environments.
 - b) The Pre-Cambrian-Permian deposits represent the core sequences of the Arabian platform as represented by continental, shallow marine, and relatively deeper marine deposits.
 - c) Triassic-Lower Cretaceous sequences products of the rift-drift stage of the Arabian Platform and deposited on passive margin as represented shallow marine and rarely continental clastics.
 - d) Cretaceous sequences represent the initial subduction stage of the southern Neotethys ocean and ophiolite obduction. This class represents shallow marine and deep marine deposits. After the emplacement of allochthonous units, continental clastics and shallow marine units were deposited on and in front of the accretionary prism while deep marine sediments acted as decollement level for the accretionary prism.
 - e) Campanian-Tertiary sequences are represented by continental, shallow, and deep marine sediments. The Paleocene sequence has similar deposition history for Upper Cretaceous sedimentary units. The Lower Eocene sediments are associated with a regional uplift event which might be related to mid-ocean ridge subduction. Middle Eocene-Oligocene shallow marine and deep marine deposits are widespread, and depozones are located at the southern margin of the basin. Lower Miocene sequences are represented by

foreland basin deposits with shallow marine and deep marine units located along the northern margin of the basin. The thickness of these units gets thinner towards the south, which indicates a wedge-shaped geometry for the depozone. Upper Miocene continental clastics show wedge-shaped geometry, which still shows the active development of the foreland basin and covers all units in the basin.

- f) The dominant sediment transportation direction is approximately due south in the basin after subduction initiation in the region.
- g) The geometries of post-Cretaceous units are wedge-shaped. Their thicknesses decrease from north to south. This northward thickening of the basin fill units indicates rapid subsidence and the creation of accommodation space ahead of the advancing thrust front.

B. Structural and Balanced Section studies have revealed that;

- a. The maximum total shortening ratio (Basement Crystalline+Sedimentary units) is 32,31% at the west, while the minimum total shortening ratio (Basement Crystalline+Sedimentary units) is 16,62% at the east. The maximum shortening ratio of sedimentary units is 9,09% at the east and the minimum shortening ratio of sedimentary units is 5,88% at the center. These values suggest that deformation is close to the northern margin of the basin and related to Miocene thrust activity.
- b. The structure of the fold and thrust belts is complicated towards the north. Along the rim, folds and thrust/reverse faults have similar trending NE-SW, E-W, and NW-SE oriented at the west, central and east, respectively.
- c. The western portion of the basin has NW-SE right-lateral strike-slip faults and NE-SE left strike-slip faults.
- d. Fold and fault analysis show that the main tectonic transport is about N to S oriented.
- e. Length-weighted rose diagram results indicate that post-Oligocene normal, strike-slip, and thrust faults/folds are approximately trending in N-S, NE-

SW/NW-SE, and E-W directions, respectively. These indicate N-S-directed compression for the region.

- f. Paleostress inversion studies show that all measurement sites are represented by almost vertical σ_3 and horizontal σ_1 directions. The sites at the western, central, and eastern portions of the basin are represented by NW-SE, N-S, and NE-SW directed compressional settings.
- g. In the northern portions of the basin, close to the rim, local and regional syntectonic unconformities are present in the Lower and Upper Miocene basin fill, which is associated with the continental collision event in the region.

C. Seismic Interpretation Studies have revealed that;

- a. The major structures in the study area are thrust faults, back thrust and folds (dominantly fault propagation folds), and possible decollement surface.
- b. Seismic sections and folds analyses show that the interlimb angle increases from north to south away from the frontal thrust fault. These are associated with the continued propagation of deformation southward from the collision zone.
- c. The developments of the folds are generally related to thrust or reverse faults except for transpressional strike-slip folds in the interior of the basin.
- d. Thrust-related anticlines are potential structural traps for hydrocarbon exploration.
- e. The number of thrust faults (predominantly north dipping) and the displacement amounts on the faults get higher towards the north.
- f. The structural style in the study area is expressed by south-verging thin-skinned deformation processes, including fault propagation fold and a decollement within Paleozoic weak zones (possibly Ordovician-Silurian shales).

D. Integration of the results of the study has revealed that;

- a. The Paleozoic time interval is represented by generally shallow marine and rarely continental and relatively deep marine units of the core sequences of the Arabian Platform.
- b. Shallow marine thick carbonates and evaporites were deposited on the passive margin of the northern Arabian platform and southern Bitlis Micro-Continent during the Triassic to Lower Cretaceous.
- c. Late Cretaceous phase attributed to initial subduction and closure of Neotethys Ocean which involves ophiolite obduction phase and growth of an accretionary prism. This is the first major tectonic phase of the basin, suggesting the development of an active margin in the region.
- d. An abrupt regional uplift during Lower Eocene gives way to the deposition of red clastic on almost the whole basin possibly related to the subduction of the mid-ocean ridge.
- e. The commencement of foreland basin deposition at the Lower Miocene marks the continental collision between the Anatolides and the Arabian Platform.

REFERENCES

- Açlan, M., Duruk, H.İ., 2018. Geochemistry, zircon U-Pb geochronology, and tectonic setting of the Taşlıçay granitoids, Eastern Anatolia, Turkey. *Arab. J. Geosci.* 11, 336.
- Agard P, Omrani J, Jolivet L, Lepvrier C, Kachrillo N (2005) Metamorphic evolution of the Sanandaj–Sirjan zone (North Central Zagros Iran)
- Akıncı, A.C., Robertson, A.H.F. & Ünlügenç, U.C. 2016. Late Cretaceous-Cenozoic subduction-collision history of the Southern Neotethys: new evidence from the Çağlayançerit area, SE Turkey. *Int J Earth Sci (Geol Rundsch)* 105, 315-337.
- Aktas, G., and Robertson, A.H.F. 1984. The Maden complex SE Turkey: evolution of a Neotethyan active margin. In *The geological evolution of the eastern Mediterranean*. Edited by J.H. Dixon and A.H.F. Robertson. Geological Society, London, Special Publications, Vol. 17, 375–402.
- Ala, M., and Moss, B. 1979. Comparative petroleum geology of SE Turkey and NE Syria. *Journal of Petroleum Geology*. 1.3-27.
- Alastair H. F. Robertson, Osman Parlak, Timur Ustaömer; Overview of the Palaeozoic–Neogene evolution of Neotethys in the Eastern Mediterranean region (southern Turkey, Cyprus, Syria). *Petroleum Geoscience* 2012; 18 (4): 381–404
- Allen, M.B., and Armstrong, H.A., 2008, Arabia-Eurasia collision and the forcing of mid-Cenozoic global cooling: Palaeogeography, Palaeoclimatology, Palaeoecology, 265, 52–58.
- Allmendinger, R., 2021. <https://www.rickallmendinger.net/stereonet>
- Anadon, P., Cabrera, L., Columbo, F., Marzo, M., and Riba, O. (1986) Syntectonic intraformational unconformities in alluvial fan deposits, eastern Ebro Basin margins (NE Spain). In: Allen, P.A. and Homewood, P. (eds) *Foreland Basins*. International Association Sedimentologists Special Publication 8, 259-271.
- Angelier, J., 1984. Tectonic analysis of fault slip data sets. *J. Geophys. Res.* 89, 5835-5848
- Babazadeh, S., Ghorbani, M. R., Bröcker, M., D'Antonio, M., Cottle, J., Gebbing, T., ... Ahmadi, P. (2017). Late Oligocene-Miocene mantle upwelling and interaction inferred from mantle signatures in gabbroic to granitic rocks from the Urumieh-Dokhtar arc, south Ardestan, Iran. *International Geology Review*, 59, 1590–1608.

- Ballato, P., Cifelli, F., Heidarzadeh, G., Ghassemi, M.R., Wickert, A.D., Hassanzadeh, J., Dupont-Nivet, G., Balling, P., Sudo, M., Zeilinger, G., Schmitt, A.K., Mattei, M., & Strecker, M.R. (2017). Tectono-sedimentary evolution of the northern Iranian Plateau: insights from middle-late Miocene foreland-basin deposits. *Basin Research*, 29.
- Barrier, E., Machlour, L. and Blaizot, M., 2014. Petroleum systems of Syria, in L. Marlow, C. Kendall and L. Yose eds, Petroleum systems of the Tethyan region. American Association of Petroleum Geoscience Memoir, 106: 335-378.
- Beyarslan M. and Bingöl, A.F., 2000. Petrology of a supra-subduction zone ophiolite (Kömürhan-Elazığ -Turkey). *Canadian Journal of Earth Sciences*. 37, 1411-1424.
- Beyarslan M., Bingöl A.F. Petrology of a supra-subduction zone ophiolite (Elazığ, Turkey) (2000) *Canadian Journal of Earth Sciences*, 37 (10), 1411 - 1424
- Beyarslan, M., Bingöl, A.F., 1991. Petrographical features of the İspendere ophiolite, Kale - Malatya, Türkiye. *Yerbilimleri (Geosound)* 19
- Beyarslan, M., Bingöl, A.F., 1996. Kömürhan Ofiyolit Biriminin Petrografik ve Petrolojik İncelenmesi. *F. Ü. Fen ve Müh. Bilimleri Dergisi* 8
- Bingöl, A.F., 1984. Geology of the Elazığ area in the Eastern Taurus region, In: Tekeli, O., Göncüoğlu, M.C. (Eds.), *Geology of The Taurus Belt*. Mineral Research and Expolaration Instutute of Turkey (MTA), Ankara, 209-216.
- Bingöl, A.F., Beyarslan, M., Lin, YC. et al. Geochronological and geochemical constraints on the origin of the Southeast Anatolian ophiolites, Turkey. *Arab J Geosci* 11, 569 (2018). <https://doi.org/10.1007/s12517-018-3880-0>
- Bozdoğan, N., O. Baycelebi and R. Willink 1987. Guneydogu Anadolu Hazro bölgesinde Paleozoyik stratigrafisi ve petrol üretkenligi: Türkiye 7. Petrol Kongresi, p. 117-130.
- Bröcker, M., Baldwin, S., & Arkudas, R. (2013). The geological significance of 40Ar/39Ar and Rb–Sr white mica ages from Syros and Sifnos, Greece: a record of continuous (re)crystallization during exhumation? *Journal of Metamorphic Geology*, 31, 629–646.
- Çaglayan M.A., R. N. Inal, M. Şengün and A. Yurtsever 1984. Structural setting of Bitlis Massif: in Tekeli, O. and Goncuoglu C. (Eds.), *International Symposium on the Geology of Taurus Belt*, The Geological Society of Turkey. P. 129-139.
- Cater, J. M. L., & Tunbridge, I. P. (1992). Palaeozoic tectonic history of SE Turkey. *Journal of Petroleum Geology*, 15 (1), 35-50.

- Cebecioglu, K. and M. Köylüoğlu 1986. Conflicting chronostratigraphic inferences on Conodont and Foraminifera occurrent in the Belek Formation: Çukurova Üniversitesi Muhendislik Fakültesi Dergisi. Seri A. C.3, S.1, p. 35-48.
- Dahlstrom, C.D.A., 1969, Balanced cross sections. *Canadian Journal of Earth Sciences*, v. 6, 743–757.
- Darin M.H., Umhoefer P.J., Thomson S.N., 2018. Rapid Late Eocene Exhumation of the Sivas Basin (Central Anatolia) Driven by Initial Arabia-Eurasia Collision. *Tectonics*, doi: 10.1029/2017TC004954
- Davoudian, A. R., Genser, J., Neubauer, F., & Shabanian, N. (2016). $^{40}\text{Ar}/^{39}\text{Ar}$ mineral ages of eclogites from North Shahrekord in the Sanandaj–Sirjan Zone, Iran: implications for the tectonic evolution of Zagros orogen. *Gondwana Research*, 37, 216-240.
- Dean, W. T., Monod, O. & Günay, Y. 1986. Lower Palaeozoic stratigraphy in the southern and central Amanos Mountains, south central Turkey. *Geological Magazine* 123, 215–26.
- Delvaux, D., Moeys, R., Stapel, G., Petit, C., Levi, K., Miroshnichenko, A., Ruzhich, V., & San'kov, V. (1997). Paleostress reconstructions and geodynamics of the Baikal region, Central Asia, Part 2. Cenozoic rifting. *Tectonophysics*, 282(1-4), 1-38.
- Dilek, Y., and Flower, M.F.J. 2003. Arc-trench rollback and fore arc accretion: 2. A model template for ophiolites in Albania, Cyprus, and Oman. Special Publication. In *Ophiolites in Earth History*. 218. Edited by Y. Dilek and P.T. Robinson. Geological Society of London, 43–68.
- Dilek, Y., Thy, P., Moores, E.M., Ramsden, Todd W. 1990. Tectonic evolution of the Troodos Ophiolite within the Tethyan Framework. *tectonics*, V.9.(4), August 1990, pp 881-823.
- Elliot, D., 1983, The construction of balanced cross-section. *Journal of Structural Geology*, v. 5, 101- 115.
- Ertürk, M. A., Sar, A., & Rizeli, M. E. (2022). Petrology, zircon U–Pb geochronology and tectonic implications of the A1-type intrusions: Keban region, eastern Turkey. *Geochemistry*, 82(3), 125882. <https://doi.org/10.1016/j.chemer.2022.125882>
- Erturk, M.A., Beyarslan, M., Chung, S. L., and Lin, T.-H. 2018. Eocene magmatism (Maden Complex) in the Southeast Anatolian Orogenic Belt: Magma genesis and tectonic implications. *Geoscience Frontiers*, 9(6): 1829–1847.
- Fleuty, M.J., 1964. The description of folds. *Proc. Geolog. Assoc. London* 75, 461–492.
- Goguel, J., 1962. *Tectonics*: Freeman, San Francisco, 348p.

- Golonka, J., 2004. Plate tectonic evolution of the southern margin of Eurasia in the Mesozoic and Cenozoic. *Tectonophysics*, 381, 235–273.
- Göncüoğlu, M.C., and Turhan, N. 1984. Geology of the Bitlis metamorphic belt. In *Geology of the Taurus Belt. Proceedings of the International Symposium on the Geology of the Taurus Belt, 26–29 September 1983*. Edited by O. Tekeli and M.C. Göncüoğlu. Mineral Research and Exploration Institute of Turkey (MTA), Ankara, 237–244.
- Görür, N., and Tuysuz, O. 1984. Cretaceous to Miocene paleogeographic evolution of Turkey: Implications for Hydrocarbon potential. *Journal of Petroleum Geology*, V.24.(2), April 2001, pp 119-146.
- Gülyüz, E., Durak, H., Özkaptan, M., Krijgsman, W., 2020. Paleomagnetic constraints on the early Miocene closure of the southern Neo-Tethys (Van region; East Anatolia): Inferences for the timing of Eurasia-Arabia collision *Glob. Planet. Chang.*, 185 (2020).
- Güven, A., A. Dinçer, M. E. Tuna and T. Çoruh 1992, Stratigraphic Evolution of the Campanian- Paleocene Autochthonous Succession of Southeast Anatolia. Ozan Sungurlu Symposium, Proceedings. In *Tectonics and Hydrocarbon Potential of Anatolia and Surrounding Regions*. Turkish Petroleum Corporation - Turkish Association of Petroleum Geologists, p. 238-261.
- Hall, Robert. Ophiolite emplacement and the evolution of the Taurus suture zone, southeastern Turkey. *GSA Bulletin* 1976; 87 (7): 1078–1088
- Hancock, P.L., 1985. Brittle microtectonics: principles and practice. *Journal of Structural Geology* 7, 437–457.
- Hills, E.S., 1961. Morphotectonics and the geomorphological sciences with special reference to Australia. *Quarterly Journal of the Geological Society*, 117(1-4), 77-90.
- Hüsing, S.K., Zachariasse, W.J., Van Hinsbergen, D.J.J., Krijgsman, W., Inceöz, M., Harzhauser, M., Mandic, O., and Kroh, A. 2009. OligoceneMiocene basin evolution in SE Anatolia, Turkey, Constraints on the closure of the eastern Tethys gateway. *Geological Society London Special Publications*, 311: 107-132.
- Janvier, P., F. Lethiers, O. Monod and O. Balkas 1984. Discovery of a vertebrate fauna at the Devonian Carboniferous boundary in Southeast Turkey. *Journal of Petroleum Geology*, V.7(2), p. 147-168.
- Jolivet, L., Faccenna, C., Huet, B., Labrousse, L., Le Pourhiet, L., Lacombe, O., et al. (2013). Aegean tectonics: Strain localization, slab tearing and trench retreat. *Tectonophysics*, 597, 1– 33

- Karaođlan, F., 2005. Gnedođru-Beđre (DođanŒehir-Malatya) arasında yzeyleyen tektonomagmatik birimlerin petrografisi ve jeokimyası. MSc Thesis, ukurova University, Adana, Turkey
- Karaođlan, F., Koller, F., Thni, M., Parlak, O., Kltzli, U., Parlak, O., 2012. U-Pb and Sm-Nd Geochronology of The Kizildađ (Hatay, Turkey) Ophiolite: Implications for The Timing and Duration of Suprasubduction Zone Type Oceanic Crust Formation in Southern Neotethys, V. Jeokimya Sempozyumu, Denizli, TR, p. 1.
- Karaođlan, F., Parlak, O., Hejl, E., Neubauer, F., Kltzli, U., 2016. The temporal evolution of the active margin along the Southeast Anatolian Orogenic Belt (SE Turkey): evidence from U/Pb, Ar/Ar and fission track chronology. *Gondwana Res.* 33, 190–208.
- Karaođlan, F., Parlak, O., Kloetzli, U., Thni, M., Koller, F., Hejl, E., & Rızaođlu, T. (2009, April). Geochronology and isotope geochemistry of the ophiolites and granitoids along the southeast Anatolian orogenic belt. In 62nd Geological Congress of Turkey, Ankara (Vol. 1317, p. 846847).
- Karaođlan, F., Parlak, O., Klotzli, U., and Thoni, M. 2013. U/Pb and Sm/Nd Geochronology of The Ophiolites from The SE Turkey: Implications for The Neotethyan Evolution. *Geodinamica Acta*, 26: 1–16. 201.
- Karaođlan, F., Parlak, O., Klotzli, U., Thoni, M., and Koller, F. 2013. U-Pb and Sm-Nd geochronology of the Kızildađ (Hatay, Turkey) ophiolite: implications for the timing and duration of supra-subduction zone type oceanic crust formation in the southern NeoTethys. *Geological Magazine*, 150(2): 283–299.
- Karaođlan, F., Parlak, O., Robertson, A., Thni, M., Kltzli, U., Koller, F., and Okay, A.I., 2013, Evidence of Eocene high-temperature/high-pressure metamorphism of ophiolitic rocks and granitoid intrusion related to Neotethyan subduction processes (DođanŒehir area, SE Anatolia), in Robertson, A.H.F., et al., eds., *Geological Development of Anatolia and the Easternmost Mediterranean Region: Geological Society of London Special Publication 372*, p. 249–272.
- Kaymakci, N. (2006). Kinematic development and paleostress analysis of the Denizli Basin (Western Turkey): Implications of spatial variation of relative paleostress magnitudes and orientations. *Journal of Asian Earth Sciences*, 27(2), 207-222.
- Kaymakci, N. White, S.H. and van Dijk P.M., 2000. Paleostress inversion in a multiphase deformed area: kinematic and structural evolution of the ankiri Basin (central Turkey), Part 1. In: Bozkurt, E., Winchester, J.A. and Piper, J.A.D. (eds.) *Tectonics and Magmatism in Turkey and the surrounding area. Geological Society London Special Publication No. 173.* 445-473.

- Kaymakci, N., İnceöz, M. & Ertepinar, P. 2006. 3D-architecture and Neogene evolution of the Malatya Basin: inferences for the kinematics of the Malatya and Ovacık fault zones. *Turkish Journal of Earth Sciences*, 15, 123–154.
- Ketin, I. 1966. Güneydoğu Anadolu'nun Kambiriyen tesekkülleri ve bunların Doğu İran Kambiriyeni ile mukayesesi: *M.T.A. Derg.* V. 66, p.75-88.
- Köylüoğlu, M. 1984. Hakkari yöresinin Dogger, Malm ve Senomaniyen birimlerinin biyostratigrafisi: *Türkiye 6. Petrol Kongresi*, p. 49-61.
- Livermore, R. Y. & Smith, A. G. 1984. Relative motions of Africa and Europa in vicinity of Turkey. In *Geology of the Taurus Belt* (eds O. Tekeli and M. C. Göncüoğlu), 1–10. Ankara: Maden Tetkik ve Arama Enstitüsü
- Mitchum, R.M.J., Vail, P.R. and Sangree, J.B. (1977) Stratigraphic Interpretation of Seismic Reflection Patterns in Depositional Sequences. In: Payton, C.E., Ed., *Seismic Stratigraphy: Applications to Hydrocarbon Exploration*, the American Association of Petroleum Geologist, Tulsa, Vol. 26, 117-133.
- Nabavi, S.T., Fossen, H., 2021. Fold geometry and folding—a review. *Earth-Sci. Rev.* 222, 103812.
- Oberhänsli, R., Bousquet, R., Candan, O., Okay, A., 2012. Dating subduction events in East Anatolia, Turkey *Turkish Journal of Earth Sciences*, 21, 1-17
- Oberhänsli, R., Candan, O., Bousquet, R., Rimmelé, G., Okay, A., Goff, J., 2010. Alpine high-pressure evolution of the eastern Bitlis complex, SE Turkey M. Sosson, N. Kaymakci, R.A. Stephenson, F. Bergerat, V. Starostenko (Eds.), *Sedimentary Basin Tectonics from the Black Sea and Caucasus to the Arabian Platform*, Special Publications, London, Geological Society, London (2010), 461-483.
- Oberhänsli, R., Koralay, E., Candan, O., Pourteau, A., Bousquet, R., 2014. Late Cretaceous eclogitic high-pressure relics in the Bitlis massif. *Geodinamica Acta* 1-17.
- Okay, A.I., Zattin, M., Cavazza, W., 2010. Apatite fission-track data for the Miocene Arabia-Eurasia collision. *Geology*. <https://doi.org/10.1130/G30234.1>.
- Özer, S. 1993. Relationships between Anatolian and Arabian plates during the Maastrichtian related to the rudist fauna. *Proceeding's 9th Petroleum Congress of Türkiye*, 255–262.
- Özgül N, Turuş A, Ozyardımcı N, Şenol M, Bingöl I, Uysal S (1982) Munzur Dağlarının Jeolojisi. MTA report no: 6995. Ankara, Turkey (in Turkish)
- Parlak, O. 2006. Geodynamic significance of granitoid magmatism in the Southeast Anatolian Orogen: geochemical and geochronological evidence from Göksun–Afşin (Kahramanmaraş, Turkey) region. *International Journal of Earth Sciences*, 95: 609–627.

- Parlak, O., Rızaođlu, T., and Bađcı, U. 2009. Tectonic Significance of the Geochemistry and Petrology of Ophiolites in Southeast Anatolia, Turkey. *Tectonophysics*, 473, 173–187.
- Perinçek, D. 1979. Geological investigation of Çelikhan-Sincik-Koçalı Area Adıyaman province: Istanbul Universitesi Fen Fakultesi Mecmuasi, Seri B 44, p.127-147.
- Perinçek, D. and I. Cemen 1992. Late Cretaceous-Paleocene Structural Evolution of the Structural Highs of Southeastern Anatolia. Ozan Sungurlu Symposium, Proceedings. In *Tectonics and Hydrocarbon Potential of Anatolia and Surrounding Regions*. Turkish Petroleum Corporation - Turkish Association of Petroleum Geologists, p. 386-403.
- Perinçek, D., 1979, The geology of Hazro-Korudađ-Çüngüs-Maden-Ergani-Hazer-Elazığ-Malatya area: Ankara, Turkey, Türkiye Jeoloji Kurumu Yayını, 34 p.
- Perinçek, D., 1989. Hakkari İli ve dolayının stratigrafisi, yapısal özellikleri, petrol imkanları: TPAO Arama Grubu rapor no.2545, 127s.
- Perinçek, D., 1990. Stratigraphy of the Hakkari province, southeast Turkey. *Turkish Association of Petroleum Geologists Bulletin* 2 (1), 21–68
- Perincek, D., and Kozlu, H. 1984. Stratigraphy and structural relation of the units in the Afşin-Elbistan-Dođanşehir Region. In *International Symposium on the Geology of the Taurus Belt, 1983*, Mineral Research and Exploration Institute, Ankara, Edited by O. Tekeli and C. Göncüođlu, 181–198.
- Perinçek, D., Duran, O., Bozdođan, N., and Çoruh, T. 1992. Stratigraphy and paleogeography evolution of the autochthonous sedimentary rock in the SE Turkey (Güneydođu Türkiye’de otokton sedimentary kayaların stratigrafisi ve paleocođrafik evrimi). *Ozan Sungurlu Symposium Proceedings* 274-305.
- Ramsay, J.G., 1967. *Folding and Fracturing of Rocks*. McGraw Hill, New York, 568p.
- Riba, O., 1976. Syntectonic unconformities of the Alto Cardener, Spanish Pyrenees: a genetic interpretation. *Sedimentary Geology*, 15(3), 213-233.
- Rigo de Righi, M., and Cortesini, A. 1964. Gravity tectonics in Foothills Structure Belt of southeast Turkey. *AAPG Bulletin*, 1911-1937.
- Rızaođlu, T., Parlak, O., Höck, V., Koller, F., Hames, W.E., Billor, Z., 2009. Andean type active margin formation in the eastern Taurides: Geochemical and geochronological evidence from the Baskil granitoid (Elazığ, SE Turkey). *Tectonophysics* 473, 188-207.
- Robertson, A.H.F. & Parlak, Osman & Rizaoglu, Tamer & Ünlügenç, Ü & İnan, N. & Taşlı, K. & Ustaömer, Timur. 2007. Tectonic evolution of the South

Tethyan ocean: Evidence from the Eastern Taurus Mountains (Elaziğ region, SE Turkey). 10.1144/GSL.SP.2007.272.01.14.

- Robertson, A.H.F., Parlak, O., Yıldırım, N., Dumitrica, P., and Taşlı, K. 2015. Late Triassic rifting and Jurassic–Cretaceous passive margin development of the Southern Neotethys: evidence from the Adıyaman area, SE Turkey.) *Int J Earth Sci (Geol Rundsch)* 105, 167–201.
- Robertson, A.H.F., Ünlügenç, U.C., İnan, N., and Taşlı, K. 2004. The Misis-Andırın complex: a mid-Tertiary melange related to late-stage subduction of the southern NeoTethys in Turkey. *Journal of Asian Earth Sciences*, 22: 413–453.
- Robertson, A.H.F., Ustaomer, T., Parlak, O., Ünlügenç, U.C., Taşlı, K., and İnan, N. 2006. The Berit transect of the Tauride thrust belt, S. Turkey: Late Cretaceous– Early Cenozoic accretionary/collisional processes related to closure of the southern NeoTethys. *Journal of Asian Earth Sciences*, 27: 108–145.
- Sar, A., Ertürk, M.A., Rizeli, M.E., 2019. Genesis of late cretaceous intra-oceanic arc intrusions in the Pertek area of Tunceli Province, eastern Turkey, and implications for the geodynamic evolution of the southern neo-tethys: results of zircon U-pb geochronology and geochemical and Sr–Nd isotopic analyses. *Lithos* 350–351
- Schildgen, T., Yıldırım, C., Cosentino, D., & Strecker, M. (2014). Linking slab break-off, Hellenic trench retreat, and uplift of the Central and Eastern Anatolian plateaus. *Earth-Science Reviews*, 128, 147-168. <https://doi.org/10.1016/j.earscirev.2013.11.006>
- Şengör, A.C. and Yılmaz, Y., 1981. Tethyan evolution of Turkey: a plate tectonic approach. *Tectonophysics*, 75(3-4), 181-241.
- Şengör, A.M.C., Y. Yılmaz and O. Sungurlu 1984. Tectonics of the Mediterranean Cimmerides: Nature and Evolution of the Western Termination of Paleotethys, *Geol. Soc. London Spec. Pub.*17, p. 77-112.
- Shan, Y., Suen, H., Lin, G., 2003. Separation of polyphase fault/slip data: an objective function algorithm based on hard division. *Journal of Structural Geology* 25, 829–840.
- Stampfli, G. and Borel, G.D. 2002. A plate tectonic model for the Paleozoic and Mesozoic constrained by dynamic plate boundaries and restored synthetic oceanic isochrons. *Earth and Planetary Science Letters*. 196 p.
- Sun, J., Sheykh, M., Ahmadi, N., Cao, M., Zhang, Z., Tian, S., Sha, J., Jian, Z., Windley, B. F., & Talebian, M. (2021). Permanent closure of the Tethyan Seaway in the northwestern Iranian Plateau driven by cyclic sea-level fluctuations in the late Middle Miocene. *Palaeogeography*,

Palaeoclimatology, Palaeoecology, 564, 110172.
<https://doi.org/10.1016/j.palaeo.2020.110172>

- Sungurlu, O. 1973. VI. bolge kuzeyinin jeolojisi ve petrol imkanlari: Turkiye 2. Petrol Kongresi Tebligleri, s. 85-107.
- Sungurlu, O., D. Perinçek, G. Kurt, E. Tuna, S. Dülger, E. Celikdemir and H. Naz 1985. Elazig-Hazar-Palu alaninin jeolojisi: T.C. Petrol Isleri Genel Mudurlugu Dergisi, no. 29, s. 85-189.
- Tardu, T. 1991. A sequence stratigraphic approach to the Mardin Group: tectonics and hydrocarbon potential of Anatolia and surrounding regions. In: Proceedings of Ozan Sungurlu Symposium. Turkish Association of Petroleum Geologists, Ankara, 306–332.
- Tearpock, D, J and Bischke, R, E, 2002, Applied Subsurface Geological Mapping: USA, A Simon&Schuster Company, 822 p.
- Tuna, D. 1973. VI. Bolge litostratigrafi birimleri adlamasinin aciklayici raporu: Turkiye Petrolleri Anonim Ortakligi, Rapor no. 813, 131 s.
- Wagner, C., and Pehlivanlı, M. 1987. Geological control in the distribution of source rocks reservoirs in upper Cretaceous carbonates of southeast Turkey. *J Petrol Sci Eng* 2: 105–114.
- Yazgan, E. 1984. Tauric-subduction (Malatya-Elazığ provinces) and its bearing on tectonics of the Tethyan realms in Turkey. In *The geological evolution of the eastern Mediterranean*. Edited by J.E. Dixon and A.H.F. Robertson. Geological Society of London Special Publication 17, 361–373.
- Yazgan, E., Chessex, R., 1991. Geology and Tectonic Evolution of the Southeastern Taurides in the Region of Malatya. *TPJD Bülteni* 3, 1-42.
- Yiğitbaş, E. and Yılmaz, Y. 1996. New evidence and solution to the Maden complex controversy of the Southeast Anatolian orogenic belt (Turkey). *Geologische Rundschau*, 85(2), 250-263.
- Yılmaz, E., and Duran, O. 1997. Güneydoğu Anadolu Bölgesi otokton ve allokton birimler stratigrafi adlama kılavuzu ('Lexicon' guide for stratigraphic nomenclature of the autochthonous and allochthonous units in the southeast Anatolian region). Turkish Petroleum Company, Educational Publication 31, 460 p.
- Yılmaz, Y. 1993. New evidence and model on the evolution of the southeast Anatolian Orogen. *Bulletin of the Geological Society of America* 105, 251–271.
- Yılmaz, Y., 2019. Southeast Anatolian Orogenic Belt revisited (geology and evolution). *Canadian Journal of Earth Sciences* 56 (11), 1163-1180.

- Yılmaz, Y., Çemen, I., Yi ğitbař, E., 2022. Tectonics of eastern anatolian plateau; final stages of collisional orogeny in Anatolia. *Earth Sp. Sci. Open Arch.* 1–40
- Yılmaz, Y., Yi ğitbas,, E. & Gen, S,. C. 1993. Ophiolitic and metamorphic assemblages of Southeast Anatolia and their significance in the geological evolution of the orogenic belt. *Tectonics*, 12, 1280–1297.

APPENDICES

A. Collected paleostress data

Fault strike	Fault dip	Striae trend	Striae plunge	Sense of Slip	T trend	T plunge	P trend	P plunge	Latitude	Longitude	Elevation (m)	Formation
5	26	54	20	TR	29	61	247	22	37,959902	41,346553	582	Selmo
331	23	37	21	TR	22	65	224	23	37,959902	41,346555	582	Selmo
342	19	32	15	TR	15	58	222	28	37,959914	41,34655	582	Selmo
19	14	67	10	TR	55	54	255	33	37,959933	41,346571	582	Selmo
325	16	44	15	TR	40	60	226	29	37,959933	41,346571	582	Selmo
72	15	77	1	TR	63	44	272	41	37,959933	41,346571	582	Selmo
312	36	35	35	TR	16	80	218	9	37,959997	41,346882	579	Selmo
309	35	30	34	TR	10	78	214	10	37,960019	41,346876	579	Selmo
356	63	16	35	TR	317	46	53	5	37,960086	41,346877	580	Selmo
332	41	9	27	TR	322	59	211	11	37,960133	41,346882	580	Selmo
349	36	26	24	TR	345	58	2266	16	37,960133	41,346882	580	Selmo
336	44	21	34	TR	325	65	222	6	37,960116	41,346882	580	Selmo
303	34	30	33	TR	23	78	211	11	37,96006	41,346888	580	Selmo
340	59	21	47	TR	301	61	48	8	37,960037	41,346894	579	Selmo
346	61	28	51	TR	302	62	56	12	37,960037	41,346894	580	Selmo
103	35	197	34	TL	204	79	15	10	38,019183	41,939864	710	Cungus
264	84	278	57	TR	209	42	332	31	38,019165	41,939832	711	Cungus
273	87	278	64	TR	207	41	341	37	38,019153	41,939826	711	Cungus
273	87	277	64	TR	207	41	340	37	38,019153	41,939826	712	Cungus
129	65	305	8	TL	349	23	84	11	38,053741	41,997705	748	Lice
128	62	304	10	TL	347	25	82	13	38,053741	41,997707	748	Lice
130	65	304	12	TL	349	26	85	8	38,053766	41,997717	747	Lice
106	65	278	16	TL	325	29	59	5	38,053779	41,997716	747	Lice
125	79	233	78	TL	31	55	218	34	38,053788	41,99768	745	Lice
89	46	153	42	TR	78	76	346	1	38,032681	42,031297	745	Cungus
320	71	351	56	TR	265	55	29	21	38,032656	42,03101	738	Cungus
319	72	341	49	TR	270	48	22	18	38,032656	42,03101	738	Cungus
320	70	351	55	TR	266	54	29	20	38,032656	42,03101	738	Cungus
313	60	59	59	TL	202	73	49	14	38,032656	42,03101	738	Cungus
312	52	14	49	TR	278	74	30	6	38,032636	42,031135	738	Cungus
312	52	14	49	TR	277	74	29	6	38,032636	42,031135	738	Cungus
129	75	233	74	TL	34	59	222	30	38,032661	42,031111	739	Cungus
122	73	288	39	TL	347	40	245	13	38,032662	42,031096	739	Cungus
125	71	292	34	TL	349	38	251	10	38,03266	42,031104	738	Cungus

228	46	262	29	TR	210	57	107	8	38,055442	42,060604	946	Gercus
231	46	258	25	TR	211	52	105	10	38,055442	42,060604	946	Gercus
230	48	265	32	TR	210	58	111	5	38,055442	42,060604	947	Gercus
192	41	240	32	TR	189	66	78	8	38,055442	42,060604	946	Gercus
244	75	259	43	TR	196	42	303	17	38,055439	42,060602	947	Gercus
230	75	244	44	TR	181	42	289	18	38,055456	42,060604	947	Gercus
246	88	248	41	TR	193	29	300	26	38,055484	42,060611	947	Gercus
63	89	243	32	TL	293	23	193	21	38,055484	42,060611	947	Gercus
235	74	244	30	TR	191	33	287	9	38,055466	42,060622	947	Gercus
20	86	195	48	TL	255	34	142	28	38,05551	42,06066	945	Gercus
18	85	193	49	TL	253	35	140	27	38,05551	42,06066	945	Gercus
10	79	170	59	TL	249	48	122	28	38,055517	42,060667	945	Gercus
221	75	228	24	NL	271	6	178	28	38,05562	42,061093	954	Hoya
243	67	249	13	NL	110	6	203	26	38,055606	42,061091	954	Hoya
232	81	234	12	NL	278	2	187	15	38,055606	42,061091	954	Hoya
228	74	237	27	NL	280	8	185	31	38,055583	42,061119	954	Hoya
228	74	238	28	NL	282	7	180	27	38,055583	42,061119	954	Hoya
228	74	237	27	NL	279	9	184	28	38,055583	42,061119	954	Hoya
228	74	239	26	NL	280	10	185	30	38,055583	42,061119	954	Hoya
228	74	237	28	NL	277	6	180	31	38,055583	42,061119	954	Hoya
223	65	241	33	NL	279	5	184	43	38,055583	42,061117	955	Hoya
229	61	241	20	NL	98	5	192	36	38,055583	42,061117	954	Hoya
250	32	285	19	NL	124	21	251	56	38,05559	42,061117	953	Hoya
251	34	284	20	NL	125	20	248	56	38,05559	42,061117	953	Hoya
251	34	284	20	NL	125	20	250	54	38,05559	42,061117	953	Hoya
252	48	270	19	NL	121	13	225	44	38,055581	42,061162	953	Hoya
245	60	254	15	NL	112	9	208	32	38,055577	42,061015	952	Hoya
245	64	253	16	NL	113	6	206	30	38,055572	42,061017	952	Hoya
256	63	260	8	NL	120	12	216	25	38,055557	42,061017	952	Hoya
245	61	252	12	NL	110	11	207	29	38,055531	42,06106	952	Hoya
248	64	254	11	NL	114	9	209	26	38,055535	42,061054	952	Hoya
78	87	253	52	NR	197	31	314	36	38,084995	41,765697	614	Hoya
63	84	230	64	NR	174	34	308	45	38,084984	41,765722	612	Hoya
63	83	230	64	NR	174	34	308	45	38,084984	41,765722	611	Hoya
254	84	266	63	NL	322	34	189	45	38,084968	41,765692	606	Hoya
255	84	268	65	NL	324	34	189	45	38,084932	41,765647	615	Hoya
255	84	265	61	NL	321	33	193	43	38,084841	41,765657	614	Hoya
85	83	252	64	NR	196	34	330	45	38,085011	41,76567	609	Hoya
80	83	246	63	NR	192	33	324	45	38,085011	41,76567	603	Hoya
80	83	244	67	NR	189	34	327	47	38,085021	41,765702	618	Hoya

262	81	273	50	NL	323	25	208	41	38,084989	41,765636	614	Hoya
267	80	291	55	NL	340	27	220	44	38,085011	41,765675	612	Hoya
60	78	226	49	NR	180	23	293	43	38,08504	41,765685	616	Hoya
256	74	62	41	NR	18	15	122	41	38,00001	41,000001	635	Hoya
266	74	63	54	NR	20	22	139	50	38,00001	41,000001	632	Hoya
276	80	84	49	NR	35	24	148	41	38,00001	41,000001	620	Hoya
275	79	82	49	NR	34	23	147	42	38,00001	41,000001	628	Hoya
86	76	201	75	TL	348	57	181	31	38,092139	41,767153	621	Gercus
99	89	270	83	TL	3	45	195	43	38,092148	41,767122	622	Gercus
81	77	162	77	TR	354	57	169	32	38,092154	41,767137	622	Gercus
218	58	236	26	TR	184	43	91	3	38,097746	41,771083	648	Hoya
206	59	228	32	TR	172	48	262	1	38,0978	41,771291	651	Hoya
211	68	227	35	TR	169	42	267	8	38,097804	41,771661	651	Hoya
190	72	194	11	TR	148	21	57	4	38,09784	41,771512	654	Hoya
221	67	230	20	TR	181	31	90	1	38,097888	41,771523	652	Hoya
218	65	253	50	TR	172	58	286	14	38,097946	41,771812	656	Hoya
221	63	254	47	TR	178	56	287	11	38,097991	41,771957	657	Hoya
222	71	237	37	TR	178	41	279	11	38,097964	41,771558	653	Hoya
220	65	232	23	TR	181	35	91	1	38,097938	41,771778	658	Hoya
218	54	239	26	TR	187	46	91	5	38,097856	41,771642	655	Hoya
212	62	231	32	TR	175	44	268	3	38,097961	41,771645	652	Hoya
19	84	196	27	NR	150	14	246	23	38,098049	41,771415	651	Hoya
187	79	198	44	TR	137	38	245	21	38,098002	41,771519	651	Hoya
187	79	198	44	TR	137	38	245	21	38,098002	41,771519	651	Hoya
192	80	201	43	TR	141	37	249	21	38,098158	41,771743	650	Hoya
190	80	198	38	TR	141	33	245	19	38,098135	41,771753	660	Hoya
190	80	198	38	TR	142	34	245	18	38,098135	41,771753	656	Hoya
204	66	204	1	NL	66	15	162	17	38,098107	41,771638	650	Hoya
198	70	198	0	NL	61	13	155	14	38,09821	41,771743	679	Hoya
197	69	197	0	NL	60	13	154	14	38,098172	41,771722	679	Hoya
196	81	52	-74	TL	95	-34	120	52	38,098026	41,771524	687	Hoya
195	80	64	-77	TL	98	-35	115	53	38,098019	41,771459	687	Hoya
194	82	104	-82	NL	104	53	104	-37	38,098019	41,771459	686	Hoya
194	82	104	-82	NL	104	52	104	-37	38,098019	41,771459	685	Hoya
192	82	11	2	TL	56	5	147	4	38,098019	41,771459	654	Hoya
194	86	36	-79	TL	95	-40	114	48	38,098039	41,771482	657	Hoya
191	84	131	-83	NL	97	50	104	-38	38,09809	41,771572	658	Hoya
189	83	9	1	TL	54	5	144	4	38,098123	41,771613	650	Hoya
189	83	9	1	TL	54	5	144	4	38,098146	41,771666	649	Hoya
189	83	9	1	TL	54	5	144	4	38,098146	41,771666	648	Hoya

187	83	7	1	TL	52	6	142	4	38,098233	41,771736	656	Hoya
189	81	54	-77	TL	91	-35	109	53	38,098227	41,771743	649	Hoya
188	83	80	-83	TL	97	-38	101	51	38,098227	41,771743	647	Hoya
194	88	194	2	NL	239	0	149	3	38,098192	41,771757	656	Hoya
194	88	194	2	NL	239	0	149	2	38,098214	41,771699	683	Hoya
179	78	180	4	NL	44	5	135	11	38,098171	41,771693	706	Hoya
179	78	180	5	NL	44	5	135	11	38,098171	41,771693	707	Hoya
179	78	180	5	NL	44	5	135	11	38,098157	41,771799	719	Hoya
142	78	321	1	TL	6	9	97	7	38,098108	41,771712	709	Hoya
177	67	356	3	TL	39	18	134	13	38,098023	41,771586	697	Hoya
177	67	356	3	TL	40	18	134	14	38,098023	41,771586	697	Hoya
177	67	356	3	TL	40	18	134	14	38,098023	41,771586	697	Hoya
181	70	1	3	TL	44	15	137	12	38,097999	41,771544	697	Hoya
181	70	1	3	TL	44	15	138	12	38,098003	41,771542	699	Hoya
181	70	1	3	TL	44	15	138	12	38,098003	41,771542	702	Hoya
23	69	47	46	TR	336	50	85	15	38,030657	42,020769	719	Cungus
19	64	48	43	TR	338	53	82	10	38,030625	42,02079	714	Cungus
19	64	47	45	TR	337	55	81	12	38,030625	42,02079	715	Cungus
19	64	50	42	TR	335	49	84	9	38,030625	42,02079	715	Cungus
10	64	81	63	TR	297	69	94	19	38,030691	42,020742	712	Cungus
10	64	80	62	TR	289	68	90	18	38,030691	42,020742	712	Cungus
3	64	67	61	TR	295	67	84	20	38,030692	42,020745	714	Cungus
3	64	70	62	TR	297	69	86	17	38,030692	42,020745	714	Cungus
20	71	51	56	TR	326	54	88	20	38,000001	42,000001	715	Cungus
30	62	89	58	TR	332	68	108	15	38,000001	42,000001	715	Cungus
28	58	95	55	TR	333	73	107	11	38,000001	42,000001	718	Cungus
24	57	78	51	TR	342	69	98	9	38,000001	42,000001	715	Cungus
209	49	227	18	TR	182	43	78	13	38,030757	42,020897	721	Cungus
212	57	229	24	TR	178	42	84	5	38,030665	42,021003	721	Cungus
220	52	230	12	TR	187	36	85	16	38,030647	42,021017	721	Cungus
312	82	122	52	TL	188	41	71	27	38,03081	42,020936	722	Cungus
124	75	154	61	TR	64	53	195	25	38,030818	42,020904	722	Cungus
124	75	154	62	TR	65	50	193	26	38,030818	42,020904	722	Cungus
138	80	147	46	TR	86	38	196	23	38,03079	42,020909	722	Cungus
271	59	353	58	TR	194	75	358	13	38,030779	42,020854	724	Cungus
261	50	348	50	TR	183	84	350	5	38,030757	42,020827	724	Cungus
266	59	4	59	TL	164	74	350	14	38,030712	42,02082	724	Cungus
265	59	306	47	TR	226	62	334	9	38,030724	42,020965	724	Cungus
273	61	313	49	TR	230	61	342	11	38,030726	42,020952	725	Cungus
272	61	313	50	TR	232	60	340	12	38,030726	42,020952	726	Cungus

166	64	333	24	NR	114	0	24	37	38,002199	42,055285	1005	Cungus
158	69	330	20	NR	109	0	19	30	38,002177	42,055269	1008	Cungus
159	71	327	31	NR	285	7	21	36	38,002214	42,055288	1008	Cungus
160	56	327	19	NR	111	9	14	38	38,002243	42,055318	1007	Cungus
159	73	327	36	NR	284	12	24	38	38,002233	42,055312	1008	Cungus
297	77	47	76	TL	200	57	31	32	38,001963	42,055038	1002	Cungus
288	76	27	75	TL	195	58	20	30	38,001967	42,05504	1002	Cungus
291	83	70	79	TL	193	51	28	37	38,001952	42,055036	1001	Cungus
290	76	31	75	TL	197	58	22	30	38,001966	42,055042	1002	Cungus
300	45	66	39	TL	130	70	229	3	38,002017	42,055034	1001	Cungus
301	44	68	37	TL	128	70	230	4	38,001964	42,055046	1001	Cungus
294	49	63	41	TL	134	69	43	0	38,001967	42,055019	1001	Cungus
23	72	24	4	TR	340	15	247	9	38,010511	42,0646	1032	Cungus
27	75	206	1	NR	342	10	251	11	38,010497	42,064591	1032	Cungus
24	79	203	4	NR	339	4	248	10	38,010497	42,064591	1032	Cungus
77	62	239	30	NR	202	1	293	43	37,000001	42,000001	1018	Gercus
74	63	231	36	NR	195	5	291	48	37,000001	42,000001	1017	Gercus
80	65	243	32	NR	205	4	299	42	37,000001	42,000001	1018	Gercus
273	57	69	32	TL	126	50	216	1	37,976993	42,062878	980	Gercus
259	52	58	24	TL	108	46	207	8	37,977033	42,06285	980	Gercus
260	45	56	22	TL	102	50	208	13	37,977075	42,062863	981	Gercus
139	86	145	54	TR	80	38	200	31	37,000001	42,000001	952	Gercus
149	51	241	51	TL	51	83	240	6	37,977306	42,064475	976	Gercus
145	58	227	57	TR	68	76	232	13	37,976982	42,064634	957	Gercus
143	60	228	60	TR	61	74	231	15	37,976982	42,064634	957	Gercus
144	54	225	53	TR	76	80	230	8	37,976982	42,064634	956	Gercus
146	54	232	53	TR	64	81	234	9	37,976982	42,064634	948	Gercus
19	55	19	0	NL	238	24	339	24	37,000001	42,000001	806	Hoya
17	55	196	1	TL	235	24	337	23	37,000001	42,000001	806	Hoya
17	51	195	1	TL	233	27	337	25	37,000001	42,000001	806	Hoya
17	52	188	11	TL	230	34	332	17	37,000001	42,000001	806	Hoya
17	52	21	4	NL	237	22	341	29	37,000001	42,000001	806	Hoya
126	87	303	44	TL	0	32	251	27	37,743936	41,287031	563	Hoya
131	85	306	44	TL	4	33	255	25	37,743936	41,287031	563	Hoya
123	87	306	47	TL	358	34	246	28	37,743936	41,287031	562	Hoya
125	88	303	50	TL	3	35	247	31	37,743936	41,287031	562	Hoya
125	87	302	44	TL	358	31	249	27	37,743936	41,287031	563	Hoya
121	87	298	43	TL	354	32	245	26	37,743936	41,287031	562	Hoya
120	87	297	45	TL	354	32	244	28	37,743921	41,287007	562	Hoya
122	87	299	45	TL	356	33	246	28	37,743921	41,287007	561	Hoya

123	84	296	50	TL	358	37	243	27	37,743921	41,287007	561	Hoya
112	79	155	74	NL	193	33	36	54	37,743905	41,287113	563	Hoya
114	77	159	72	NL	194	31	40	55	37,743905	41,287113	563	Hoya
109	78	165	75	NL	193	32	30	56	37,743905	41,287113	563	Hoya
107	78	161	75	NL	190	32	28	56	37,743905	41,287113	562	Hoya
103	78	155	75	NL	186	33	25	55	37,743905	41,287113	562	Hoya
94	78	153	76	NL	178	32	13	56	37,743905	41,287113	563	Hoya
111	78	162	74	NL	193	32	33	56	37,743907	41,287097	563	Hoya
109	78	160	74	NL	191	32	31	55	37,743907	41,287097	563	Hoya
96	83	145	80	NL	180	37	12	52	37,743916	41,287059	563	Hoya
95	83	131	78	NL	176	37	15	51	37,743916	41,287059	563	Hoya
92	86	132	83	NL	177	40	7	48	37,743889	41,287046	564	Hoya
93	87	115	82	NL	176	41	11	47	37,743889	41,287046	564	Hoya
100	87	115	78	NL	179	40	22	46	37,743889	41,287046	564	Hoya
84	89	91	82	NL	167	43	2	45	37,743892	41,287069	564	Hoya
93	86	121	81	NL	176	40	11	48	37,74389	41,287065	563	Hoya
107	83	160	81	NL	192	38	23	51	37,743932	41,287009	564	Hoya
106	83	148	79	NL	189	37	24	51	37,743932	41,287009	564	Hoya
106	86	139	82	NL	190	41	22	48	37,743932	41,287009	564	Hoya
106	86	140	82	NL	190	40	22	48	37,743932	41,287009	564	Hoya
100	85	137	81	NL	184	39	18	49	37,743938	41,287023	564	Hoya
100	85	137	81	NL	184	39	18	49	37,743938	41,287023	564	Hoya
106	84	134	78	NL	186	38	27	49	37,743937	41,287017	564	Hoya
97	83	139	79	NL	180	37	16	51	37,743937	41,287017	564	Hoya
105	84	165	83	NL	192	39	19	50	37,743946	41,287021	564	Hoya
101	84	149	81	NL	186	38	17	50	37,743946	41,287021	564	Hoya
97	84	128	78	NL	178	38	18	50	37,743974	41,287014	564	Hoya
99	69	155	65	NL	178	22	30	63	37,74396	41,286959	562	Hoya
98	69	155	65	NL	178	23	30	63	37,74396	41,286959	562	Hoya
124	79	158	72	NL	201	33	51	53	37,74396	41,286959	562	Hoya
109	69	163	64	NL	188	22	42	63	37,743981	41,286961	562	Hoya
111	73	172	70	NL	193	27	34	60	37,743985	41,286962	562	Hoya
114	77	185	76	NL	200	31	30	57	37,743985	41,286962	562	Hoya
105	77	170	75	NL	190	31	23	57	37,743969	41,286909	564	Hoya
101	77	162	75	NL	185	31	20	57	37,743969	41,286909	563	Hoya
96	77	176	76	NL	184	32	9	58	37,743969	41,286909	564	Hoya
97	77	175	76	NL	185	32	10	57	37,743969	41,286909	564	Hoya
96	77	175	76	NL	184	32	11	58	37,743969	41,286909	563	Hoya
102	74	170	72	NL	187	28	21	60	37,743993	41,286903	563	Hoya
105	77	154	73	NL	186	31	29	56	37,743993	41,286903	564	Hoya

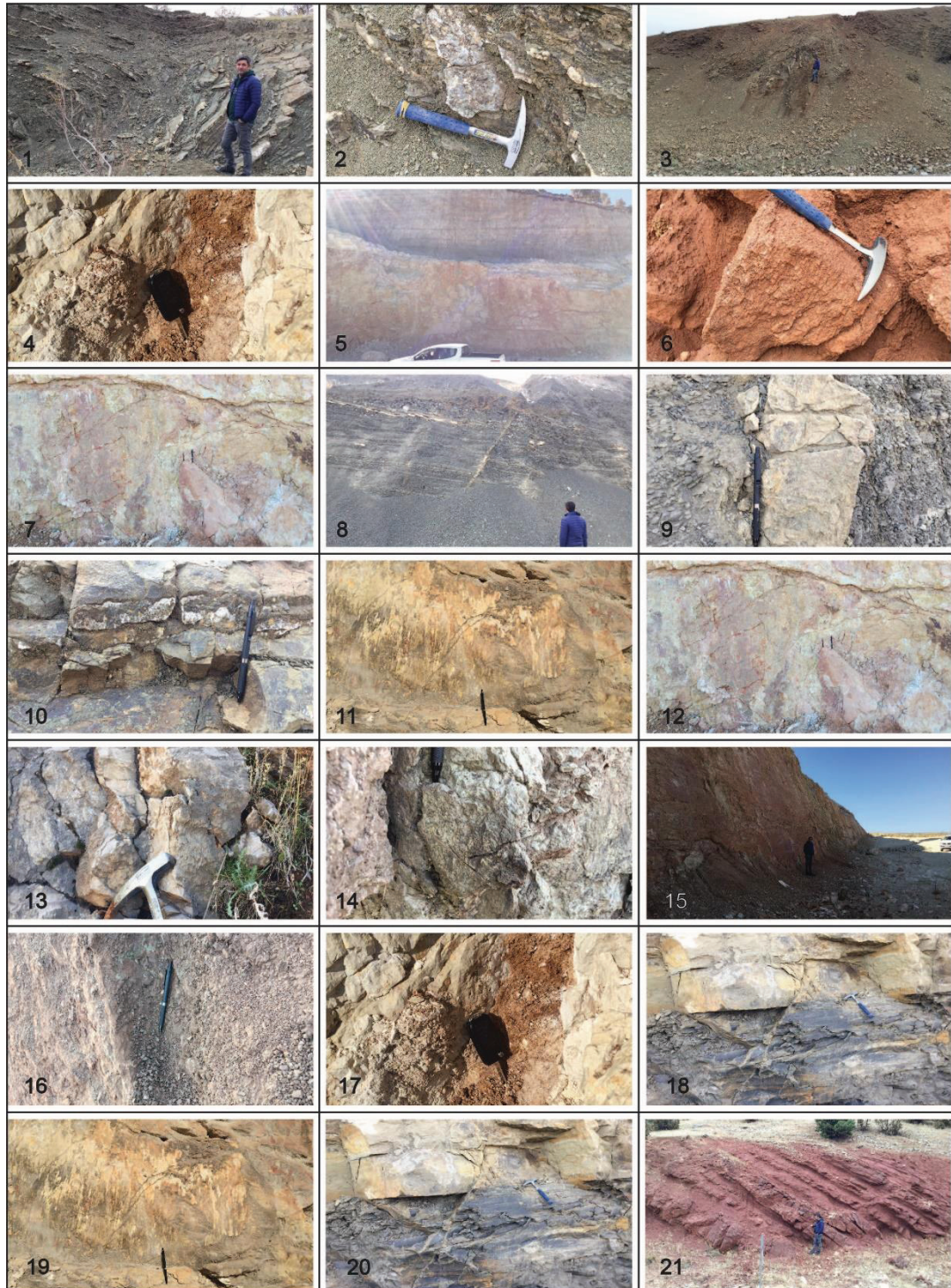
97	77	175	76	NL	185	32	11	57	37,743993	41,286902	564	Hoya
102	77	184	77	NL	191	31	14	58	37,743993	41,286902	563	Hoya
56	86	222	74	TL	311	47	160	39	37,701838	41,461132	647	Hoya
59	85	218	75	TL	315	48	161	38	37,701838	41,461132	648	Hoya
56	86	223	72	TL	309	48	161	38	37,701838	41,461132	648	Hoya
63	83	217	75	TL	318	49	164	37	37,701838	41,461132	647	Hoya
71	80	213	74	TL	326	53	172	33	37,701838	41,461132	648	Hoya
74	83	228	74	TL	329	50	176	36	37,701838	41,461132	648	Hoya
71	82	221	74	TL	325	51	173	35	37,701838	41,461132	647	Hoya
66	81	215	73	TL	320	51	168	34	37,701838	41,461132	648	Hoya
57	81	205	73	TL	311	52	159	34	37,701838	41,461132	648	Hoya
57	82	207	74	TL	313	51	159	35	37,701838	41,461132	648	Hoya
65	80	205	74	TL	321	53	169	33	37,701839	41,461129	648	Hoya
58	83	210	75	TL	315	50	160	36	37,701839	41,461129	648	Hoya
240	89	245	78	TR	162	44	319	42	37,701839	41,461129	648	Hoya
61	76	185	73	TL	318	58	158	30	37,701839	41,461135	649	Hoya
55	74	180	70	TL	309	59	154	28	37,701829	41,461134	649	Hoya
55	74	181	70	TL	309	59	154	28	37,701829	41,461134	649	Hoya
58	87	228	74	TL	312	45	163	40	37,701829	41,461134	648	Hoya
60	83	212	75	TL	316	50	162	36	37,701831	41,461129	648	Hoya
300	66	336	52	TR	252	58	9	15	37,562553	41,365893	1040	Gercus
304	67	340	54	TR	252	58	14	17	37,562537	41,365893	1040	Gercus
300	67	337	54	TR	249	58	10	17	37,562537	41,365893	1040	Gercus
299	66	339	55	TR	247	60	10	17	37,56254	41,365893	1040	Gercus
296	63	338	52	TR	249	62	7	13	37,56254	41,365893	1040	Gercus
296	70	330	56	TR	242	56	6	20	37,562524	41,365902	1040	Gercus
297	70	328	54	TR	245	54	5	19	37,562525	41,365899	1040	Gercus
295	69	328	54	TR	243	56	4	18	37,562527	41,365912	1040	Gercus
296	69	332	57	TR	241	57	7	19	37,562504	41,36589	1040	Gercus
293	71	322	54	TR	241	53	1	20	37,562508	41,365888	1040	Gercus
291	70	321	54	TR	239	54	359	19	37,562508	41,365888	1039	Gercus
291	67	351	64	TR	222	65	11	21	37,562456	41,365933	1039	Gercus
291	68	336	60	TR	232	61	5	20	37,562456	41,365933	1040	Gercus
286	67	344	63	TR	220	65	6	20	37,562472	41,365933	1040	Gercus
283	65	348	62	TR	215	68	5	19	37,562473	41,365929	1040	Gercus
291	65	347	60	TR	230	66	10	18	37,562473	41,365929	1040	Gercus
292	68	354	65	TR	221	65	13	22	37,562473	41,365929	1040	Gercus
290	71	343	66	TR	221	61	9	24	37,562473	41,365929	1040	Gercus
291	71	350	68	TR	218	62	12	25	37,562473	41,365929	1040	Gercus
289	69	335	61	TR	229	61	5	21	37,562473	41,365929	1040	Gercus

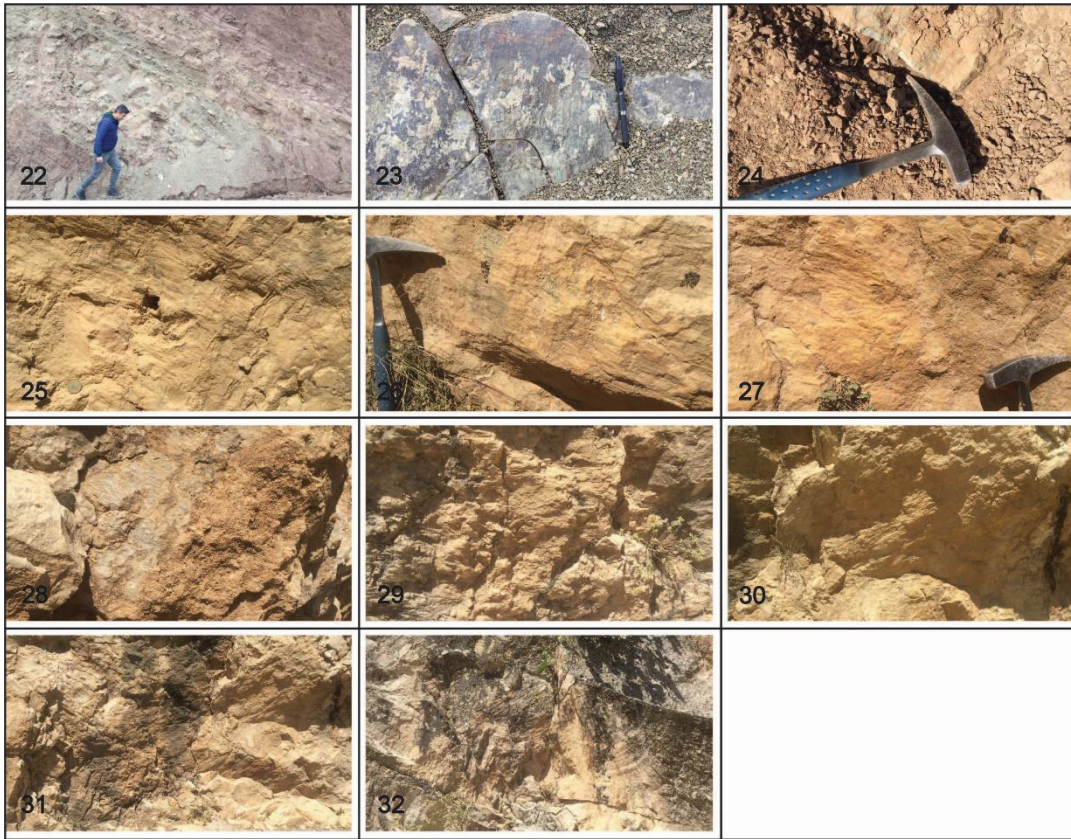
291	70	330	60	TR	233	58	4	21	37,562368	41,36618	1040	Gercus
289	70	332	61	TR	228	59	4	22	37,562372	41,366168	1042	Gercus
295	71	340	63	TR	232	59	11	24	37,562372	41,366168	1041	Gercus
294	71	332	61	TR	234	58	7	23	37,562384	41,366161	1042	Gercus
293	71	332	61	TR	234	58	7	23	37,562384	41,366162	1042	Gercus
296	60	359	57	TR	240	71	16	14	37,56235	41,366248	1042	Gercus
292	68	351	64	TR	224	64	13	21	37,56235	41,366248	1042	Gercus
288	61	4	60	TR	215	73	13	15	37,56235	41,366248	1042	Gercus
294	64	344	57	TR	240	65	10	16	37,56235	41,366248	1042	Gercus
294	64	344	57	TR	240	64	10	16	37,56235	41,366248	1042	Gercus
285	66	328	56	TR	232	61	358	17	37,562355	41,366249	1042	Gercus
289	68	326	55	TR	236	58	359	18	37,562355	41,366249	1042	Gercus
295	60	359	57	TR	238	71	15	13	37,562355	41,366249	1042	Gercus
334	43	41	40	TR	337	77	232	3	37,552389	41,754496	946	Hoya
342	45	39	39	TR	333	72	235	2	37,552384	41,754493	946	Hoya
334	54	20	44	TR	303	66	44	4	37,552355	41,754532	966	Hoya
330	61	2	43	TR	291	56	34	8	37,552357	41,754573	965	Hoya
337	52	22	42	TR	311	65	46	2	37,552348	41,754595	965	Hoya
339	44	33	37	TR	332	70	230	4	37,552322	41,754637	969	Hoya
332	72	5	59	TR	275	55	43	23	38,230517	40,775288	951	Hoya
336	66	10	51	TR	287	57	44	15	38,230551	40,775231	934	Hoya
338	65	7	45	TR	295	53	42	12	38,230584	40,775189	929	Hoya
337	70	1	47	TR	290	49	40	16	38,230652	40,775121	931	Hoya
330	73	2	61	TR	270	55	41	24	38,230631	40,775117	930	Hoya
333	57	54	56	TR	260	77	59	12	38,230671	40,774987	929	Hoya
333	56	58	55	TR	253	78	61	11	38,230671	40,774987	931	Hoya
339	46	61	45	TR	324	85	65	1	38,23069	40,774954	932	Hoya
1	40	58	35	TR	6	72	252	7	38,230681	40,774937	933	Hoya
331	60	43	58	TR	265	73	54	14	38,230708	40,774903	931	Hoya
331	59	46	58	TR	263	74	55	13	38,230708	40,774903	930	Hoya
337	64	41	61	TR	272	68	58	18	38,230708	40,774903	926	Hoya
332	60	43	58	TR	266	73	55	14	38,230715	40,774845	926	Hoya
57	53	115	49	NL	133	6	22	72	37,843918	41,726115	844	Germav
60	52	109	45	NL	131	4	30	68	37,843918	41,726115	842	Germav
52	52	113	48	NL	129	6	17	74	37,843918	41,726115	841	Germav
63	52	120	47	NL	138	5	32	72	37,843884	41,726119	842	Germav
59	51	115	45	NL	133	3	32	72	37,843879	41,726102	844	Germav
52	53	123	51	NL	134	7	5	78	37,843879	41,726102	845	Germav
58	48	122	44	NL	135	2	39	76	37,843839	41,726055	840	Germav
55	54	110	48	NL	129	6	20	70	37,843916	41,726115	846	Germav

58	53	127	51	NL	139	7	14	77	37,84396	41,726168	841	Germav
53	53	126	52	NL	136	7	4	78	37,84396	41,726168	842	Germav
53	53	126	51	NL	135	7	6	78	37,84396	41,726168	832	Germav
295	72	14	71	TR	211	62	22	26	37,482355	37,706963	614	Gaziantep
321	69	46	68	TR	235	65	50	23	37,482355	37,706963	614	Gaziantep
306	77	20	76	TR	220	57	33	32	37,482349	37,706974	614	Gaziantep
305	80	9	78	TR	221	54	31	34	37,482349	37,706974	614	Gaziantep
308	69	35	68	TR	220	65	37	23	37,482343	37,707001	614	Gaziantep
309	69	26	68	TR	226	65	37	23	37,482346	37,707003	614	Gaziantep
309	69	29	68	TR	225	65	36	23	37,482346	37,707003	615	Gaziantep
185	59	3	2	TL	45	23	143	18	37,844989	38,415963	680	Hoya
184	51	186	1	TR	147	27	43	24	37,844989	38,415963	680	Hoya
186	54	186	2	TR	148	26	46	22	37,844987	38,415969	677	Hoya
180	59	90	-58	TL	90	-13	90	75	37,844987	38,415969	676	Hoya
184	53	4	1	TL	43	25	145	24	37,844987	38,415969	676	Hoya
196	71	14	4	TL	59	16	152	10	37,844987	38,415969	676	Hoya
190	66	7	6	TL	51	21	146	12	37,844987	38,415969	676	Hoya
195	47	11	4	TL	49	32	156	24	37,845003	38,415982	676	Hoya
184	49	186	2	TR	148	29	42	26	37,845003	38,41596	675	Hoya
195	68	12	8	TL	56	21	150	9	37,845003	38,41596	676	Hoya
192	67	9	8	TL	54	22	147	9	37,845003	38,41596	676	Hoya
272	57	312	45	TR	235	62	339	7	37,840641	38,404426	758	Hoya
275	66	314	54	TR	225	59	346	16	37,840641	38,404426	758	Hoya
266	70	303	58	TR	210	57	338	21	37,840611	38,404429	758	Hoya
264	66	307	56	TR	211	61	337	17	37,840611	38,404429	758	Hoya
255	54	316	50	TR	216	73	332	7	37,840556	38,404414	758	Hoya
243	49	291	40	TR	222	67	132	0	37,840556	38,404456	759	Hoya
244	51	287	39	TR	220	63	311	0	37,840556	38,404456	759	Hoya
241	49	284	37	TR	221	63	127	2	37,840589	38,404471	759	Hoya
230	45	282	38	TR	220	69	120	3	37,840589	38,404471	759	Hoya
261	63	301	51	TR	214	61	331	13	37,840603	38,404479	758	Hoya
247	62	300	56	TR	195	66	323	15	37,840572	38,404496	758	Hoya
256	71	292	59	TR	199	56	328	22	37,840572	38,404496	758	Hoya
287	55	4	54	TR	224	78	12	9	37,838055	38,310914	991	Midyat Group
287	59	11	58	TR	205	75	15	14	37,83804	38,310922	992	Midyat Group
288	57	10	57	TR	210	77	15	12	37,83804	38,310922	993	Midyat Group
287	56	10	55	TR	211	78	14	11	37,838027	38,310977	992	Midyat Group
295	58	12	57	TR	224	76	20	12	37,83802	38,310976	992	Midyat Group
253	76	6	75	TL	155	58	347	31	37,825651	38,307625	831	Midyat Group
258	81	3	80	TL	165	53	350	35	37,825651	38,307621	832	Midyat Group

262	86	326	86	TR	174	48	351	41	37,825614	38,307615	832	Midyat Group
260	85	308	83	TR	175	49	346	40	37,825614	38,307615	832	Midyat Group
254	84	29	81	TL	157	50	349	38	37,82561	38,307623	832	Midyat Group
258	82	10	81	TL	165	52	351	37	37,825611	38,307617	832	Midyat Group

B. Paleostress location photos





CURRICULUM VITAE

PERSONAL INFORMATION

Surname, Name: Tuncer, Mustafa
Nationality: Turkish (TC)

EDUCATION

Degree	Institution	Year of Graduation
MS	Missouri S&T Geology and Geophysics	2013
BS	Firat University Geological Engineering	2009

WORK EXPERIENCE

Year	Place	Enrollment
2013-Present	Turkish Petroleum Corporation	Structural Geologist

FOREIGN LANGUAGES

English